ANTONIO CAGGIANO

Meso-mechanical analysis of Steel Fiber Reinforced Cementitious Composites

Dottorato di Ricerca
in Ingegneria delle Strutture e del Recupero Edilizio ed Urbano

Università degli Studi di Salerno
Sede amministrativa

Doctorado
en Ciencias Exactas e Ingeniería

Universidad Nacional de Tucumán
Sede Convenzionata per la Tesi in Co-Tutela Internazionale

Antonio Caggiano

MESO-MECHANICAL ANALYSIS OF STEEL FIBER REINFORCED CEMENTITIOUS COMPOSITES

X Ciclo - Nuova Serie (2008- 2011)

UNIVERSITÀ DI SALERNO
DIPARTIMENTO DI INGEGNERIA CIVILE
Dottorato di Ricerca in Ingegneria delle Strutture e del Recupero Edilizio ed Urbano
X Ciclo N.S. (2008-2011)

UNIVERSIDAD NACIONAL DE TUCUMAN (ARGENTINA)
FACULTAD DE CIENCIAS EXACTAS Y TECNOLOGÍA
Doctorado en Ciencias Exactas e Ingeniería

Tesi di Dottorato in Co-Tutela Internazionale

MESO-MECHANICAL ANALYSIS OF STEEL FIBER REINFORCED CEMENTITIOUS COMPOSITES

Antonio Caggiano

I Tutors
Prof. José Guillermo Etse
Prof. Enzo Martinelli

Il Coordinatore
Prof. Ciro Faella

To my family
To my uncle Rosario Fabio

Acknowledgements

I would like to express my highest gratitude to Enzo and Guillermo, advisors of this thesis, for their time, effort and guidance during this work. They were (and are) like (academical) fathers. Really thanks!!! I would like to thank the wonderful people I met during this "fantastical journey". Starting from all my colleagues of the University of Salerno, I would sincerely like to thank Carmen, Carmine, Gaetano, Jamil and Marco for the nice atmosphere at the laboratory which have contributed to create. My special thanks to Prof. Ciro Faella, Ph.D. coordinator and head of our group. Then, going to Argentina, my second country (in the last five years I lived more there than in Italy), I would like to deeply thank my colleagues Marianela, Paula, Sonia, Hernan, Javier, Juan and Victor for our nice and fruitful time spent at the Universities of Buenos Aires and Tucuman. Also to Eng. Raul Husni, Eng. Gregorio Pytlowany and Eng. Claudia Traiber of FIUBA for their continuous support. I extend my gratefulness to the authorities of UNISA and I also gratefully acknowledge the hospitality received in the Argentinean institutions of Buenos Aires (UBA) and Tucuman (UNT). I also acknowledges Officine Maccaferri S.p.A. for the financial support during the experimental research. Calcestruzzi Irpini S.p.A., General Admixtures S.p.A. and PreFabios S.r.l. are also acknowledged for having supplied materials for the experimental campaign. Further acknowledgments to Vittorio Cammarano and Diego Morrone for the collaboration in the experimental activity during their M.Sc. projects.

At last, it is very difficult to express here, in a few lines, how much I appreciate the support of my family and the people close to me. At first, I sincerely thank my girlfriend (in the next weeks my wife) Sandra for her love, unconditional support, patience and encouragements during these last years. I would like to thank to my family, my parents Andreina and Domenico, my sister Caterina, my grandparents Rina, Pina and Giovanni, to Carmine for being always present. To my grandparent Antonio and my uncle Rosario present in my heart every day. I would like to express my highest thank to the family of my girlfriend, her parents Victoria and Miguel, Adrian and Florencia.

Caggiano, Salerno, Italia, April 13th 2013 A. C.

Abstract

The mechanical behavior of cement-based materials is greatly affected by crack propagation under general stress states. The presence of one or more dominant cracks in structural members modifies its response, possibly leading to brittle failure modes. The random dispersion of short steel fibers in cement materials is a new methodology used for enhancing the response in the post-cracking regime. The behavior of Fiber-Reinforced Cementitious Composite (FRCC), compared to conventional plain concrete, is characterized by several advantages, e.g., higher tensile and shear resistance, better post-cracking ductility, higher fracture energy, etc.

In this framework, this thesis deals with both the experimental investigation and computational modeling of the mechanical behavior of FRCC. A great part of the work is intended at reporting the formulation and validation of a novel constitutive model aimed at simulating the stress-cracking response of FRCC and considering most complex fracture occurrences in mixed-modes of failure.

Firstly, the results of an extensive experimental campaign, performed at the Laboratory of Materials testing and Structures (LMS) of the University of Salerno, is presented in which the possible influence of combining different fiber types on the resulting properties of Steel Fiber Reinforced Concrete (SFRC) is investigated. Particularly, the study concerns the four-point bending behavior of pre-notched SFRC beams where the influence of the amount of fibers and types on the first-crack strength and the whole post-cracking behavior is analyzed.

After this, an innovative approach for reproducing the fiber effects on the cracking phenomena of the concrete/mortar matrix is proposed. The well-known discrete crack approach based on zero-thickness interface elements is used to model the interaction between fibers and mortar as well as its degradation during fracture processes under mode I, II and/or mixed ones. The matrix degradation is modeled by means of a fracture energy-based softening law formulated in the framework of the flow theory of plasticity. Then, two fundamental aspects of the fiber-mortar interaction are considered in the model, i.e., the bond behavior of fibers bridging the crack opening and the dowel effect derived by possible relative transverse displacements of the two faces of the crack. The

inclusion of fibers and the above two effects are taken into account by means of the well-known “Mixture Theory”. Particular emphasis and importance is dedicated to the description and modeling of the overall debonding behavior of fibers embedded in cementitious matrices. Actually, the adhesive interaction between fibers in concrete matrix is of key importance in controlling the post-cracking response of FRCC. A unified formulation for simulating the overall bond behavior of fibers embedded in cementitious matrices is also presented. The proposed unified formulation is intended as a key element to be possibly employed in numerical models aimed at explicitly simulating the mechanical behavior of FRCC by taking into account the discrete nature of such materials and the contributions of the various constituents within the framework of the so-called meso-mechanical approach.

The predictive capabilities of the aforementioned discontinuous approach for failure analyses of fiber reinforced cementitious composite are evaluated at different levels of observation. Particularly, the discrete crack formulation is employed and validated to simulate the fracture behavior of FRCC at constitutive, mesoscopic and macroscopic levels of observations. Several numerical results are performed to demonstrate if such proposal, based on the non-linear interface formulation, is capable to lead realistic predictions of failure processes of FRCC under different load scenarios and considering a wide spectrum of fiber contents and types. It is also analyzed if the proposed formulation is able to capture the significant influence of the fiber content on the maximum strength and post-peak ductility in mode I, II and mixed ones showing the capability of the cracking formulation to capture the complex interaction mechanisms between fibers and matrix.

Furthermore, a simpler stress-crack opening model based on a hinge-crack approach, already available in the scientific literature, is proposed while the experimental results reported in this thesis are taken as reference for its validation. The model represents a reformulation of a fictitious crack model and is based on fracture mechanics concepts where the stress-crack opening relationship is accounted in a similar way obtainable by considering the pure “mode I” case of the discontinuous proposal formulated in general sense for mixed-modes of fracture. A closed-form solution for the stress-crack opening law with the explicit consideration of the fiber actions is considered for such a formulation. The model predictions, compared with the experimental measures, are performed to demonstrate the soundness of the model to reproduce the mechanical response of SFRC members in terms of Force-Crack Tip Opening Displacement ($CTOD$) curves.

At last, both plain concrete and FRCC are analyzed and modeled by means of a novel microplane-based plasticity formulation. A continuum (smeared-crack) formulation, based on the non-linear microplane theory combined with the well-known “Mixture

Theory", is considered for describing the fiber effects on the failure behavior of FRCC. The constitutive formulation, failure analyses and the interactions between cementitious matrix and steel fibers are similarly approached as outlined for the discontinuous proposal. The capabilities of the microplane model to capture the significant enhancement in the post-cracking behavior of FRCC, with particular emphasis on the fracture and post-peak strengths, are finally evaluated by considering some experimental data available in scientific literature.

Contents

List of Figures

List of Figures

List of Tables

1 Introduction

1.1 Scientific framework and general overview

In the last century, concrete has become the most widely used construction material and, then, a great part of the existing built stock, as well as the majority of infrastructures currently under construction are made of Reinforced Concrete (RC). In spite of the wide variability of the relevant physical and mechanical properties of cohesive-frictional media, cement-based materials like concretes are characterized by low strength and brittle response in low confinement and tensile stress states. These deficiencies can be mitigated by randomly adding short reinforcements into the cementitious mortar [Gettu, 2008].

The development of innovative cementitious materials, going to the direction of High Performance Concretes (HPCs) in general sense, represents a new field of interest of the Material Science and Structural Engineering. In this sense, Fiber-Reinforced Cementitious Composite (FRCC), obtained by randomly mixing short fibers (made out of steel, plastic, natural materials, recycled reinforcements, etc.) into conventional cementitious materials, is a structural material characterized by a significant residual tensile strength in post-cracking regime in comparison to plain concrete and enhanced capacity to absorb strain energy due to fiber bridging mechanisms across the opening cracks [Brandt, 2008, di Prisco et al., 2009, Nguyen et al., 2010].

Fiber-Reinforced Cementitious Composites (FRCCs) may result in a less brittle and possible quasi-ductile behavior, even in the case of tensile loading, and exhibit strain-hardening processes with multiple cracks and relatively large energy absorption prior to failure. Composites with these relevant features take the name of High Performance Fiber-Reinforced Cementitious Composites (HPFRCCs) [Naaman and Reinhardt, 2006].

1.1.1 Fiber types: material and geometry

Fiber Reinforced Cementitious Composite (FRCC) is a concrete made of hydraulic cement, aggregates and discrete reinforcing fibers. There are several fiber types employed for engineering applications and classified according to their material. Particularly the following categories can be listed:

- steel fibers of different shapes and dimensions;
- glass fibers;
- fibers of synthetic materials such as polypropylene, polyethylene and polyolefin, polyvinyl alcohol (PVA);
- recycled ones (PET, from waste tires);
- natural fibers.

Referring to its geometry, fiber is defined as "short" and "discrete". One of the proprieties which characterizes its geometry is represented by the "aspect ratio": it represents the ratio between the fiber length and the equivalent diameter. The latter is calculated as the diameter of a circle having an area equal to the cross-section of the considered fiber.

The most important short reinforcements, for structural concrete, are surely represented by the steel fibers. The length and diameter of such fibers, used for FRCC, do typically not exceed the 75 mm and 1 mm, respectively. As example the Figure 1.1 outlines various steel fiber geometries characterized by different shapes for improving the fiber-matrix bond and aimed at increasing the efficiency of the bridging effect of fibers.

Recent researches on Fiber-Reinforced Concrete (FRC) also address to the possible use of mixed fibers of different material and/or geometry which can, in principle, play a synergistic role in enhancing flexural and post-cracking response of FRC members. This kind of fiber-reinforced cement-based composites are known as Hybrid FRC (HyFRC). Experimental tests aimed at investigating the HyFRC failure behavior in direct tension have been performed, among others, by Sorelli et al. [2005] and Park et al. [2012]. The mechanical behavior measured by means of indirect tensile tests have been proposed on Hy-Polypropylene FRC [Hsie et al., 2008], Hy-Steel FRC [Banthia and Sappakittipakorn, 2007, Kim et al., 2011] or combining several material fibers: i.e., Carbon/Steel/Polypropylene FRC [Yao et al., 2003] or Steel/Palm/Synthetic FRC [Dawood

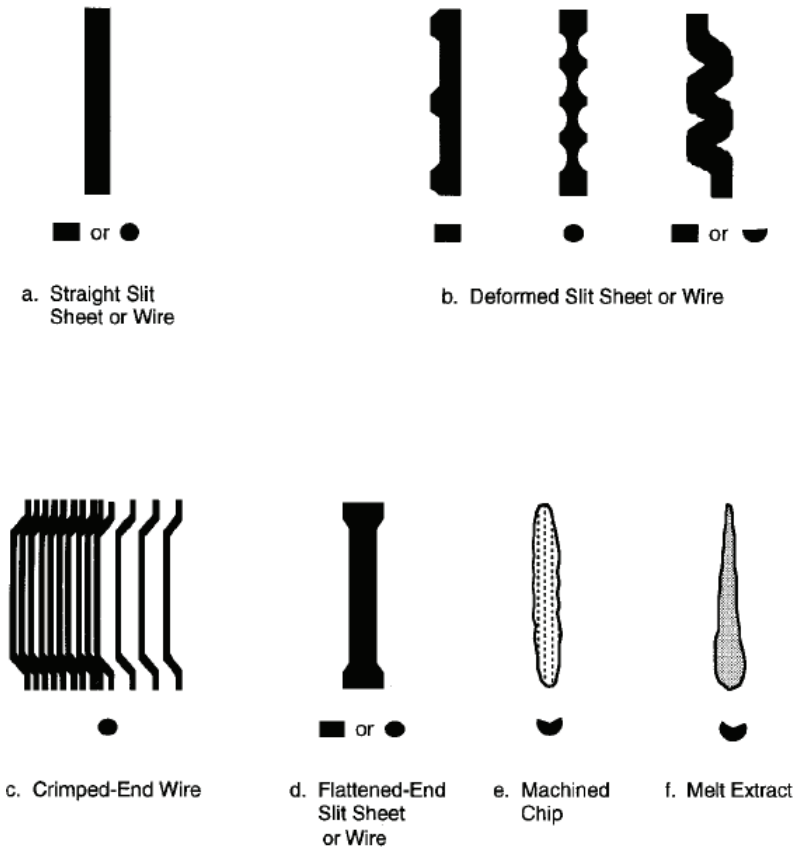

Figure 1.1: Steel fiber types proposed by ACI-544.1-96 [1996].

and Ramli, 2011, 2012]. The experimental results on contoured double cantilever beam specimens with steel and polypropylene FRC have been discussed by Banthia and Nandakumar [2003]. Other relevant contributions regarding HyFRC with lightweight aggregates [Libre et al., 2011], high-volume coarse fly ash [Sahmaran and Yaman, 2007], RC beams with mixed fibers [Ding et al., 2010], HyFRC exposed to high temperatures [Chen and Liu, 2004, Ding et al., 2012] or self compacting HyFRC [Ding et al., 2009, Dawood and Ramli, 2010, Akcay and Tasdemir, 2012] have also been proposed within the scientific community.

1.1.2 Mechanical behavior and characterization

Since fiber bridging mechanisms mainly take place under cracked regime of the concrete matrix, the mechanical behavior of uncracked members is rather influenced by

the fiber addition. This represents the main reason that the **first crack** tensile strength of FRCC is mainly related to the matrix strength and very low influenced by the fiber contents.

Contrarily, the **post-cracking** tensile residual strengths are the most influenced mechanical properties due to the fiber bridging mechanisms. These quantities can be experimental obtained by means of direct or indirect tensile tests. Due to the well-known difficulties in realizing experimental studies throughout direct uniaxial tests in tension, the adoption of bending systems in pre-notched beams is the most common method (as largely used in the most widespread international standards and codes) for the FRCC characterization. However, although the bending response involves only mode I of failure, is quite different from the uniaxial tension: for example a FRCC, with a strain-softening response in tension, could behave in strain-hardening manner in bending. The possible classification of FRCC, based on the critical volume fractions of fibers to achieve strain-hardening or deflection-hardening responses under tension and/or flexion, $V_{fcri(tension)}$ and $V_{fcri(bending)}$ respectively (being V_f the fiber volume fraction), is proposed in Figure 1.2.

In compression, the effect of fibers on the peak strength can be practically considered negligible. Actually, for the compressive stress ranges, the constitutive behavior up to peak strength for the plain concrete is commonly similar for the FRCC. Then, fibers mainly improve the ductility of the composite in post-peak region (this fact is valid not only under compression states but in general under all modes of loading: such as tension, shear, torsion and flexion).

Several recently published experimental researches, related to the mechanical characterization of FRCC, allow to clarify relevant aspects of such a material. Among others, the evaluation of the workability dependence on the fiber distributions by Ferrara and Meda [2006] and the analysis of the fiber orientations on the compaction procedures by Gettu et al. [2005] can be taken as a reference of experimental campaigns aimed at studying the proprieties of FRCC at fresh state. Experimental tests aimed at investigating the FRCC failure behavior in compression and tension have been performed, among others, by Ezeldin and Balaguru [1992] and Barros and Figueiras [1999], respectively. Also, the work by Shannag et al. [1997] that defines the mechanisms governing the fiber pull-out response, and those by Buratti et al. [2011] and Tlemat et al. [2006] that analyze the post-cracking behavior of three- and four-point bending tests, respectively. Finally, it should be noted the failure behavior evaluations of Steel Fiber Reinforced Concrete (SFRC) subjected to multiaxial compressive states by Fantilli et al. [2011] and to the Brazilian test conditions by Liu et al. [1997]. Moreover, fibers spread up within the

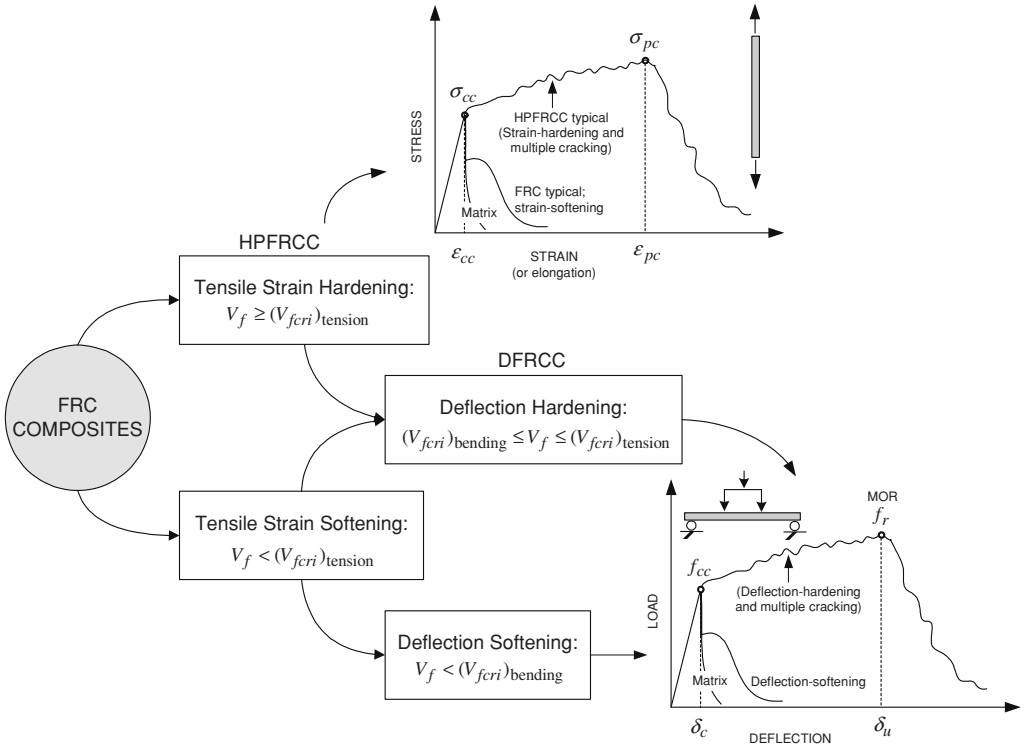

Figure 1.2: FRC composites based on the classification proposed by Naaman and Reinhardt [2006].

concrete matrix also influence its durability [Mechtcherine, 2012], as they control the crack opening and reduce the diffusion phenomena which lead to corrosion [El-Dieb, 2009]. While the benefits of fibers on strength and ductility have been demonstrated in Valle and Buyukozturk [1993] and Khaloo and Kim [1997] based on direct shear test results on FRCC specimens characterized by different strength levels. Also, the positive effect of fibers on the dynamic response under impact actions has been investigated by Xu et al. [2012].

1.2 Theoretical proposals for concrete-like materials

In the recent past, several theoretical models have been proposed for investigating the mechanical behavior of cement-based material like concrete and FRCC. Plenty of these researches deal with the investigation of the fracture behavior of both plain concrete and FRCC and are aimed at obtaining a realistic prediction of the physical

and mechanical behavior of concrete at different scales of observation. An extended literature review of the proposed constitutive theories for modeling concrete behavior can be founded in Dolado and van Breugel [2011].

In this section a detailed and comprehensive review on two main aspects of concrete modeling is reported. On the one hand the classification of the most popular constitutive theories of concrete failure regarding their **observation scales** is treated in subsection 1.2.1, on the other hand a literature review of the cracking models and discontinuous approaches aimed at modeling quasi-brittle materials is reported in subsection 1.2.2.

1.2.1 Observation scale and modeling

Concrete and other cementitious materials are multiphase (composite) materials. It can be considered as a homogeneous continuum material at the macroscale, while at lower levels of observation, it should be considered as a multiphase material as highlighted in Figure 1.3.

Based on the above discussion and referring to the fiber-reinforced concrete, it can be stated that constitutive models, currently available in the scientific literature for simulating the mechanical response of such a composite, can be classified on the basis of their observation scale as proposed in the following subsections.

Structural-scale models

These models, based on the general continuum approach, capture the essence of structural members made of FRCC. The major objective of these formulations is to build up a simply method for predicting the structural behavior of FRCC structures. In these models, the bridging fiber effect is typically incorporated through "stress-crack opening relationships" in which the transformation of the crack opening in strain (as commonly adopted for structural-type model) is achieved by means of the so-called "stress-crack width". Typical examples of structural-scale formulations are those related to either cross-sectional moment versus curvature or panel shear force versus lateral displacements. For instance, structural-scale formulations for FRCC structures have been proposed by Stang and Olesen [1998] and Lee and Barr [2003] who characterize the complete load-deflection curve of FRCC three-point beams, as well as Billington [2010] that proposes a formulation for retrofit analysis of structures made of ductile FRCC. Regarding the bending behavior of FRCC beams, a comprehensive overview can

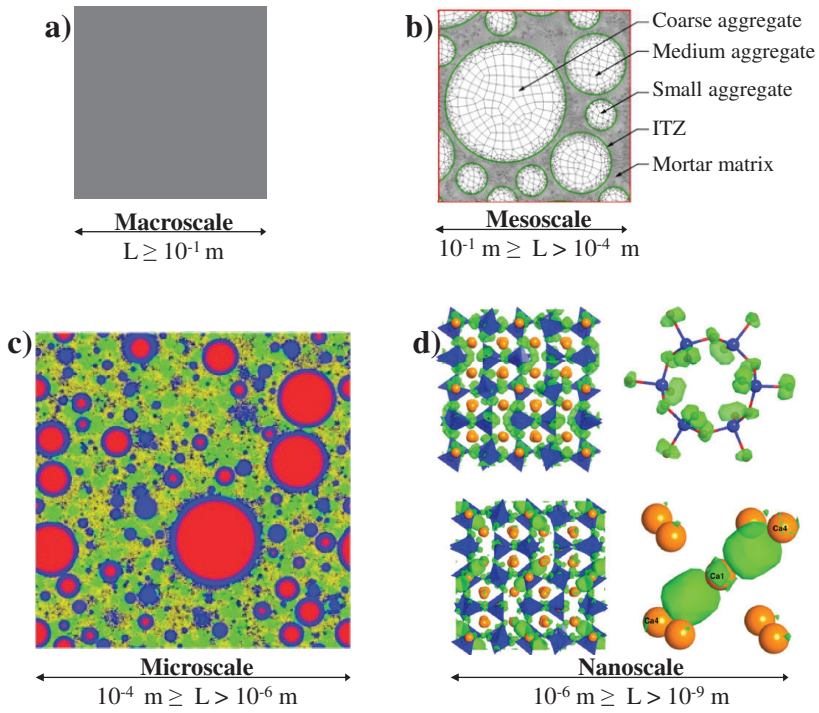

Figure 1.3: Concrete materials under different scales of observation: (a) macroscale continuum, (b) 2-D mesoscale concrete analysis [Kim and Al-Rub, 2011], (c) modeling the hydration of cements at microscale [Bishnoi and Scrivener, 2009] and (d) simulations by means of electrophilic and nucleophilic attack at a nanoscale standpoint [Puertas et al., 2011].

be found in the RILEM-TC162-TDF [2003] where different constitutive relationships for structural applications and based on the stress equilibrium in the critical cracked section have been presented.

Macroscale models

In the field of the computational failure mechanics, intended as the set of mathematical and computational tools aiming at identifying the failure mechanisms and predicting the critical and post-critical behavior of structures, the "material failure" represents one of its main ingredients. Cement-based materials can be ideally considered as continuum media and modeled within the theoretical framework of the material failure. Such constitutive proposals are based on the classical continuum formulations (i.e., strain localization [Cervera et al., 2010], smeared cracking [Einsfeld et al., 1997]) or the enriched continuum ones (e.g., Cosserat media [Jeong et al., 2011], gradient enrichment

[Vrech and Etse, 2009], non-local models [Nguyen, 2008]).

Among others, the contributions for FRCC by Hu et al. [2003], who propose a single smooth biaxial failure surface for FRCC, the one by Seow and Swaddiwudhipong [2005], who introduce a five parameter failure criterion for FRCC with both straight and hooked-end steel fibers, and the paper by Minelli and Vecchio [2006], dealing with a model based on a modification of the compression field theory, are worthy of mention. Other relevant contributions can be found in Beghini et al. [2007] and Guttema [2003].

Mesoscale models

A better understanding of concrete failure mechanics subjected to external loading can be obtained by considering the mesoscale behavior of the material. The mesoscale of concrete can be idealized by considering different phases which constitute such a composite. Thereby, the interaction among the different phases of the composite (i.e. fibers, matrix and coarse aggregates and their interfaces) is explicitly considered. Mesoscale approaches aimed at modeling fracture phenomena in quasi-brittle materials can be divided into:

- continuum models [Kim and Al-Rub, 2011],
- discrete models [Lopez et al., 2008a,b] and
- combinations between them dealing with the so-called continuum/discrete hybrid models [Grassl and Rempling, 2008].

Novel meso-mechanical approaches have recently been utilized for modeling the fracture behavior in FRCC. Key contributions in this field are due to Schauffert and Cusatis [2012] and Schauffert et al. [2012] who consider the effect of fibers dispersed into a Lattice Discrete Particle Model (LDPM), the lattice-based model by Leite et al. [2004], the work of Oliver et al. [2012] based on a two scale approach in which the macroscopic model at the structural level takes into account the meso-structural phenomenon associated with the fiber-matrix bond-slip action, the proposals of Bolander and Saito [1997] and Leung and Geng [1998] in which each fiber has been modeled as a discrete entity, the mesoscale two-step homogenization approach proposed by Gal and Kryvoruk [2011], as well as the models of Radtke et al. [2010] and Cunha et al. [2012] in which the FRCC has been considered as a two-phase material.

These approaches provide a much more powerful and physically-based description of the material behavior, modeling with special accuracy the fracture processes and the

mechanical properties of plain and fiber reinforced concretes. The apparent macroscopic behavior observed in each proposal is a direct consequence of the more complex mesoscopic phenomena that take place at the level of the material heterogeneities. Furthermore, the principal disadvantages of these approaches are related, on the one hand to the higher computational cost, and, on the other hand to the huge number of variables involved in the model formulation.

Microscale models

Microscale models are based on the observation level in which the cement paste is described in terms of their chemical constituents whose thermodynamical reaction, during the time, plays a key role.

Typical constitutive proposals are aimed at modeling the microstructure of the composite in which the cement paste is represented by "a network" of cement particles. These latter, reacting together with a variety of components, lead to obtain hydration products. The numerical modeling of this kind of hardened formations requires a broad scale of mathematical formulations and numerical techniques [van Breugel, 1991]. The outcome of a micro-model could be used to derive material properties for modeling concrete at higher observation levels (i.e., at the meso or macroscales) [Schlangen et al., 2007]. The basic properties of the concrete at the micro-level, during the development of the microstructure when the concrete hardens, has been performed for example with the HYMOSTRUC model proposed by van Breugel [1991] and extended to 3D analyses by Koenders [1997].

In this field, contributions dealing with the microstructure hydration/dehydration concepts have often been treated as competitive approaches for describing properties of early age concrete [De Schutter, 2004, Caggiano et al., 2012d] and concrete degradation under high temperatures (i.e., Pont and Ehrlacher [2004], Ulm and Coussy [1999a] and Ulm and Coussy [1999b]), respectively.

Nanoscale models

Atomistic simulations at nano-level have typically been conceived for modeling the cementitious crystals (namely, tobermorite and jennite). Particularly, several and innovative researches have been carried out to accurately describe and model the crystalline phases of cementitious materials such as the C_3A [Manzano et al., 2009b], etringite [Manzano et al., 2008], C_3S, $\beta - C_2S$ and portlandite [Manzano et al., 2009a].

Despite the innovative nature of these researches, they are still few employed in the field of material science and/or structural and civil engineering.

Multi-scale models

Materials, in general, are characterized by an intrinsic non-homogeneous structure. For example at the micro-structural level, they can be composed by a number of heterogeneities that actually govern the overall mechanical response of the material at higher scales of observation (i.e., macro and structural scales). Thus, suitable theoretical tools, based on multi-scale formulations, represent the direct link to describe a more general failure behavior, captured at higher observation levels, by analyzing phenomena intrinsically developed at lower scales of analysis.

In those models coupling effects of the different scales of observation are taken into account: i.e. nano-, micro-, meso-, macro- and structural scales of observation. The objective of these formulations is to develop an efficient approach to simulate the multi-scale and multi-physics nature of the problem under consideration. In this topic, it is worth mentioning the works proposed by Kabele [2002], Hund and Ramm [2006], Etse et al. [2012] and Sanchez et al. [2013], among others.

1.2.2 Crack modeling strategies and approaches

The mechanical behavior of concrete-based materials is greatly affected by crack propagation under general stress states. The presence of one or more dominant cracks in a concrete member modifies its structural behavior, possibly leading to brittle failure modes. The random dispersion of short steel fibers in cement materials is a new methodology used for enhancing the response in the post-cracking regime. As already mentioned, the behavior of Fiber-Reinforced Cementitious Composite (FRCC), compared to conventional plain concrete, is characterized by several advantages: i.e., higher tensile and shear resistance, better post-cracking ductility, higher fracture energy, etc.

Theoretical models and numerical tools are needed for describing both cracking onset and propagation in non-homogeneous quasi-brittle materials such as FRCC. In fact, simulating cracking phenomena in solids is still an open issue in computational mechanics. Concrete cracks have traditionally been treated by means of classical continuum or smeared-crack approaches in which the fracture zone is considered to be distributed in a certain region of the solid [De Borst and Gutierrez, 1999]. Despite its advantages from the computational point of view, classical concrete models based on

the smeared crack approach suffer a strong FE-size dependence of the localization band width [Oliver, 1989, Rots et al., 1985]. Different regularization procedures have been proposed to avoid this severe deficiency of the smeared-crack approach [Willam et al., 1984]. On the one hand, several continuum models are based on fracture mechanics concepts leading to fracture energy release regularization, but still suffering from loss of objectivity of the deformation pattern [Etse and Willam, 1994]. In this field, fracture energy-based concrete models are, among others, due to Bazant and Oh [1983], Shah [1990], Carpinteri et al. [1997], Comi and Perego [2001], Duan et al. [2007] and Meschke and Dumstorff [2007]. On the other hand, more sophisticated constitutive theories have been proposed to solve the strong mesh dependency which appears when the governing equations turn ill posed [Carosio et al., 2000]. They are based on rate dependency, higher strain gradients, micropolar theory, etc. Among others, it can be here referred the contributions by Vardoulakis and Aifantis [1991], de Borst et al. [1995], Peerlings et al. [2004], Lee and Fenves [1998] and Etse et al. [2003].

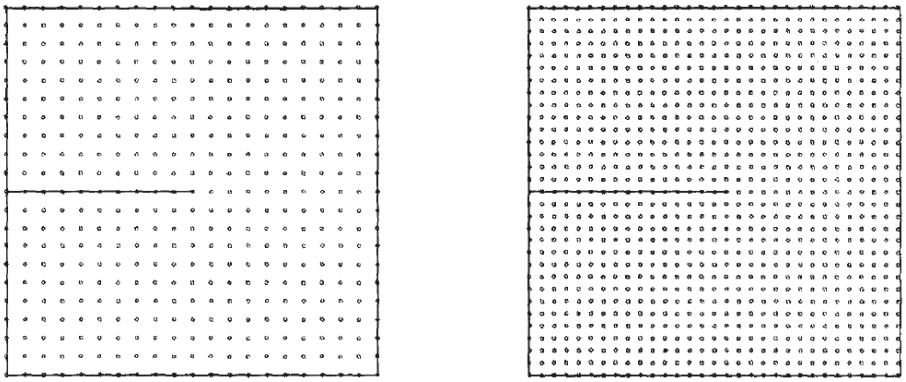

Figure 1.4: Numerical specimens based on the Element-Free Galerkin method by Belytschko et al. [1995] for near-tip crack problems.

Discrete Crack Approaches (DCAs) aimed at incorporating strain or, moreover, displacement discontinuities into standard FE procedures have progressively became an attractive and effective alternative to the smeared-crack approach. Several proposals are currently available in literature to introduce crack discontinuities within FE domains and are outlined in the following paragraphs.

Element-Free Galerkin (EFG) method: this represents an attractive tool to model the crack propagation in brittle materials. The EFG approach differs from the classical Finite Element Method (FEM) because the discretization is achieved by only nodal data

(Figure 1.4): no element connectivity is stated. The description of the geometry and the numerical model formulation of the problem is only given on a set of nodes jointly with a description of exterior and interior boundaries. Significant contributions to static elasticity and fracture mechanics have been proposed in Belytschko et al. [1995], Belytschko et al. [2000], Singh et al. [2011] and Zhang et al. [2008].

Lattice models: within the framework of discontinuous crack approaches and fracture behavior of concrete elements, the lattice-based model is a simple and effective tool for understanding the physics of fracture processes in concrete members [Yip et al., 2006]. Lattice type models can be based on either truss [Schorn and Rode, 1987] or beam elements as in Figure 1.5 [Lilliu and van Mier, 2003].

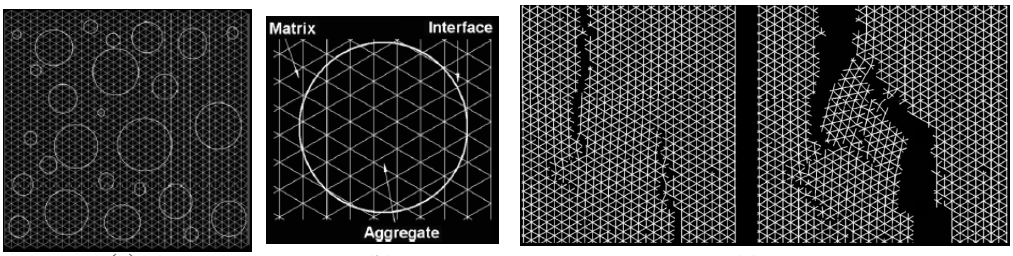

Figure 1.5: Meso-mechanical simulation by means of the beam lattice model [Lilliu and van Mier, 2003]: (a) geometry, (b) definition of matrix, interface and aggregates, (c) crack pattern simulations.

Strong discontinuity approaches: they incorporate displacement discontinuities in the finite element formulations for capturing arbitrary crack propagations within fixed FE mesh without loosing mesh objectivity. Particularly, new types of finite elements, essentially formulated by enriching the (continuous) displacement fields with additional discontinuities, are proposed. It can be distinguished two families of strong discontinuity depending on the technique to enrich the displacement field:

- the Embedded strong discontinuity Finite Elements (E-FEM), proposed among others by Dvorkin et al. [1990], Oliver [1996], Oliver et al. [2002] and Armero and Linder [2009], which are able to reproduce displacement "jumps" through "elemental discontinuity enrichments" (Figure 1.6a), and

- the eXtended Finite Element Method (X-FEM) in which the discontinuity of the displacement field is captured by means of "nodal enrichments" (Figure 1.6b) by Wells and Sluys [2001] and Liu et al. [2011].

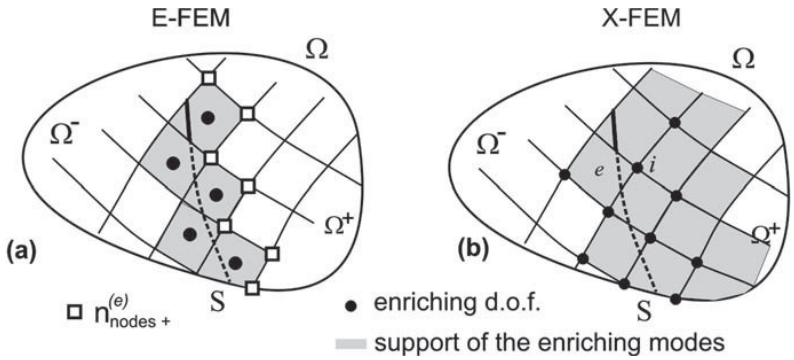

Figure 1.6: Elemental (E-FEM) and eXtended (X-FEM) enrichment approaches [Oliver et al., 2006].

An interesting comparison between the E-FEM and X-FEM approaches, to model strong discontinuities in concrete materials, has been highlighted by Oliver et al. [2006].

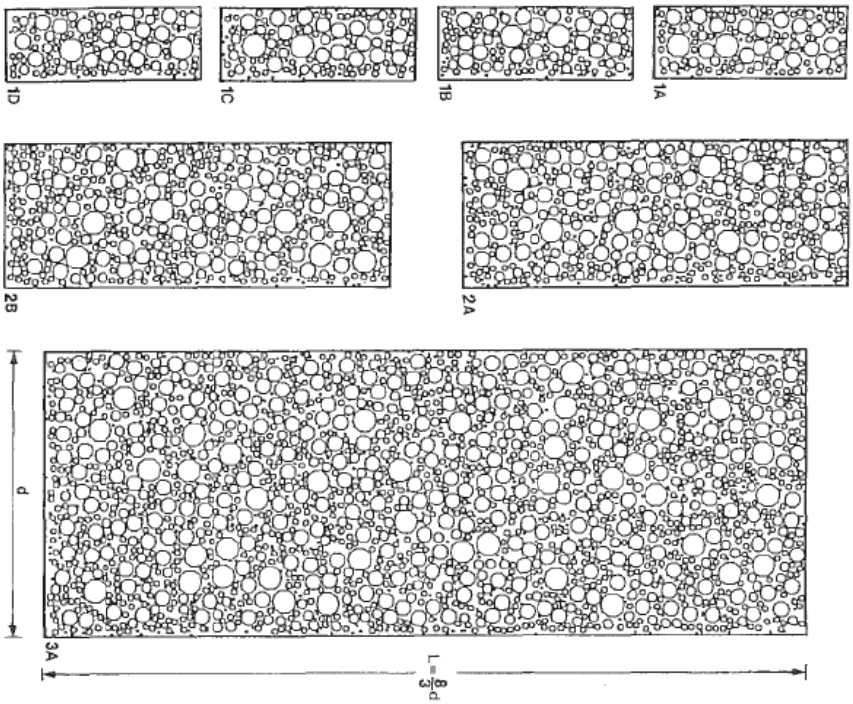

Figure 1.7: Unnotched specimens in tension of various sizes with randomly generated particles by Bazant et al. [1990].

Particle models: these models are based on the formulation of the microscopic inter-

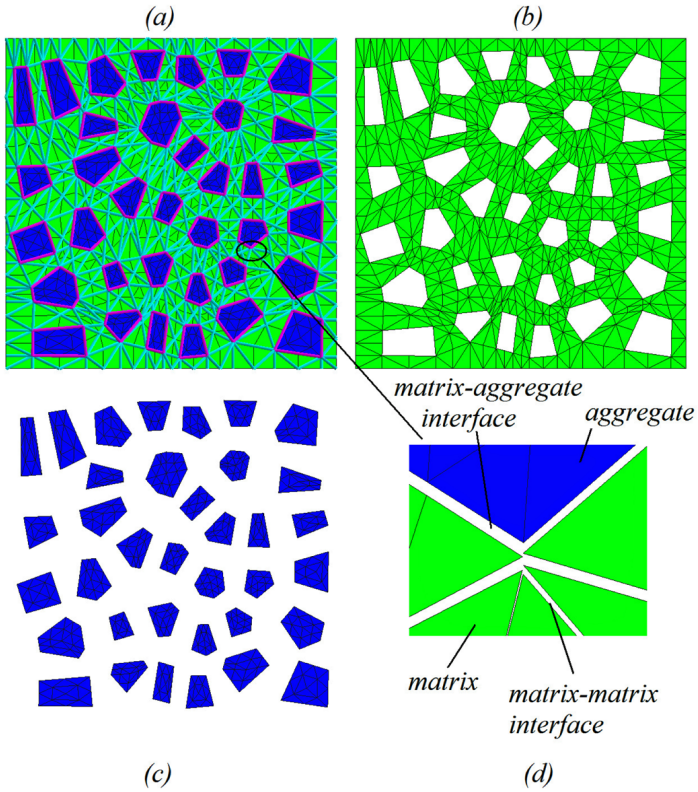

Figure 1.8: FE mesoscale discretization [Lopez et al., 2008a,b]: (a) 6 x 6 aggregate-arrangement, (b) matrix, (c) coarse aggregates and (d) interfaces.

particle contact layers of the matrix particles [Jirasek and Bazant, 1994]. The pioneer proposals of particle simulation have been reported in the works of Cundall [1971], Rodriguez [1974] and Kawai [1980]. These works mainly modeled the behavior of granular solids (such as sand) considering rigid particles that interact by friction. Furthermore, a particle model for brittle composite materials has been proposed by Zubelewicz and Bazant [1987] and Bazant et al. [1990], for simulating cracking localization in concrete elements. Figure 1.7 outlines several particle schemes adopted by Bazant et al. [1990] for studying the size effect on the failure peak load for unnotched specimens in tension.

Zero-thickness interface models: as an alternative to the continuous method, the discrete approach based on interface elements has been followed by several authors. This approach is based on the use of zero-thickness joints which connect continuum solid elements and possibly represent potential crack lines as outlined in Figure 1.8. The material failure in crack processes is captured by means of those elements for discrete

constitutive analyses, relating contact stresses (in normal and/or tangential direction) and the corresponding relative displacements (crack opening and sliding) with specific constitutive models, e.g., Hillerborg et al. [1976], Carol et al. [1997], Pandolfi and Ortiz [2002], Lorefice et al. [2008], etc. Interface formulations may only include traction-separation laws [Olesen, 2001, Oh et al., 2007, Buratti et al., 2011, Pereira et al., 2012] or, eventually, constitutive relations based also on more complex mixed-modes of fracture [Carol et al., 1997, Hillerborg et al., 1976, Pandolfi et al., 2000, Park et al., 2010].

Among the different procedures in the framework of the discrete crack approach, the one based on zero-thickness interface elements is particularly interesting due to the simplicity of the involved numerical tools, as the non-linear kinematics are fully defined within the displacement field.

1.3 Codes and Standards for Fiber-Reinforced Cementitious Composites

State-of-the-art review

In the last decades, a large amount of studies have been performed in order to better understand the mechanical properties of Fiber-Reinforced Cementitious Composite (FRCC). However, for many years the lack of international codes, standards and guidelines for the design purpose of FRCCs limit their expansion in structural applications. As a matter of fact, the FRCC in past has principally been employed for controlling non-structural aspects, such as cracking improvements, durability enhancements, etc.

The incorporation of fibers as reinforcement in partial substitution of the classical steel rebars has increasingly been considered attractive in the last twenty years after the publication of many design guidelines and codes in Europe: for example, the Sweden code [Stalfiberbetong, 1995], the Swiss recommendations [SIA-162-6, 1999], the German code [DBV, 2001], the Austrian guidelines [Faserbeton-R, 2002], the French recommendations [AFGC-SETRA, 2002], the guidelines provided by the RILEM Committee [RILEM-TC162-TDF, 2003], the Italian guidelines [CNR-DT-204, 2006], the Spanish code [EHE08, 2008] and the very recent fib Model-Code [2010a]. Further design considerations have been introduced by the American standards ACI-544.4R-88 [1996] and ACI-318-08/318R-08 [2008].

Some of these codes explicitly distinguish non-structural against structural applications based on the fiber types and dosages employed in such applications. Particularly, FRCCs

for structural members are those able to guarantee minimum mechanical performance mainly measured in terms of appropriate experimental monitored parameters, such as toughness indexes, post-cracking strength values, etc.

Several constitutive models have been proposed in the current national and international codes in order to design FRCC structures. These constitutive proposals mainly deal with the tensile characterization of the FRCC behavior through either stress-strain (σ-ϵ) or stress-crack opening displacement ($\sigma - w$) curves [Blanco et al., 2013].

This section is aimed at reviewing and classifying the main proposals highlighted by standards and recommendations available in literature. Particular focus is given in subsection 1.3 to the fib Model-Code [2010a] which is largely considered as the most advanced worldwide reference for FRCC in structural applications.

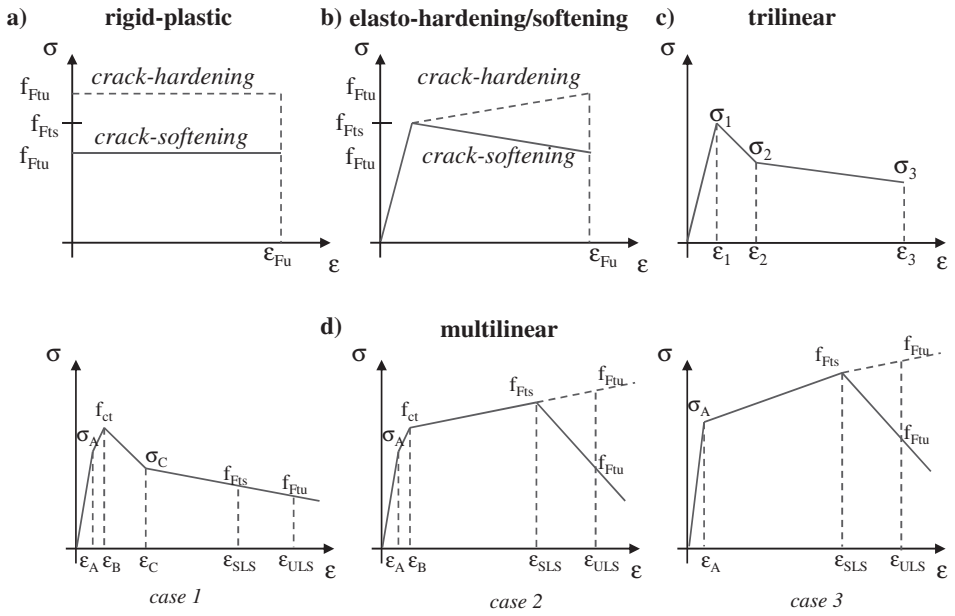

Figure 1.9: Constitutive $\sigma - \epsilon$ laws for the tensile behavior of FRCC: a) rectangular and b) bilinear shapes [CNR-DT-204, 2006], c) trilinear law [RILEM-TC162-TDF, 2003] and d) multilinear rules [fib Model-Code, 2010a].

The post-cracking tensile behavior and the parameters which identify such a relationship represent the key "ingredients" to design FRCC members. On the one hand, there are several guidelines which propose a different type of $\sigma - \epsilon$ diagram to be used for design purposes: i.e., the rectangular shapes by DBV [2001], CNR-DT-204 [2006], EHE08 [2008], fib Model-Code [2010a], the bilinear proposals [DBV, 2001, CNR-DT-204, 2006],

trilinear relationships [DBV, 2001, RILEM-TC162-TDF, 2003] and multilinear models [DBV, 2001, fib Model-Code, 2010a] (Figure 1.9). On the other hand, the main parameters whose define the constitutive laws in each one of the above models are derived by means of experimental tests which procedures are reported by others companion codes. For this purpose, test recommendations of several countries such as Italy [UNI-11039-1, 2003, UNI-11039-2, 2003], USA [ACI-544.2R-89, 1996, ASTM-C-1018, 1998], Spain [UNE-83510, 1989], France [NFP-18409, 1993], Belgium [NBN-B-15-238, 1992], Japan [JSCE-SF4, 1984], Germany [DIN-1048, 1991], Netherlands [CUR, 1994], Norway [NB, 1993], EU standards [EN-14651, 2005] and the Rilem international test procedure [RILEM-TC162-TDF, 2002] can be taken as references.

These codes have mainly been used as guides to experimentally obtain two principal quantities, alternatively adopted in design:

- (i) the equivalent flexural strength (f_{eq}) otherwise
- (ii) the residual flexural strength (f_R).

The first one (f_{eq}) is related to the work capacity of the material, derived by means of the area enclosed under the experimental force-crack tip/mouth opening displacements [Caggiano et al., 2012a], while the second parameter (f_R) corresponds to the stress associated to the force at a certain deflection measures or crack opening values [Barros et al., 2005].

The fib Model Code 2010

Recently, the lack of the international guidelines and codes for Fiber-Reinforced Concrete (FRC) elements in structural applications has strongly been filled by the publication of a new fib Model-Code [2010a]. This new document aims at updating and reviewing the previous CEB-FIP-90 [1993] recommendations. In this regard, FRC has been introduced into the "Technical Groups fib TG 8.3" (*Fibre reinforced concrete*) and "fib TG 8.6" (*Ultra high performance FRC*). In this subsection the fundamental assumptions and main design rules for FRCC, proposed into the fib Model-Code [2010a], are reported and discussed.

Uniaxial behavior: compressive and tensile stress-strain

One of the most important aspects of the mechanical response of FRC is represented by its behavior in tension. Different test methods are proposed for assessing the post-

cracking behavior of FRC. However, the bending test on prismatic specimens represents the most popular and the widely used experimental technique for this purpose. It is relatively simple to realize and may represent the boundary conditions of many practical situations.

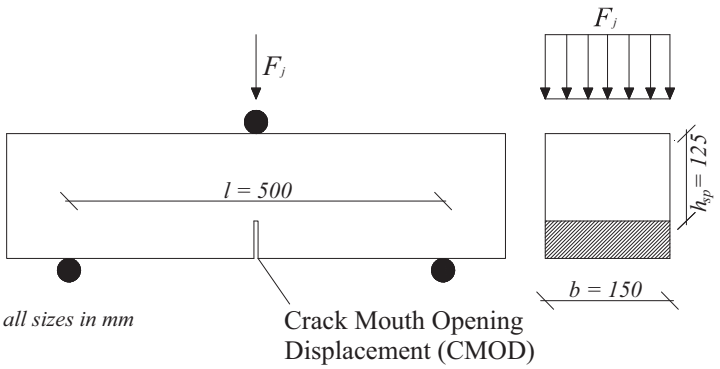

Figure 1.10: Experimental set-up and geometry details of the notched beams under three-point bending test [fib Model-Code, 2010a].

The fib Model-Code [2010a] considers residual flexural strengths determined by performing 3-point bending tests (Figure 1.10) on notched prisms according to EN-14651 [2005]. Particularly, the residual flexural strengths, $f_{R,j}$, are defined as

$$f_{R,j} = \frac{3F_j l}{2bh_{sp}^2} \tag{1.1}$$

being l and b the span length and width of the specimens, respectively, while h_{sp} is the distance between the notch tip and the top of the specimen; the j index refers to the considered Crack Mouth Opening Displacement ($CMOD$) while F_j is the load corresponding to $CMOD = CMOD_j$.

Since the compressive strength is not particularly influenced by the presence of fibers (up to a volume fraction of about 1%), the fib Model-Code [2010a], as it is also suggested by almost all worldwide guidelines, accepts that the compressive relations valid for plain concrete can be further applied to FRC.

Post-cracking strength and classification

The post-cracking residual tensile strength of FRC represents an important design parameter for members. It is mainly influenced by the fiber types and geometry,

materials and fraction contents. Two residual values are typically taken as reference in design: at first, it is considered the crack opening for Serviceability Limit State (SLS) verifications, then a second crack should be significant for the Ultimate Limit State (ULS) [Eurocode-2, 2004].

The European standard EN-14651 [2005] proposes four different residual strengths: i.e., f_{R1}, f_{R2}, f_{R3} and f_{R4} (Figure 1.11). They correspond to specific values of the $CMOD_j$: $CMOD_1 = 0.5mm$, $CMOD_2 = 1.5mm$, $CMOD_3 = 2.5mm$ and $CMOD_4 = 3.5mm$, respectively. Particularly, f_{R1} and f_{R3} are the FRC residual strengths representative for the SLS and ULS, respectively.

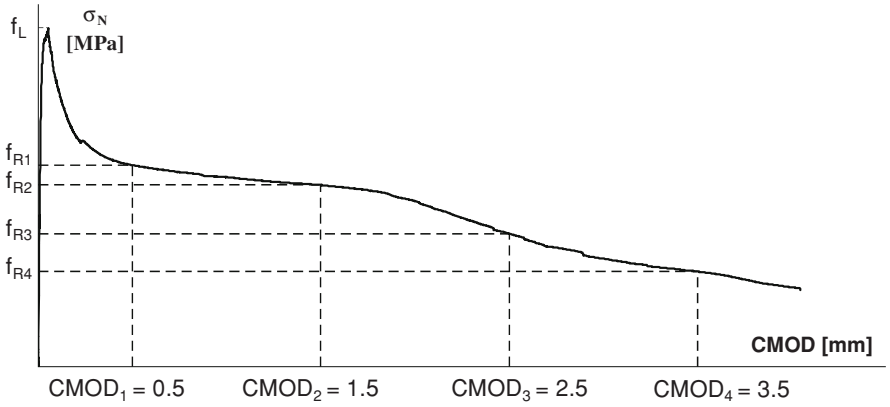

Figure 1.11: Typical curve of the nominal stress versus $CMOD$ for FRC [EN-14651, 2005].

Then, post-cracking residual strength and FRC toughness can be classified by using two parameters: the first, which outlines the strength class, is given by f_{R1}, while the second parameter (identified with the letter "a", "b", "c", "d" or "e") recognizes the ratio between f_{R3} and f_{R1}. Particularly, the strength classes, based on the characteristic value of f_{R1} (i.e., $f_{R1,k}$), are defined through the following values of f_{R3}/f_{R1} ratio: 1.0 (if $f_{R1,k} \geq 1.0\,MPa$), 1.5 (if $f_{R1,k} \geq 1.5\,MPa$), 2.0 (if $f_{R1,k} \geq 2.0\,MPa$), 2.5 (if $f_{R1,k} \geq 2.5\,MPa$), 3.0 (if $f_{R1,k} \geq 3.0\,MPa$), 4.0 (if $f_{R1,k} \geq 4.0\,MPa$), 5.0 (if $f_{R1,k} \geq 5.0\,MPa$), 6.0 (if $f_{R1,k} \geq 6.0\,MPa$), 7.0 (if $f_{R1,k} \geq 7.0\,MPa$) and 8.0 (if $f_{R1,k} \geq 8.0\,MPa$).

The $f_{R3,k}/f_{R1,k}$ ratio (being $f_{Ri,k}$ characteristic values of f_{Ri}) can be represented with the letters "a", "b", "c", "d" or "e", corresponding to the following characteristic strength values:

- "a" if $0.5 \leq f_{R3,k}/f_{R1,k} \leq 0.7$;
- "b" if $0.7 \leq f_{R3,k}/f_{R1,k} \leq 0.9$;

- "c" if $0.9 \leq f_{R3,k}/f_{R1,k} \leq 1.1$;
- "d" if $1.1 \leq f_{R3,k}/f_{R1,k} \leq 1.3$;
- "e" if $1.3 \leq f_{R3,k}/f_{R1,k}$.

Minimum mechanical performances are required for FRC in practical designs according to the fib Model-Code [2010a]. Based on the above classifications, fiber reinforcements can be used in substitution (even partially) of conventional reinforcements at ultimate limit state, if the following relationships are respected

- $f_{R1,k}/f_{L,k} > 0.4\,MPa$
- $f_{R3,k}/f_{R1,k} > 0.5\,MPa$

being $f_{L,k}$ the characteristic value of the nominal strength corresponding to the peak load (or the highest load value in the $CMOD$ range $0-0.05\,mm$) according to the test specimen of EN-14651 [2005].

Constitutive laws for Limit State Analyses

Two alternative stress-crack opening relationships, as schematically proposed in Figure 1.12, are considered by the fib Model-Code [2010a] for the ULS:

- a **rigid-plastic model**, based on a unique reference strength, f_{Ftu}. Such a value is determined by means of the following relationship

$$f_{Ftu} = \frac{f_{R3}}{3} \tag{1.2}$$

- **rigid-linear post-cracking behavior** (hardening, perfectly plastic or softening), formulated by means of two strength values: i.e., f_{Fts} and f_{Ftu}, respectively. These quantities used for the diagram of Figure 1.12b are defined through the following equations

$$f_{Fts} = 0.41\,f_{R1} \tag{1.3}$$

$$f_{Ftu} = f_{Fts} - \frac{w_u}{CMOD_3}\left(f_{Fts} - 0.5f_{R3} + 0.2f_{R1}\right) \geq 0. \tag{1.4}$$

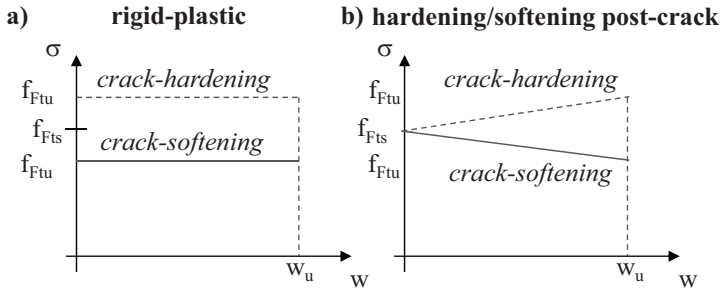

Figure 1.12: Post-cracking constitutive laws for ULS states [fib Model-Code, 2010a].

In the above relationships, f_{Fts} is the serviceability residual strength, relative to a crack opening value representative of the SLS analysis, while f_{Ftu} represents the post-cracking strength for the ULS. At last, w_u is the maximum crack opening accepted in structural design and its value depends on the required ductility.

When concrete cracks are treated by means of classical smeared-crack models, as usually accepted in design procedures, the fracture zone must necessarily be considered as distributed in a certain region of the body. Based on this, classical models behave with a loss of objectivity under softening responses. Actually, the definition of a stress-strain law is based on the identification of a crack width and on the corresponding structural characteristic length. The link between the stress-crack law ($\sigma - w$) and the stress-strain constitutive relationship ($\sigma - \epsilon$) is given by the introduction of a characteristic length, l_{cs},

$$\varepsilon = w / l_{cs}. \tag{1.5}$$

The characteristic length, for elements with conventional rebars, may be calculated as

$$l_{cs} = \min\{s_{rm}, y\} \tag{1.6}$$

being s_{rm} the mean distance between two cracks, while y represents the distance between neutral axis and the tension side of the cross section. Further details can be obtained into the fib Model-Code [2010a].

In bending sections without traditional reinforcement, under combined tensile-flexural or combined compressive-flexural stresses, with resulting force external to the cross-section, the simplified expression of $y = h$ (being h the specimen height) can be as-

sumed due to the very reduced extension of the compressed region. The same assumption can be taken for slabs.

In case of serviceability limit states analysis, the constitutive relationship adopted for plain concrete in uniaxial tension, can be also used up to the peak strength f_{ct}. Then, in post-cracking regime, the multilinear laws proposed in Figure 1.9d are considered. The post-cracking residual strength is defined by means of two points corresponding to (ϵ_{SLS}, f_{Ftsd}) and (ϵ_{ULS}, f_{Ftud}), where ϵ_{SLS} and ϵ_{ULS} are defined according to the considered limit states as outlined by the fib Model-Code [2010a].

Partial safety factors

Based on the stress-crack opening displacement relationship reported in Figure 1.12 and used for the ULS-design, the following strength values must be considered in design

$$f_{Ftsd} = \frac{f_{Ftsk}}{\gamma_F} \tag{1.7}$$

and

$$f_{Ftud} = \frac{f_{Ftuk}}{\gamma_F} \tag{1.8}$$

being f_{Ftsk} and f_{Ftuk} the characteristic values for the strength values given in Eqs. (1.3) and (1.4). The values for the material partial safety factors γ_F are recommended according to the fib Model-Code [2010a]:

- *FRC in compression*: γ_F as for plain concrete;
- *FRC in tension (limit of linearity)*: γ_F as for plain concrete;
- *FRC in tension (post-cracking residual strength)*: $\gamma_F = 1.5$.

Finally, for serviceability limit states, the partial factors should be taken as 1.0.

Design of FRC members

The above constitutive laws and post-cracking strengths are then used for design rules as outlined in the "PART III: DESIGN" of the fib Model-Code [2010b]. For the sake of

brevity, the description of the design rules is omitted in this work. These details are beyond the scopes of this thesis. However, further details can be founded in the fib Model-Code [2010b].

1.4 Motivation

Over the last few decades, the use of fibers into the cementitious matrix, aimed at mitigating the main deficiencies of concrete-like materials (i.e., the relatively low tensile strength, the poor resistance to crack opening and propagation, etc.), played an important role in the field of the civil and building engineering.

A large amount of experimental studies can be found in the scientific literature dealing with different topics of these composites. At the same time, simple numerical models based on empirical or semi-empirical formulae have been proposed in order to analyze and quantify the post-cracking response of FRCC. The entire progress made in the modeling of the fiber effects on concrete/mortar matrix has classically been based on the continuum smeared crack approach. This includes most of the proposals related to macroscale models where the fiber-reinforced matrix is considered as a continuum. The main drawback of those models resides to the fact that their constitutive laws cannot taken into account the explicit fiber effects on the cracking phenomena.

Beyond the above drawback, classical or continuum models for simulating quasi-brittle materials, like concretes and mortars, are characterized by the strong FE-size dependence of the localization band width and, consequently, the loss of objectivity of their results. On the contrary, Discrete Crack Approaches (DCAs), in which the discontinuity of the displacement field due to cracking is directly accounted into the finite element formulation, are actually insensitive to mesh sizes.

The need to realistically predict the failure and mechanical behavior of fiber-reinforced concretes when different fiber types and contents are considered, in addition to all what is above exposed, motivated the work included in this thesis. Particularly, the key objective of this research is the proposal of a new constitutive discontinuous model for FRCC. A zero-thickness joint model is formulated for simulating the fracture behavior of fiber-reinforced concretes in which the coupled action between concrete and fibers is explicitly accounted in an original way.

The proposed formulation and the consequent possibility of modeling the behavior of FRCC starting from both their components and the interactions among them is the key novelty of the work discussed in this thesis. As a matter of principle, the huge

aleatoric nature of FRCC (mainly deriving by the randomness of fiber orientation and distribution, aggregate size and collocation, mixing and casting procedures and so on, so forth) is the key reason why simulating the global behavior of FRCCs starting from their constituents can lead to unreliable predictions of the global response of the composite material as a whole. Nevertheless, the basic interactions among the various components, which actually affect the global response of FRCC, can be mechanically modeled as presented in this thesis and the natural randomness of the component properties and distribution can be handled within the framework of well established statistical procedures whose application is beyond the scopes of the proposed work.

1.5 Objectives and activities of the thesis

The general objective of this thesis is to improve the general state of knowledge in the field of civil engineering regarding the mechanical behavior of FRCC and its model formulations. Particularly, a great part of the thesis concerns the developments of numerical tools aimed at analyzing failure processes of fiber-reinforced concretes which involve the explicit characterization of fiber effects on concrete crack phenomena.

The specific activities of this thesis are listed below:

- to analyze a great number of experimental evidence available in the scientific literature but also to consider an own experimental campaign performed on concretes with different fiber contents and aimed at clearly establishing the differences between the mechanical behaviors of plain concrete against FRCC.
- to reformulate and validate an existing interface model for normal/shear cracking for quasi-brittle materials like concretes and mortars.
- to propose an effectiveness and accurate method to account the fiber actions on the concrete cracks.
- to formulate a constitutive model capable to realistically predict the bond behavior of fibers embedded in cementitious matrix.
- to develop a maximum strength criterion valid for accounting the dowel effect of steel fibers crossing concrete cracks.
- to present a constitutive model for FRCC interfaces based on the well-known “Mixture Theory” which combines the three internal “components” such as the

fracture energy-based plasticity formulation for plain mortar/concrete, the fiber bond-slip formulation and the fiber dowel action.

- to validate the proposed constitutive theories above mentioned against experimental data extracted from the literature.
- to evaluate the predictive capability the proposed interface constitutive theory in numerical analysis of failure processes of FRCCs at both mesoscopic and macroscopic levels of observation.
- to deeply analyze the FRCC model prediction when different load scenarios and fiber quantities and qualities are considered.
- to consider the composite model formulation, firstly employed into the interface proposal, for formulating and validating a simple non-linear cracked hinge model aimed at predicting the structural post-cracking behavior of beams under four-point bending.
- to propose a continuum (smeared-crack) formulation, based on the non-linear microplane theory combined with the well-known "Mixture Theory" for describing the failure behavior of FRCC.

As aforementioned, a great part of this work deals with the formulation of a novel interface constitutive model for discontinous fracture analysis of FRCC. For this purpose, FRCC can be regarded as a four-phase material (Figure 1.13), composed by:

- (i) coarse aggregates;
- (ii) plain mortar;
- (iii) plain interfaces modeling the cementitious matrix-to-coarse aggregate interaction and
- (iv) FRCC interfaces for the matrix-to-matrix crack modeling.

In this methodology, only the coarse aggregates are explicitly discretized in the FE mesh and embedded in a matrix phase representing the cementitious mortar plus smaller aggregates and fibers. In principle, an explicit meso-geometry permits to correctly model fracture and failure processes in concrete which are generally governed by the main composite heterogeneities.

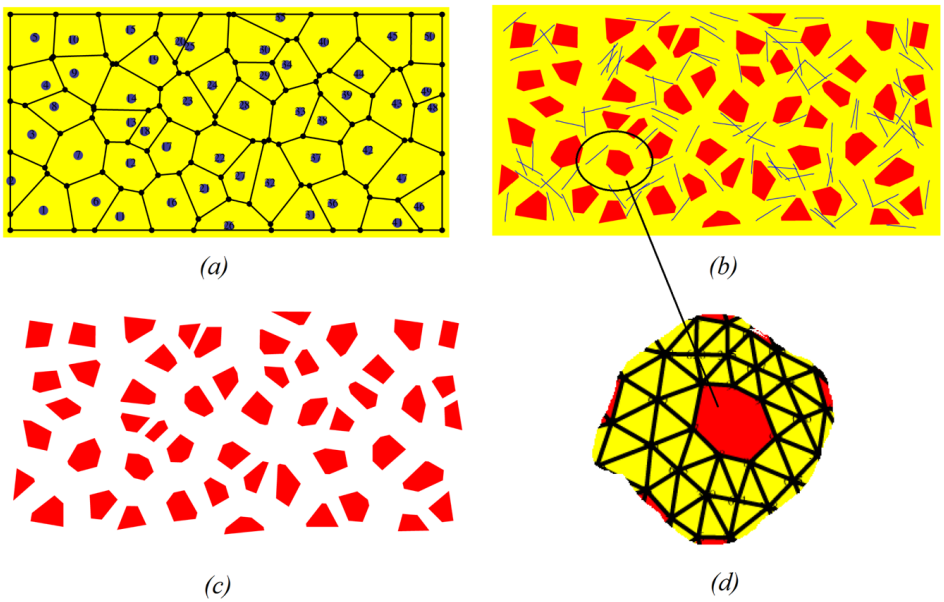

Figure 1.13: 2D meso-structure geometry: (a) Delaunay triangulation/Voronoi tessellation [Idiart, 2009], (b) FRCC meso-probe, (c) coarse aggregates and (d) position of the interface elements.

The non-linear behavior of steel fiber-reinforced concrete/mortar is fully captured by means of the model formulation for zero-thickness joint elements proposed in this thesis. The constitutive proposal is based on the original idea of Carol et al. [1997] which is modified and extended in this thesis to fiber concrete composites on the basis of the well-known "Mixture Theory" [Trusdell and Toupin, 1960], also employed by Manzoli et al. [2008] for RC members.

1.6 Thesis structure and main contents

After this Introduction chapter, the thesis is structured as outlined in the following descriptive paragraphs.

Chapter 2 reports the results of an extensive experimental campaign realized on several prismatic concrete specimens, which have been cast by using different types and amounts of steel fibers and successively tested under four-point bending. Particularly, Steel Fiber-Reinforced Concrete (SFRC) specimens have been considered with two different fiber contents (i.e., 0.5% and 1.0% of volume fraction). Moreover, for each fiber content, five different combinations of long and short fibers have been considered

with the aim of investigating the eventual influence of those combinations on the resulting behavior of SFRC specimens.

Chapter 3 presents a novel model for Fiber-Reinforced Cementitious Composites (FRCCs) based on a cohesive-frictional interface theory. The formulation of a zero-thickness joint model is discussed for simulating the fracture behavior at mesoscopic level of fiber-reinforced concretes. Particularly, the "Mixture Theory" is used for describing the coupled action between concrete and fibers. Then, the softening behavior of the interface model due to crack propagation is outlined by means of an incremental approach, which is similar to the one usually adopted in the classical flow theory of plasticity. A novel bond-slip model is presented in order to correctly simulate the axial effect of fibers on concrete cracks. Also, the composite action between concrete and fiber reinforcements is completed by considering the transversal fiber effect by means of a dowel model.

Chapter 4 reports a unified formulation for simulating the overall bond behavior of fibers embedded in cementitious matrices. Such a formulation is based on a bond model defined in terms of the interface stresses and the corresponding relative displacements. The considered formulation addresses the behavior of fibers under tensile axial stresses which result in a "mode II" debonding phenomenon. The proposed unified formulation has straightforwardly been employed into the interface proposal described in Chapter 3. The adoption of the presented formulation within the general framework of discontinuous cracking models of FRCC is simultaneously the key motivation and the most relevant development of Chapter 4. Finally, numerical analyses for validating the proposed formulation against relevant experimental pull-out results are discussed.

In Chapter 5, the soundness and capabilities of the proposed interface model for FRCC, presented in Chapter 3, are discussed by considering several numerical simulations and results. In the first section, the interface model is calibrated by using experimental results performed on SFRC probes tested under pure tensile stress cases by considering the experimental results by Li et al. [1998]. Furthermore, the stress history on concrete panels by Hassanzadeh [1990] are considered to asses the predictive capability of the model in terms of failure behavior of SFRC specimens in mixed-modes of fracture. Then, the second section is intended to study the incidence of steel fibers on the post-cracking performance for several stress states under overall possible failure modes. For this purpose, several interface cracking conditions are considered and analyzed through a defined "cracking indicator".

Chapter 6 explores the analyses of boundary value problems by means of the Finite

Element Method in order to show numerical simulations at structural level obtained with the proposed interface constitutive model. The attention of this chapter is focused on the analysis of the failure behavior of Steel Fiber-Reinforced Concretes (SFRCs) evaluated at both macro and mesoscale levels of observation.

Chapter 7 deals with a non-linear cracked hinge model aimed at reproducing the bending fracture behavior of fiber-reinforced concrete beams. The model is based on the fracture mechanics concepts of the fictitious crack model where the stress-crack opening relationship is accounted in a similar way obtainable by considering the pure "mode I" case of the discontinuous proposal formulated in Chapter 3. A closed-form solution for the stress-crack opening relationship, with the explicit consideration of the fiber effects, is presented. The applicability of this simplest model is demonstrated by simulating the bending fracture specimens under four-point bending conditions, which are the objects of the Chapter 2.

A novel fracture energy-based microplane model for simulating the failure behavior of FRCC within a continuum standpoint is proposed in Chapter 8. A constitutive normal/shear "microstress" formulation is considered on each microplane for describing the FRCC mechanical response and its fracture processes. The constitutive laws employed at the microplane level, featuring the fracture energy-based softening formulation for plain concrete, as well as the description of the fiber-to-concrete interactions, are proposed. Fiber-concrete interaction is explicitly considered by means of the well known "Mixture Theory" in a similar way proposed for the interface model of the Chapter 3. Some numerical applications, aimed at demonstrating the predictive capabilities and soundnesses of the constitutive proposal, are addressed and discussed in the same chapter.

Finally, Chapter 9 summarizes the main final remarks and conclusions which can be drawn out from this thesis. Moreover, further developments and the straightforward extensions of this work related to both continuous and discontinuous mechanical analyses of quasi-brittle materials, are proposed and discussed.

2 Experimental characterization of steel fiber notched concrete beams

This section presents the results of an experimental activity carried out on Fiber-Reinforced Concrete (FRC) obtained by mixing short and long hooked-end steel fibers. Eleven mixtures have been considered including plain concrete as a reference and Steel FRC with 0.5% and 1.0% of fiber volume fractions. The experimental campaign is aimed at observing the key aspects of the mechanical behavior of FRC in bending. Notched plain and fiber-reinforced concrete specimens have been tested under Four-Point Bending (4PB) according to UNI-11039-1 [2003] and UNI-11039-2 [2003]. The structural behavior has been evaluated in terms of traction-separation law of FRC and the possible influence of both amount and type of fibers has been investigated.

In section 2.1, a short overview of the standards and codes, dealing with the flexural test experiments in FRCC, is proposed. Then, section 2.2 describes the analyzed mixtures and experimental test methods employed in the proposed research. Section 2.3 reports the experimental results of both compression and bending tests. Finally, some concluding remarks are discussed in section 2.4.

2.1 Flexural tests for obtaining residual strengths

Steel Fiber-Reinforced Concrete (SFRC), obtained by mixing short fibers and cement-based mixtures, are becoming extensively used materials in civil engineering applications [Ferro et al., 2007, di Prisco et al., 2009].

Main benefits of SFRC are the very high ductility improvement of structural components and the significant enhancement of residual strengths in final or cracked stage [Barros and Figueiras, 1999]. The superior ductility of structures made of SFRC, partic-

ularly in post-peak regime, are typically observed through flexural tests, under both pure mode I type [Gopalaratnam and Gettu, 1995] and mixed failure modes [Carpinteri and Brighenti, 2010].

Several National and International Codes deal with the flexural test methods for measuring the relevant mechanical properties of FRC [JSCE-SF4, 1984, UNE-83510, 1989, NBN-B-15-238, 1992, NFP-18409, 1993, ASTM-C-1018, 1998, SIA-162-6, 1999, DBV, 2001, RILEM-TC162-TDF, 2002, UNI-11039-1, 2003, UNI-11039-2, 2003, EN-14651, 2005, DAfStB, 2010].

The bending test of prismatic specimens is the most common and widely used experimental technique for assessing the post-cracking behavior of FRC. It is relatively easy to realize and can be representative of many practical situations. The specimens are supported on two points and can be loaded in one or two points to obtain Three-Point Bending (3PB) [Olesen, 2001, Zhang and Li, 2004, Carpinteri and Brighenti, 2010] or Four-Point Bending (4PB) tests [Banthia and Trottier, 1995, Oh et al., 2007].

The results of a bending test can be represented in terms of vertical load-displacement curve [Gopalaratnam et al., 1991, Barros et al., 2005, Kim et al., 2008] or, in case of notched specimens, by means of the flexural load against the Crack (Tip or Mouth) Opening Displacement ($CTOD$ or $CMOD$, respectively) [Oliver et al., 2006, Park et al., 2010, Buratti et al., 2011]. The main purpose of this test is to determine the enhanced toughness of FRC compared to conventional concrete.

2.2 Experimental campaign

In the framework of the research activity of this thesis, several notched specimens have been fabricated and tested for examining the mechanical properties of plain and fiber-reinforced concrete. Eleven mixtures, made with two different types of steel fibers and various amount of them, have been considered. Moreover, a mixture of plain concrete without fibers has been taken as a reference and labeled as “REF”.

The tests have been performed according to UNI-11039-1 [2003] for definitions, classification and d designation and UNI-11039-2 [2003] for the test method. The most important aspects of the experimental campaign are described in the following.

2.2.1 Materials

The mixtures considered in the research program have been made by employing a maximum aggregate size of 20 mm according to UNI-EN-12620 [2002] and UNI-11039-1 [2003] specifications, a constant cement content of 320 kg/m^3 and a water to cement ratio w/c of 0.51. Table 2.1 describes the reference concrete mixture. Coarse natural aggregates have been defined as $N1$ when the grain dimension ranges between 2 and 10 mm and $N2$ for the grain size from 10 to 20 mm, while fine aggregates (namely sand) have a maximum aggregate size equals to 2 mm as shown in Figure 2.1. The aggregate grading of the reference concrete is proposed in Figure 2.2 in comparison with the classical Fuller grain size distribution.

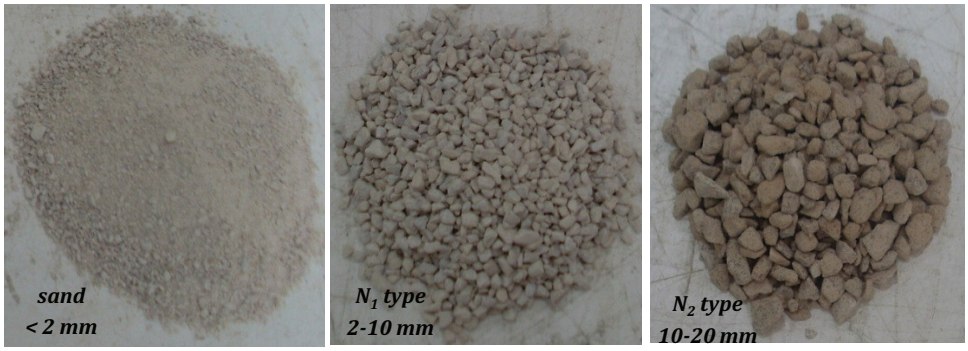

Figure 2.1: Fine and coarse aggregates employed in the experimental campaign.

Table 2.1: Mix design per cubic meter of the reference concrete.

Material	Density	Absorption	Dosage
Sand	2690 kg/m^3	1.20 %	1012 kg
Coarse agg. N1	2690 kg/m^3	0.70 %	134 kg
Coarse agg. N2	2690 kg/m^3	0.50 %	764 kg
Cement 42.5R	3030 kg/m^3	-	320 kg
Water	1000 kg/m^3	-	180 lt
Water absorption	1000 kg/m^3	-	17 lt
Superplasticizer	1050 kg/m^3	-	2.7 lt

Two types of steel reinforcements have been employed in FRCs: Wirand Fibers FF3 type (namely “long fibers”) and Wirand Fibers FS7 type (“short fibers”) as shown in Figure 2.3. Table 2.2 outlines the geometric and mechanical properties of fibers. The aspect ratio of the ‘long” and “short” steel fibers are 67 and 60, respectively, and the number of fibers/kg are 5700 and 16100, respectively.

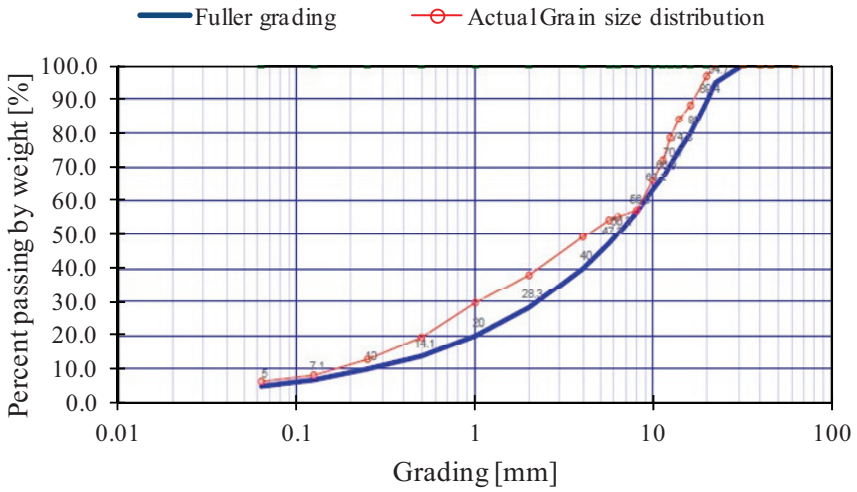

Figure 2.2: Grain size distribution of the "REF" mixture.

Table 2.2: Geometric and mechanical properties.

Fibers	Diameter	Length	Tensile strength	Ultimate strain
Wirand FF3	0.75 mm	50 mm	> 1100 MPa	< 4%
Wirand FS7	0.55 mm	33 mm	> 1200 MPa	< 2%

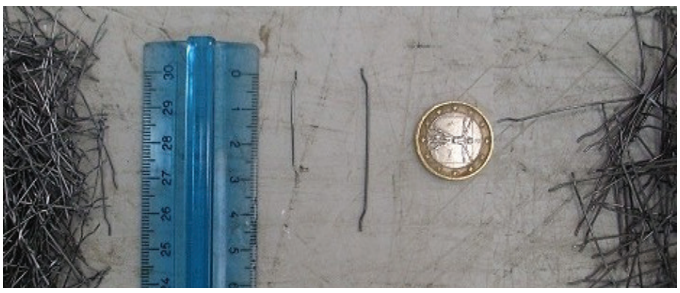

Figure 2.3: Fiber types: FS7 (short fiber) and FF3 (long fiber).

2.2.2 Test method

Tests have been carried out according to the procedures described in UNI-11039-2 [2003]. Particularly, prismatic $150 \times 150 \times 600\ mm^3$ specimens have been tested in displacement control under four-point bending as shown in Figure 2.4a. The main geometric parameters of the adopted beams are detailed in Figure 2.4b.

Each specimen has preliminarily been notched (through a 2.0 mm wide-slit) of 45 mm depth and starting from the bottom surface of the sample. The specimens have been

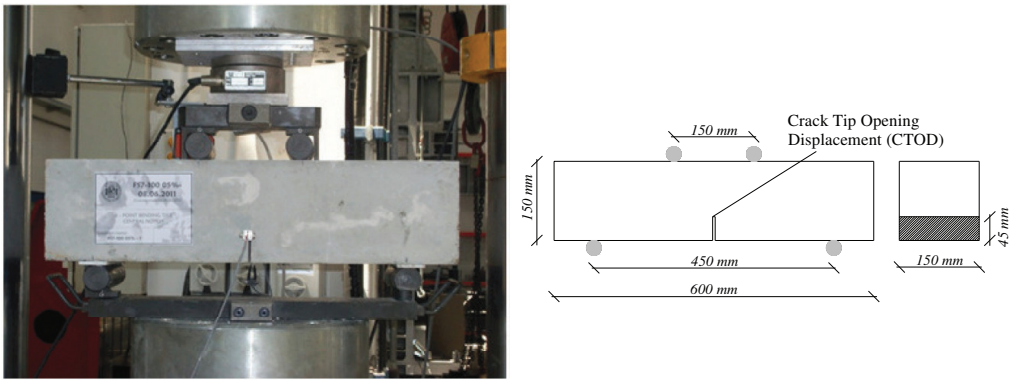

(a) (b)

Figure 2.4: Four-point bending test: (a) experimental set-up and (b) geometry of the notched beams.

(a) (b)

Figure 2.5: Four-point bending test: (a) load-cell and (b) crack opening transducers.

tested under displacement control (having displacement rate of 0.005 mm/min) by recording the load by means of a load-cell as in Figure 2.5a, the displacements and the crack openings. The latter have been measured by means of dedicated displacement transducers, as shown in Figure 2.5b, which monitor the relative displacements of the two sides of the notch.

2.2.3 Test programme

Three series of specimens have been tested (Table 2.3): plain (or reference) concrete specimens (labeled as “REF”) and steel fiber-reinforced specimens with 0.5% and 1.0% of fiber content. All specimens have been cast by using the concrete mixture detailed in Table 2.1 with the exception of the superplasticizer. Its quantity has duly been adjusted in each mixture with the aim to obtain similar workability, measured by a slump value

of about 150 mm. The prismatic concrete specimens have been cured under water (100% humidity) at a constant temperature of 22^oC, for 28 days as in Figure 2.6.

Table 2.3: Key proprieties of the concrete mixtures.

Mixture	Amount of Fibers	Long fibers (FF3)	Short fibers (FS7)
REF	-	-	-
S100 - 05	40 kg/m^3	-	100 %
S75 - 05	40 kg/m^3	25 %	75 %
LS50 - 05	40 kg/m^3	50 %	50 %
L75 - 05	40 kg/m^3	75 %	25 %
L100 - 05	40 kg/m^3	100 %	-
S100 -10	80 kg/m^3	-	100 %
S75 - 10	80 kg/m^3	25 %	75 %
LS50 - 10	80 kg/m^3	50 %	50 %
L75 - 10	80 kg/m^3	75 %	25 %
L100 - 10	80 kg/m^3	100 %	-

Figure 2.6: Underwater curing of specimens during 28 days at constant temperature of approximately 22^oC.

For each mixture, three beams have been cast and tested in four-point bending. Moreover, three cubes of $150\times150\times150$ mm^3 (Figure 2.7) have also been cast in polyurethane molds [EN-12390-3, 2009] and then tested (in displacement control) for measuring the compressive strength of the SFRCs at the time of testing. One of them (labeled as "white") has been extracted before the fiber mixing, with the aim to capture the actual contribution of fibers on the compressive response of the considered SFRC.

Figure 2.7: SFRC samples to be tested in compression.

2.3 Experimental results

The main mechanical proprieties determined in the experimental tests are presented in the following subsections. At first, concrete specimens tested under compression are proposed in subsection 2.3.1, then the experimental results on prismatic beams loaded in four-point bending tests are detailed in subsection 2.3.2.

2.3.1 Compression

The results of compression tests are summarized in Table 2.4 in terms of cube compressive strengths. The same table also reports the mean values of density measured in hardened samples of the various concrete mixtures under consideration.

Table 2.4: Densities and cube compressive strengths measured in each mixture.

Mixture Label	Density [kg/m^3]		R_c at 28 days [MPa]	
	white	SFRC	white	SFRC (mean of two)
REF	2371		42.59 (mean of three)	
S100-05	2376	2413	40.57	39.01
S75-05	2411	2439	41.79	40.88
LS50-05	2390	2430	44.80	43.36
L75-05	2410	2428	48.03	45.41
L100-05	2407	2443	43.70	42.74
S100-10	2353	2488	40.33	44.91
S75-10	2342	2458	38.44	39.54
LS50-10	2362	2448	43.77	40.87
L75-10	2391	2455	45.27	48.56
L100-10	2418	2519	38.54	49.39

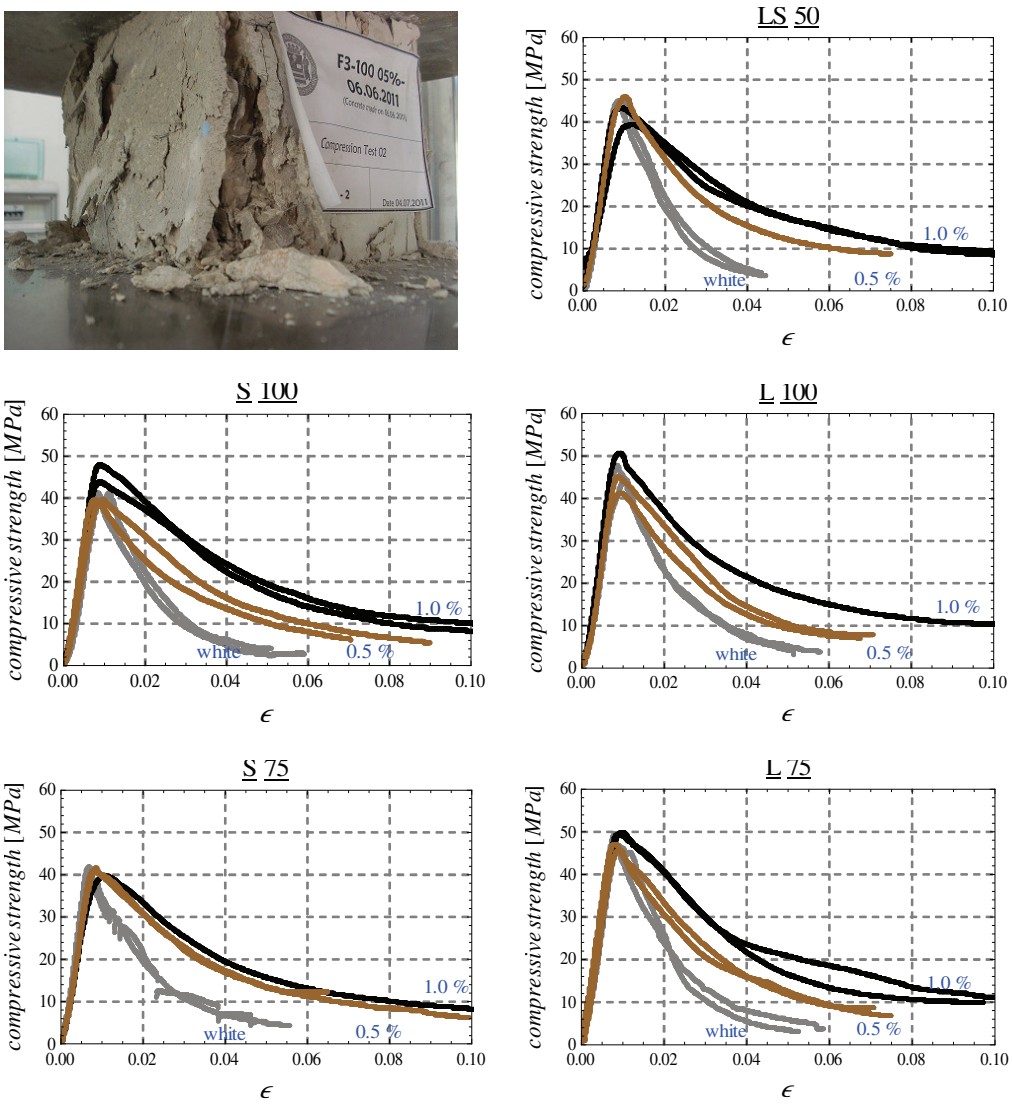

Figure 2.8: Compressive stress - strain curves of "white" concretes and SFRCs having $\rho_f = 0.5\%$ and $\rho_f = 1.0\%$ of fiber volume contents.

Figure 2.8 plots, the stress-strain curves obtained with "white" specimens and SFRCs having $\rho_f = 0.5\%$ and $\rho_f = 1.0\%$ of fiber volume contents. The vertical axis represents the average uniaxial stress, while the corresponding strain, obtained as the vertical displacement divided by the specimen height (150 mm), is represented on the $x-$axis.

The experimental results in Figure 2.9 show very similar compressive strengths in both "white" and fiber-reinforced specimens. As largely accepted in the scientific

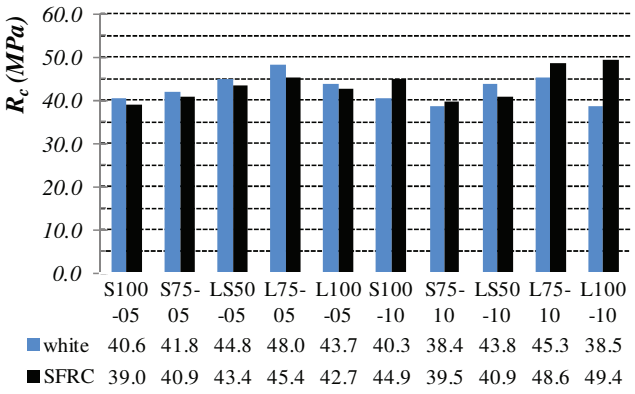

Figure 2.9: Cube compressive strengths of the SFRC samples [EN-12390-3, 2009].

literature [Nataraja et al., 1999, Fantilli et al., 2011], no significant difference can be observed in terms of mean values of both the so-called "white" and fiber reinforced specimens (42.53 and 43.47 MPa, respectively). The better performances of SFRCs compared to "white" samples can be appreciable only in terms of post-peak ductility when compressive failure processes are considered, as clearly observed in Figure 2.8.

The very high stability of the obtained results in compression is demonstrated by the relative standard deviations

$$\begin{aligned} s_{n,white} &= \sqrt{\frac{\sum_{i=1}^{n}\left(R_{c,i,white}-R_{c,m,white}\right)^2}{n}} \\ s_{n,SFRC} &= \sqrt{\frac{\sum_{i=1}^{n}\left(R_{c,i,SFRC}-R_{c,m,SFRC}\right)^2}{n}} \end{aligned} \tag{2.1}$$

measuring $s_{n,white} = 2.82\%$ and $s_{n,SFRC} = 3.41\%$ for "white" and SFRCs, respectively. In Eq. 2.1, $R_{c,i,white}$ and $R_{c,i,SFRC}$ represent the compressive strengths in "white" and SFRC specimens, above reported in Table 2.4. Finally, $R_{c,m,white}$ and $R_{c,m,SFRC}$ are the corresponding mean values.

2.3.2 Four-point bending tests

Four-point bending tests have been performed with the aim of characterizing the tensile post-cracking behavior of the considered SFRC samples. The UNI-11039-1 [2003] and UNI-11039-2 [2003] standard guidelines have been taken into account. Ten SFRC types, as well as plain reference concrete, have been tested and compared. Figure 2.10 shows the curves of the vertical load, P, versus the corresponding $CTODm$ curves,

obtained in experimental tests. $CTODm$ represents the mean of the two opposite Crack Tip Opening Displacements ($CTODs$) registered by the transductor devices (Figure 2.5b).

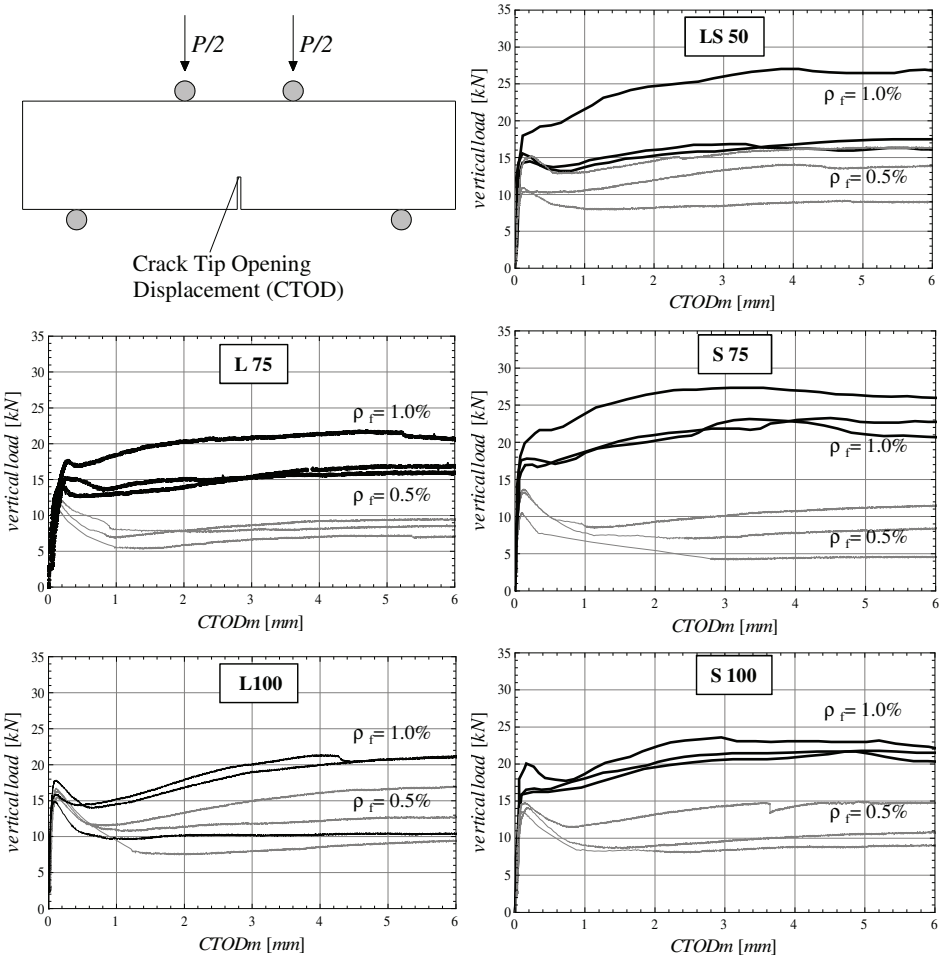

Figure 2.10: Vertical force - $CTODm$ curves: black lines refer to specimens with 1.0% of fiber volume content while grey lines indicate the 0.5% of fiber fraction.

The experimental results demonstrate that fibers significantly enhance the post-cracking toughness of the SFRC in both $\rho_f = 0.5\%$ and $\rho_f = 1.0\%$. The scatter observed in force-$CTODm$ curves has usually been due to the non-regular distributions of fibers inside the specimens. A lower sensitivity emerges for compressive strength which has actually been less influenced by fibers.

The first-crack strength values, f_{lf}, defining the post-cracking response of the SFRC

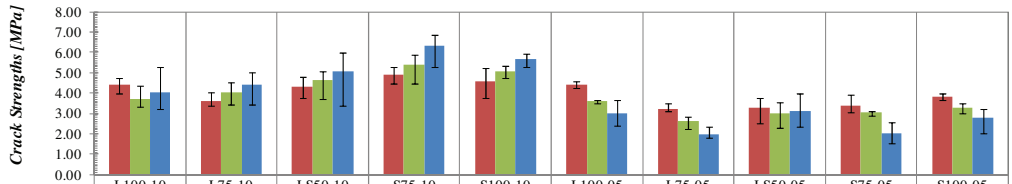

	L100-10	L75-10	LS50-10	S75-10	S100-10	L100-05	L75-05	LS50-05	S75-05	S100-05
flf	4.41	3.60	4.34	4.91	4.57	4.41	3.25	3.30	3.40	3.84
feq(0-0.6)	3.74	4.04	4.61	5.39	5.06	3.58	2.60	3.03	3.05	3.27
feq(0.6-3.0)	4.03	4.42	5.08	6.31	5.67	3.02	2.00	3.12	2.03	2.78

Figure 2.11: First crack strength, f_{lf}, and the equivalent crack ones, $f_{eq(0-0.6)}$ and $f_{eq(0.6-3.0)}$ [UNI-11039-2, 2003]. *The vertical segments quantify the min-max range observed for each concrete mixture.*

composite, have been evaluated by means of the following expression [UNI-11039-2, 2003]

$$f_{lf} = \frac{P_{lf} \cdot l}{b(h-a_0)^2} \tag{2.2}$$

where P_{lf} represents the first crack strength $[N]$; b, h and l are the width $[mm]$, height $[mm]$ and length $[mm]$ of the beam, respectively; a_0 $[mm]$ is the notch depth. Figure 2.11 reports the mean values of first crack strength and the two equivalent crack strengths, defined in standard $CTODm$ ranges, i.e. $[CTODm_0; CTODm_0 + 0.6\,mm]$ and $[CTODm_0 + 0.6; CTODm_0 + 3.0\,mm]$. These quantities, known as $f_{eq\,(0-0.6)}$ and $f_{eq\,(0.6-3.0)}$, have been defined as follows

$$\begin{aligned} f_{eq\,(0-0.6)} &= \frac{l}{b(h-a_0)^2}\frac{U_1}{0.6} \\ f_{eq\,(0.6-3.0)} &= \frac{l}{b(h-a_0)^2}\frac{U_2}{2.4} \end{aligned} \tag{2.3}$$

where U_1 and U_2 represent work capacity measures derived by means of the following relationships

$$\begin{aligned} U_1 &= \int_{CTODm_0}^{CTODm_0+0.6} P[CTODm]dCTODm \\ U_2 &= \int_{CTODm_0+0.6}^{CTODm_0+3.0} P[CTODm]dCTODm \end{aligned} \tag{2.4}$$

These two parameters represent the area under the $P-CTODm$ curves between the

range $[CTODm_0\ ;\ CTODm_0 + 0.6\,mm]$ and $[CTODm_0 + 0.6;\ CTODm_0 + 3.0\,mm]$ for U_1 and U_2, respectively.

Figure 2.12 shows the energy absorption values of each sample, calculated by means of the Eq. (2.4), while Figure 2.11 reports the values of strength parameters according to Eqs. (2.2) and (2.3) and measured for the various tested specimens. Keeping in mind the mechanical meaning of these parameters, Figure 2.11 shows that specimens reinforced with 1.0% of steel fibers exhibit a significant hardening behavior in the flexural post-cracking regime, whereas a softening behavior has generally been observed for specimens with 0.5% of fibers. It is demonstrated that a higher presence of short fibers increases the peak and post-peak strengths for small crack openings in cases with 1.0% of fiber contents. On the other hand, SFRC specimens with only presence of long fibers (L100-10) deals with a composite characterized by an immediately post-peak softening behavior in the first crack range $[CTODm_0; CTODm_0 + 0.6\,mm]$: i.e., $f_{eq_{(0-0.6)}} < f_{lf}$; then, a flexural re-hardening response takes place in the second crack range $[CTODm_0 + 0.6; CTODm_0 + 3.0\,mm]$: $f_{eq_{(0.6-3.0)}} > f_{eq_{(0-0.6)}}$. The results also clarify that the composite with the best performance has been represented by the S75-10 mixture.

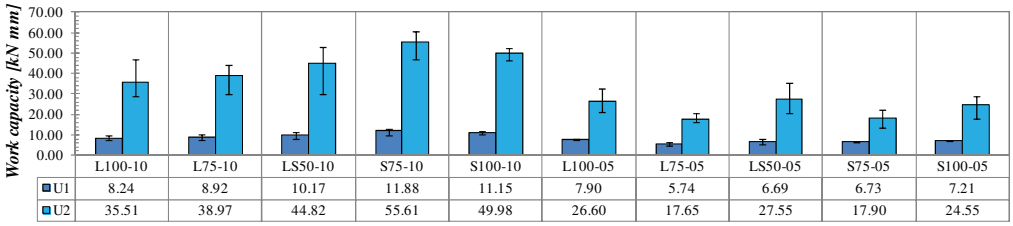

	L100-10	L75-10	LS50-10	S75-10	S100-10	L100-05	L75-05	LS50-05	S75-05	S100-05
U1	8.24	8.92	10.17	11.88	11.15	7.90	5.74	6.69	6.73	7.21
U2	35.51	38.97	44.82	55.61	49.98	26.60	17.65	27.55	17.90	24.55

Figure 2.12: Energy absorption measures U_1 and U_2 according to UNI-11039-2 [2003]. *The vertical segments quantify the min-max range observed for each concrete mixture.*

Experimental results on SFRC with low fiber contents (0.5%) have been characterized by high sensitivity to the number of fibers crossing the cracked section. It follows that a lower stability of the experimental results can be recognized. Furthermore, as for the 1.0% types, the presence of short fibers enhances the post-peak strength for small cracks (as shown in Figure 2.11 for the cases of LS50-05, S75-05 and S100-05), but these residual strengths rapidly decrease, as fibers debond from the cementitious matrix.

Further ductility indices can be considered as objective measurements of the fiber bridging effect. Based on the UNI-11039-2 [2003] code, the two following ductility

measures have been calculated

$$D_0 = f_{eq_{(0-0.6)}} / f_{lf} \tag{2.5}$$

and

$$D_1 = f_{eq_{(0.6-3.0)}} / f_{lf} \tag{2.6}$$

Figure 2.13 depicts the values of ductility indices defined by Eqs. (2.5) and (2.6) and measured for the various tested beams.

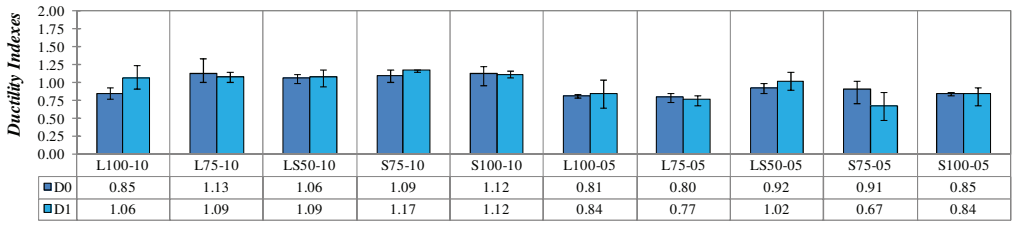

	L100-10	L75-10	LS50-10	S75-10	S100-10	L100-05	L75-05	LS50-05	S75-05	S100-05
D0	0.85	1.13	1.06	1.09	1.12	0.81	0.80	0.92	0.91	0.85
D1	1.06	1.09	1.09	1.17	1.12	0.84	0.77	1.02	0.67	0.84

Figure 2.13: Indices of the ductility according to UNI-11039-2 [2003]. *The vertical segments quantify the min-max range observed for each concrete mixture.*

Class	$F_{2.0}$	$F_{2.5}$	$F_{3.0}$	$F_{3.7}$	$F_{4.5}$	$F_{5.5}$	$F_{6.5}$	$F_{7.7}$	$F_{9.0}$
First Crack Resistance (Minimum Value)	2.0	2.5	3	3.7	4.5	5.5	6.5	7.7	9

Ductility Indices (Minimum Value)	Ductility Class						
	D_{S0}	D_{S1}	D_{S2}	D_P	D_{H0}	D_{H1}	D_{H2}
D_0	< 0.5	≥ 0.5	≥ 0.7	≥ 0.9	≥ 1.1	≥ 1.3	≥ 1.55
D_1	≥ 0.3	≥ 0.5	≥ 0.7	≥ 0.9	≥ 1.1	≥ 1.3	≥ 1.55
Type of response	crack-softening			perfectly plastic	crack-hardening		

Figure 2.14: Classifications based on the first crack resistances and the ductility indices by UNI-11039-1 [2003] code.

According to the classification of UNI-11039-1 [2003] reported in Figure 2.14, when the specific ductility index (referred to the considered $CTODm$ range) is greater than the unit, the material is considered as a crack-hardening medium under flexure. When those indices are approximatively equal to 1 the SFRC exhibits a plastic post-cracking behavior. If D_0 or $D_1 \leq 1$ the post-cracking response is mainly softening. In practical design, minimum mechanical performances are required to SFRC composites. Particularly, only if $f_{eq_{(0-0.6)}} \geq 0.5 \cdot f_{lf}$ or $D_0 \geq 0.5$ the post-cracking resistance can

be considered. Fiber reinforcements can substitute (also partially) the conventional reinforcements at ultimate limit state if the above limits are fulfilled [UNI-11039-1, 2003].

2.4 Closing remarks

This chapter reports the results of a series of experimental tests aimed at investigating the behavior of FRC beams under four-point bending. Particularly, the proposed experimental campaign focuses on investigating the possible influence of combining two different types of fibers on the resulting properties of FRC. Thus, five combinations of long/short hooked-end fibers have been considered in the concrete mixtures and two different amounts of steel fibers have been employed for each of them.

The following observations emerged by analyzing the experimental results:

- the first-crack strength and the whole post-cracking behavior have mainly been influenced by the amount of fibers: crack-softening response has been observed for all specimens with $\rho_f = 0.5\%$, whereas a rather plastic behavior characterizes the post-cracking response of specimens with $\rho_f = 1.0\%$;
- a slight influence of fiber combination has been observed in terms of first-crack strength: this parameter has been almost irrelevant in the case of low amount of fibers, while results in a slightly more regular trend in the case of $\rho_f = 1.0\%$ fibers;
- the ductility indices determined for all specimens point out that no clear influence can be recognized to fiber combination in affecting the overall response of FRC in the post-cracking regime.

As a matter of fact, the very low influence of fiber combination on the observed FRC behavior is the key conclusion of the experimental activity in this thesis. However, it is worth highlighting that this cannot be considered as a general conclusion, as the two “different” fibers have been characterized by the same material, similar geometric details (i.e., hooked-ends) and rather close values of aspect ratios. Thus, the possible synergistic effect of combining different types of fibers should be investigated by considering two (or more) kinds of really “more different” fibers (i.e., in terms of materials, geometric and detailing).

3 Zero-thickness interface model for FRCC

This chapter deals with the formulation of a zero-thickness interface model conceived within the general framework of the discrete-crack approach and aimed at simulating the mechanical response of Fiber-Reinforced Cementitious Composites (FRCCs). Following a cohesive-frictional interface proposal, already available in scientific literature for plain concrete, the formulation of an interface constitutive model is further developed and extended to capture the key mechanical phenomena controlling the FRCC behavior. An original approach is introduced for reproducing the complex influence of fibers on cracking phenomena of concrete/mortar matrix. Particularly, the interface model takes into account both the bond-slip strength and dowel mechanisms generated by fibers crossing the concrete cracks.

This novel interface model for FRCC is mainly based on the flow Theory of Plasticity and Fracture Mechanics concepts to control the energy release during cracking processes under both mode I and/or II of fracture. The constitutive law represents an extension of the previous interface formulation for plain concrete approached by Carol et al. [1997] and by Lopez et al. [2008a,b] to take into account the interaction between cement/mortar and steel fibers. The well-known "Mixture Theory" is adopted for modeling the interactions between fibers and the surrounding cementitious composite.

In this chapter, section 3.1 briefly reports the main issues of the interface model for FRCC and outlines the key assumptions utilized in the constitutive proposal. Section 3.2 summarizes an overview of "Mixture Theory" concepts [Trusdell and Toupin, 1960] and its use on the given discontinuous proposal. The interface model, aimed in principle at reproducing the post-peak softening behavior due to crack propagations in plain concrete is outlined in section 3.3. It is formulated by means of an incremental approach, which is similar to the one usually adopted in the classical flow theory of

plasticity. A novel bond-slip model for simulating the axial effect of fibers on concrete cracks is presented in section 3.4. Then, the composite action between concrete and fiber reinforcements is also completed by considering the dowel effect of fibers as proposed in section 3.5. Some concluding remarks are finally reported in section 3.6 to highlight the key aspects of the model formulated in this chapter.

3.1 Interface constitutive model for FRCC

The proposed constitutive model for FRCC interfaces is based on an application of the "Mixture Theory" and includes three internal "components" listed below:

1. a *fracture energy-based cracking formulation for plain mortar/concrete interfaces* which relates normal and tangential stress components with the corresponding relative displacements in the plane of the interface. Its maximum strength criterion is defined according to the three-parameter hyperbolic failure surface by Carol et al. [1997]. Main features of this model are summarized in section 3.3.

2. a*fiber bond-slip formulation* to describe the uniaxial inelastic behavior of steel fibers crossing the interfaces by means of an elastoplastic model as indicated in section 3.4.

3. a *formulation for fiber dowel action* based on elastic foundation concepts to obtain the dowel force-displacement relationship. Further details of the constitutive model are proposed in section 3.5.

For the sake of simplicity, the model is formulated in 2D, as proposed by Lopez et al. [2008a,b] in a similar formulation for simulating the mesoscale fracture behavior on plain concrete. Particularly, they demonstrate that the results obtained in 2D successfully reproduce the experimental behavior under several basic stress states.

3.2 Outline of the Mixture Theory

3.2.1 Composite material model

According to the fundamental assumptions of the Mixture Theory formulated in Truesdell and Toupin [1960], each infinitesimal volume of the mixture is ideally occupied by all mixture constituents (i.e. "phases"), that are subjected to the same displacement

fields. Consequently, the composite stress is obtained from the addition of the mixture stresses weighted by the volume fraction of each mixing constituent.

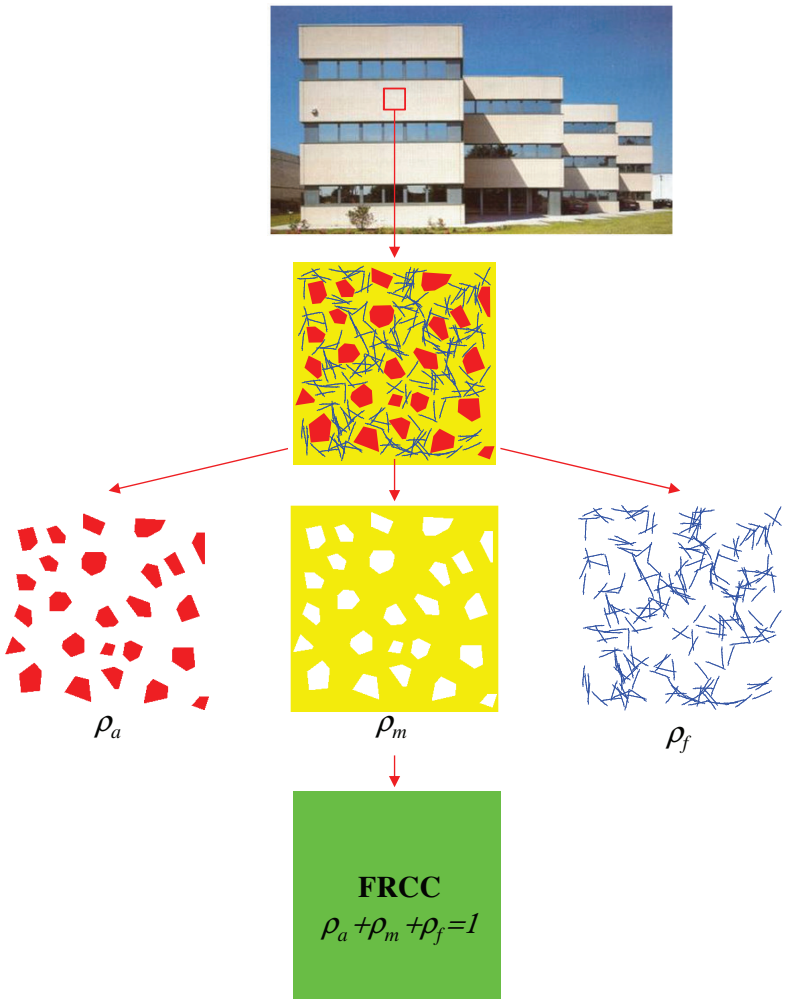

Figure 3.1: Main assumptions of fiber-reinforced cementitious composite in the framework of the well-known "Mixture Theory" [Trusdell and Toupin, 1960].

The composite schematization of a considered steel FRCC panel, as in Figure 3.1, takes into account three main phases: (i) coarse aggregates, (ii) cementitious matrix or mortar and (iii) steel fibers. The mechanical properties of the considered composite material can be defined according to the "Mixture Theory" above mentioned. For instance, a

generic mechanical parameter of the composite can be derived as

$$p_c = \rho_a p_a + \rho_m p_m + \rho_f p_f \tag{3.1}$$

being p_c the considered mechanical parameter (i.e., the elastic modulus or the Poisson's ratio) while $\rho_\#$ refers to the volume fraction of each # component (Figure 3.2): i.e., $\# = _c$ for the considered composite, $\# = _a$ for coarse aggregates, $\# = _m$ for matrix and $\# = _f$ for fibers.

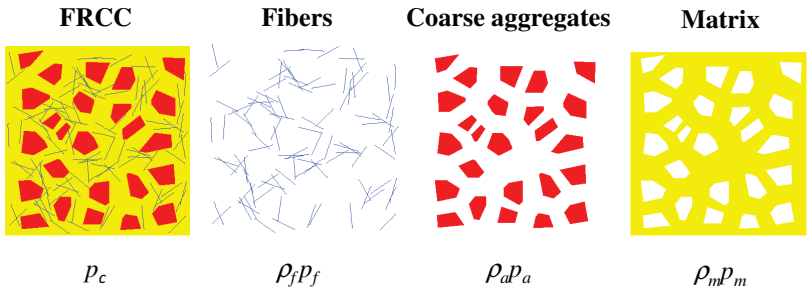

Figure 3.2: Mixture components of the FRCC continuum material.

In a similar way, it can be considered a generic relative displacement vector at the interface $\boldsymbol{u}$ (Figure 3.3), where the axial displacement of the single fiber is given by $u_N = \boldsymbol{u} \cdot \boldsymbol{n}_N$ (being $\boldsymbol{n}_N$ the fiber direction), while in the transversal direction $u_T = \boldsymbol{u} \cdot \boldsymbol{n}_T$. Thereby, $\boldsymbol{n}_T$ is a unitary vector orthogonal to $\boldsymbol{n}_N$. Consequently, the axial and tangential fiber strains can be derived as $\varepsilon_N = u_N / l_f$ and $\gamma_T = u_T / l_f$, respectively, being l_f the fiber length (each fiber is ideally assumed to cross the interface fracture surface at its mid-length, i.e. at $l_f/2$).

The interface constitutive model is formulated in incremental form, as generally assumed for the flow theory of plasticity. According to the hypotheses of the composite model, the rate of the stress vector at the interface $\dot{\boldsymbol{t}} = [\dot{\sigma}, \dot{\tau}]^t$ (being σ and τ the normal and tangential interfacial composite stresses, respectively) is calculated by means of the following $\rho_\#$-weighted sum

$$\dot{\boldsymbol{t}} = w[\rho_i]\, \dot{\boldsymbol{t}}^i + \sum_{f=0}^{n_f} w[\rho_f] \left(\dot{\sigma}_f \left[\dot{\varepsilon}_N\right] \boldsymbol{n}_N + \dot{\tau}_f \left[\dot{\gamma}_T\right] \boldsymbol{n}_T \right). \tag{3.2}$$

The indices i and f refer to interface and fiber, respectively; σ_f and τ_f mean the bond-slip force and dowel effect of the single considered fiber; n_f is the number of fibers crossing the interface. The weighting function of the plain interfaces $w[\rho_i]$ is generally

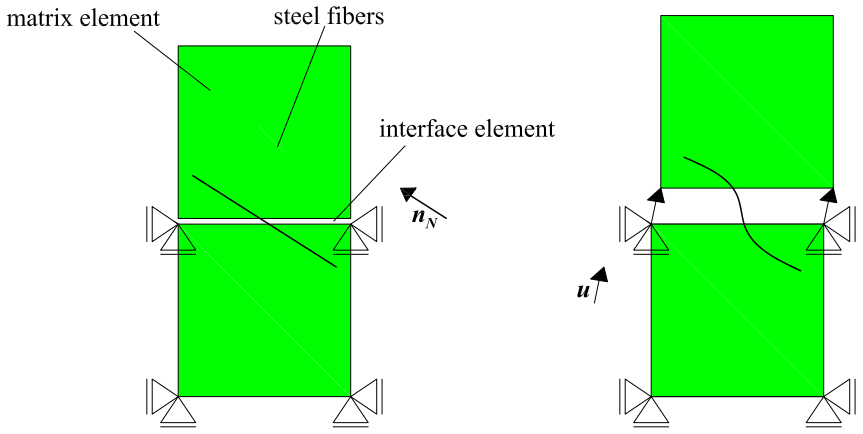

Figure 3.3: Schematic configuration of an interface element crossed by one fiber.

assumed equal to one, while $w[\rho_f]$ takes into account the effectiveness decay of fiber contributions to the total stress as the fiber content increases. It can be formulated as a function of the total fiber content ρ_f,

$$w[\rho_f] = \left[1 - \alpha_f \rho_f\right] \rho_{f,1} \tag{3.3}$$

being $\rho_{f,1}$ the fiber content of a single reinforcement, while α_f is a material parameter to be calibrated.

The fiber bridging effect, formulated herein in terms of bond-slip and dowel mechanisms, are schematically represented in the interface plane as in Figure 3.4.

The number of fibers per interface, radially distributed in the crack plane, is explicitly considered in the proposed formulation. No random distribution of fibers is considered. It would have required complex (though well-established) statistical procedures and is beyond the scopes of this thesis. Particularly, the interface model deals with the schemes reported in Figure 3.5, in which a regular iso-angular spacing between fibers crossing the interface is considered.

The evaluation of the total number of fibers which cross the interface is essentially

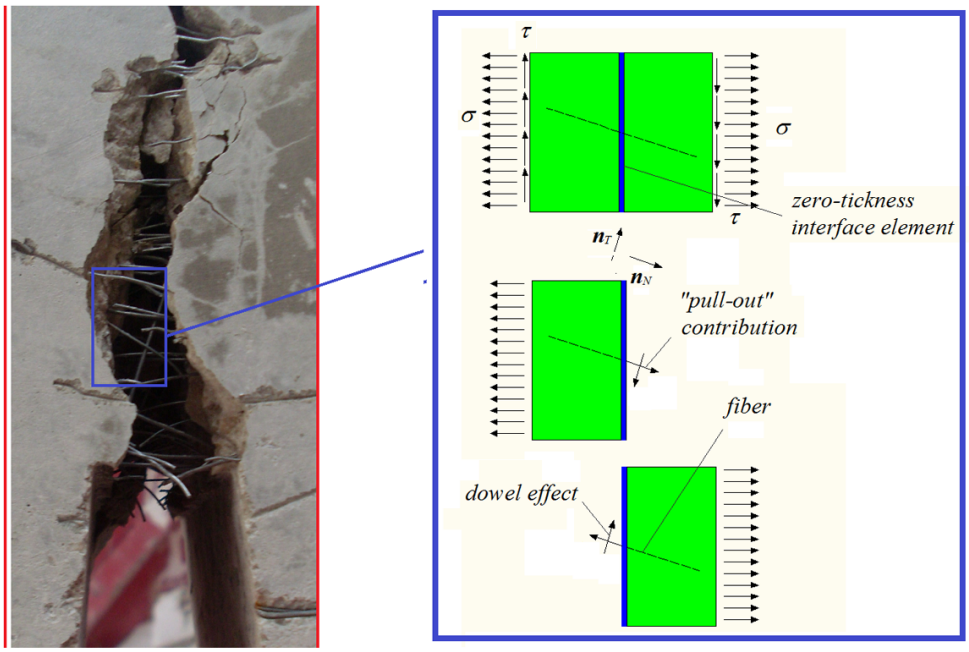

Figure 3.4: Fiber effects on the plane of the zero-thickness interface.

founded on the relationship proposed by Krenchel [1975]

$$n_f = \alpha_{\tilde{N}} \frac{\rho_f}{A_f} A_i \tag{3.4}$$

where ρ_f is the fiber content, A_f and A_i are the cross-sectional area of a single fiber and the area of the considered interface, respectively.

The calculation of the orientation factor $\alpha_{\tilde{N}}$ has been investigated by many researchers [Krenchel, 1975, Soroushian and Lee, 1990, Li et al., 1991, Stroeven, 1999, Kooiman, 2000, Dupont and Vandewalle, 2005, Laranjeira et al., 2012]. The proposal outlined by Dupont and Vandewalle [2005] is taken as a reference in this work.

3.2.2 Constitutive models of each single phase

The relationship between stresses and relative displacements, developed throughout the generic fracture interface, can be formulated in the following incremental form, as

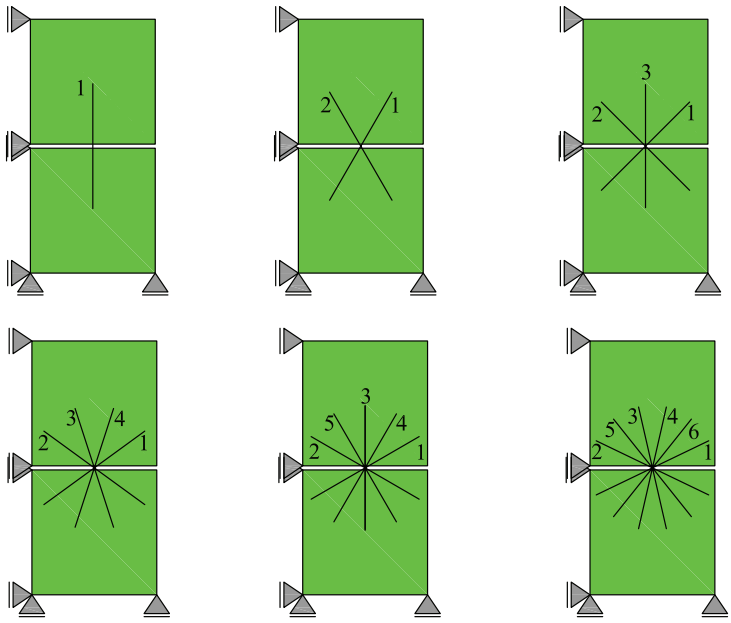

Figure 3.5: Considered fibers crossing the interface: as example the cases of 1, 2, 3, 4, 5 and 6 reinforcements are presented.

usual in classical plasticity-based model

$$\dot{\boldsymbol{t}} = \boldsymbol{E}^{ep} \cdot \dot{\boldsymbol{u}} \tag{3.5}$$

being $\dot{\boldsymbol{t}}$ the rate vector of the composite joint stresses and $\dot{\boldsymbol{u}}$ the interface displacement rate vector, respectively.

As previously proposed, the formulation of the composite interface is based on assuming that each infinitesimal surface is ideally occupied by all components. Each component is subjected to the same displacement field, while the corresponding composite stress is given by the weighted sum of the component stresses. For the same assumption the constitutive tangent operator, $\boldsymbol{E}^{ep}$, is given by the following expression

$$\boldsymbol{E}^{ep} = w[\rho_i]\boldsymbol{C}^{ep} + \sum_{f=0}^{n_f} w[\rho_f] \left(\frac{E_f^{ep}}{l_f} \boldsymbol{n}_N \otimes \boldsymbol{n}_N + \frac{G_f^{ep}}{l_f} \boldsymbol{n}_T \otimes \boldsymbol{n}_T \right) \tag{3.6}$$

based on the weighting functions $w[\rho_\#]$ ($\# = i, f$) of Eq. (3.3), where $\rho_\#$ represents the volume fraction of the # composite phase, $\boldsymbol{n}_N \otimes \boldsymbol{n}_N$ and $\boldsymbol{n}_T \otimes \boldsymbol{n}_T$ identify the second

order dyadic tensor constructed on the fiber direction and its orthogonal of a generic fiber with respect to the global Cartesian reference system.

The tangent operators $\left[\boldsymbol{C}^{ep}, E_f^{ep}, G_f^{ep}\right]$ of Equation [3.6] are defined as follows:

- *for the fracture energy-based plain interface model*

$$\boldsymbol{C}^{ep} = \partial \boldsymbol{t}^i / \partial \boldsymbol{u}, \tag{3.7}$$

  formulated in terms of normal (σ_N) and shear (σ_T) stresses ($\boldsymbol{t}^i = [\sigma_N, \sigma_T]^t$) of plain concrete joints corresponding to the relative displacements $\boldsymbol{u}$ (further details are explained in section 3.3);

- *for the bond-slip fiber-to-concrete model*

$$E_f^{ep} = d\sigma_f / d\varepsilon_N, \tag{3.8}$$

  being σ_f and ε_N the axial stress and strain of fibers at cracks (ideally assuming that each fiber crosses the interface fracture surface at its mid-length, i.e. $l_f/2$); a closed-form analytical constitutive model for the debonding fiber process (in terms of $\sigma_f - \varepsilon_N$ law) is considered (see section 3.4 for further details);

- *for the dowel action model*

$$G_f^{ep} = d\tau_f / d\gamma_T, \tag{3.9}$$

  in which the elastic branch of the shear stress-strain law ($\tau_f - \gamma_T$) is derived by modeling the fiber embedded into the cement matrix as an elastic beam on a Winkler foundation (as presented in section 3.5).

3.3 Fracture energy-based model for plain mortar/concrete interface

This section summarizes the interface model originally proposed in Gens et al. [1988] for application in soil-mechanics and extended to plain concrete by Carol et al. [1997]. The constitutive equation, in the framework of the rate-independent plasticity theory, can be presented in incremental form as

$$\dot{\boldsymbol{u}} = \dot{\boldsymbol{u}}^{el} + \dot{\boldsymbol{u}}^{cr} \tag{3.10}$$

$$\dot{\boldsymbol{u}}^{el} = \boldsymbol{C}^{-1} \cdot \dot{\boldsymbol{t}}^i \tag{3.11}$$

$$\dot{\boldsymbol{t}}^i = \boldsymbol{C} \cdot (\dot{\boldsymbol{u}} - \dot{\boldsymbol{u}}^{cr}) \tag{3.12}$$

where $\dot{\boldsymbol{u}} = [\dot{u}, \dot{v}]^t$ is the rate of the relative joint displacement vector, decomposed into the elastic and plastic components, $\dot{\boldsymbol{u}}^{el}$ and $\dot{\boldsymbol{u}}^{cr}$, respectively. $\boldsymbol{C}$ defines a fully uncoupled normal/tangential elastic stiffness matrix

$$\boldsymbol{C} = \begin{pmatrix} k_N & 0 \\ 0 & k_T \end{pmatrix} \tag{3.13}$$

while $\dot{\boldsymbol{t}}^i = [\dot{\sigma}_N, \dot{\sigma}_T]^t$ is the incremental stress vector defined in the interface coordinates, being σ_N and σ_T the normal and shear components, respectively.

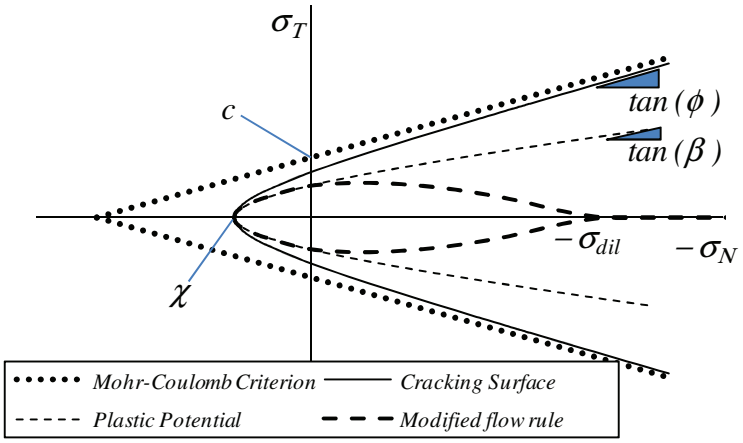

Figure 3.6: Failure hyperbola by Carol et al. [1997], Mohr-Coulomb surface, plastic potential and the modified flow rule according to Eq. (3.19) of the interface model.

The vector of the plastic displacement rate, according to a non-associated flow rule, is defined as

$$\dot{\boldsymbol{u}}^{cr} = \dot{\lambda}\boldsymbol{m} \tag{3.14}$$

where $\dot{\lambda}$ is the non-negative plastic multiplier derived by means of the classical Kuhn-Tucker loading/unloading and consistency conditions which take the following form

$$\begin{aligned} &\dot{\lambda} \geq 0, \quad f \leq 0, \quad \dot{\lambda} \cdot f = 0 \quad \text{Kuhn} - \text{Tucker} \\ &\dot{f} = 0 \qquad\qquad\qquad\quad \text{Consistency} \end{aligned} \tag{3.15}$$

where $f = f[\sigma_N, \sigma_T]$ defines the yield condition of the model on the bases of the following three-parameter formulation (outlining the hyperbola represented in Figure

3.6)

$$f = \sigma_T^2 - (c - \sigma_N \tan\phi)^2 + (c - \chi \tan\phi)^2. \tag{3.16}$$

The tensile strength χ (vertex of the hyperbola), the cohesion c and the frictional angle ϕ are material parameters needed for identifying the interface model. Eq. (3.16) outlines two principal failure modes:

- *Mode I type of fracture*: maximum strength surface is reached along its horizontal axis;
- *asymptotic Mode II type of fracture*: maximum strength surface is reached on its asymptotic region in which the hyperbola approaches a Mohr-Coulomb criterion (see Figure 3.6).

Eq. (3.14) describes a general non-associated flow rule which controls the direction $\boldsymbol{m}$ of interface fracture displacements. In the proposed formulation the non-associated plastic direction is described by means of the transformation matrix operator $\boldsymbol{A}$

$$\boldsymbol{m} = \boldsymbol{A} \cdot \boldsymbol{n} \tag{3.17}$$

being

$$\boldsymbol{n} = \frac{\partial f}{\partial \boldsymbol{t}^i} = \left[\frac{\partial f}{\partial \sigma_N}, \frac{\partial f}{\partial \sigma_T}\right]^t = \left[2\tan\phi(c - \sigma_N \tan\phi), 2\sigma_T\right]^t \tag{3.18}$$

and

$$\boldsymbol{A} = \begin{cases} \begin{pmatrix} \frac{\tan\beta}{\tan\phi} & 0 \\ 0 & 1 \end{pmatrix} & \text{if} \quad \sigma_N \geq 0 \\ \begin{pmatrix} \left[1 - \frac{|\sigma_N|}{\sigma_{dil}}\right] \frac{\tan\beta}{\tan\phi} & 0 \\ 0 & 1 \end{pmatrix} & \text{if} \quad -\sigma_{dil} \leq \sigma_N < 0 \\ \begin{pmatrix} 0 & 0 \\ 0 & 1 \end{pmatrix} & \text{if} \quad \sigma_N < -\sigma_{dil} \end{cases} \tag{3.19}$$

where β is the so-called dilation angle of the plastic potential, represented in Figure 3.6: $0 \leq \tan\beta \leq \tan\phi$. Thereby, the parameter σ_{dil} represents the normal stress at which the dilatancy vanishes, see in Carol et al. [1997] and Lopez [1999].

3.3.1 Single internal state variable

The fracture work w_{cr} spent during the opening-sliding fracture process controls the actual evolutions of the material parameters χ, c and $\tan\phi$ in softening regime of the interface constitutive law. The variable w_{cr} defines the necessary amount of released energy to open a single crack in tensile and/or shear fracture mode due to normal σ_N and/or tangential σ_T joint stresses, respectively.

Hence the incremental fracture work spent $\dot{w}_{cr}$, in a generic fracture process, is defined as follows [Carol et al., 1997]

$$\dot{w}_{cr} = \sigma_N \cdot \dot{u}^{cr} + \sigma_T \cdot \dot{v}^{cr}, \ if\ \sigma_N \geqslant 0 \tag{3.20}$$

$$\dot{w}_{cr} = \left[\sigma_T - |\sigma_N|\, tan(\phi)\right] \cdot \dot{v}^{cr}, \ if\ \sigma_N < 0 \tag{3.21}$$

while the total dissipated work is obtained by integrating the fracture work increments during fracture process time frame.

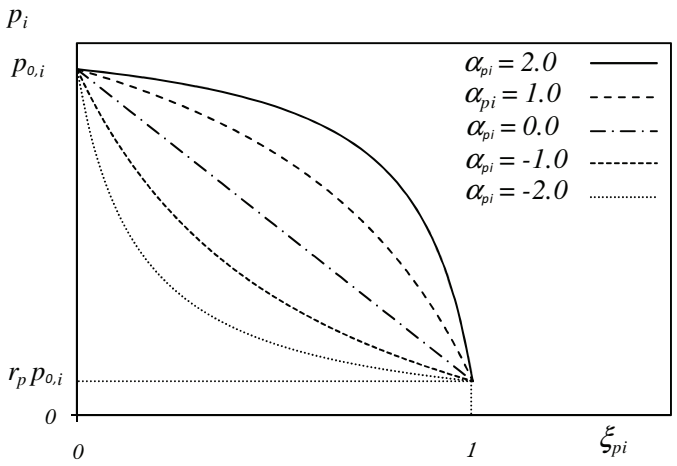

Figure 3.7: Evolution law of the interface fracture parameters.

3.3.2 Evolution laws of the fracture surface

In this formulation, the decay function proposed in Caballero et al. [2008] is considered for all internal parameters of the yield condition, see Eq. (3.16), as

$$p_i = \left[1 - \left(1 - r_p\right) S[\xi_{p_i}]\right] p_{0i} \tag{3.22}$$

with p_i alternatively equals to χ, c or $tan\phi$. Last equation defines the typical degradation law of the internal parameters from their maximum or initial values, $p_i = p_{0i}$, to the residual ones, $p_i = r_p p_{0i}$, in terms of the scaling function $S[\xi_{p_i}]$, where

$$S[\xi_{p_i}] = \frac{e^{-\alpha_{p_i}}\xi_{p_i}}{1+(e^{-\alpha_{p_i}}-1)\xi_{p_i}} \tag{3.23}$$

in which the parameter α_{p_i} controls the decay form of the internal parameter as shown in Figure 3.7, while the non-dimensional variable ξ_{p_i} introduces the influence of the ratio between the current fracture work spent and the available fracture energy, in the decay function Eq. (3.22) as

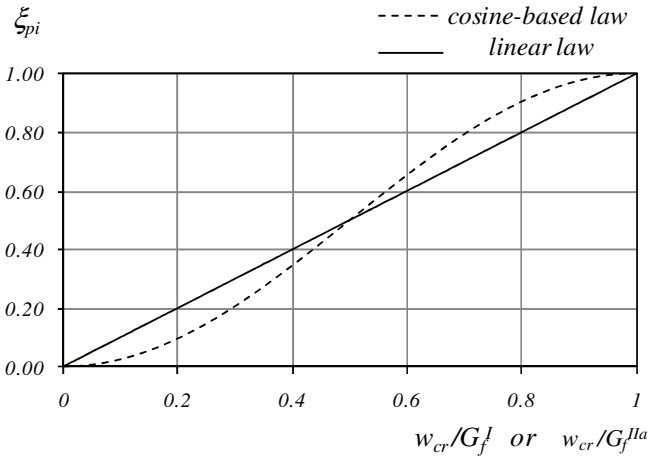

Figure 3.8: Cosine-based vs. linear law related to the ratio between the work spent w_{cr} and the available fracture energies G_f^I or G_f^{IIa}.

$$\xi_\chi = \begin{cases} \frac{1}{2}\left[1-cos\left(\frac{\pi w_{cr}}{G_f^I}\right)\right] & \text{if } w_{cr} \le G_f^I \\ 1 & \text{otherwise} \end{cases} \tag{3.24}$$

$$\xi_c = \xi_{\tan\phi} = \begin{cases} \frac{1}{2}\left[1-cos\left(\frac{\pi w_{cr}}{G_f^{IIa}}\right)\right] & \text{if } w_{cr} \le G_f^{IIa} \\ 1 & \text{otherwise} \end{cases} \tag{3.25}$$

according to the C^1 continuity function proposed in Caballero et al. [2008]. Figures 3.8 and 3.9 show typical curves obtained with Eqs. (3.24) or (3.25) and the respective derivates compared to the original linear proposal in Carol et al. [1997].

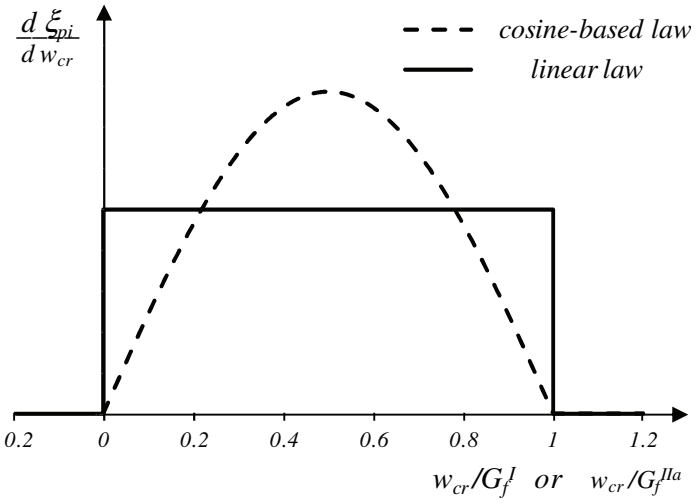

Figure 3.9: Comparison of the derivates between the cosine-based law against the linear rule.

3.3.3 An overview of the interface model for plain concrete/mortar

In the above subsections a rate-independent fracture energy-based plasticity model has been presented and the main aspects of the interface formulation have completely been detailed.

Table 3.1: Overview of the interface model for Plain Concrete/Mortar.

	Fracture - based energy interface model
Constitutive equation	$\dot{\boldsymbol{t}}^i = \boldsymbol{C}\cdot\left(\dot{\boldsymbol{u}} - \dot{\boldsymbol{u}}^{cr}\right)$ $\dot{\boldsymbol{u}} = \dot{\boldsymbol{u}}^{el} + \dot{\boldsymbol{u}}^{cr}$
Yield condition	$f\left(\boldsymbol{t}^i,\kappa\right) = \sigma_T^2 - (c - \sigma_N \tan\phi)^2 + (c - \chi\tan\phi)^2$
Flow rule	$\dot{\boldsymbol{u}}^{cr} = \dot{\lambda}\,\boldsymbol{m}$ $\boldsymbol{m} = \boldsymbol{A}\cdot\boldsymbol{n}$
Cracking work evolution	$\dot{\kappa} = \dot{w}_{cr}$ $\dot{w}_{cr} = \sigma_N\cdot\dot{u}^{cr} + \sigma_T\cdot\dot{v}^{cr}$ if $\sigma_N \geq 0$ $\dot{w}_{cr} = \left[\sigma_T - \lvert\sigma_N\rvert\, tan(\phi)\right]\cdot\dot{v}^{cr}$ if $\sigma_N < 0$
Evolution law	$p_i = \left[1 - \left(1 - r_p\right) S[\xi_{p_i}]\right] p_{0i}$
Kuhn - Tucker / Consistency	$\dot{\lambda} \geq 0, \quad f\left(\boldsymbol{t}^i,\kappa\right) \leq 0, \quad \dot{\lambda}\, f\left(\boldsymbol{t}^i,\kappa\right) = 0, \quad \dot{f}\left(\boldsymbol{t}^i,\kappa\right) = 0$

This final subsection is aimed at compactly reporting all the interface ingredients

above discussed. Particularly, in Table 3.1 the adopted yield criterion, the flow rule, the cracking work evolution laws and the well-known Kuhn-Tucker and consistency conditions are compactly reported.

3.4 One-dimensional bond-slip model for fibers

This section deals with formulating the proposed one-dimensional plasticity model for the steel fiber stress-strain response to be considered within the composite model described in Eq. (3.2). Particularly, the total strain rate $\dot{\varepsilon}_N$ can be decomposed into elastic ($\dot{\varepsilon}_N^{el}$) and plastic ($\dot{\varepsilon}_N^{pl}$) components as

$$\dot{\varepsilon}_N = \dot{\varepsilon}_N^{el} + \dot{\varepsilon}_N^{pl} \tag{3.26}$$

and the total stress rate results

$$\dot{\sigma}_f = E_f(\dot{\varepsilon}_N - \dot{\varepsilon}_N^{pl}) \tag{3.27}$$

where E_f represents the uniaxial elastic modulus which encompasses both the uniaxial response of the steel fiber and the bond-slip effect of the short steel reinforcement in mortar/concrete interfaces. In case of isotropic hardening, the yield condition takes the following form

$$f_f = |\sigma_f| - (\sigma_{y,f} + Q_f) \leq 0 \tag{3.28}$$

with $\sigma_{y,f} \geq 0$ the initial yield stress and Q_f the internal softening variable in post-elastic regime. Its evolution law is defined as

$$\dot{Q}_f = \dot{\lambda}_f H_f \tag{3.29}$$

while the one of the plastic strain rate results

$$\dot{\varepsilon}_N^{pl} = \dot{\lambda}_f \partial f_f / \partial \sigma_f = \dot{\lambda}_f sign[\sigma_f] \tag{3.30}$$

being $\dot{\lambda}_f$ the plastic multiplier and H_f is the softening module.

Then, the Kuhn-Tucker loading/unloading conditions are given by

$$\dot{\lambda}_f \geq 0,\ f_f(\sigma_f, Q_f) \leq 0,\ \dot{\lambda}_f f_f(\sigma_f, Q_f) = 0 \tag{3.31}$$

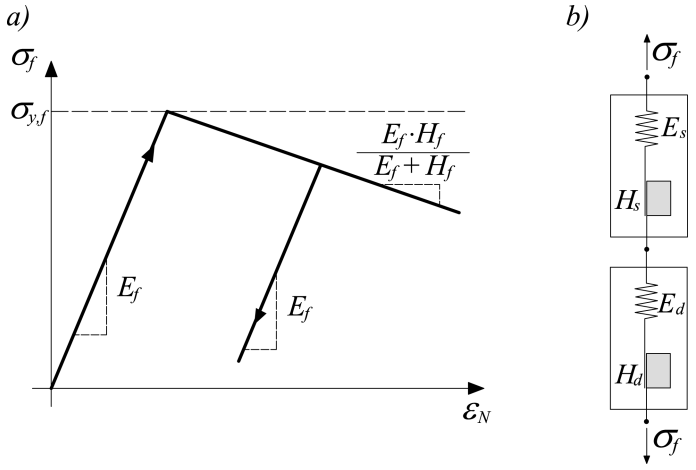

Figure 3.10: (a) Uniaxial model of fiber bond-slip and (b) serial model for the axial/debonding behavior.

by imposing the consistency condition $\dot{f}_f(\sigma_f, Q_f) = 0$.

The constitutive stress-strain relationship can be written as

$$\dot{\sigma}_f = E_f^{ep} \dot{\varepsilon}_N \tag{3.32}$$

where the elasto-plastic tangent module E_f^{ep} takes the two distinct following values [Simo and Hughes, 1998]

$$\begin{cases} E_f^{ep} = E_f & \rightarrow \text{elastic/unloading response} \\ E_f^{ep} = \frac{E_f \cdot H_f}{E_f + H_f} & \rightarrow \text{elasto-plastic regime} \end{cases} . \tag{3.33}$$

Fiber strain ε_N can be simply decomposed into two parts, one due to the intrinsic uniaxial deformation $\varepsilon_{N,s}$ and the other associated to the interface debonding $\varepsilon_{N,d}$,

$$\varepsilon_N = \varepsilon_{N,s} + \varepsilon_{N,d}. \tag{3.34}$$

Assuming a serial system with two 1D elasto-plastic components, corresponding to the fiber axial behavior and the fiber-matrix debonding (see Figure 3.10b), the resulting total elastic flexibility $1/E_f$ is given as

$$\frac{1}{E_f} = \frac{1}{E_s} + \frac{1}{E_d} \tag{3.35}$$

where E_s and E_d are the steel fiber elastic modulus and the equivalent elastic one of matrix-fiber debonding, respectively. Two limiting situations can be recognized:

- $E_d \to 0$, in which the serial structure response and, consequently, the uniaxial fiber strength vanish (debonding).
- $E_d \to \infty$, representing the perfect bonding case between fiber and matrix.

The bond-slip axial constitutive model can be completed by defining the following material parameters

$$\sigma_{y,f} = min[\sigma_{y,s}, \sigma_{y,d}] \tag{3.36}$$

$$H_f = \begin{cases} H_s & \text{if } \sigma_{y,s} < \sigma_{y,d} \\ H_d & \text{otherwise} \end{cases} \tag{3.37}$$

whereby $\sigma_{y,s}$ and $\sigma_{y,d}$ are the yield stress and the equivalent interface elastic limit, respectively.

The parameters E_d, $\sigma_{y,d}$ and H_d required for the bond-slip model characterization, can be calibrated by analyzing a simple pull-out scheme as proposed in the following subsections and derived in detail in Chapter 4.

3.4.1 Pull-out analysis of a single fiber

Figure 3.11 shows an isolated fiber loaded by an axial force, P_i. The fiber is embedded in a cementitious matrix for a l_{emb} length measure. The equilibrium scheme, proposed in in Figure 3.11, is used to simulate the complete slipping behavior.

The following basic equations are used for analyzing the fiber-to-concrete debonding process:

- The *equilibrium rule*: $\frac{d\sigma_f[x]}{dx} = -\frac{4\tau_a[x]}{d_f}$, being σ_f the axial stress of the fiber, τ_a the shear bond stress and d_f the diameter of the fiber.
- The *fiber constitutive law in axial direction*: $\sigma_f[x] = E_s \frac{ds[x]}{dx}$, with E_s the elastic steel modulus and $s[x]$ the slip between fiber and surrounding concrete mortar based on the assumption of Figure 3.11.

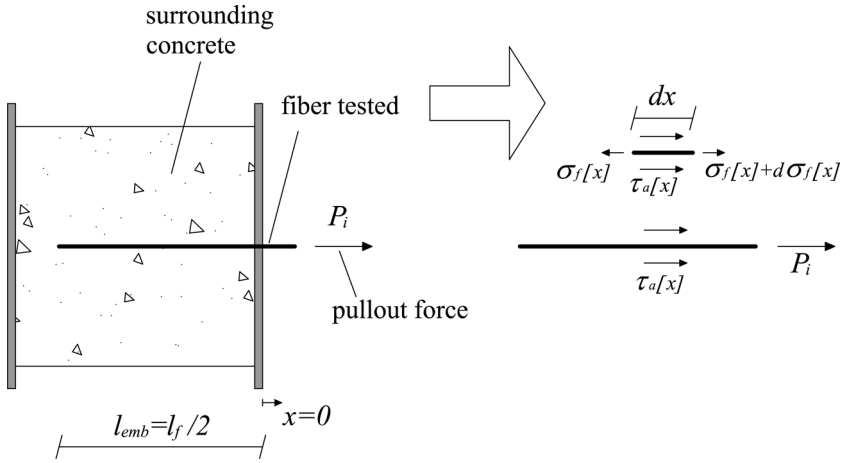

Figure 3.11: Pull-out of a single fiber.

- *Bond constitutive law*: $\tau_a[x] = \begin{cases} -k_E s[x] & s[x] \le s_e \\ -\tau_{y,a} + k_S (s[x] - s_e) & s_e < s[x] \le s_u \\ 0 & s[x] > s_u \end{cases}$,

  where, assuming a bilinear $\tau_a - s$ law, k_E and $-k_S$ represents the slope of the elastic and softening branches of the bond-slip relationship, respectively, whereas $\tau_{y,a}$ is the maximum shear stress. Thus, $s_e = \frac{\tau_{y,a}}{k_E}$ and s_u represent the elastic and the ultimate slips, respectively.

As schematically reported in Table 3.2 and based on the approaches proposed for studying FRP laminates under pull-out by Yuan et al. [2004] for long anchorages and Caggiano et al. [2012c] for both short and long ones, different states of the bond response can be defined. The fiber-to-concrete interface is in elastic bond state (E) if $s[x] \le s_e$, in softening state (S) when $s_e < s[x] \le s_u$, or the bond is crushed if $s[x] > s_u$. A combination of these three stress states can occur throughout the bonding length during the pull-out process of the single fiber (see Table 3.2).

Fully elastic behavior of fibers is assumed. This is strictly true in the case of synthetic fibers, while can be accepted for steel ones when the length l_{emb} results in the condition of $P_{i,max} \le \sigma_{y,s} A_f$, where $\sigma_{y,s}$ is the yielding stress and A_f the area of the fiber transverse section.

For the sake of simplicity, the description of the complete analytical pull-out model is reported in Chapter 4, which is completely dedicated to modeling the bond behavior of fiber-to-concrete joints under pull-out actions.

Table 3.2: Bond response of the fiber-concrete joint depending on the slip $s[x]$ developed throughout the embedment length.

Slips	Type of joint adherence
$s[x] \leq s_e \forall x \in [-l_{emb}, 0]$	Elastic Response (E)
$s[x] \leq s_e \forall x \in [-l_{emb}, -l_e]$ $s_e < s[x] \leq s_u \forall x \in [-l_e, 0]$	Elastic – Softening Response (ES)
$s_e < s[x] \leq s_u \forall x \in [-l_{emb}, 0]$	Softening Response (S)
$s[x] \leq s_e \forall x \in [-l_{emb}, -l_e]$ $s_e < s[x] \leq s_u \forall x \in [-l_e, -l_u]$ $s[x] > s_u \forall x \in [-l_u, 0]$	Elastic – Softening – Debonding (ESD)
$s_e < s[x] \leq s_u \forall x \in [-l_{emb}, -l_u]$ $s[x] > s_u \forall x \in [-l_u, 0]$	Softening – Debonding Response (SD)
$s[x] > s_u \forall x \in [-l_{emb}, 0]$	Debonding Failure (D)

being $-l_e\,(0 \leq l_e \leq l_{emb})$ and $-l_u\,(0 \leq l_u \leq l_{emb})$ the abscissas of the points in which the local slip $s[x]$ is equal to the elastic limit (s_e) and the ultimate value (s_u), respectively.

3.4.2 Verification of the pull-out model

Some numerical examples are reported in this section to show the predictive capacity of the proposed bond-slip analytical model. The verification examples include pull-out tests of both straight and hooked-end steel fibers. Test data by Lim et al. [1987] regarding pull-out probes are considered which relevant properties of fibers are listed as follows:

- *Straight fibers*: $d_f = 0.565\,mm$ (diameter), $\sigma_{y,s} = 345\,N/mm^2$ (strength), $E_s = 210\,GPa$ (elastic modulus).
- *Hooked fibers*: $d_f = 0.500\,mm$ (diameter), $\sigma_{y,s} = 1130\,N/mm^2$ (strength), $E_s = 200\,GPa$ (elastic modulus).

Figure 3.12 shows the $P_i - s_i$ curves (pull-out action vs. applied slip) for straight and hooked-end steel fibers with different embedment lengths based on the model parameters defined in Table 3.3.

The proposed model leads to good predictions of the behavior of both fiber types, capturing the increment of strength as the embedment measure increases. It is worth nothing that the presence of hooked-ends in fibers determines an increase in shear

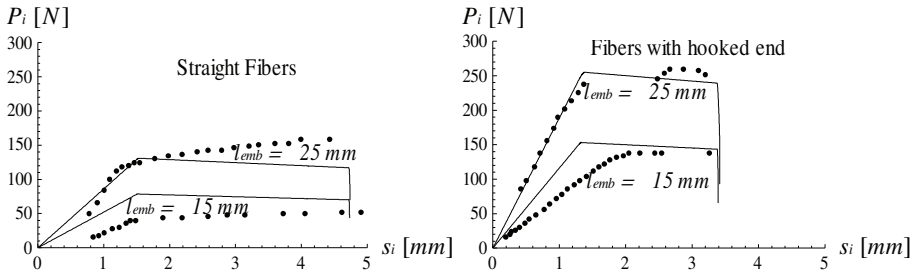

Figure 3.12: Pull-out tests (discontinuous lines) by Lim et al. [1987] on straight and hooked-end steel fibers vs. numerical results (continuous lines).

Table 3.3: Model parameters for the pull-out tests by Lim et al. [1987].

	MaterialParameters			
	$\tau_{y,a}[MPa]$	$k_E[MPa/mm]$	$k_S[MPa/mm]$	$s_u[mm]$
StraightFibers	3.0	2.0	0.1	4.725
HookedFibers	6.0	5.0	0.2	3.380

strength, $\tau_{y,a}$, compared to straight fibers and a reduction in their ductility. As a matter of fact, the elastic and softening slopes (k_E and k_S, respectively) increase considering hooked-end fibers, while a decrease in the ultimate slip, s_u, passing from straight to hooked fibers can be observed.

3.5 Dowel effect of steel fibers crossing cracks in cementitious matrix

A 1D elasto-plastic model is considered to take into account the dowel effect of fibers crossing one single crack. This model describes the evolution law of the shear fiber strains $\dot{\gamma}_T$ and the dowel stress $\dot{\tau}_f$ in incremental form (needed relationship in the composite model outlined in Eq. 3.2) representing the interaction between fiber and matrix as follows

$$\dot{\gamma}_T = \dot{\gamma}_T^{el} + \dot{\gamma}_T^{pl} \tag{3.38}$$

$$\dot{\tau}_f = G_f\left(\dot{\gamma}_T - \dot{\gamma}_T^{pl}\right) \tag{3.39}$$

being $\dot{\gamma}_T^{el}$ and $\dot{\gamma}_T^{pl}$ the elastic and plastic shear strain components, respectively, and G_f the equivalent shear modulus.

Within the framework of the flow plasticity theory, the complete model is described by means of the following set of equations:

- *Yield function*: $g_f = |\tau_f| - (\tau_{y,f} + Q_{dow}) \leq 0$, when τ_f is the dowel shear stress, $\tau_{y,f}$ the dowel strength and Q_{dow} the stress-like internal parameter.
- *Softening law*: $\dot{Q}_{dow} = \dot{\lambda}_f H_{dow}$, where $\dot{\lambda}_f$ and H_{dow} are the plastic multiplier and the hardening/softening modulus, respectively.
- *Flow rule*: $\dot{\gamma}_T^{pl} = \dot{\lambda}_f \partial g_f / \partial \tau_f = \dot{\lambda}_f sign[\tau_f]$, where $\dot{\gamma}_T^{pl}$ is the rate of the plastic dowel strain.

The Kuhn-Tucker loading/unloading conditions (with the consistency relationship) complete the formulation of the model. The constitutive law between the dowel shear stress, τ_f, and the corresponding equivalent shear strain, γ_T, can be written in incremental form as follows

$$\dot{\tau}_f = G_f^{ep} \dot{\gamma}_T \tag{3.40}$$

being G_f^{ep} the tangent modulus expressed in terms of the initial dowel stiffness G_f and the hardening/softening modulus H_{dow}, depending on considering the cases of either loading or unloading/elastic response

$$\begin{cases} G_f^{ep} = G_f & \rightarrow \text{unloading/elastic} \\ G_f^{ep} = \frac{G_f \cdot H_{dow}}{G_f + H_{dow}} & \rightarrow \text{loading} \end{cases} \tag{3.41}$$

in which usually $H_{dow} = 0$.

3.5.1 Dowel stiffness

The analytical model, used to predict the dowel behavior of fibers embedded in cementitious composites, is based on the analysis of an elastic beam on a Winkler foundation, see Figure 3.13. The following differential equation for the deflection equilibrium of a Winkler's beam can be written

$$\frac{d^4\Delta(x)}{x^4} + 4\lambda^4\Delta(x) = 0 \qquad \text{with} \qquad \lambda^4 = \frac{k_c}{4E_sJ_s} \tag{3.42}$$

being $\Delta(x)$ the deflection of the beam, k_c the elastic stiffness of the spring foundation modeling the surrounding cementitious matrix, E_s and J_s are the elastic modulus of the steel and the inertia of the fiber, respectively, and finally λ represents a characteristic length of the Winkler beam.

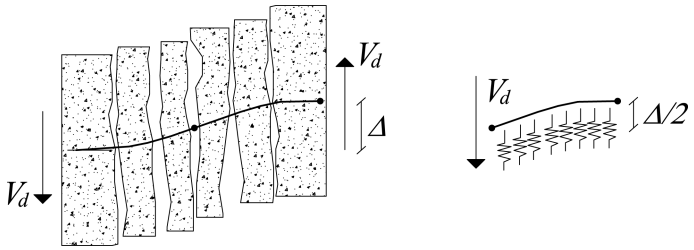

Figure 3.13: Dowel effect based on the well-known Winkler beam theory.

The fiber is analyzed as a "semi-infinite" beam on Winker foundation [El-Ariss, 2007], then the following equations govern the problem

$$\begin{aligned}
\Delta(x) &= A_1 e^{-\lambda x}\cos(\lambda x) + A_2 e^{-\lambda x}\sin(\lambda x)\\
M_d(x) &= 2E_s J_s \lambda^2 e^{-\lambda x}[A_2\cos(\lambda x) - A_1\sin(\lambda x)]\\
V_d(x) &= -2E_s J_s \lambda^3 e^{-\lambda x}[(A_2 - A_1)\sin(\lambda x) + (A_1 + A_2)\cos(\lambda x)]
\end{aligned} \tag{3.43}$$

being M_d and V_d the bending moment and the dowel action at $l_f/2$ of the steel fiber, while A_1 and A_2 are constants deriving by the boundary conditions.

The analytical solution of the semi-infinite Winkler's beam problem is based on the assumption that the crack width is considered null and supposing that in $x = 0$ the moment is null (inflection point) [El-Ariss, 2007]. Then, considering an applied dowel force, V_d, at the loaded-end ($x = 0$), the following analytical displacement field is obtained

$$\Delta(x) = -\frac{e^{-\lambda x}\cos(\lambda x)}{2\lambda^3 E_s J_s} V_d. \tag{3.44}$$

Finally, the $V_d - \Delta$ law in correspondence of the considered crack ($x = 0$) takes the following analytical form

$$\begin{aligned}
V_d = \lambda^3 E_s J_s \Delta \rightarrow \frac{V_d}{A_f} &= \frac{l_f}{A_f}\lambda^3 E_s J_s \frac{\Delta}{l_f}\\
&\Rightarrow G_f = \frac{l_f}{A_f}\lambda^3 E_s J_s
\end{aligned} \tag{3.45}$$

also expressed in terms of $\tau_f - \gamma_T\left(\frac{V_d}{A_f} - \frac{\Delta}{l_f}\right)$ law, from which the dowel stiffness, G_f, can be derived. In Equation [3.45] $A_f = \pi\frac{d_f^2}{4}$ is the cross sectional area of a single fiber.

The elastic stiffness of the spring foundation, k_c, represents the foundation stiffness that in this case is defined by the stiffness of the surrounding matrix. Experimental tests performed on RC-members [Dei Poli et al., 1992] show that typical values of k_c vary from 75 to 450 N/mm^3. In other tests [Soroushian et al., 1987], it can be observed that the coefficient k_c increases with the strength of the surrounding mortar matrix as well as with the volume fraction of the reinforcement. Furthermore, the dowel stiffness is somehow inversely proportional to the fiber diameter.

The elastic foundation stiffness of the surrounding concrete, k_c, assumes the following empirical expression [Soroushian et al., 1987]

$$k_c = \kappa_1 \frac{\sqrt{f_c}}{{d_f}^{2/3}} \tag{3.46}$$

being f_c the compression strength of the surrounding cementitious composite and κ_1 a coefficient to be calibrated.

3.5.2 Dowel strength

Typical failures in the fiber dowel are characterized by local crushing of the surrounding matrix and/or yielding of the steel fiber. For these reasons, the following empirical expression [Dulacska, 1972], considering both failure modes, is employed

$$V_{d,u} = k_{dow} d_f^2 \sqrt{|f_c||\sigma_{y,s}|} \tag{3.47}$$

being k_{dow} a non-dimensional coefficient whose typical value $k_{dow} = 1.27$ could be assumed as a reference for RC-structures [Dulacska, 1972].

Finally, the equivalent dowel strength $\tau_{y,f}$ can be defined for the dowel action

$$\tau_{y,f} = \frac{V_{d,u}}{A_f} \tag{3.48}$$

and employed in the yielding criterion introduced at the beginning of this section.

3.6 Closing remarks

A new constitutive theory for failure analysis of Fiber-Reinforced Cementitious Composites (FRCCs) has been proposed in this chapter. An innovative approach for reproducing

the fiber effects on the cracking phenomena of the concrete/mortar matrix has been considered. The well-known discrete crack approach based on zero-thickness interface elements has been taken as a reference framework. The matrix degradation under mode I and II cracking modes has been modeled by means of a fracture energy-based softening law formulated in the framework of the flow theory of plasticity. Two fundamental aspects of the fiber-mortar interaction have been considered in the model, i.e. the bond behavior of fibers bridging the crack opening and the dowel effect derived by possible relative transverse displacements of the two faces of the crack. The inclusion of fibers and the above two effects have been taken into account by means of the well-known Mixture Theory.

The discontinuous model proposed in this work can be employed in mesoscopic analyses aimed at simulating failure processes possibly developing at the mortar-mortar and mortar-aggregate interfaces see a.o. Lopez [1999] and Idiart [2009]. The strategy proposed in this chapter for modeling failure behavior of FRCCs based on the discrete crack approach and on interface elements can be straightforwardly extended to other well-known numerical techniques. In this regards, finite elements with additional degrees of freedom by Oliver et al. [2002, 2006] (with Embedded discontinuities known as E-FEM), or with additional nodal degrees of freedom [Moes and Belytschko, 1999, Hettich et al., 2008] (eXtended-FEM) could be considered as alternative numerical frameworks for FRCCs modeling. Other interesting procedures that could be also mentioned with the strategy here proposed for FRCCs are the so-called lattice models [van Mier et al., 2002, Lilliu and van Mier, 2003], the particle-based formulations [Bazant et al., 1990, Rabczuk and Belytschko, 2006], the Element-free Galerkin [Belytschko et al., 1995, Zhang et al., 2008] and the hybrid-Trefftz stress-based formulation in Kaczmarczyk and Pearce [2009].

4 Bond behavior of fibers in cementitious materials: a unified formulation

This chapter presents a unified formulation for simulating the overall bond behavior of fibers embedded in cementitious matrices. In principle, such a formulation is based on assuming a model to simulate interface bond stresses and the corresponding relative displacements. Two alternative models are actually considered. The first one is based on a simplified bilinear relationship and can be analytically handled; the second one assumes a refined fracture energy-based plasticity model which requires for its integration a numerical approach. Both models considered in the proposed formulation address the behavior of fibers under tensile axial stress which results in a "mode II" debonding phenomenon. Finally, numerical results are reported for both validating the proposed models against relevant experimental results and pointing out the differences between the prediction obtained from both considered proposals.

4.1 Importance of the bond-slip modeling

A sound knowledge of fiber-matrix interaction is of key importance for simulating the response of structural members made out of FRCC. As a matter of principle, the effectiveness of fibers embedded in cement-based matrices mainly depends on several factors, such as fiber length, diameter, fiber type (e.g., smooth, hooked-end, flattened, twisted, etc.) and materials of both reinforcement and surrounding matrix. Moreover, the bond behavior is a complex phenomenon actually controlled by physical and chemical interactions between fiber and matrix.

In the last decades, several innovative researches have been carried out to better understand the interface mechanisms and features under consideration of both physical and chemical aspects involved. The superior performance of hooked-ended and "non-

smooth" fibers has clearly been pointed out in experimental studies by Naaman and Najm [1991] and Laranjeira et al. [2010]. Further experimental evidence about such a role is available in Cunha et al. [2010], whereas the effect of fiber length on the pull-out mechanism of polypropylene fibers has been outlined in Singh et al. [2004]. However, the bond behavior of fibers embedded in cementitious matrix is not only affected by the above mentioned fiber properties, but moreover by the matrix quality. For instance, experimental researches on smooth fibers embedded in concrete of Normal (N-) and High Strength Concretes (HSCs) by Shannag et al. [1997] point out the fact that bond behavior can be enhanced as the matrix strength increases. Moreover, the inclusion of nano-particles in cement matrices is one of the most recent solutions, with the twofold objective of enhancing the durability of the fiber-to-matrix interface [Butler et al., 2009] and improving the adhesion properties between fibers and matrix [Wang et al., 2009].

Thus, since several parameters play a significant role in the fiber-matrix interaction in FRCC, the formulation of sound mechanical models for simulating the bond behavior of fibers embedded in cementitious materials is a fairly challenging issue. As a matter of principle, two main families of such models can be recognized in the scientific literature[Stang et al., 1990, Li and Chan, 1994]: the first one can be defined as *stress-based approaches* [Katz and Li, 1995, Ghavami et al., 2010], while the second one is represented by the so-called *energy-based bond-slip models* [Shah and Ouyang, 1991, Fantilli and Vallini, 2007].

Besides the particular interest in simulating the mechanical response of single fibers, the above mentioned models should be intended as a key contribution towards the possible modeling of the structural behavior of FRCC members based on the explicit simulation of the fiber influence on cracking processes. As a matter of fact, the most common mechanical models currently employed for simulating the behavior of FRCC are based on continuous smeared-crack approaches [Seow and Swaddiwudhipong, 2005] and generally deriving by previous proposals originally formulated for plain concrete [Folino et al., 2009, Folino and Etse, 2012]. Although such models are generally accepted for simulating the cracking behaviors of FRCC, it should be noted that their calibration is necessarily based on experimental results directly obtained on the FRCC material under consideration, as the fiber-matrix bond interaction deeply affects the post-cracking regime and the corresponding material parameters (mainly related with the fracture energy to be considered in smeared-crack approaches).

To overcome this drawback, alternative models aimed at explicitly simulating the actual discrete nature of FRCC have recently been formulated within the framework of the so-called discontinuous-based approaches [Oliver et al., 2008, Caggiano et al., 2012b].

The discrete-crack approach and the consequent possibility of modeling the behavior of FRCC starting from both their components (i.e., the bond-slip mechanisms), and the interactions among them is the main issue of the proposal reported in Chapter 3. Therein, the accurate description of the fiber-matrix bond behavior is the key element to formulate and identify such a meso-mechanical model.

This chapter proposes a unified formulation for simulating the overall bond behavior of fibers embedded in cementitious matrices, based on the fundamental assumptions reported in section 4.2. Two alternative models are actually considered. The first one is based on the simple elasto-plastic behavior with isotropic linear softening as outlined in section 4.3. Conversely, the second one is founded on the fracture energy-based contact model outlined in section 4.4 and is employed in a numerical solution of the fiber-matrix interaction problem. Finally, section 4.5 presents the results of simulations obtained through the two models considered in the presented unified formulation of the tensile response of fibers embedded in concrete matrices. Moreover, the theoretical investigation about the influence of relevant parameters (such as fiber anchorage length and diameter) is also outlined in the same section.

4.2 Bond behavior of fibers in concrete matrix: Basic assumptions

The basic assumptions for Finite Element (FE) simulation of bond behavior of fiber embedded in cementitious materials are presented in this section. Fiber reinforcement is modeled by one-dimensional two-nodes iso-parametric truss element. The interface slip between reinforcing steel and the surrounding concrete is simulated by means of interface elements as schematically shown in Figure 4.1.

4.2.1 Behavior of steel fibers

The mechanical behavior of steel in fibers is modeled as a 1-D elastic-perfectly plastic material. The incremental stress-strain law can be written as

$$\dot{\sigma}_f = E_f^{ep} \dot{\varepsilon}_f \tag{4.1}$$

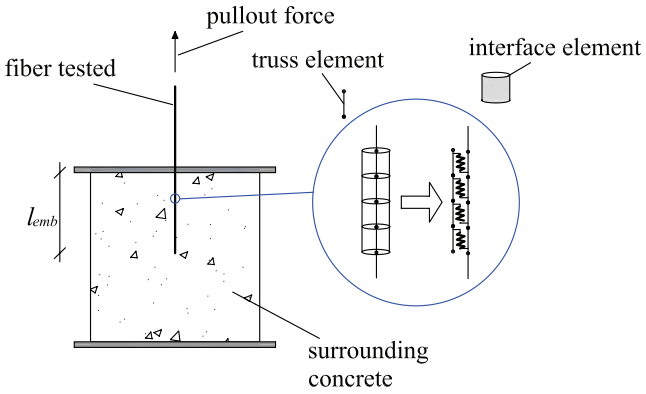

Figure 4.1: Considered scheme of fiber under pull-out loading.

being $\dot{\sigma}_f$ the axial stress rate of the fiber, $\dot{\varepsilon}_f$ the rate axial strain and the tangent elasto-plastic modulus E_f^{ep} takes the following two distinct values

$$\begin{cases} E_f^{ep} = Ef \quad elastic/unloading\,regime \\ E_f^{ep} = 0 \quad loading\,with\,\dot{\lambda_f} > 0 \end{cases} \tag{4.2}$$

where $\dot{\lambda}_f$ is the non-negative plastic multiplier obtained by means of the Kuhn-Tucker and consistency conditions and E_f represents the uniaxial elastic module of the fiber.

Finally, the yielding criterion takes the following expression

$$f_f = |\sigma_f| - \sigma_{y,f} \leq 0 \tag{4.3}$$

in which $\sigma_{y,f} \geq 0$ is the yield limit of the steel.

4.2.2 Interface bond-slip models

Two rate-independent contact laws are proposed in this work with the aim to study the fiber-to-concrete debonding:

- **Elasto-plastic model with linear strain-softening**: the same one adopted in the composite model outlined in Chapter 3.
- **Fracture energy-based debonding model**: a richer proposal based on fracture energy-based concepts and conceived within a work-softening plasticity formulation;

Table 4.1 describes the key aspects of both models. In particular, $f(\tau,\kappa)$ and $g(\tau,\kappa)$ represent the two yielding criteria based on the interface shear stress τ and the internal (strain-like) variable κ of each considered model; τ_y represents the failure shear strength.

Table 4.1: Interface bond-slip models.

	Fracture energy-based model	Strain-softening elasto-plasticity
Loading criterion	$f(\tau,\kappa)=\tau^2-\tau_y^2\le 0$	$g(\tau,\kappa)=\lvert\tau\rvert-(\tau_{y,0}+Q)\le 0$
Stress-like internal variables	$\tau_y=\tau_{y,0}\left(1-\frac{w_{sl}}{G_f}\right)$ $\quad \dot{\kappa}=\dot{w}_{sl}=\tau\cdot\dot{s}^p$	$\dot{\kappa}=\dot{Q}=\dot{\lambda}\cdot k_H$
Plastic flow	$\dot{s}^p=\dot{\lambda}\frac{\partial f}{\partial\tau}=2\cdot\dot{\lambda}\cdot\tau$	$\dot{s}^p=\dot{\lambda}\frac{\partial g}{\partial\tau}=\dot{\lambda}\cdot sign[\tau]$
Constitutive equation	$\dot{\tau}=k_E(\dot{s}-\dot{s}^p)$	
Loading-unloading condition	$\dot{\lambda}\ge 0,\ f\le 0,\ \dot{\lambda}\cdot f=0$	$\dot{\lambda}\ge 0,\ g\le 0,\ \dot{\lambda}\cdot g=0$
	$\dot{\tau}=k_{tan}^{ep}\cdot\dot{s}$	
Constitutive tangent operator	$k_{tan}^{ep}=k_{E,2}\cdot\left(1-\frac{\left(\frac{\partial f}{\partial\tau}\right)^2+\Delta\lambda\frac{\partial f}{\partial\tau}\left(\frac{\partial f}{\partial\kappa}\frac{\partial\kappa}{\partial s^p}\right)\cdot\frac{\partial^2 f}{\partial\tau^2}}{\left(\frac{\partial f}{\partial\tau}\right)^2+H/k_{E,2}}\right)$	$k_{tan}^{ep}=k_E\left(1-\frac{k_E}{k_E+k_H}\right)$
	$k_{tan}^{ep}=k_E \quad elastic/unloading$	

Both bond-slip models can be directly implemented in plasticity-type constitutive laws for interface elements. The rate of elastic relative slip, $\dot{s}^e$, is introduced and related to the shear stress through the elastic stiffness, k_E. In the framework of the incremental plasticity theory, the following basic equation can be used

$$\dot{s}=\dot{s}^e+\dot{s}^p \qquad \dot{s}^e=\frac{\dot{\tau}}{k_E} \tag{4.4}$$

where the inelastic, $\dot{s}^p$, and the total interface slip $\dot{s}$ are introduced in rate form.

Integrating each constitutive model, the constitutive laws can be defined in terms of the tangent elasto-plastic constitutive operator, k_{tan}^{ep}, which is specified for loading or unloading/elastic processes in Table 4.1.

4.3 Elasto-plastic joint/interface model with isotropic linear softening

This section presents a classical one-dimensional plasticity model aimed at simulating the bond-slip behavior of fiber-to-concrete interface.

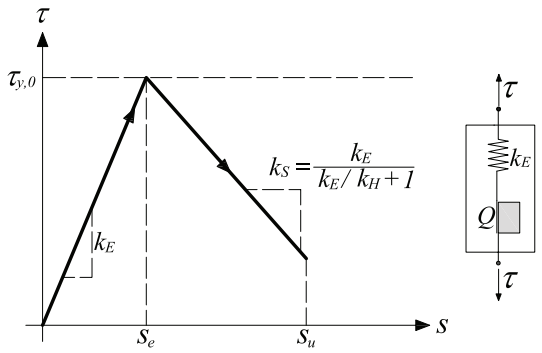

Figure 4.2: Bond-slip plasticity model with linear softening.

Based on the additive split of the relative interface displacements and the incremental elastic law given in Eq. (4.4), the model is formulated by means of the following yield criterion

$$g(\tau,\kappa) = |\tau| - (\tau_y + Q) \leq 0 \tag{4.5}$$

in which the stress-like evolution, in post-elastic regime, is driven by the internal hardening variable Q, which variation depends on the hardening/softening parameter k_H (to see Table 4.1), obtaining a strain-softening contact law for $k_H < 0$ in post-elastic response (Figure 4.2).

The plastic flow is again captured by means of the Kuhn-Tucker loading/unloading and consistency conditions. The incremental bond-slip law, can be written as

$$\dot{\tau} = k_{tan}^{ep}\dot{s} \tag{4.6}$$

where the tangent elasto-plastic module, k_{tan}^{ep}, can be derived as widely reported in literature [Simo and Hughes, 1998] and reported in Table 4.1.

4.3.1 Basic assumptions and closed-form solution

The complete (closed-form) analytical solution of the bilinear $\tau - s$ relationship (Figure 4.2) is presented. Moreover, the pull-out behavior of fiber-to-cementitious matrix is discussed.

The model is based on the "small displacement" assumption, and supposes that all strains developed in the matrix layer surrounding the fiber are "lumped" at the fiber-

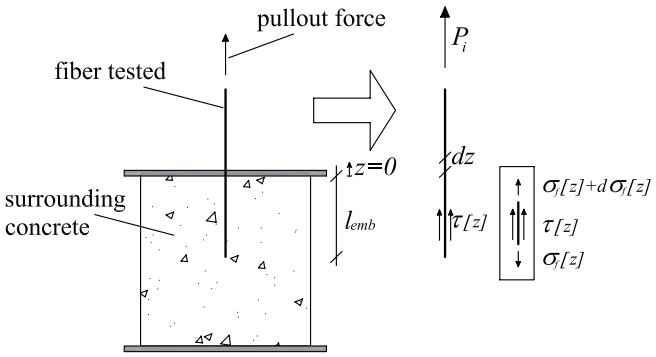

Figure 4.3: Schematic components of pull-out analysis for the analytical solution.

matrix interface. According to the plasticity model described in section 4.3, the contact law ($\tau - s$) presents a bilinear form, featuring an initial linear ascending branch, with the k_E initial slope, followed, when the elastic limit $\tau_{y,0}$ is reached, by a linear softening branch whose slope is now defined as $k_S = k_E\left(1 - \frac{k_E}{k_E+k_H}\right)$. The model is completed considering an ultimate slip, s_u, at which the bond transferred stress is considered null. The full analytical solution is applied to a single fiber, as schematized in Figure 4.3.

Based on the assumption that the fiber diameter d_f and the local bond-slip relationship keep unchanged throughout the fiber bond length, l_{emb}, the following infinitesimal equilibrium condition can be formulated

$$\frac{d\sigma_f[z]}{dz} = -\frac{4\tau[z]}{d_f} \tag{4.7}$$

where $\tau[z]$ is the shear stress transferred at the interface and $\sigma_f[z]$ the axial steel stress.

Assuming that bond failure occurs for fiber stresses lower than the corresponding yield limit (as generally observed in experimental investigations), the following constitutive laws to model both the mechanical response of fiber and the interface adherences, respectively, can be written

$$\sigma_f[z] = E_f\frac{ds[z]}{dz} \tag{4.8}$$

and

$$\begin{cases} \tau[z] = -k_E s[z] & \rightarrow \text{if } s[z] \leq s_e \\ \tau[z] = -\tau_{y,0} + k_S\,[s[z] - s_e] & \rightarrow \text{if } s_e < s[z] \leq s_u \\ \tau[z] = 0 & \rightarrow \text{if } s[z] > s_u \end{cases} \tag{4.9}$$

being $s[z]$ the slip measured at generic z coordinate while $s_e = \tau_{y,0}/k_E$ is the elastic slip value.

After substituting Eq. (4.8) into Eq. (4.7), the following differential equation can be obtained in terms of $s[z]$

$$\frac{d^2 s[z]}{dz^2} + \frac{4\tau[z]}{d_f E_f} = 0 \tag{4.10}$$

representing the general governing differential equation of the bonded joint between fiber and concrete which can be integrated assigning the local shear stress-slip law as defined in Eq. (4.9).

Eq. (4.10) can be solved, under appropriated boundary conditions, in order to obtain the complete problem in closed form: i.e., in terms of slips $s[z]$, shear stress distribution $\tau[z]$, axial fiber stress $\sigma_f[z]$ and, finally, the global pull-out response $P_i - s_i$ at the loaded-end.

In particular, three main differential equations must be integrated:

- *Elastic $\tau - s$ case*: $s[z] \leq s_e$, the adherence law is represented by fully reversible bond slips described by the following differential equation

$$\frac{d^2 s[z]}{dz^2} - \alpha_1^2 s[z] = 0 \tag{4.11}$$

whose general integral solution is

$$s[z] = A_1 \sinh[\alpha_1 z] + A_2 \cosh[\alpha_1 z] \tag{4.12}$$

where A_1 and A_2 are two unknown constants to be determined under appropriate boundary conditions while $\alpha_1 = 2\left(\frac{k_E}{d_f E_f}\right)^{1/2}$.

- *Softening* $\tau - s$ *case*: $s_e < s[z] \leq s_u$, the interface bond law is represented by slips in post-elastic regime and described by the following differential equation

$$\frac{d^2 s[z]}{dz^2} + \alpha_2^2 s[z] - 4\frac{k_E + k_S}{E_f} s_e = 0 \tag{4.13}$$

whose general integral solution is

$$s[z] = A_3 \cos[\alpha_2 z] + A_4 \sin[\alpha_2 z] + \frac{k_E + k_S}{k_S} s_e \tag{4.14}$$

with $\alpha_2 = 2\left(\frac{k_S}{d_f E_f}\right)^{1/2}$, A_3 and A_4 are integration constants.

- *Debonded* $\tau - s$ *case*: $(s[z] > s_u)$, the shear stress locally transferred between concrete and fiber is zero. It follows that

$$\frac{d^2 s[z]}{dz^2} = 0 \tag{4.15}$$

whose general integral solution is

$$s_3[z] = A_5 z + A_6 \tag{4.16}$$

being A_5 and A_6 integration constants.

4.3.2 Full-range bond-slip behavior

This section presents the analytical description of the complete debonding process by means of a stage-by-stage integration of the relevant equations whose form depends on the actual state of the interface.

Both interface-slip distribution $s[z]$ and the global force-displacement pull-out response $P_i - s_i$ are investigated. For the sake of brevity, many details of the analytical integration are not reported herein but can be easily derived as explained in Caggiano et al. [2012c].

For low load levels all the transferred shear stresses, along the interface, are in the elastic state. In this case, the stage is defined as **Elastic (E)** one whose solutions in terms of $P_i - s_i$ curve and slips $s[z]$ are detailed in Table 4.2.

Once the applied slip at the loaded-end reaches the elastic limit, a new stage takes place called **Softening-Elastic (SE)**. Then the fiber anchoring interface can be subdivided

Table 4.2: Analytical bond-slip model of the bilinear $\tau - s$ relationship.

Closed-form full range pull-out behavior

Elastic stage - E: $s_i \leq s_e$

$$P_i = \pi {\alpha_1}^{-1} \tanh(\alpha_1 l_{emb}) d_f k_E s_i$$

- Elastic solution $z \in [-l_{emb}, 0]$: $s[z] = \frac{\cosh[\alpha_1 (lemb+z)]}{\cosh[\alpha_1 l_{emb}]} s_i$

Softening-Elastic stage - SE: $s_i > s_e$

$$s_i = \left(1 + \frac{k_E}{k_S}(1 - \cos[\alpha_2 l_e]) - \frac{\sqrt{k_E}}{\sqrt{k_S}} \sin[\alpha_2 l_e] \tanh[\alpha_1 (l_e - l_{emb})]\right) s_e$$

$$P_i = \frac{\pi}{2} {d_f}^{3/2} \left(k_E / \sqrt{k_S} \sin[\alpha_2 l_e] - \sqrt{k_E} \cos[\alpha_2 l_e] \tanh[\alpha_1 (l_e - lemb)]\right) \sqrt{E_f} s_e$$

- Softening solution $z \in [-l_e, 0]$: $s[z] = \left(1 + \frac{k_E}{k_S}(1 - \cos[\alpha_2 (l_e + z)]) - \frac{\sqrt{k_E}}{\sqrt{k_S}} \tanh[\alpha_1 (l_e - l_{emb})] \sin[\alpha_2 (l_e + z)]\right) s_e$

- Elastic solution $z \in [-l_{emb}, -l_e]$: $s[z] = \frac{\cosh[\alpha_1 (l_{emb}+z)]}{\cosh[\alpha_1 (l_e - l_{emb})]} s_e$

"Short fibers": $l_{emb} \leq l_{sl}$

Softening stage - S: $s_i > s'_B$

$$P_i = \pi d_f {\alpha_2}^{-1} \tan[\alpha_2 l_{emb}] ([k_E + k_S] s_e - k_S s_i)$$

- Softening solution $z \in [-l_{emb}, 0]$:

$$s[z] = (s_i - [k_E/k_S + 1] s_e) \cos[\alpha_2 (l_{emb} + z)] \sec[\alpha_2 l_{emb}] + (k_E/k_S + 1) s_e$$

"Long fibers": $l_{emb} > l_{sl}$

Debonding-Softening-Elastic stage - DSE: $s_i > s_u$

$$s_i = \left(1 + \frac{k_E}{k_S} + \frac{k_E}{k_S} l_u \alpha_2 \sin[\alpha_2 (l_e - l_u)] - \frac{k_E}{k_S} \cos[\alpha_2 (l_e - l_u)] - \frac{1}{2} \alpha_1 \tanh[\alpha_1 (l_e - l_{emb})] \left(\frac{d_f E_f}{2 k_S} \alpha_2 \sin[\alpha_2 (l_e - l_u)] + 2 l_u \cos[\alpha_2 (l_e - l_u)]\right)\right) s_e$$

$$P_i = \left(\frac{\sin[\alpha_2 (l_e - l_u)]}{\sqrt{k_S}} - \frac{\cos[\alpha_2 (l_e - l_u)] \tanh[\alpha_1 (l_e - l_{emb})]}{\sqrt{k_E}}\right) \cdot \frac{\pi}{2} d_f^{3/2} \sqrt{E_f \tau_{y,0}}$$

- Debonding solution $z \in [-l_u, 0]$:

$$s[z] = \left(1 + k_E/k_S - k_E/k_S \cos[\alpha_2 (l_e - l_u)] - \sqrt{k_E}/\sqrt{k_S} \tanh[\alpha_1 (l_e - l_{emb})] (\alpha_2 (l_u + z) \cos[\alpha_2 (l_e - l_u)] + \sin[\alpha_2 (l_e - l_u)]) + k_E/k_S \alpha_2 (l_u + z) \sin[\alpha_2 (l_e - l_u)]\right) s_e$$

- Softening solution $z \in [-l_e, -l_u]$: *already reported in the SE-stage*

- Elastic solution $z \in [-l_{emb}, -l_e]$: *already reported in the SE-stage*

Debonding-Softening stage - DS: $\forall P_i \in [0, P'_C]$ ***Debonding-Softening stage - DS***: $\forall P_i \in [0, P_C]$

$$s_i = s_u + P_i \left[\frac{\alpha_2}{\pi k_S} \tan^{-1}\left(\frac{k_E \alpha_2}{\pi d_f [k_E k_S s_u - \tau_{y,0} (k_E + k_S)]} P_i\right) + \frac{{\alpha_2}^2 l_{emb}}{\pi k_S}\right]$$

- Debonding solution $z \in [-l_u, 0]$: $s[z] = s_u - \left(s_u - \tau_{y,0} \frac{k_E + k_S}{k_E k_S}\right) \alpha_2 (l_u + z) \tan[\alpha_2 (l_{emb} - l_u)]$

- Softening solution $z \in [-l_{emb}, -l_u]$: already reported in the SE-stage (it is now necessary to replace $l_{emb} \rightarrow l_e$).

into two parts: (i) part I closer to the loaded-end in which $s[z] > s_e$ and (ii) the remaining part in which $s[z] \leq s_e$. The expressions of the interface slips for the two parts of the bonded interface, $s[z]$, the pull-out force P_i and the slip s_i, reported in Table 4.2, depend on the value of the given parameter $l_e \in [0, l_{emb}]$ which determines the configuration of the bonded interface. It represents the abscissa of the point at which the local slip is equal to the elastic limit $s[-l_e] = s_e$.

The evolution of the fiber debonding process, after reaching the SE-stage, follows two possible alternatives: (i) the applied slip s_i in $z = 0$ reaches the ultimate slip value s_u, while the minimum slip $s[-l_{emb}] < s_e$: this case represents the transition to the new **Debonding-Softening-Elastic (DSE)** stage; (ii) the slip at the free-end of the fiber, reaches the elastic limit, $s[-l_{emb}] = s_e$ while $s_i < s_u$: this instance follows to the new only **Softening (S)** stage. The anchoring length $l_{emb} = l_{sl}$ which controls whether the stage SDE or S actually occurs can be conceptually recognized as the border between "short" and "long" anchorage conditions.

This length can be now defined as follows

$$l_{sl} = {\alpha_2}^{-1} \sec^{-1}\left(\frac{\tau_0}{\tau_0\left(\frac{k_S}{k_E}+1\right) - k_S s_u}\right) \tag{4.17}$$

Fibers which anchorage $l_{emb} > l_{sl}$ are defined as "long fibers", on the contrary, when $l_{emb} \leq l_{sl}$ the debonding process follows the second of the two mentioned evolutions considering the case of "short fibers". The conceptual map reported in Figure 4.4 outlines this possible switch in the mechanical behavior depending on the bonding length l_{emb} (and the interface law) of fibers embedded in a cementitious substrate. Moreover, Table 4.2 outlines the complete bond-slip process in case of both short and long steel fibers.

Short fibers

Based on a "stage-by-stage" evolution of the system behavior, the complete bond-slip response for short anchoring fibers is studied with a only **Softening (S-)**stage that follows the previous SE-stage. All the bond interface is modeled by means of the softening branch of Figure 4.2. A linear-type softening response is obtained by the global $P_i - s_i$ curve for the S-stage as plotted in Figure 4.5 (trait $B' - C'$) which expression is reported in Table 4.2.

The point B', in the global pull-out curve, posses the following coordinates

$$s'_B = \left(1 + \frac{k_E}{k_S}\left(1 - \cos[\alpha_2 l_{emb}]\right)\right) s_e \tag{4.18}$$

$$P'_B = \pi {\alpha_2}^{-1} d_f \tau_0 \sin[\alpha_2 Lc] \tag{4.19}$$

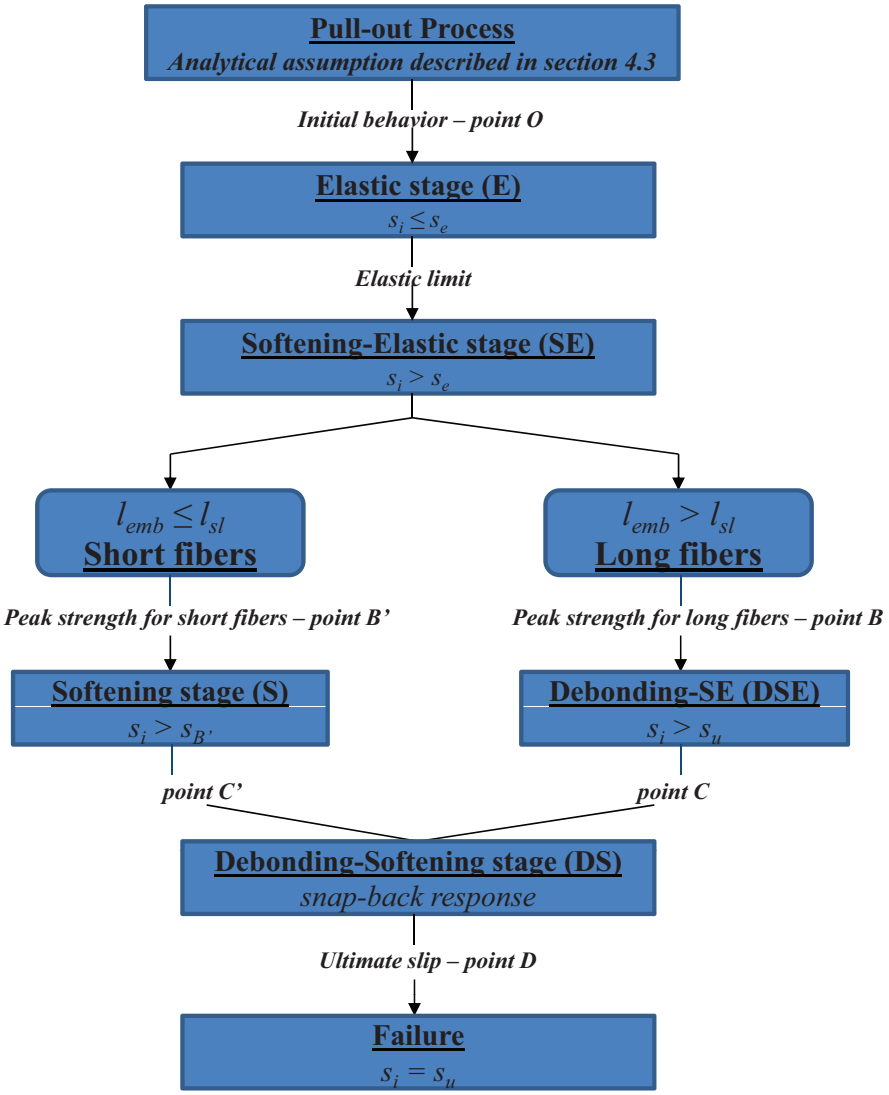

Figure 4.4: Schematic representation of the overall debonding process.

while the other extreme (C' of Figure 4.5) is given by the following coordinates

$$s'_C = s_u \tag{4.20}$$

$$P'_C = \pi \alpha_2{}^{-1} d_f \tan[\alpha_2 l_e]([k_E + k_S] s_e - k_S s_u). \tag{4.21}$$

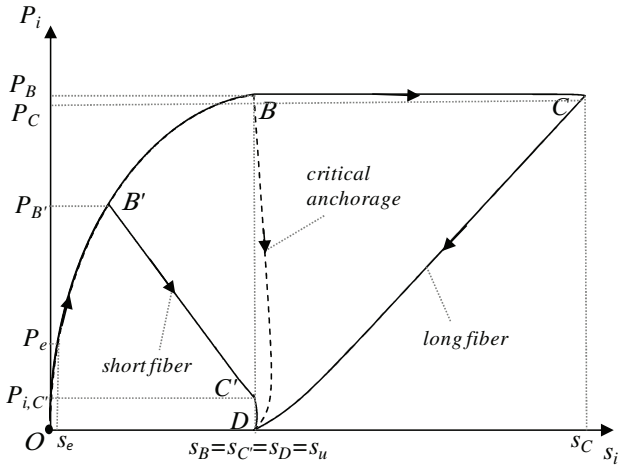

Figure 4.5: Typical analytical curves of the applied load P_i vs. debonding displacement s_i in case of short and long anchorage condition.

Long fibers

In case of "long" anchorage ($l_{emb} > l_{sl}$), the bond-slip process following the previous SE-stage is characterized by a debonded zone in the neighbors of the loaded-end, whose length is identified as l_u. The analytical solution of this stage, namely **Debonding-Softening-Elastic (DSE)**, is detailed in Table 4.2 in terms of slips $s[z]$ and global pull-out curve $P_i - s_i$. The closed relations depend on the two parameters l_e and l_u which determine the configuration states of the fiber-to-concrete bond. The values of those two parameters are strictly connected by means of the following relationship

$$l_u = l_e - \alpha_2^{-1}\sec^{-1}\left(\frac{k_E + k_S d_f \tanh^2[\alpha_1(l_e - l_{emb})]}{k_E + k_S - \frac{k_S s_u}{s_e} + k_1}\right) \tag{4.22}$$

with

$$k_1 = \left[k_S{}^2\tau_0{}^2\tanh^2[\alpha_1(l_e - l_{emb})]\left((s_e - s_u)(k_E k_S s_u - \tau_0(2k_E + k_S)) + \tau_0{}^2\tanh^2[\alpha_1(l_e - l_{emb})]\right)\right]^{1/2}.$$

Consequently, the debonding process in this stage can be followed by assuming the value l_e and then evaluating l_u through Eq. (4.22). Once the elastic contact vanishes ($l_e = l_{emb}$), the DSE-stage terminates reaching its ultimate point C, which coordinates is analytically obtained as follows

$$s_C = \left(1 + \frac{k_E}{k_S}\left[1 + \alpha_2 l_u \sin[\alpha_2(l_{emb} - l_u)] - \cos[\alpha_2(l_{emb} - l_u)]\right]\right) s_e \tag{4.23}$$

$$P_C = \pi {\alpha_2}^{-1} d_f \sin[\alpha_2(l_{emb} - l_u)]\tau_0. \tag{4.24}$$

Debonding-Softening (DS) stage represents the ultimate scenario for both "short" and "long" fibers in which the equilibrium is governed by two types of bond behaviors: i.e., one in which the bond adherence is in softening range ($s_e < s[z] \leq s_u$) while in the remaining part the contact is crashed ($s[z] > s_u$).

Table 4.2 reports both the expressions of $P_i - s_i$ and interface slip distribution $s[z]$ for the DS stage. The obtained results show an unstable behavior characterized by a snap-back softening response ($C-D$ branch for "long fibers" and part $C'-D$ branch for "short fibers") as shown in Figure 4.5.

4.4 Fracture energy-based interface model

The proposed model, described in Table 4.1, is based on the plastic yield condition, $f(\tau,\kappa) \leq 0$,

$$f(\tau,\kappa) = \tau^2 - \tau_y^2 \leq 0. \tag{4.25}$$

The evolution of the yielding surface during the debonding process is driven by means of the following scaling law

$$\tau_y = \tau_{y,0}\left(1 - \frac{w_{sl}}{G_f}\right) \tag{4.26}$$

measured by means of the internal variable κ, defined as the work (w_{sl}) spent during the debonding process ("mode II" of fracture) as follows

$$\dot{\kappa} = \dot{w}_{sl} = \tau \cdot \dot{s}^p. \tag{4.27}$$

The plastic slip rate is governed by the flow rule $\dot{s}^p = \dot{\lambda}\frac{\partial f}{\partial \tau}$, where the plastic multiplier, $\dot{\lambda}$, can be determined in a finite load-step by using the plastic consistency condition, $f_{n+1}(\Delta\lambda) = 0$, satisfying the yield condition f at the $n+1$ load-step, under persistent plastic deformations during the load-interval from n to $n+1$.

4.4.1 Incremental plastic multiplier

In order to find the accurate value of the incremental inelastic multiplier, $\Delta\lambda$, in a finite load-step, the full consistency is imposed according to the following truncated Taylor

series

$$\Delta\lambda_{n+1}^{k+1} = \Delta\lambda_{n+1}^{k} - \frac{f_{n+1}^{k}}{\left(\frac{\partial f}{\partial \Delta\lambda}\right)_{n+1}^{k}} \tag{4.28}$$

identifying with k the local iteration step of the Newton-Raphson method of Eq. (4.28). The quantity $\frac{\partial f}{\partial \Delta\lambda}$ can be developed as follows

$$\frac{\partial f}{\partial \Delta\lambda} = \frac{\partial f}{\partial \tau} \cdot \frac{\partial \tau}{\partial \Delta\lambda} + \left[\frac{\partial f}{\partial \tau_y} \frac{\partial \tau_y}{\partial \kappa} \frac{\partial \kappa}{\partial s^p} \right] \cdot \frac{\partial s^p}{\partial \Delta\lambda} \tag{4.29}$$

The first derivative of the shear stress τ with respect to $\Delta\lambda$ can be obtained as

$$\frac{\partial \tau}{\partial \Delta\lambda} = -k_E \cdot \left(\Delta\lambda \frac{\partial^2 f}{\partial \tau^2} \cdot \frac{\partial \tau}{\partial \Delta\lambda} + \frac{\partial f}{\partial \tau} \right) \tag{4.30}$$

then solving for $\frac{\partial \tau}{\partial \Delta\lambda}$

$$\frac{\partial \tau}{\partial \Delta\lambda} = -\left(\frac{k_E}{1 + \Delta\lambda k_E \cdot M} \right) \cdot \frac{\partial f}{\partial \tau} = -k_{E,2} \cdot \frac{\partial f}{\partial \tau} \tag{4.31}$$

where $k_{E,2} = \left[k_E^{-1} + \Delta\lambda M \right]^{-1}$ is the modified elastic stiffness and $M \left(= \frac{\partial^2 f}{\partial \tau^2} = 2 \right)$ represents the Hessian operator.

The derivative $\frac{\partial s^p}{\partial \Delta\lambda}$ can be evaluated as

$$\frac{\partial s^p}{\partial \Delta\lambda} = \left[\frac{\partial f}{\partial \tau} - \Delta\lambda M \cdot k_{E,2} \cdot \frac{\partial f}{\partial \tau} \right]. \tag{4.32}$$

The remaining terms to calcule Eq. (4.29) are listed below

$$\frac{\partial f}{\partial \tau} = 2 \cdot \tau \tag{4.33}$$

$$\frac{\partial f}{\partial \tau_y} = -2 \cdot \tau_y \tag{4.34}$$

$$\frac{\partial \tau_y}{\partial \kappa} = -\frac{\tau_{y,0}}{G_f} \tag{4.35}$$

$$\frac{\partial \kappa}{\partial s^p} = \tau \tag{4.36}$$

being $\tau_{y,0}$ the shear strength while G_f the fracture energy under mode II of crack.

4.4.2 Algorithmic tangential operator

The non-linear behavior, within a finite increment step, is solved by adopting the classical Newton-Raphson solution to solve the non-linear FE equations. The model is formulated by means of the construction of the algorithmic tangent operator to ensure a higher convergence rate than the continuous consistent one [Simo and Hughes, 1998].

Considering the differentiated form of the incremental shear-slip law, a linearized tangential format of Eq. (4.4) can be obtained

$$\begin{aligned} \Delta\tau &= k_E \cdot \left(\Delta s - \Delta\lambda \frac{\partial f}{\partial \tau}\right) \Rightarrow \\ & d\Delta\tau = k_E \cdot \left(d\Delta s - d\Delta\lambda \frac{\partial f}{\partial \tau} - \Delta\lambda d\frac{\partial f}{\partial \tau}\right) \end{aligned} \tag{4.37}$$

in which

$$d\frac{\partial f}{\partial \tau} = \frac{\partial^2 f}{\partial \tau^2} \cdot d\Delta\tau = M \cdot d\Delta\tau \tag{4.38}$$

Substituting the Eq. (4.38) into (4.37) and solving for $d\Delta\tau$

$$d\Delta\tau = k_{E,2} \cdot \left(d\Delta s - d\Delta\lambda \frac{\partial f}{\partial \tau}\right) \tag{4.39}$$

being $d\Delta\lambda$ the linearized plastic multiplier.

Based on the first-order differential form of the consistency condition, the linearized tangential format of the plastic multiplier $d\Delta\lambda$ can be derived as

$$df = \frac{\partial f}{\partial \tau} \cdot d\Delta\tau + \frac{\partial f}{\partial \kappa}\frac{\partial \kappa}{\partial s^p} \cdot d\Delta s^p = 0 \tag{4.40}$$

where the differential form of the plastic slip takes the following expression

$$d\Delta s^p = d\Delta\lambda \frac{\partial f}{\partial \tau} + \Delta\lambda \frac{\partial^2 f}{\partial \tau^2} \cdot d\Delta\tau \tag{4.41}$$

and substituting Eqs. (4.41) and (4.39) into (4.40) and solving for $d\Delta\lambda$, the following expression can be obtained as

$$d\Delta\lambda = \frac{\frac{\partial f}{\partial \tau} \cdot k_{E,2} + \Delta\lambda \left(\frac{\partial f}{\partial \kappa} \frac{\partial \kappa}{\partial s^p} \right) \cdot \frac{\partial^2 f}{\partial \tau^2} \cdot k_{E,2}}{\left(\frac{\partial f}{\partial \tau} \right)^2 \cdot k_{E,2} + H} \cdot d\Delta s \tag{4.42}$$

in which the scalar hardening parameter H assumes the following expression

$$H = -\left[\frac{\partial f}{\partial \tau_y} \frac{\partial \tau_y}{\partial \kappa} \frac{\partial \kappa}{\partial s^p} \right] \cdot \left[\frac{\partial f}{\partial \tau} - \Delta\lambda \frac{\partial^2 f}{\partial \tau^2} \cdot k_{E,2} \cdot \frac{\partial f}{\partial \tau} \right]. \tag{4.43}$$

Substituting $d\Delta\lambda$ into Eq. (4.39), the constitutive law and the algorithmic tangent operator k_{tan}^{ep} can be obtained

$$d\Delta\tau = k_{E,2} \left(1 - \frac{\left(\frac{\partial f}{\partial \tau} \right)^2 \cdot k_{E,2} + \Delta\lambda \frac{\partial f}{\partial \tau} \left(\frac{\partial f}{\partial \kappa} \frac{\partial \kappa}{\partial s^p} \right) \cdot \frac{\partial^2 f}{\partial \tau^2} \cdot k_{E,2}}{\left(\frac{\partial f}{\partial \tau} \right)^2 \cdot k_{E,2} + H} \right) \cdot d\Delta s \tag{4.44}$$

in compact form, $d\Delta\tau = k_{tan}^{ep} \cdot d\Delta s$.

4.4.3 Shear-slip test

The example proposed in this section outlines the interface response under direct fracture mode II. A relative shear slip is applied at the Gauss-point level to capture the fundamental behavior of the proposed model.

The parameters which control the numerical predictions are obtained by considering the elastic stiffness $k_E = 120\,MPa/mm$ and the initial shear strength $\tau_{y,0} = 2.2\,MPa$. Figure 4.6 reports the tangential stress vs. relative slip plots for different values of the fracture parameter: $G_f = 0.05, 0.10, 0.15, 0.20$ and $0.25\,N/mm$, respectively. It shows

that, as expected, no differences can be observed in terms of elastic stiffness. Then, different non-linear branches describe the inelastic softening response. Fracture energy is clearly the key parameter controlling this stage of the mechanical response.

The elastic contact is already equal for each case until the yield stress in shear is reached. After the peak strength the shear-slip response exhibits a descending exponential branch characterized by an asymptotic vanishing of the shear stress. The fracture energy-based formulation correctly captures the dependence of the post-peak ductility on the fracture energy G_f.

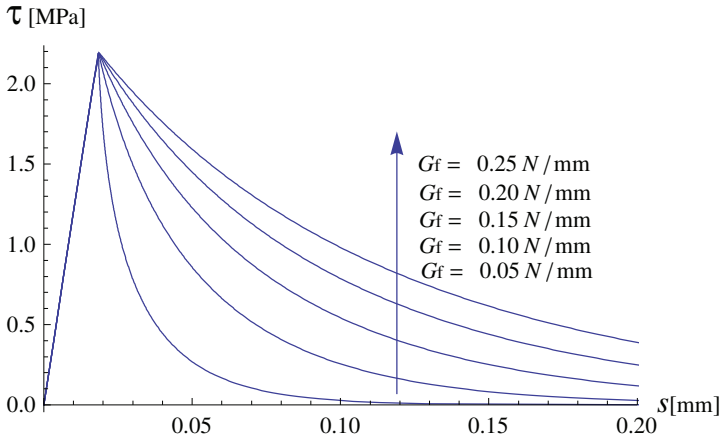

Figure 4.6: Bond-slip model: shear stress (τ) vs. relative slip (s) for different values of fracture energy G_f.

4.5 Numerical results and experimental validation

This section presents a comparison between numerical simulations and experimental results. The effects of matrix strength, fiber length and diameter are analyzed in the following with the aim of emphasizing the predictive capability of the proposed unified formulation.

4.5.1 Effect of matrix strength and fiber anchorage

The above described formulations are validated through the analysis of data from experimental tests conducted by Shannag et al. [1997]. The bond behavior of steel fibers embedded in two different cementitious matrices is investigated for:

- High Strength cement based Matrix (HSM) characterized by a compressive strength of 150 MPa and
- Conventional mortar (CSM) with compressive strength of 40 MPa.

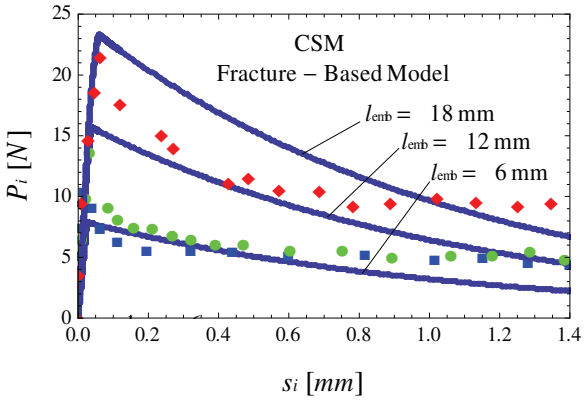

Figure 4.7: Fracture energy-based model results (continuous lines) vs. experimental data (square, circular and rhomboidal points) by Shannag et al. [1997].

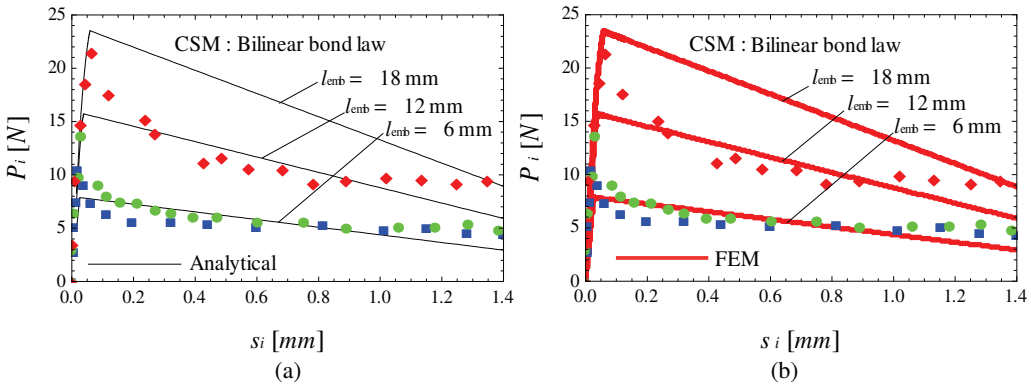

Figure 4.8: (a) Analytical and (b) FEM results (continuous lines) for bilinear $\tau - s$ against the experimental data (square, circular and rhomboidal points) by Shannag et al. [1997].

Three different fiber anchoring lengths are also considered: i.e., $l_{emb} = 6\,mm$, $12\,mm$ and $18\,mm$, respectively. Smooth steel fibers, having a tensile strength of 2990 MPa, a module of elasticity of 200 GPa with diameter of $0.19\,mm$, have been used by Shannag et al. [1997] and analyzed herein.

Numerical simulations are performed by considering the material interface parameters schematically described in Table 4.3. Non-linear FEM analyses are based on 20

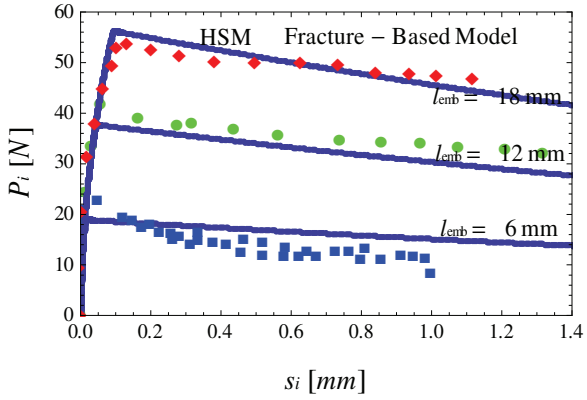

Figure 4.9: Fracture energy-based model results (continuous lines) vs. experimental data (square, circular and rhomboidal points) by Shannag et al. [1997].

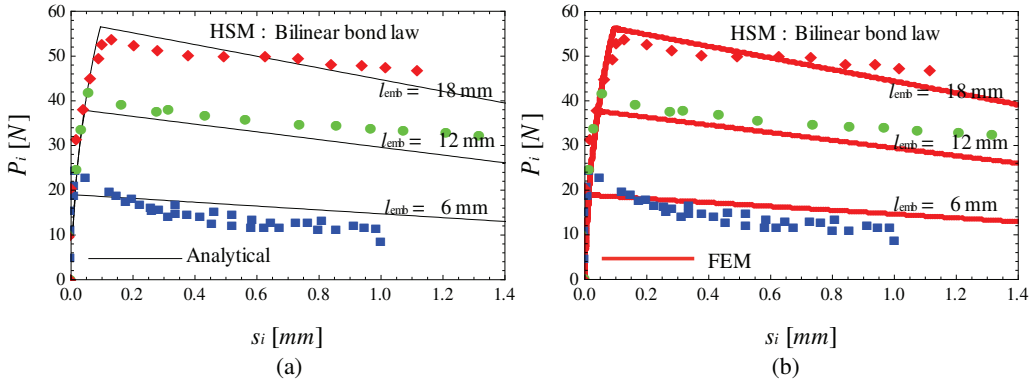

Figure 4.10: (a) Analytical and (b) FEM results (continuous lines) for bilinear $\tau - s$ vs. the experimental data (square, circular and rhomboidal points) by Shannag et al. [1997].

Table 4.3: Model parameters according to the tests by Shannag et al. [1997].

	Fracture – Based Model		Plasticity – Based Model	
CSM	$\tau_{y,0} = 2.2\,MPa$	$s_u = 1.56\,mm$	$\tau_{y,0} = 2.2\,MPa$	$s_u = 1.56\,mm$
	$k_E = 200\,MPa/mm$	$G_f = 2.42\,N/mm$	$k_E = 200\,MPa/mm$	$k_S = 1\,MPa/mm$
HSM	$\tau_{y,0} = 5.3\,MPa$	$s_u = 1.46\,mm$	$\tau_{y,0} = 5.3\,MPa$	$s_u = 1.46\,mm$
	$k_E = 1000\,MPa/mm$	$G_f = 23.41\,N/mm$	$k_E = 1000\,MPa/mm$	$k_S = 1.2MPa/mm$

trusses and 20 interface elements (Figure 4.1) as optimal balance between accuracy and efficiency.

Several predictive curves in terms of load-displacement response at the loaded-end of the fiber under bond-slip behavior are analyzed. Figure 4.7 to 4.10 report the comparisons between experimental and numerical load-slip behaviors for both HSM and CSM.

The significant improvement (up to three times) of the bond strength in case of HSC, compared to conventional mortar, is well captured by the proposed models. The effect of the concrete quality is directly reflected on the bond-contact parameters as outlined in Table 4.3. Particularly, it can be observed that the shear strength, $\tau_{y,0}$, increases in direct relation to the compressive strength of the surrounding matrix.

Furthermore, Figures 4.7 to 4.10 show that the increment of the pull-out response is directly related to the anchoring length (varying from 6 to 18 mm). It can be also noted that the fracture energy-based model captures more accurately the bond-slip process than the analytical bilinear relationship. Figure 4.8 and 4.10 show that the results based on the analytical relationship are almost identical to the predictions of the FEM results. This means that the adopted mesh is sufficient to limit the modeling errors associated to the FE-discretization.

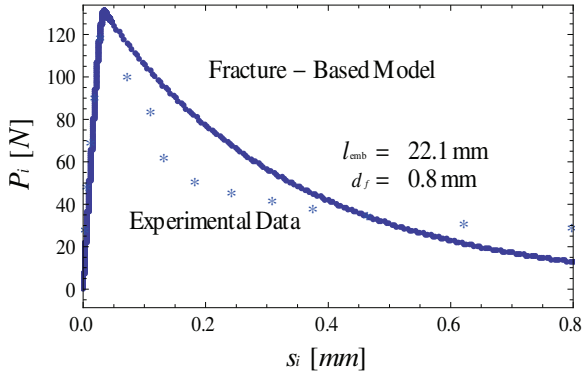

Figure 4.11: Numerical prediction (continuous line) vs. experimental data (points) [Banholzer et al., 2006]: fiber diameter of 0.8 mm and anchorage of 22.1 mm.

4.5.2 Fiber anchorage and diameter effects

This section presents some predictions based on experimental data from pull-out tests carried out on steel fibers anchored in concrete systems. Particularly, the fracture based model described in section 4.4 is calibrated to predict the load-displacement curves of straight and smooth steel fibers, with different diameters and anchoring lengths, tested under pull-out loads by Banholzer et al. [2006].

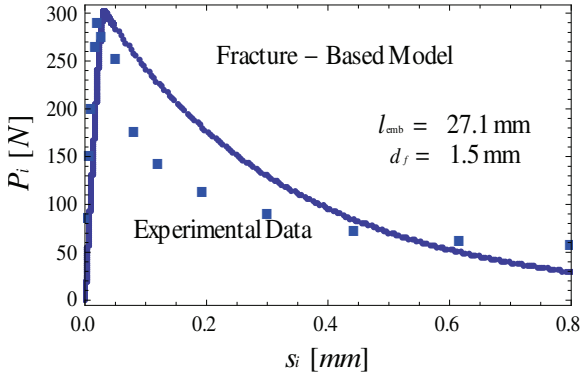

Figure 4.12: Numerical prediction (continuous line) vs. experimental data (points) [Banholzer et al., 2006]: fiber diameter of 1.5 mm and anchorage of 27.1 mm.

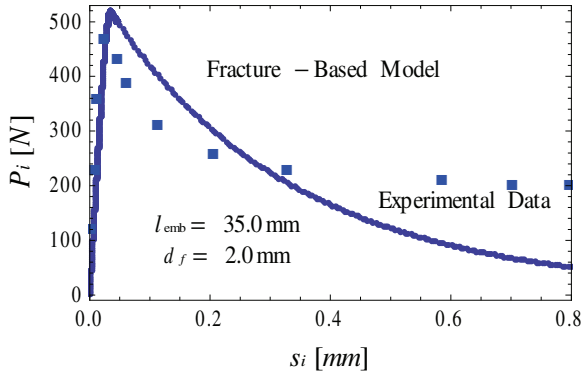

Figure 4.13: Numerical prediction (continuous line) vs. experimental data (points) [Banholzer et al., 2006]: fiber diameter of 2.0 mm and anchorage of 35.0 mm.

The following material parameters, dealing with an unified fracture energy-based $\tau - s$ rule, are employed for all predictions in this section:

- $\tau_{y,0} = 2.4\,MPa$ (shear strength),
- $s_u = 0.83\,mm$ (ultimate slip),
- $k_E = 120\,MPa/mm$ (initial elastic stiffness) and
- $G_f = 0.80\,N/mm$ (fracture energy under mode II).

Figure 4.11 to 4.13 show as the numerical simulations are generally in good agreement with the experimental results observed in pull-out tests. Load-slip curves are signifi-

cantly affected by both fiber diameter which varies from $d_f = 0.8$ to $2.0\,mm$, and the embedded lengths, varying from $l_{emb} = 22.1$ to $35.0\,mm$. The proposed procedure is able to realistically capture the influences of both parameters.

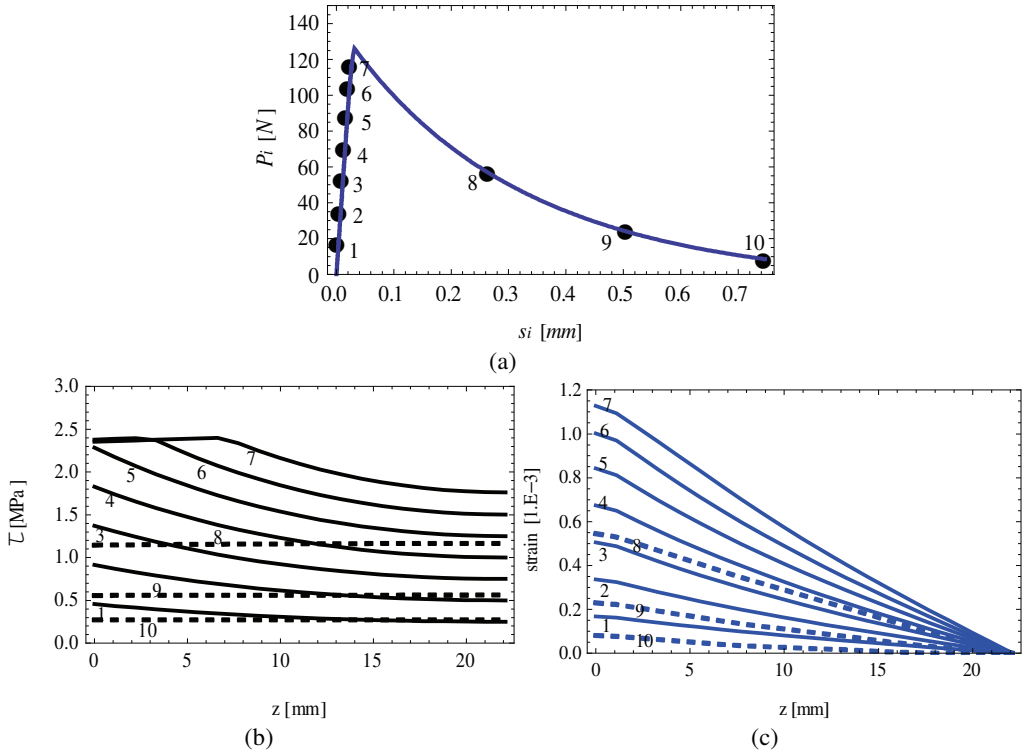

Figure 4.14: Pull-out simulation for a steel fiber diameter of $0.8\,mm$ and an embedded length of $22.1\,mm$ by Banholzer et al. [2006]: (a) load-slip curve $P_i - s_i$, (b) interface shear stress distributions $\tau - z$ and (c) axial strain distributions $\varepsilon_s - z$.

Only the numerical results based on the fracture energy modeling are outlined and compared against the experimental evidence in this section. The bilinear bond-slip relationship posses, as demonstrated in subsection 4.5.1, a limited prediction capability for pull-out tests, compared to the fracture energy-based proposal. For this reason the bilinear bond-slip behavior is neglected in this section.

Finally, the discussion focuses on the detailed simulation of the complete debonding processes developing in the three cases whose overall response is described in Figure 4.11 to 4.13. To this end, fiber-to-concrete bond stresses and fiber strain distributions throughout the bond length are obtained by means of numerical simulations. Figure 4.14 to 4.16 show such results for different bond lengths and diameters. In particular, Figures 4.14b, 4.15b and 4.16b report the distribution of interface shear stresses

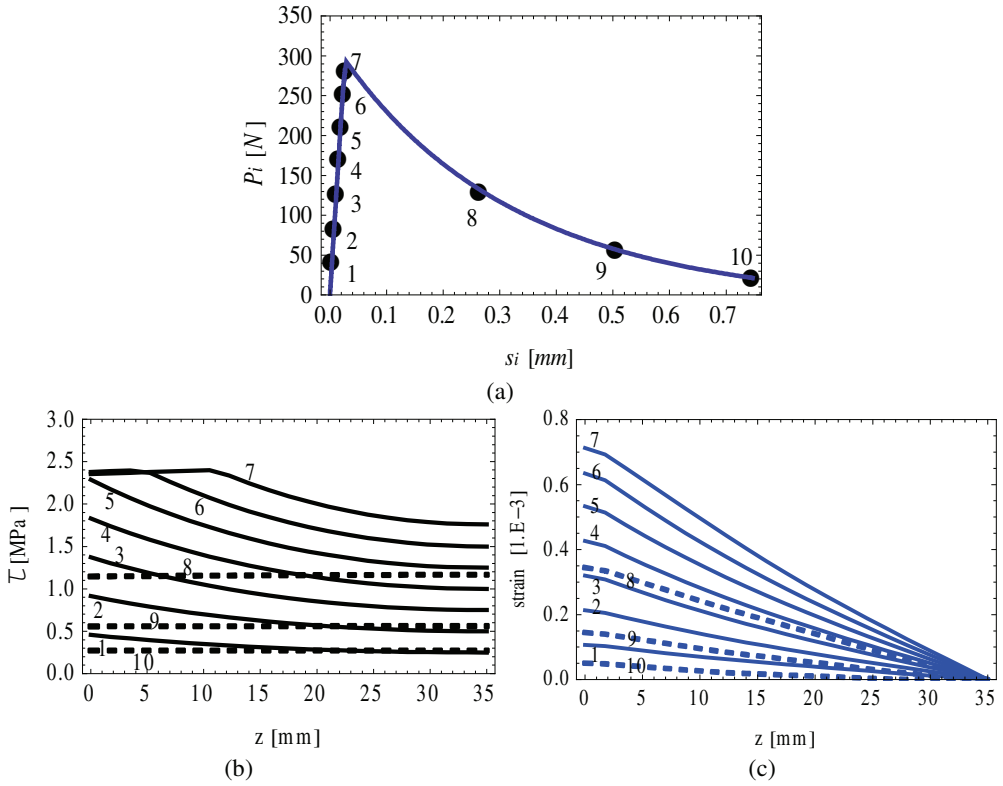

Figure 4.15: Pull-out simulation for a steel fiber diameter of 1.5 mm and an embedded length of 27.1 mm by Banholzer et al. [2006]: (a) load-slip curve $P_i - s_i$, (b) interface shear stress distributions $\tau - z$ and (c) axial strain distributions $\varepsilon_s - z$.

throughout the bond length for the same forces labeled by the dots represented in Figures 4.14a, 4.15a and 4.16a for the three specimens under consideration. Figures 4.14c, 4.15c and 4.16c report the axial strain distribution, namely $\varepsilon_s[z] = \frac{ds}{dz}$, throughout the fiber length: each curve refers to several force levels represented by the dots of the $P_i - s_i$ curves.

4.6 Closing remarks

This chapter presents a unified formulation for describing the overall bond-slip response of fibers embedded in cementitious matrices. Following remarks can be drawn out related to both the model formulation and their applications:

- The proposed unified formulation has been intended as a key element to be

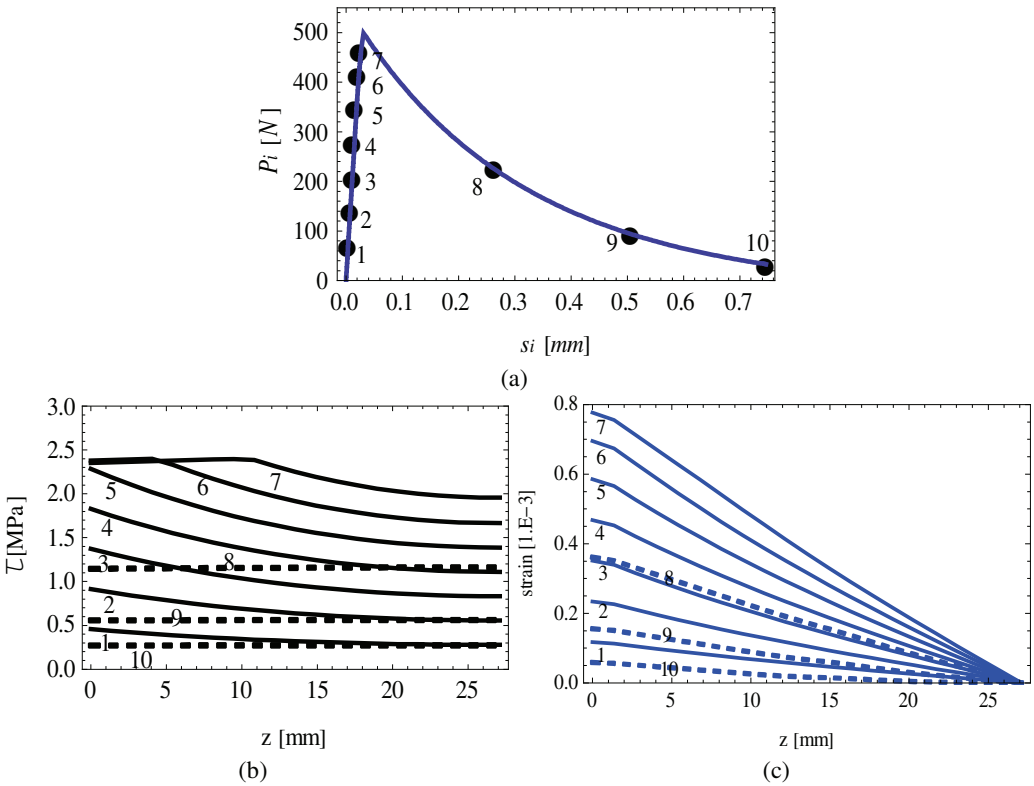

Figure 4.16: Pull-out simulation for a steel fiber diameter of 2.0 mm and an embedded length of 35.0 mm by Banholzer et al. [2006]: (a) load-slip curve $P_i - s_i$, (b) interface shear stress distributions $\tau - z$ and (c) axial strain distributions $\varepsilon_s - z$.

employed in the numerical model proposed in Chapter 3 to explicitly simulate the mechanical behavior of FRCC by taking into account the discrete nature of such materials and the contributions of the various constituents within the framework of the so-called meso-mechanical approach;

- Two alternative constitutive models have been proposed for obtaining the above mentioned formulation: i.e., the first one has been based on the simpler elasto-plastic behavior with isotropic linear softening, while, the second one has been founded on a more complex fracture energy-based contact model;

- The limits derived by assuming a simplified bilinear $\tau - s$ relationship for simulating the response of fibers under tensile stresses emerge in the final comparative analysis: although such a relationship allows for a fully analytical solution of the problem under consideration, it lacks in simulating the highly non-linear response which develops in the post-peak stage;

- Thus, a more complex, but more accurate fracture energy-based softening model has also been presented and the key aspects of the numerical procedure needed for handling such a relationship are outlined;
- The solutions obtained by considering both models have been validated against experimental results obtained on pull-out tests of smooth and straight steel fibers, currently available in the scientific literature;
- Both models demonstrate the capability of the proposed unified formulation to capture the key aspects of the complete pull-out response of fibers embedded in cementitious matrices and taking into account the possible influence of relevant parameters, such as bond length and fiber diameter.

As a final comment, it is worth highlighting that the proposed formulation can be straightforwardly employed in numerical models aimed at simulating the behavior of FRCC through a discrete-crack approach, as such model (i.e., meso-mechanical one) explicitly simulates the bond-slip response of fibers embedded in cementitious matrices. The adoption of the presented formulation within the framework of general meso-mechanical models of FRCC is, at the same time, the key motivation and the most relevant development of this chapter.

Despite the weaknesses described for the above mentioned bilinear relationship, numerical simulations are generally in good agreement with the corresponding experimental data. Moreover, the mesoscale formulation proposed by means of the zero-thickness interface formulation presented in Chapter 3 and then validated in the following Chapters (5 and 6), actually considers the bilinear proposal for the fiber debonding into the complete formulation for FRCC failure analysis.

5 Model performance and numerical predictions

This chapter proposes a preliminary calibration and some applications of the proposed interface model for FRCC failure analysis. Numerical simulations against available experimental test data are presented for investigating the soundness and capabilities of the proposed methodology.

5.1 Numerical analyses

For the calibration purpose, experimental results on Steel Fiber-Reinforced Concrete (SFRC) specimens, tested in pure tension, are considered while for the evaluation of model predictions, failure processes under mixed-modes of fracture, in plain and SFRC notched specimens, are taken into account.

5.1.1 Calibration of the interface model for SFRC

In this section, the interface model is calibrated by using experimental results performed on SFRC specimens tested in pure traction. One interface element, with different fiber contents, connecting two 4-node plane stress isoparametric elements is employed for this purpose. Particularly, the basic element patch, shown in Figure 5.1, is considered.

The number of fibers per interface is evaluated by means of the expression proposed by Krenchel [1975]

$$n_f = \alpha_{\vec{N}} \frac{\rho_f}{A_f} A_i \tag{5.1}$$

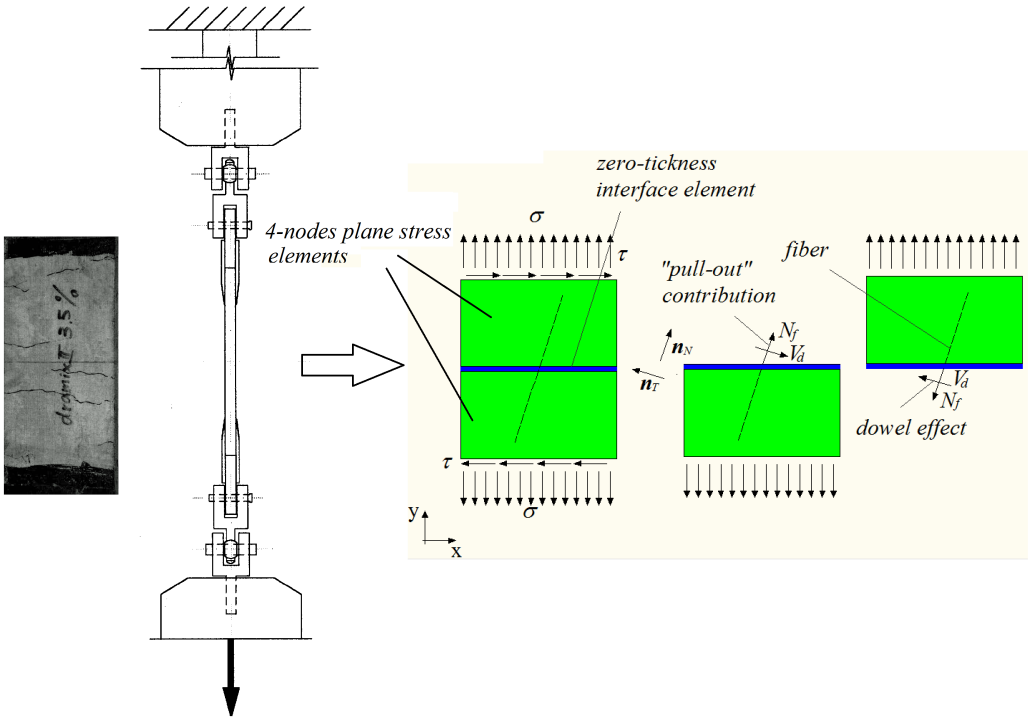

Figure 5.1: Test set-up of tensile tests performed by Li et al. [1998] and the corresponding analysis model.

where ρ_f is the fiber content and $\alpha_{\tilde{N}}$ the orientation factor (assuming the value of 0.405 [Soroushian and Lee, 1990]), while A_f and A_i are the cross-sectional areas of a single fiber and of the interface, respectively.

The tensile tests on SFRC specimens, presented in Li et al. [1998], are firstly considered. Two different kinds of fibers, both with hooked-ends, are utilized as follow:

- **Dramix steel fibers** (diameter $d_f = 0.5\ mm$, length $l_f = 30\ mm$, density $\gamma_f = 7.8\ g/cm^3$, tensile strength $f_{fu} = 1.20\ GPa$ and $E_f = 200\ GPa$).
- **Harex steel fibers** (with arched cross section of area $= 2.2 \times 0.25\ mm^2$, length $l_f = 32\ mm$, density $\gamma_f = 7.8\ g/cm^3$, tensile strength $f_{fu} = 0.81\ GPa$ and $E_f = 200\ GPa$).

An indirect calibration of the numerical model, previously formulated in Chapter 3, is performed to identify its parameters. The set of such parameters (i.e., the equivalent elastic modulus of fibers, E_d, the equivalent interface elastic limit, $\sigma_{y,d}$, and the other

ones mentioned in Chapter 3), collected within the vector $\mathbf{q}$, are derived through the following least-square procedure

$$\bar{\mathbf{q}} = \arg\min_{\mathbf{q}} \left[\sum_{i=1}^{n} \left(\sigma_{th} \left[\varepsilon_{\exp,i}; \mathbf{q} \right] - \sigma_{\exp,i} \right)^2 \right] \tag{5.2}$$

being $\sigma_{th}\left[\varepsilon_{\exp,i};\mathbf{q}\right]$ the model prediction of the tensile stress corresponding to the experimental strain $\varepsilon_{\exp,\mathrm{i}}$ and the set of internal parameters $\mathbf{q}$, while $\sigma_{\exp,\mathrm{i}}$ is the corresponding experimental stress. In Eq. (5.2), n represents the number of available tensile stress measurements of the considered experimental test.

For the least-square calibration of the model parameters, experimental data on SFRC by Li et al. [1998] for both *Dramix* and *Harex* type of steel fibers are considered. The case of plain concrete is also included in the calibration analysis. The parameters of the proposed model, optimally adjusted according to Eq. (5.2), include the elastic parameters of the rigid continuum elements representing the mortar matrix: $E_c = 37\,GPa$ and $\nu = 0.18$. The parameters of the inelastic interface result: $k_N = 1000\,MPa/mm$, $k_T = 200\,MPa/mm$, $\tan\phi_0 = \tan\beta = \tan\phi_r = 0.6$, $\chi_0 = 4.0\,MPa$, $c_0 = 7.0\,MPa$, $G_f^I = 0.12\,N/mm$, $G_f^{IIa} = 1.2\,N/mm$, $\sigma_{dil} = 10\,MPa$, $\alpha_\chi = -0.15$. The remaining interface parameters are considered equal to zero.

Some of the relevant fiber parameters are derived from the main mechanical parameters of the constitutive materials, while the other ones are obtained with the above indicated calibration procedure. In summary, fiber parameters result: $E_d = E_s$, $\sigma_{y,d} = 18\%\ \sigma_{y,s}$, $k_c = 440 N/mm^3$, $\alpha_f = 7.7$ and $H_s = H_d = H_{dow} = 0$.

The available experimental results of direct tensile tests, represented by dotted lines in Figures 5.2 and 5.3, are compared with the corresponding model predictions represented by solid lines. Particularly, the predicted stresses-strain curves reported in Figures 5.2 and 5.3 are obtained as the average of local stresses in the single-crack model of Figure 5.1.

Moreover, in Figures 5.2 and 5.3 the experimental results obtained by Li et al. [1998] are compared with the corresponding numerical simulations performed through the calibrated numerical model. The specimens reinforced with either *Dramix* or *Harex* fibers are considered with fiber contents ($\rho_f = 0$, 2, 3 and 6%). The results of the simulations demonstrate that the proposed interface model leads to accurate predictions of SFRC failure behavior in the direct tensile test when low, medium and high fiber contents are considered.

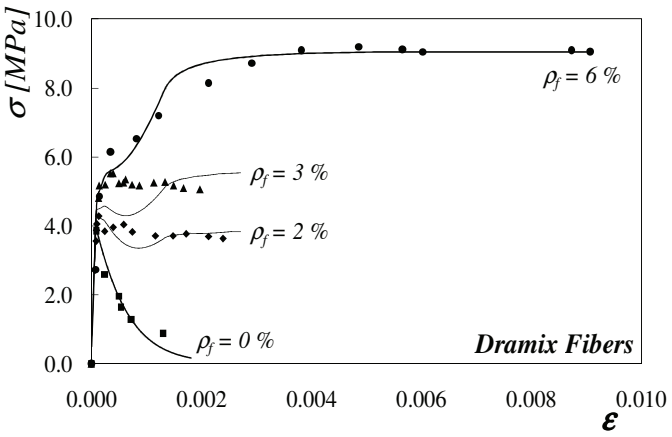

Figure 5.2: Experimental data [Li et al., 1998] and numerical simulation for SFRC with *Dramix* fibers.

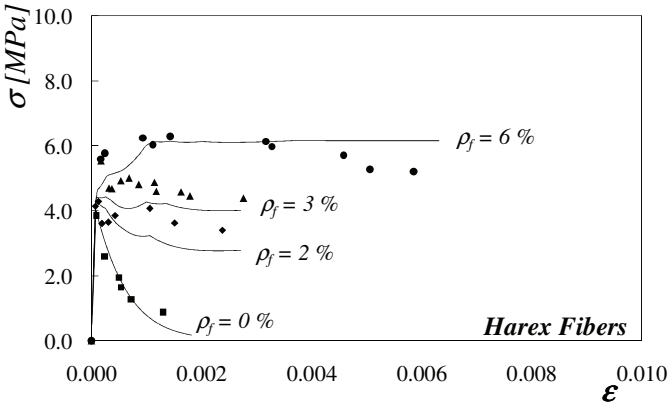

Figure 5.3: Experimental data [Li et al., 1998] and numerical simulation for SFRC with *Harex* fibers.

Beyond the general accuracy of the model predictions and, consequently, the soundness of its assumptions and formulation, the results in Figure 5.2 and 5.3 emphasize the strong relationship between the mechanical behavior of FRCC and the fiber content and quality. A progressive transition from the brittle failure mode characterizing the behavior of plain concrete in tension to a more and more ductile post-peak response can be clearly recognized when the fiber content increases.

Finally, the diagrams in Figures 5.2 and 5.3 show the different behavior of SFRC based on *Dramix* and *Harex* fibers, both hooked at the end. The more ductile performance

shown in Figure 5.2 is probably due to the fact that the volume of the single *Dramix* fiber is significantly smaller (almost three times [Li et al., 1998]) than that of *Harex* types (Figure 5.3). Consequently, a significantly higher number of fibers are present in the reinforced with the former specimens (for the same considered fiber content) and this results in a more homogeneous material.

5.1.2 SFRC failure behavior under mixed-modes of fracture

To asses the predictive capability of the proposed interface model in terms of failure behavior of SFRC specimens, the stress history on plane concrete panels by Hassanzadeh [1990] are considered in this subsection.

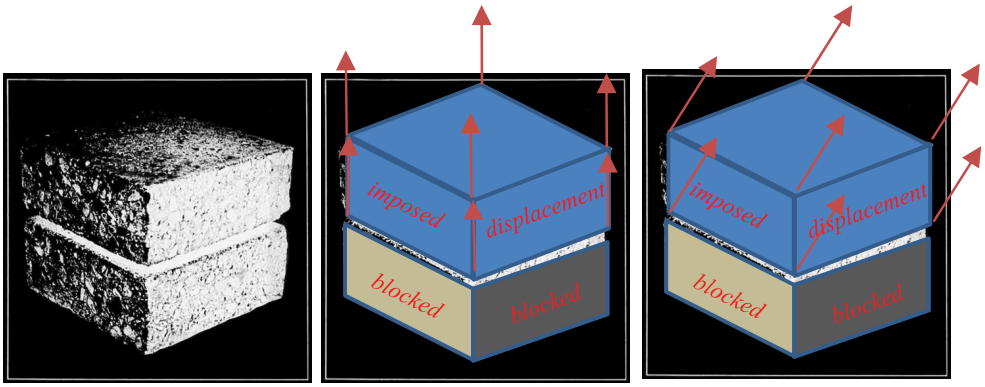

(a) (b) (c)

Figure 5.4: Test set-up by Hassanzadeh [1990]: (a) concrete sample, (b) tensile state and (c) mixed fracture displacements.

These experimental tests are performed on prismatic concrete specimens of 0.07×0.07 m^2 cross section with a 0.015 m deep notch along their perimeters (Figure 5.4a). Both normal and transverse relative displacements are imposed simultaneously to the two parts of the notched specimen with the aim of reproducing the cracking processes in concrete under mode I and II types of fracture depending on the angle between the two displacement components. During the first part of these tests only normal tensile displacements u are applied, as in Figure 5.4b, until the peak strength is reached. In the second part of the test (Figure 5.4c), tensile displacements are combined with transverse ones, applied on the upper part of the notched specimen, and defining a pre-fixed angle (namely, $\tan\theta = u/v$).

For the numerical analysis of the Hassanzadeh [1990] tests, the FE-discretization and boundary conditions shown in Figure 5.5 are considered. Four different cases are eval-

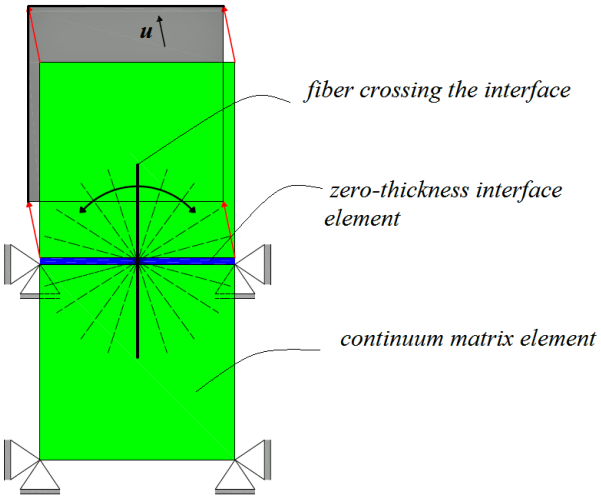

Figure 5.5: Boundary conditions and FE-discretization with one single interface crossed by short fibers for Hassanzadeh [1990] tests on SFRC panels.

uated with $\theta = 90^o$, 75^o, 60^o, 30^o and in each case zero ($n_f = 0$), ten ($n_f = 10$), twenty ($n_f = 20$) and thirty ($n_f = 30$) steel fibers, crossing the joint element, are considered.

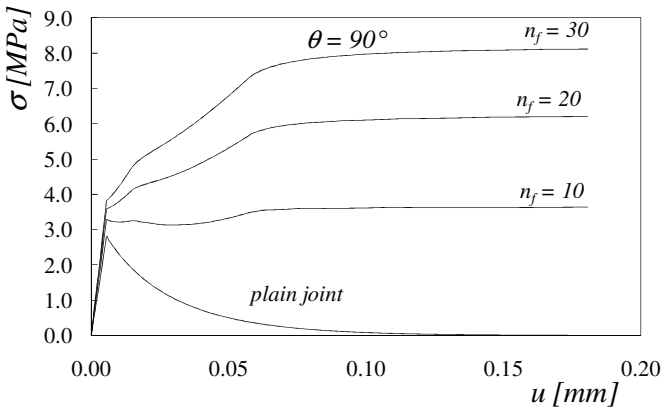

Figure 5.6: Normal stress vs. relative vertical displacement performed with different amount of fibers and $\theta = 90^o$.

The interface model parameters, calibrated starting from the experimental data by Hassanzadeh [1990], are: $k_N = 500\ MPa/mm$, $k_T = 200\ MPa/mm$, $\tan\phi_0 = \tan\beta = \tan\phi_r = 0.6$, $\chi_0 = 2.8\ MPa$, $c_0 = 7.0\ MPa$, $G_f^I = 0.08\ N/mm$, $G_f^{IIa} = 10\,G_f^I = 0.8\ N/mm$, $\sigma_{dil} = 15\ MPa$. All remaining parameters, characterizing the interface model, are considered null. For the continuum elements, the elastic parameters $E_m = 25\ GPa$ and $\nu = 0.2$ are

considered, representing the Young modulus and Poisson's ratio, respectively. *Dramix* fibers are used in those analyses characterized with the same parameters detailed in subsection 5.1.1.

Figure 5.6 shows the results with different number of fibers corresponding to the uniaxial tensile test ($\theta = 90^o$). It can be clearly observed that the model is able to simulate the increment in both ductility and energy released when the number of fibers increase.

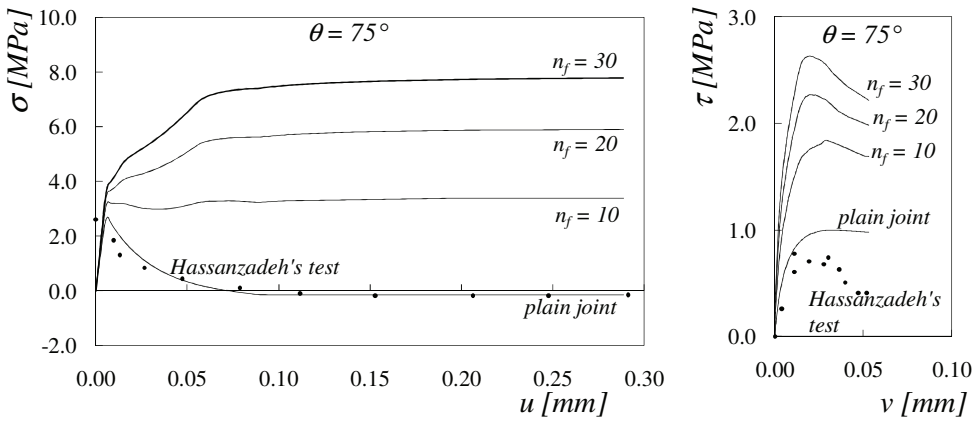

Figure 5.7: Hassanzadeh [1990] tests with different number of fibers and $\theta = 75^o$: a) normal stress vs. relative normal displacement and b) shear stress vs. relative tangential displacement.

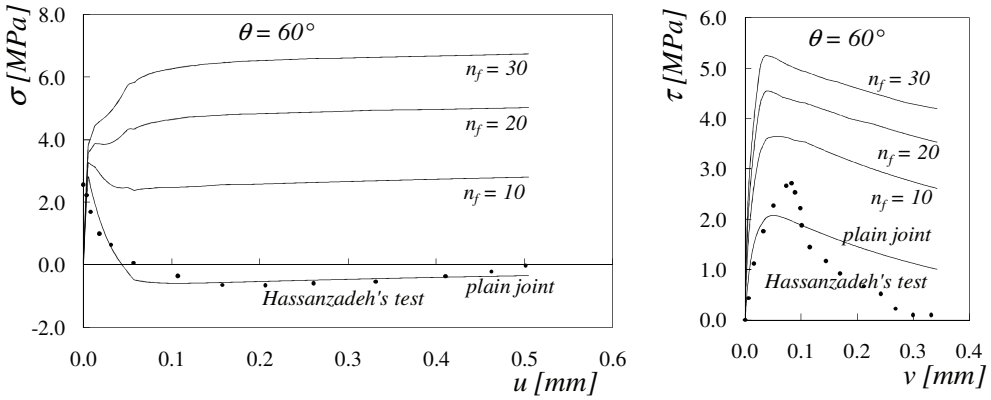

Figure 5.8: Hassanzadeh [1990] tests with different number of fibers and $\theta = 60^o$: a) normal stress vs. relative normal displacement and b) shear stress vs. relative tangential displacement.

Figures 5.7a, 5.8a and 5.9a show the model predictions in terms of normal stresses vs. displacements ($\sigma - u$) of Hassanzadeh [1990] experiments for $\theta = 75^o$, 60^o and

30^o, respectively. As it can be observed, the combined action of normal and shear displacements causes a more pronounced softening branch in post-peak regime. The tensile strength tends to zero more rapidly and, moreover, changes its sign becoming a compressive stress, due to the fact that the normal dilatancy, produced by the applied shear displacements, exceeds the fixed normal opening rate.

The inclusion of steel fibers leads to an increment in the tensile strength, as well as of the ductility in post-peak regime. Simultaneously, the compression branch of the normal stress continuously reduces and then disappears. In other word, the steel fibers reduce the material dilatancy.

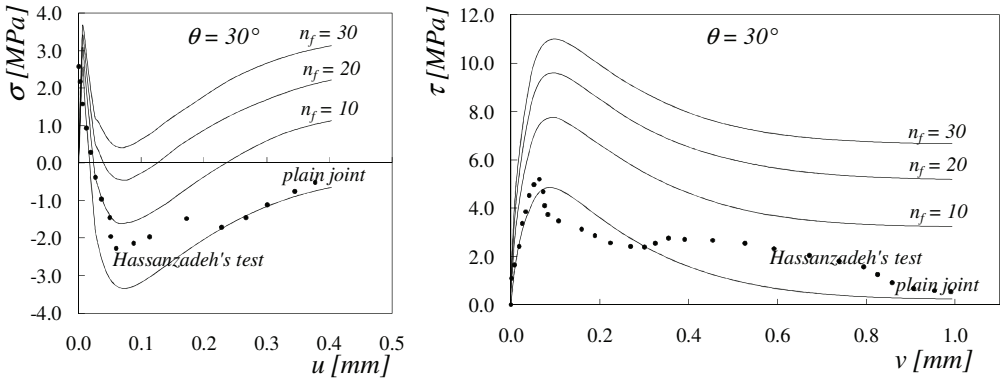

Figure 5.9: Hassanzadeh [1990] tests with different number of fibers and $\theta = 30^o$: a) normal stress vs. relative normal displacement and b) shear stress vs. relative tangential displacement.

Figures 5.7b, 5.8b and 5.9b report the shear stresses against the relative transverse displacements. The significant influence of fiber content on both peak stress and post-peak toughness can be (again) easily recognized.

The simulation of the interface model in this section demonstrates the capability of the proposed formulation to capture the variation of stiffness, strength, ductility and the overall behavior of concrete due to the presence of steel fibers both in pure tensile failure mode and under mode II type of fracture with different levels of confinement pressure, originated by constraining the dilatancy of both plain and fiber concretes.

5.1.3 Parametric study

The parametric analyses presented in this section are performed by means of the two linear elastic four node FEs connected by one interface element. The considered FE set-up and boundary conditions are discussed in Figure 5.5. Therefore, the inelas-

tic behavior of the FE set-up in Figure 5.5 is directly related to the interface model predictions.

Fiber length

Two different fiber types, namely "Dramix type I" and "type II", whose fundamental characteristics are reported in Table 8.1, are utilized in the SFRC specimens under consideration. The model parameters, considered in the following numerical analyses and adjusted according to the experimental data by Li and Li [2001] are listed below: $k_N = 98.75\,GPa$, $k_T = 32.92\,GPa$, $\tan\phi_0 = \tan\beta = \tan\phi_r = 0.6$, $\chi_0 = 4.0\,MPa$, $c_0 = 7.0\,MPa$, $G_f^I = 0.12\,N/mm$, $G_f^{IIa} = 1.2\,N/mm$. Moreover, the parameters considered for the fiber-to-concrete interaction mechanisms are:

- $\tau_{y,a} = 1.95\,MPa$, $k_E = 52.5 MPa/mm$ and $k_S = 1.70 MPa/mm$ for the bond-slip strength;
- $\kappa_1 = 6.5$, $f_c = 10 \cdot \chi_0$ and $k_{dow} = 0.23$ for the dowel effect.

The indirect calibration procedure outlined in subsection 5.1.1 is performed to identify the model parameters above outlined.

Table 5.1: Fiber types employed in the experimental tests by Li and Li [2001].

	Density $[g/cm^3]$	$d_f[mm]$	$l_f[mm]$	$\sigma_{y,s}[GPa]$	$E_s[GPa]$
Dramix type I	7.8	0.5	30	1.20	200
Dramix type II	7.8	0.5	50	1.20	200

Model predictions are compared with the experimental data by Li and Li [2001]. The comparisons in terms of force-displacement diagrams are shown in Figures 5.10 and 5.11. Particularly, the stress-crack opening response for SFRC with steel "Dramix type II" fibers, and fiber contents of 3.0% and 4.0%, are reported in Figure 5.10. While Figure 5.11 shows numerical and experimental comparisons of stress-crack opening displacements of tests on SFRC with "Dramix type I" fibers, and fiber contents of 7.0% and 8.0%.

The numerical predictions compared against experimental results demonstrate a very good agreement. Actually, the interface model is able to realistically reproduce the overall response behaviors of SFRC.

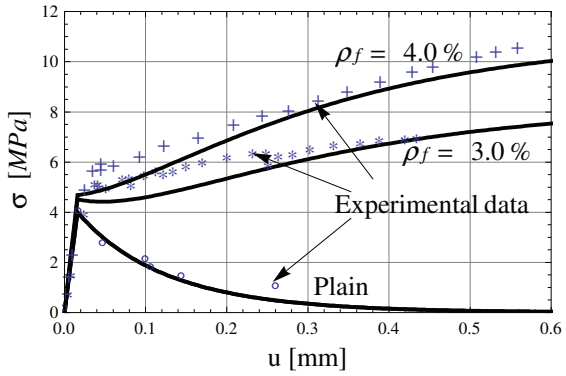

Figure 5.10: Comparison between numerical predictions and experimental results by Li and Li [2001]: SFRC with "Dramix type II" fibers.

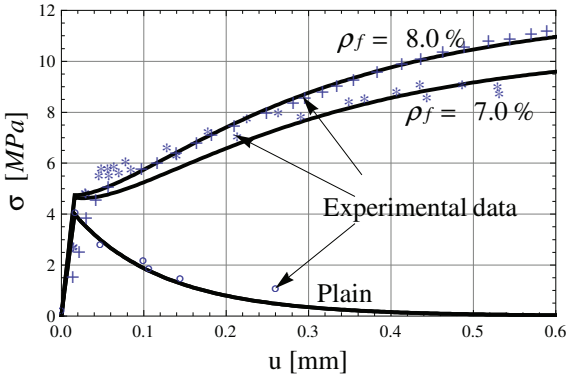

Figure 5.11: Comparison between numerical predictions and experimental results by Li and Li [2001]: SFRC with "Dramix type I" fibers.

It should be noted that all previous numerical predictions are obtained by just modifying the fiber contents (ρ_f) and/or fiber types (changing the l_f value), according to the experimental properties.

Debonding strength

Stress-crack opening predictions of SFRC with steel "Dramix Type II" fibers are evaluated when full and 50% of the debonding strength capacity of steel fibers to concrete are considered. This results, depicted in Figure 5.12a, clearly illustrate the capability of the interface model to realistically reproduce the incidence of the main parameters which control the interaction between concrete and steel fiber in mode I type of fracture.

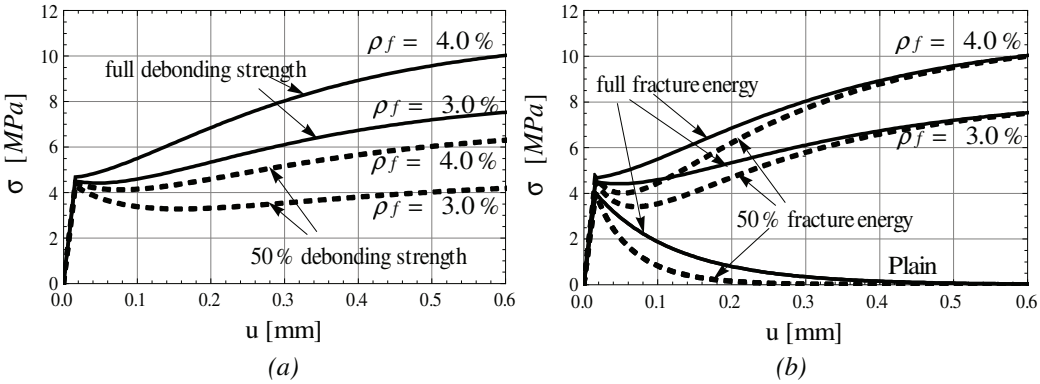

Figure 5.12: Comparison between numerical predictions of the test by Li and Li [2001] on SFRC with "Dramix type II" fibers: (a) full debonding vs. 50% of the debonding strength and (b) full fracture energy, G_f^I, vs. 50% of G_f^I.

Fracture energy release

Figure 5.12b reports the stress-crack opening behavior observed in the same experiment on SFRC, but corresponding to the case of 50% of the concrete fracture energy release in mode I. As can be observed in Figure 5.12, the interface model is able to capture the influence of fundamental properties of the constituents in the overall response behavior.

Dowel strength

Finally, the stress history on concrete blocks by Hassanzadeh [1990] is evaluated as it activates failure processes under both mode I and II types of fracture. These experimental tests, already simulated in subsection 5.1.2, are performed on prismatic concrete notched specimens in which both normal and transverse relative displacements are co-imposed on the upper border of the notched specimen while the remaining borders are fixed with the aim of reproducing cracking processes in concrete under mode I and II types of fracture. During the first part of these tests only normal tensile displacements u are applied until the peak strength is reached. Then, tensile displacements are combined with transverse ones v defining a prefixed load angle ($\tan\theta = u/v$).

Figure 5.13a shows the model predictions in terms of $\sigma - u$ and $\tau - v$ curves, analyzing the case in which $\theta = \pi/6$ on both plain and SFRC concrete panels. The proposed application consider the model parameters previously calibrated and reported in subsection 5.1.2. Numerical analyses demonstrate the very good agreement of the numerical

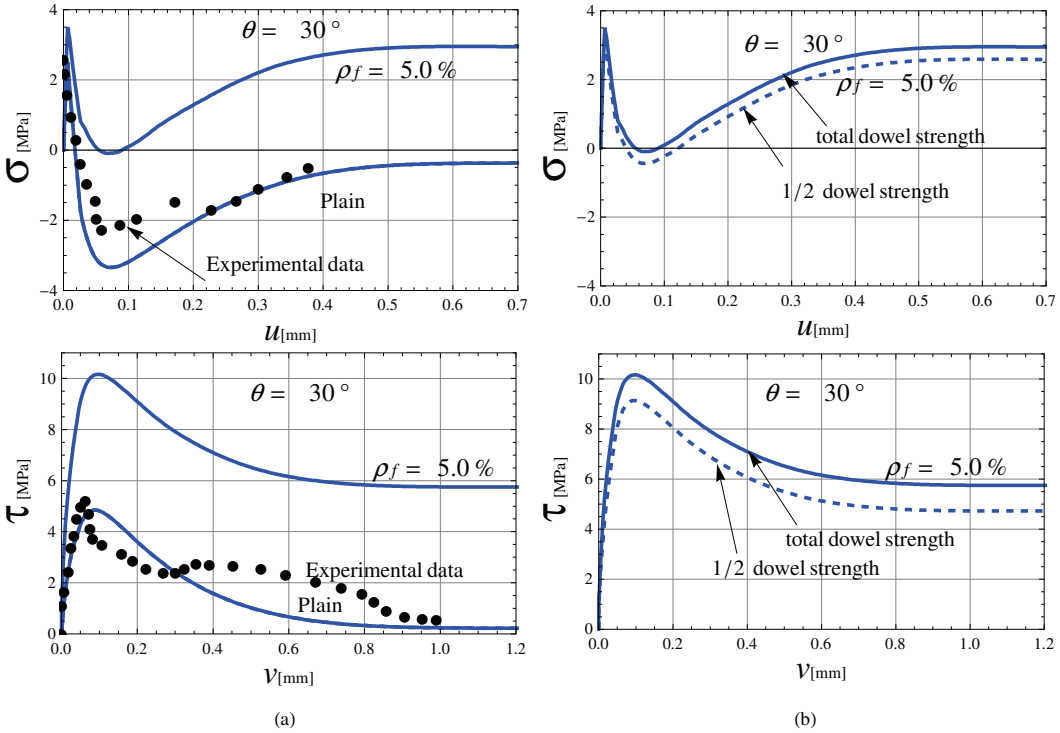

Figure 5.13: (a) Experimental test by Hassanzadeh [1990] and numerical predictions for SFRC with "Dramix type I" fibers with $\rho_f = 5.0\%$ and (b) effect of the dowel strength on the stress-opening displacements in mixed-modes of fracture.

prediction with the plain interface regarding the experimental results on plain concrete tests by Hassanzadeh [1990]. On the other hand, the results also illustrate the significant influence of fiber reinforcements on the peak strength and post-peak ductility of the concrete panel response (when $\rho_f = 5.0\%$).

Figure 5.13b deals with the stress-crack opening predictions of SFRC when a reduction of the 50% for the dowel strength is considered. Model predictions mainly capture the fundamental influence of the dowel effect on the overall response behavior under mixed failure modes. As expected, it controls the transverse interaction between concrete and steel fiber in this complex failure mode.

5.2 Cracking analysis of the proposed interface model for FRCC

This section is aimed at analyzing the influence of steel fibers and the stress state lying on the initial yielding surface on the post-cracking performance and failure

modes. As a matter of principle, the method applied herein could be intended as a similar approach as the one used for continuum-based models, where the localization analysis is mainly performed by employing the analytical solution of the classical discontinuous bifurcation condition [Folino, 2012]. Strong differences can be noted between the localized failure analyses of classical continuum approaches compared with the discontinuous analysis proposed and discussed in this section.

The numerical results presented in this section are based on the cracking analysis by considering different SFRC qualities and load scenarios. They illustrate a wide range of failure modes which characterize the post-peak response of both plain concrete and SFRC under different stress histories. Moreover, a dimensionless "cracking indicator" is discussed and analyzed.

5.2.1 Post-cracking behavior

An extensive post-cracking analysis is proposed based on the FRCC interface model outlined in section 5.1. For this purpose, several interface cracking conditions are considered for different load scenarios. Following the normalized indicator for diffuse failure by Hill's condition of stability [Etse, 1992, Etse and Willam, 1994] in smeared crack models, it is proposed the following normalized "Cracking Indicator" (CI) for discrete crack condition as in case of interface models,

$$CI(\theta,\rho) = \frac{\boldsymbol{N}^t \cdot \boldsymbol{E}^{ep} \cdot \boldsymbol{N}}{\boldsymbol{N}^t \cdot \boldsymbol{E} \cdot \boldsymbol{N}} \tag{5.3}$$

being θ the initial cracking angle (with $\tan\theta = u/v$ as highlighted in Figure 5.14) and $\boldsymbol{N}$ the unit vector defining the normal of a potential cracking direction expressed as

$$\boldsymbol{N} = [N_1, N_2]^t = [\cos(\rho), \sin(\rho)]^t \tag{5.4}$$

The angles ρ is depicted in Figure 5.14 and describes the set of all possible vectors $\boldsymbol{N}$ of the failure surface. $\boldsymbol{E}^{ep}$ and $\boldsymbol{E}$ are the constitutive tangent operator and the elastic one, respectively, defined in Chapter 3. The superscript ^{t} deals with the transposition vectorial operation.

The performance of the "cracking indicator" is proposed in terms of the ρ-angle (between $\boldsymbol{N}$ and the σ_T direction, as depicted in Figure 5.14). Particularly, $\rho = \frac{\pi}{2}$ indicates a pure tensile fracture mode path, while $\rho = 0$ outlines a direct shear without dilatancy. For any given θ angle, a particular value for ρ (labeled as critical one ρ_{cr}) exists for

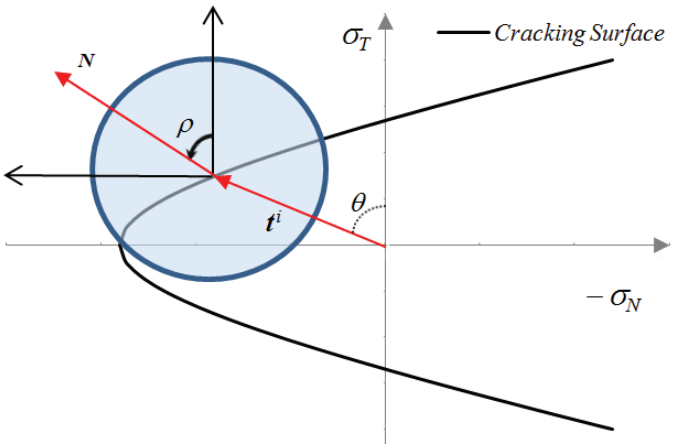

Figure 5.14: ρ and θ angles defined in the interface stress space.

which the mentioned CI parameter assumes its minimum: ρ_{cr} defines the weakness direction of the considered composite interface.

5.2.2 Failure performance and cracking indicators for mixed fracture modes

In this subsection, the post-cracking analysis under mixed-modes condition and peak stress is presented. The analyses are performed for three different SFRC: i.e., plain concrete, Dramix steel fibers with 3.0 and 6.0%. All the numerical predictions refer to the model parameters identified in section 5.1.1. Different initial θ-angles, at peak stress under mixed-modes of fracture, are considered.

A set of six interface stress states are selected and analyzed for the three types of SFRC under consideration. These stress states are indicated on the maximum interface strength following the numeration of Figure 5.15. The particular stress states considered in the analyses of this section are listed below:

- Point 1: Uniaxial Tensile (UT): $\frac{\sigma_N}{\sigma_T} = \frac{1}{0} \Longrightarrow \theta = \frac{\pi}{2}$;
- Point 2: Tension-Shear (TS2): $\frac{\sigma_N}{\sigma_T} = \frac{1}{2-\sqrt{3}} \Longrightarrow \theta = \frac{5\pi}{12}$;
- Point 3: Tension-Shear (TS3): $\frac{\sigma_N}{\sigma_T} = \frac{1}{\frac{1}{\sqrt{3}}} \Longrightarrow \theta = \frac{\pi}{3}$;
- Point 4: Tension-Shear (TS4): $\frac{\sigma_N}{\sigma_T} = \frac{1}{1} \Longrightarrow \theta = \frac{\pi}{4}$;
- Point 5: Tension-Shear (TS5): $\frac{\sigma_N}{\sigma_T} = \frac{1}{\sqrt{3}} \Longrightarrow \theta = \frac{\pi}{6}$;

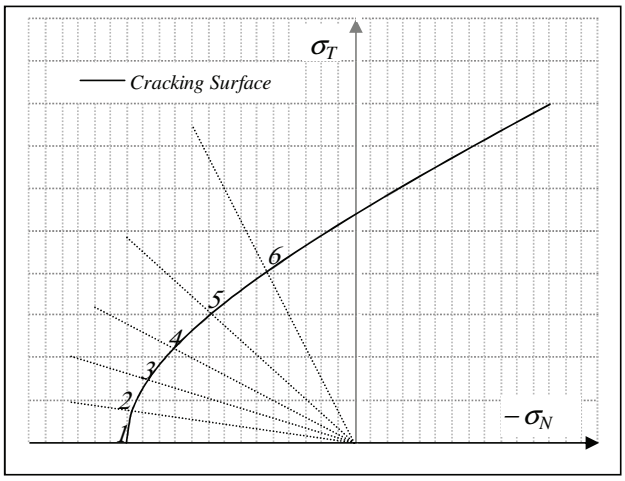

Figure 5.15: Schematic interface stress states selected for the post-cracking analysis.

- Point 6: Tension-Shear (TS6): $\frac{\sigma_N}{\sigma_T} = \frac{1}{2+\sqrt{3}} \Longrightarrow \theta = \frac{\pi}{12}$.

The results of these analyses, performed with the FRCC interface model at peak stresses, are presented in Figure 5.16, while the same post-cracking performance results are also depicted in polar plots in Figures 5.17, 5.18 and 5.19. The critical angles, ρ_{cr}, at which the CI parameter assumes its minimum value, for the above considered materials (plain concrete and FRCCs with Dramix steel fibers having the 3.0 and 6.0% of fiber content) are (Figure 5.15):

- Point 1: Uniaxial Tensile (UT): $\theta = \frac{\pi}{2} = 90°$, $\rho_{cr,PI} = 90°$, $\rho_{cr,3.0\%} = 90°$ and $\rho_{cr,6.0\%} = 90°$;
- Point 2: Tension-Shear (TS2): $\theta = \frac{5\pi}{12} = 75°$, $\rho_{cr,PI} = 83.15°$, $\rho_{cr,3.0\%} = 85.31°$ and $\rho_{cr,6.0\%} = 86.03°$;
- Point 3: Tension-Shear (TS3): $\theta = \frac{\pi}{3} = 60°$, $\rho_{cr,PI} = 76.65°$, $\rho_{cr,3.0\%} = 80.26°$ and $\rho_{cr,6.0\%} = 80.98°$;
- Point 4: Tension-Shear (TS4): $\theta = \frac{\pi}{4} = 45°$, $\rho_{cr,PI} = 67.99°$, $\rho_{cr,3.0\%} = 73.77°$ and $\rho_{cr,6.0\%} = 75.21°$;
- Point 5: Tension-Shear (TS5): $\theta = \frac{\pi}{6} = 30°$, $\rho_{cr,PI} = 57.17°$, $\rho_{cr,3.0\%} = 65.11°$ and $\rho_{cr,6.0\%} = 67.27°$;

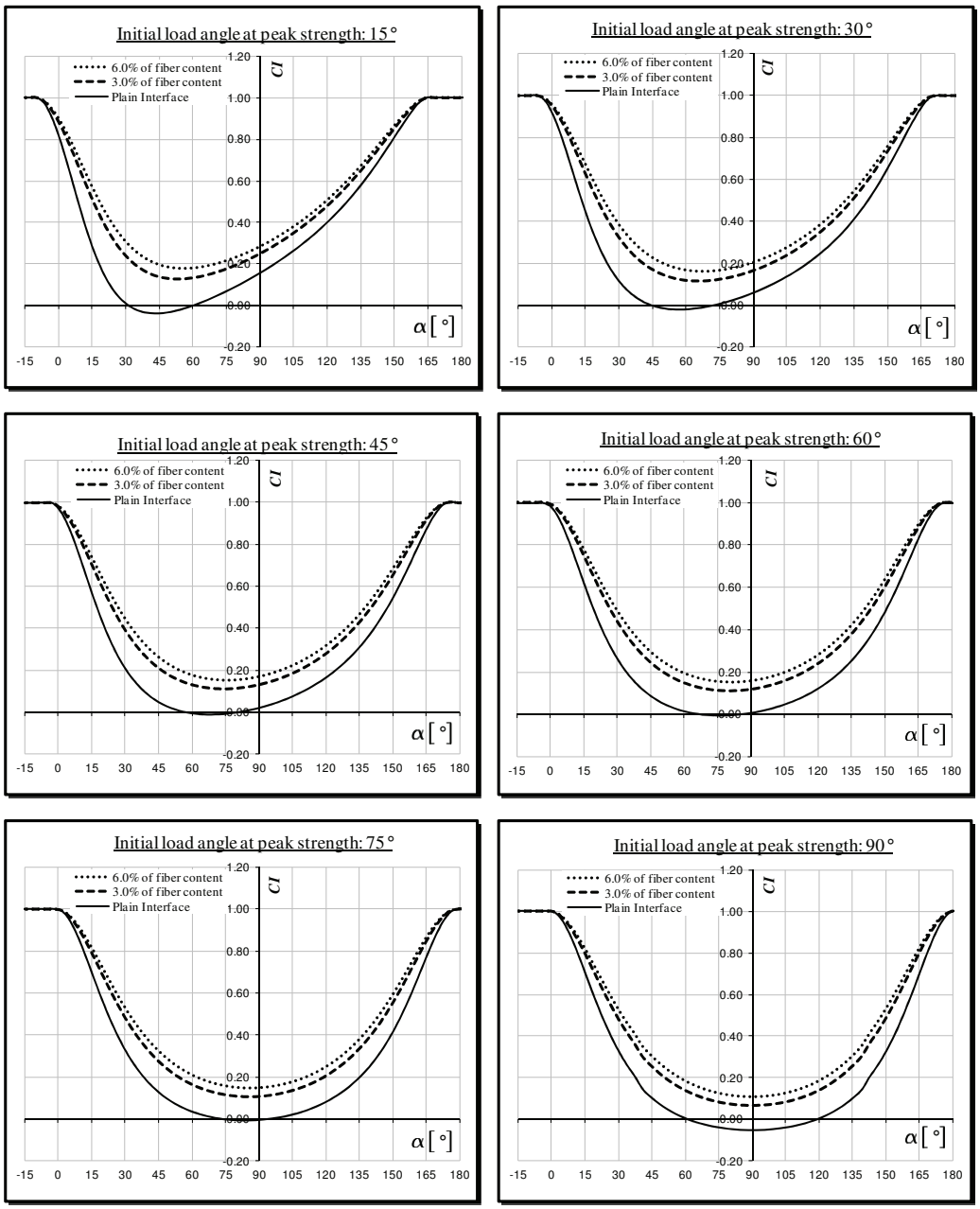

Figure 5.16: Post-cracking analysis at peak stress for different concrete types: plain concrete and SFRC with "Dramix type I" fibers having fiber contents of 3.0% and 6.0%.

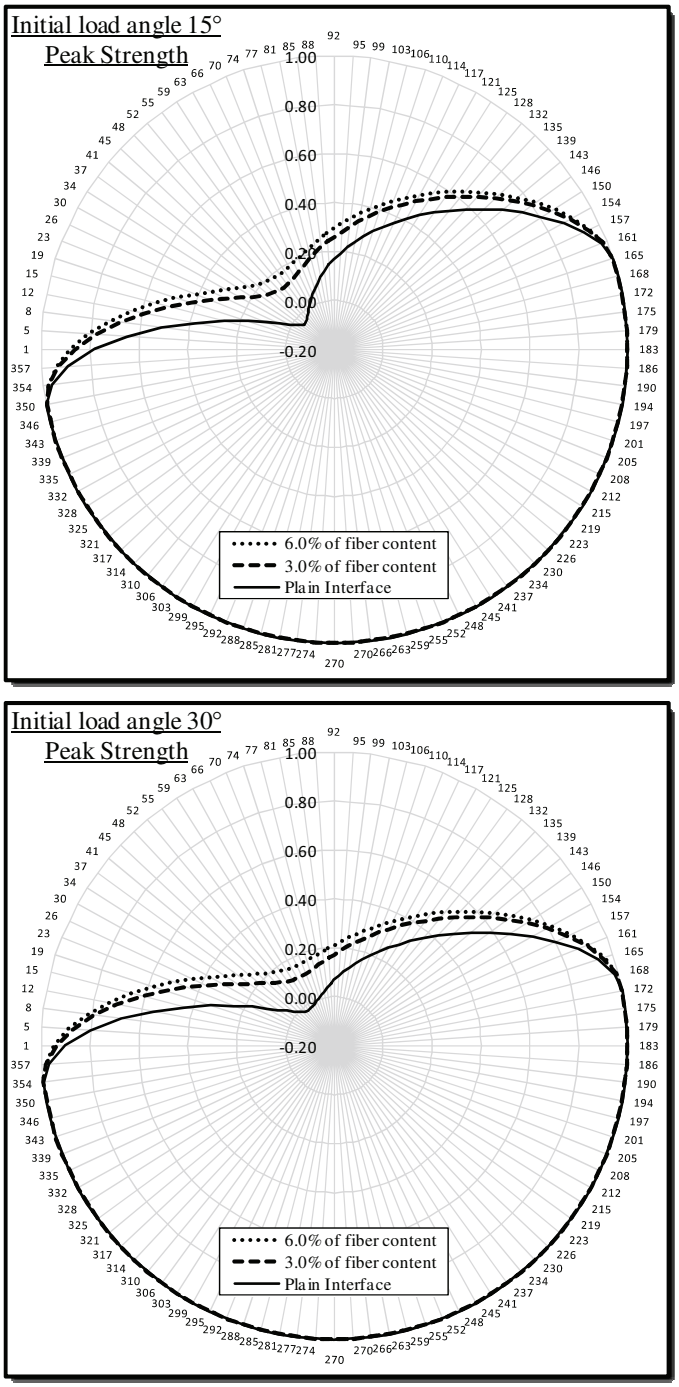

Figure 5.17: Polar plots of post-cracking analysis of TS5 and TS6 for different concrete types: plain concrete and SFRC with "Dramix type I" fibers having fiber contents of 3.0% and 6.0%.

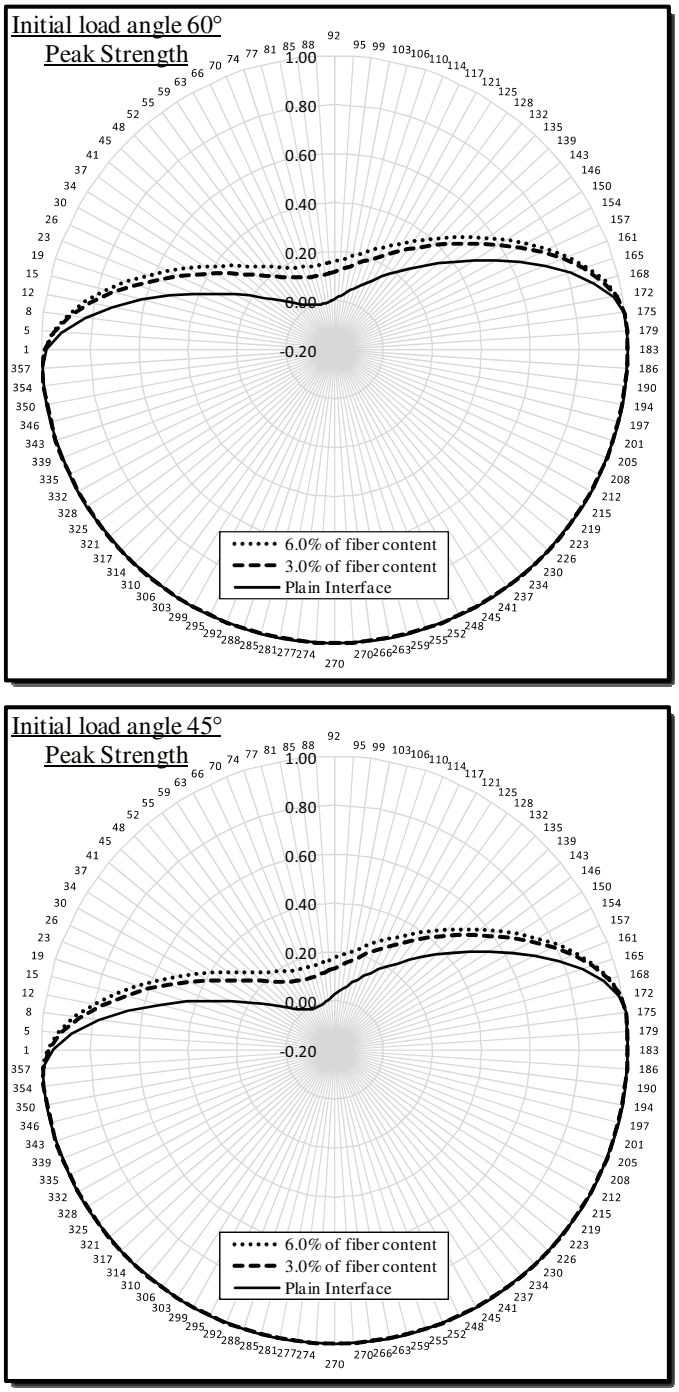

Figure 5.18: Polar plots of post-cracking analysis of TS3 and TS4 for different concrete types: plain concrete and SFRC with "Dramix type I" fibers having fiber contents of 3.0% and 6.0%.

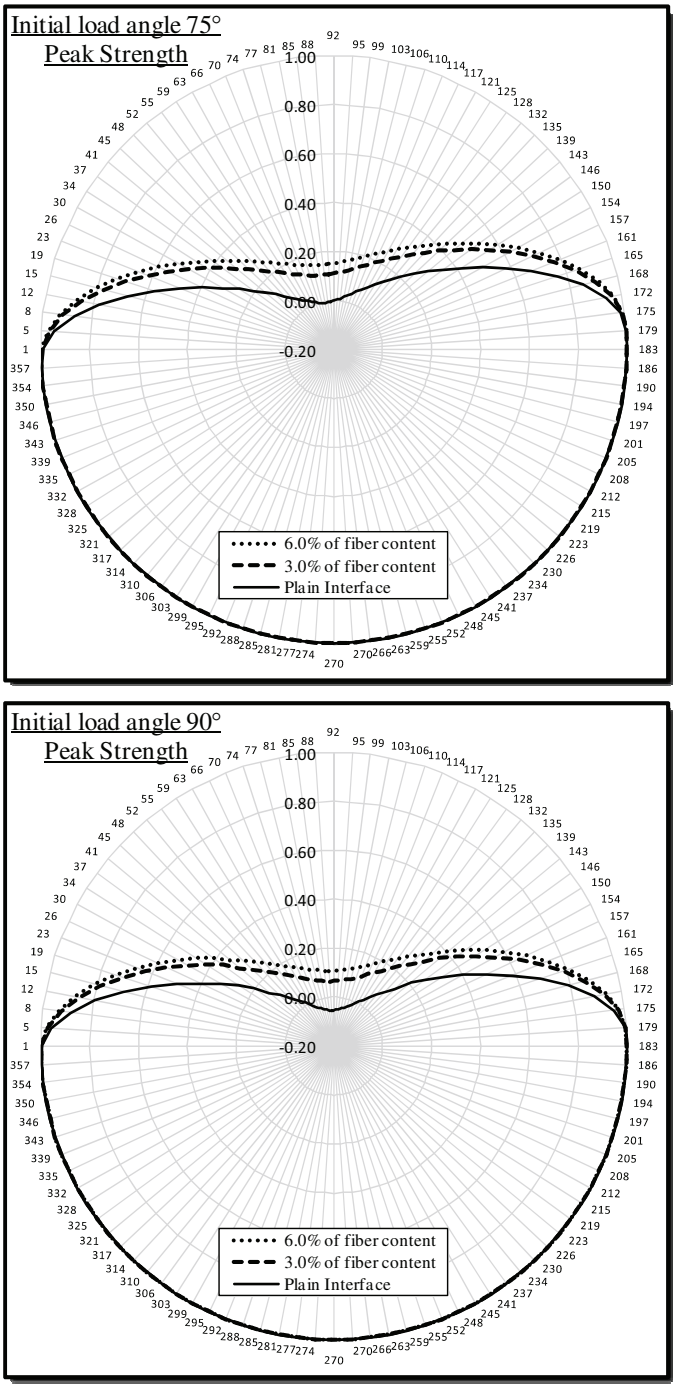

Figure 5.19: Polar plots of post-cracking analysis of TS2 and UT for different concrete types: plain concrete and SFRC with “Dramix type I” fibers having fiber contents of 3.0% and 6.0%.

- Point 6: Tension-Shear (TS6): $\theta = \frac{\pi}{12} = 15°$, $\rho_{cr,PI} = 43.47°$, $\rho_{cr,3.0\%} = 52.85°$ and $\rho_{cr,6.0\%} = 55.73°$;

where the subscript PI indicates the "Plain Interface", while 3.0% and 6.0% outline the fiber percentages.

The following conclusions can be itemized by observing these results:

- The first comment deals with the observation that CI assumes negative values only for plain concrete and, in particular zones, of the ρ angle. Only positive CIs characterize the SFRC specimens (Figure 5.16): this is due to the post-cracking softening response of the unreinforced concrete, whereas the SFRC with 3.0% and 6.0% of fiber contents are charactertized by a post-cracking hardening behavior.
- In the case of UT-test, the angle θ (initial load angle) coincides with ρ_{cr} (angles at which the CI reaches its minimum value) for each type of composite: i.e., plain concrete and SFRCs. Practically, no difference is observed for the weak cracking directions in the considered concretes, resulting $\theta = \rho_{cr} = \frac{\pi}{2}$ for both plain and SFRC with 3.0% and 6.0% of fiber contents.
- The cracking indicator approaches the unity value when the stress increment deals with a pure elastic response of the considered interface law: the polar plot mainly outlines a curve as part of circle with a unitary radius. From a mechanical standpoint, these points represent stress increments in compression/shear states, where the proposed interface model for FRCC mainly behaves in a elastic manner.
- For the different initial load stages ρ, it can be observed that the critical angles ρ_{cr}, at which corresponds the minimum values for the CI parameter, slightly turns toward failure modes I of fracture $\rho_{cr} \longrightarrow \frac{\pi}{2}$ as the fiber concrete increases.
- As a final comment, it can be stated that the influence of the fibers is relevant in all cases, but it is more pronounced in the mixed fracture modes (acting in both CI values and the critical value of the ρ angle) than for the tensile one where only the value of CI is influenced.

5.3 Closing remarks

This chapter proposes the numerical application at the material level (Gauss-point) of the interface model for simulating the cracking behavior of Fiber-Reinforced Cementitious Composites (FRCCs). The proposed formulation of the interface element for

connecting nodes of two adjacent cement matrix elements has been one of the key contributions of this chapter. Thus, the contribution of fibers bridging cracks possibly developing throughout those interfaces has been modeled within the zero-thickness elements, along with the bonding behavior of cement matrix.

Finally, applications of the numerical procedure on both notched specimens tested under mixed fracture modes and FRCC samples in tension demonstrate the soundness of the proposed model and its accuracy in simulating the cracking behavior of fiber-reinforced concrete members. The proposed simulations of experimental tests under several complex stress states highlight the predictive capacity of the proposed interface model to reproduce the mechanical behavior of FRCCs. In particular, the role of fiber content in turning the brittle behavior of plain concrete in tensile regime into a more ductile and even hardening response has accurately been reproduced by the model, after the calibration of the internal mechanical parameters based on experimental results.

6 Structural scale failure analysis of FRCC

Since the interface model formulated in Chapter 3 and further described in Chapter 4 has basically been employed in "material scale" simulations (Chapter 5), this chapter is specifically aimed at demonstrating the potential of using such a model for simulating the "structural scale" response of FRCC members according to the "discontinuous approach" of the Finite Element Method. Particularly, structural problems of Steel Fiber Reinforced Concrete (SFRC) are analyzed at both meso and macroscale levels of observation (e.g., with or without the explicit consideration of the FRCC meso-structure). Both uniaxial tensile and compressive tests, three-points bending specimens and direct shear tests are evaluated with different FRCC qualities in order to analyze the soundness and capabilities of the proposed model.

6.1 Influence of the interface positions at structural scale

In this section, the predictive potential of the interface model for SFRC members is assessed under the following stress states:

- Unixial tensile case;
- Unixial compressive case;
- Direct shear test with free dilatancy (in the normal direction);
- Direct shear test with blocked dilatancy (in the normal direction).

Figure 6.1 reports the 2-D composite geometry and the corresponding structural FE discretization by considering three numerical test models. The continuum elements

are assumed as linear elastic, whereas all non-linearities are lumped within the zero-thickness interfaces defined throughout the adjacent edges of the finite continuous elements. Particularly, the non-linear fracture energy-based law and fiber actions (in terms of both bridging and dowel effects) are considered in those elements according to the formulation outlined in Chapter 3.

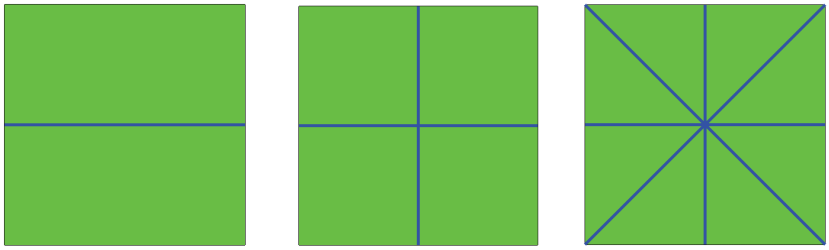

Figure 6.1: FE discretization including the cases of: (a) one, (b) four and (c) eight interfaces.

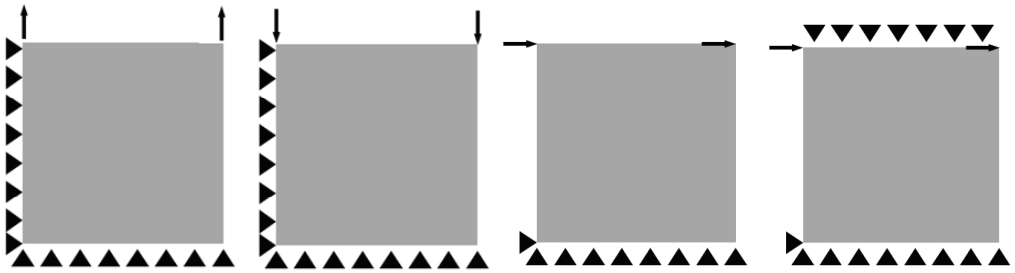

Figure 6.2: Boundary conditions of (a) uniaxial tensile and (b) compressive cases, (c) shear with unconstrained dilatancy and (d) shear with constrained dilatancy.

The simulation of concrete specimens tested as proposed in Figure 6.2a-d is performed in this section. Plane stress hypothesis and displacement-based control are also assumed. For the purpose of the numerical evaluations, three material types are considered:

- plain concrete,
- steel fiber reinforced concrete with fiber percentage $\rho_f = 2.0\%$ and
- with $\rho_f = 5.0\%$.

The same material parameters used for FRC with Dramix steel fiber in tensile problems of the previous Chapter 5 (cfr. section 5.1) are adopted.

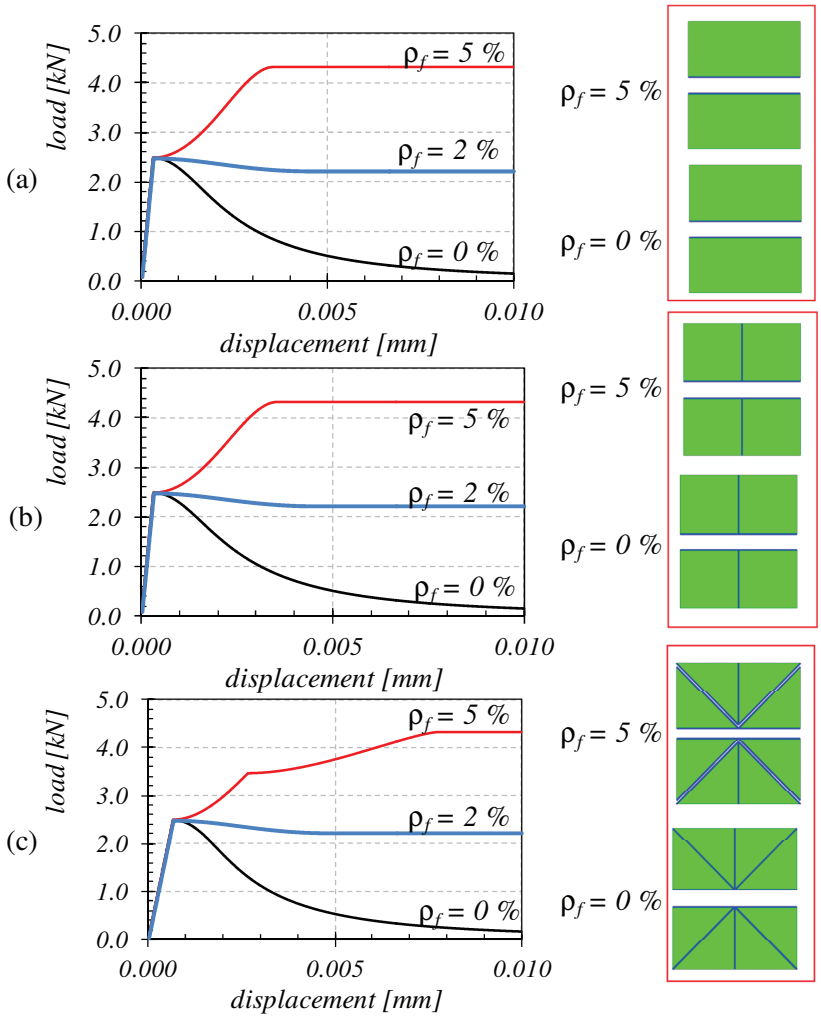

Figure 6.3: Vertical load-displacement behavior of plain concrete and SFRCs under tension (left side) and crack paths (right side).

Figures 6.3-6.6 show the force-displacement curves obtained at the loaded of the numerical models depicted in Figures 6.1 and 6.2. It can be observed that the load-displacement responses on the analyzed concrete composite samples are significantly influenced by fiber reinforcement on both structural strength and post-peak behavior. Fiber bridging effects on cracked concrete are realistically captured by the considered discontinuous-based approach. Actually, the post-peak response of fiber-reinforced concrete is much more ductile than that of plain concrete. Figures 6.3-6.6 also illustrate the cracked configurations at ultimate stages by means of the numerical simulations.

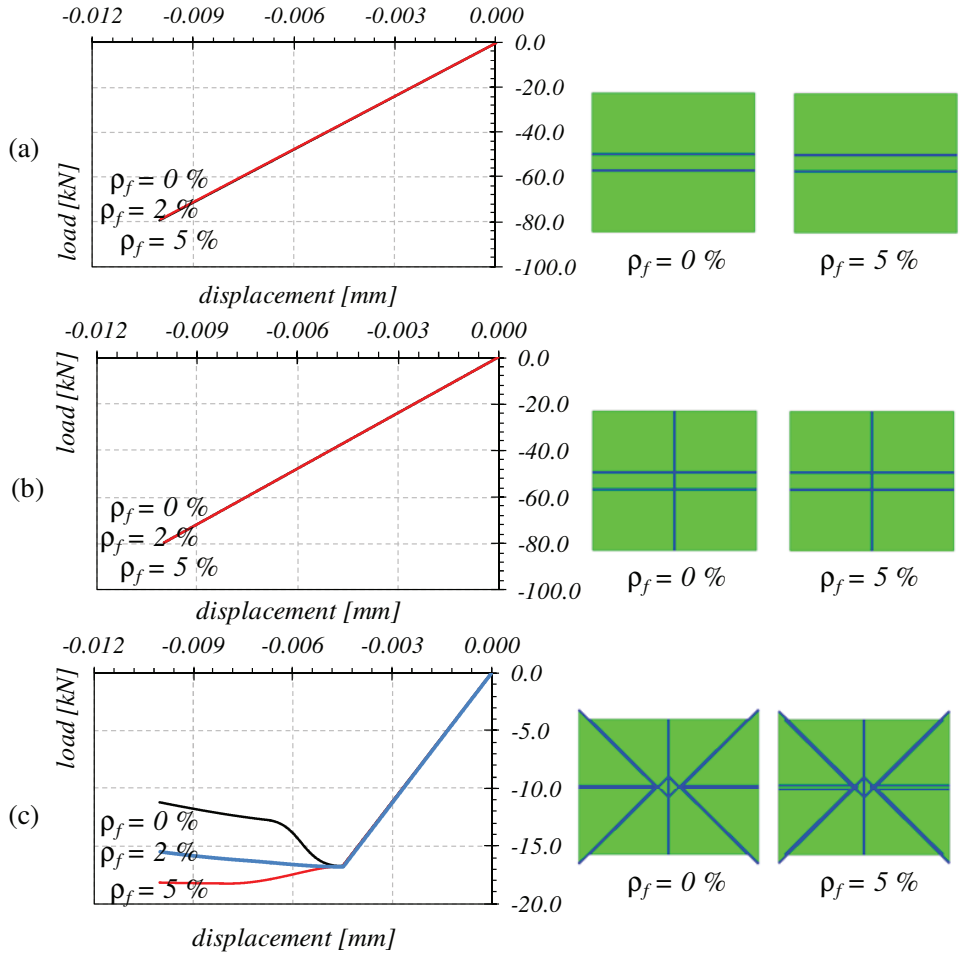

Figure 6.4: Vertical load-displacement behavior of plain concrete and SFRCs under compression (left side) and crack paths (right side).

Figure 6.3 deals with the case of pure tension Figure 6.2a. It can be observed that the same load-displacement responses (but also the same cracked configurations at failure stage) are obtained for both low and medium level of fiber content (i.e., 0% and 2%, respectively). Moreover, the same behavior is obtained for SFRC with 5% and considering the case of one and four interfaces (Figure 6.3a and b). A slight difference can be observed in SFRC with 5% of fiber content and by considering the scheme with eight interfaces. As a matter of result, a more diffuse crack-pattern takes place (right side of the figure) and a slightly different load-displacement response is obtained with a more pronounced crack-hardening behavior.

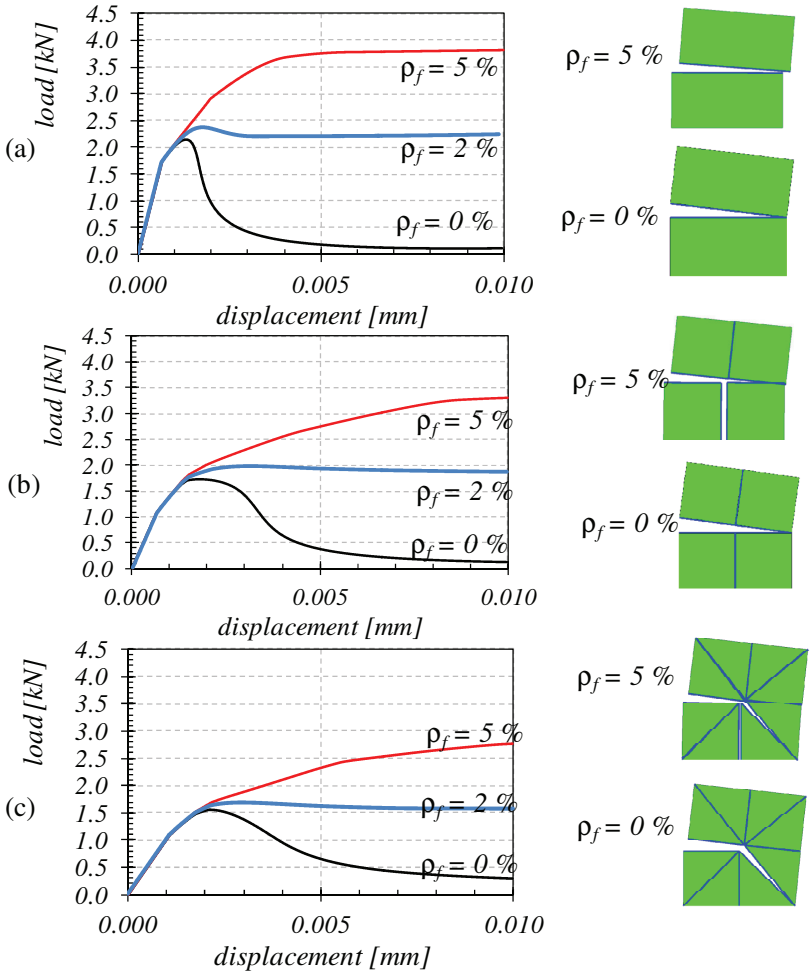

Figure 6.5: Lateral load-displacement behavior of plain concrete and SFRCs in direct shear with free dilatancy in the vertical direction (left side) and crack paths (right side).

Figure 6.4 deals with the simulation of the homogeneous compression. Linear elastic responses are obtained for the one and four interfaces scheme (Figure 6.4a and b). This is reasonable if it is kept in mind that no failure is expected for the proposed interface model under compression (at a Gauss-point level). Regarding the specimens with eight interfaces, it can be observed a structural failure of the numerical probe where the cracks mainly evolve under mixed-modes of fracture and along the inclined interface elements.

Figure 6.5 outlines the results of numerical simulation obtained for the direct shear test whereby vertical displacements at top of the sample are unconstrained (Figure

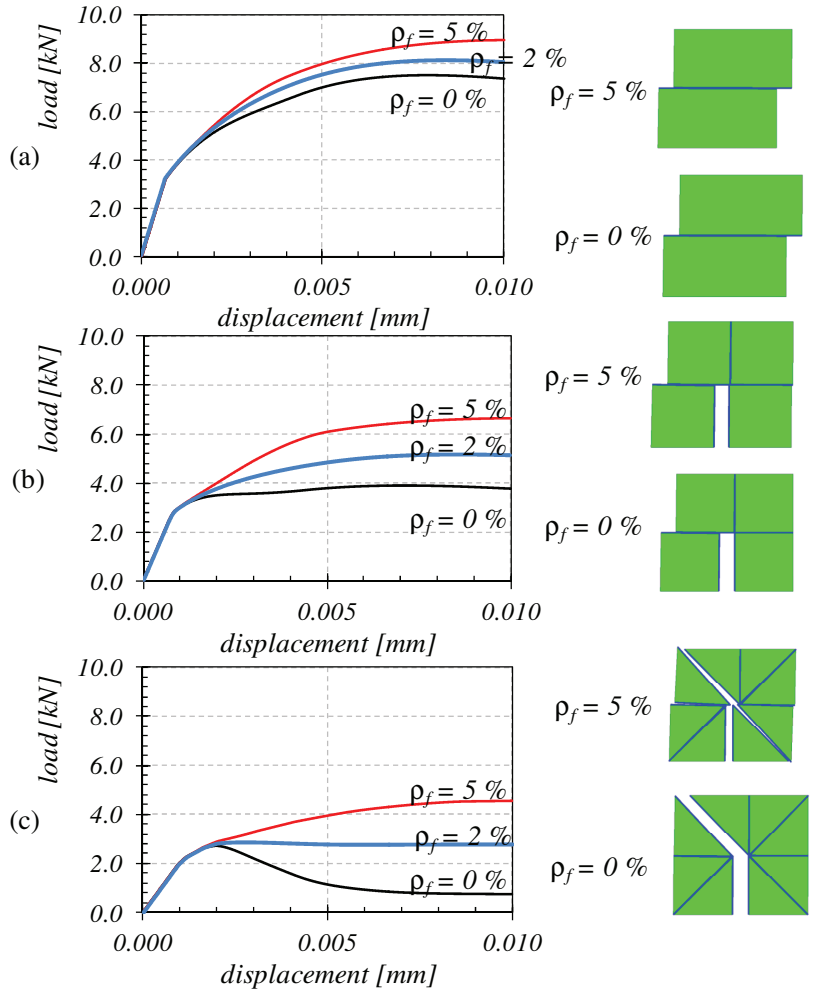

Figure 6.6: Lateral load-displacement behavior of plain concrete and SFRCs in direct shear with blocked dilatancy in the vertical direction (left side) and crack paths (right side).

6.2c). From Figure 6.5a to 6.5c a strength decreases can be recognized for each kind of concrete. Specimens tested under direct shear are characterized by failure condition under mixed (shear/normal) fracture modes. Interface elements inclined with respect to the shear force approach “mode I” type of failure (that represents the weakest failure mode). This is clearly more evident in specimens with four and eight interfaces. This is the main reason why the global structural response in those numerical tests is characterized by lower strengths, due to the activation of closer “pseudo-mode I” of fracture. These comments are also valid for the case of direct shear test in which the vertical displacements are constrained. Moreover, in these tests (Figure 6.6), it can be

also added the comment that, when vertical displacements are blocked compressive vertical actions affect the behavior of samples, due to the fact that the normal dilatancy produced by the applied shear displacements is restrained by the fixed null opening rate. It follows that FRC panels loaded under combined shear and compression reach higher strengths compared to direct shear without vertical constraints.

Finally, it can be stated that all analyzed specimens with steel fiber reinforcements result in a less brittle and possible quasi-ductile behavior, exhibiting strain-hardening processes with multiple cracks and relatively large energy absorption after the peak strength.

6.2 Macroscopic and mesoscopic FE analysis with FRC interfaces: three-point bending tests

In this section, several numerical analyses performed both at macro and mesoscopic scales regarding failure behavior of plain concrete and SFRC members at structural level are presented.

6.2.1 Notched beams under three-point bending at macroscale

To assess the soundness of the proposed non-linear cracking model for interface elements, the results of a plain concrete test on a notched beam under three-point bending are firstly considered (Figure 6.7). Several interface elements are placed between adjacent isoparametric 3-node elements for modeling the fracture process of beams tested under the layout shown in Figure 6.7.

Table 6.1: Material parameters based on the experimental data by Rots et al. [1985].

	Material Parameters		
Interface Elements	$k_N\,[MPa/mm]$ $1.E+06$	$k_T\,[MPa/mm]$ $1.E+06$	$\chi_0\,[MPa]$ 3.3
	$c_0\,[MPa]$ 5.0	$tg\phi_0 = tg\phi_r = tg\beta$ 0.5	$G_f^I\,[N/mm]$ 0.124
	$G_f^{II}\,[N/mm]$ 1.240	$\sigma_{dil}\,[MPa]$ 3.0	α_χ -0.15
Continuum Elements	$E_m\,[MPa]$ (elastic module) 30000.0		ν (Poisson's ratio) 0.2

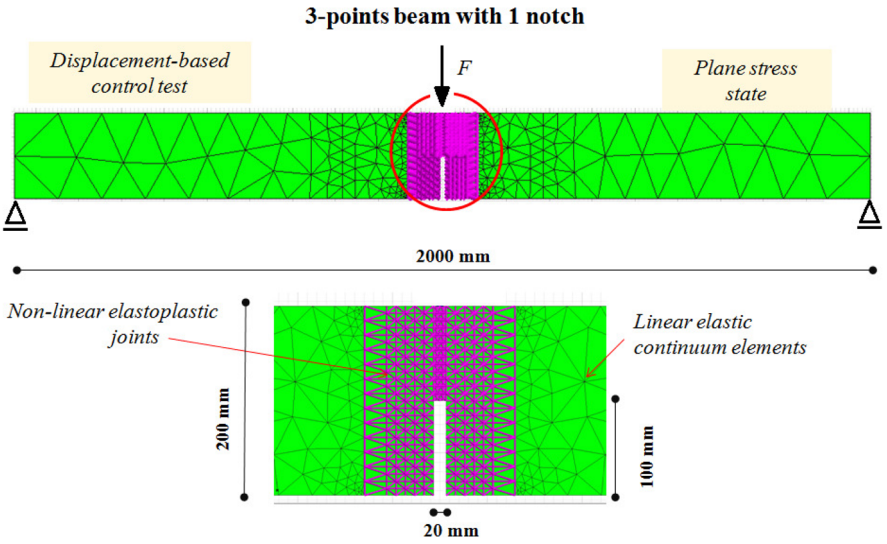

Figure 6.7: Three-point bending test discretization on a notched beam for discrete failure analyses.

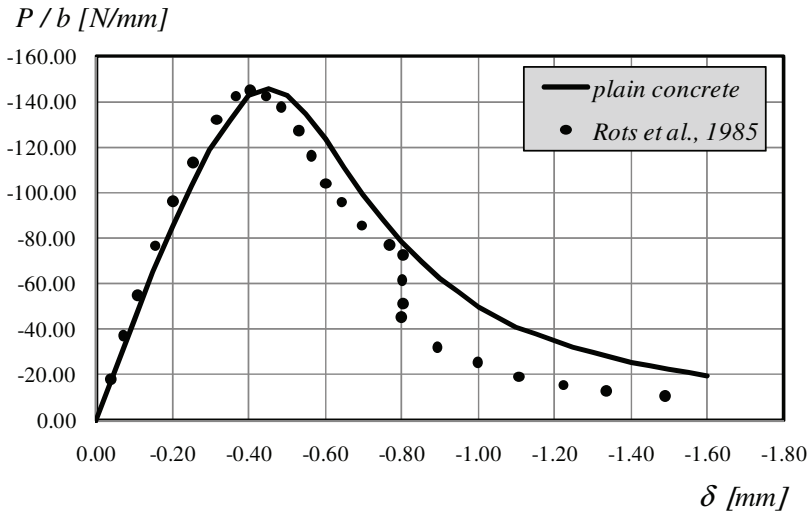

Figure 6.8: Numerical results vs. experimental data by Rots et al. [1985] on a three-point beam.

Plane stress conditions, considering a depth of the beam $b = 50\,mm$ according to the experimental tests by Rots et al. [1985], are imposed in the numerical analyses at the macroscopic level of observation. A test on plain concrete specimens is performed by imposing a homogeneous vertical displacement at mid-length of the considered beam. The results in terms of vertical applied deflection (δ) vs. vertical specific force (P/b) are

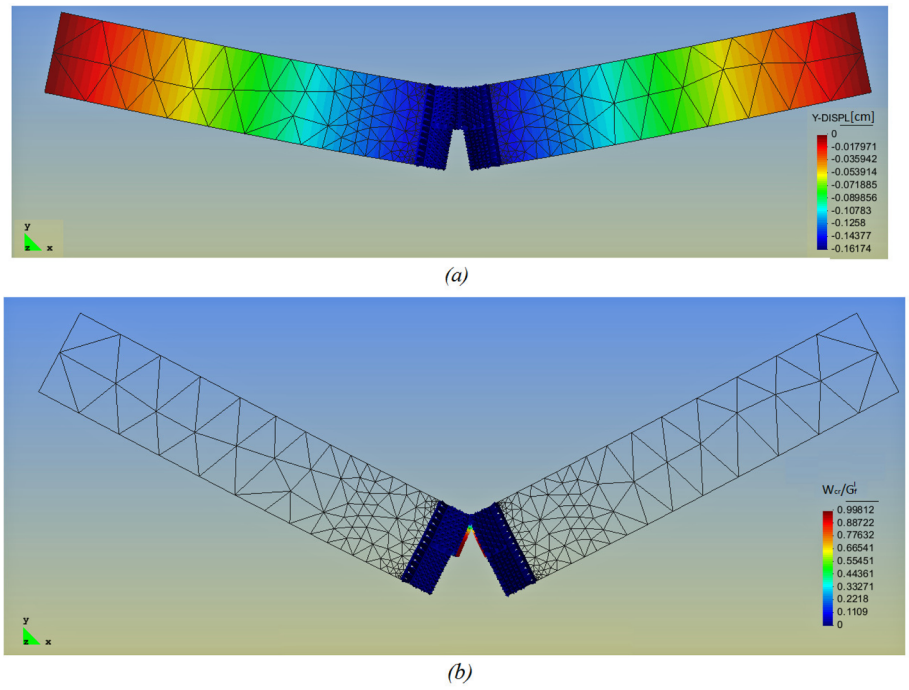

Figure 6.9: Failure configuration in terms of (a) vertical displacement mesh informations and (b) work spent to available energy ratio of w_{cr}/G_f^I.

plotted in Figure 6.8, where the numerical test is compared against the experimental measures obtained by Rots et al. [1985].

The proposed interface model for discrete crack analyses of concrete members leads to accurate simulations of both the peak strength and post-peak behavior. A realistic deformed configuration at failure is also plotted in Figure 6.9, where the mesh results in terms of vertical displacements and in terms of the w_{cr}/G_f^I ratio on the developed crack is represented. Table 6.1 outlines the values of the key parameters related to the analysis of the three-point flexural test presented in this section. The remaining parameters are set to zero in the proposed simulation.

6.2.2 FE analysis of SFRC at mesoscopic scale

In this section, the interface elements for SFRC are employed to obtain a mesoscopic scale simulation in which the aforementioned joints connect continuous elements corresponding to cement mortar and coarse aggregates.

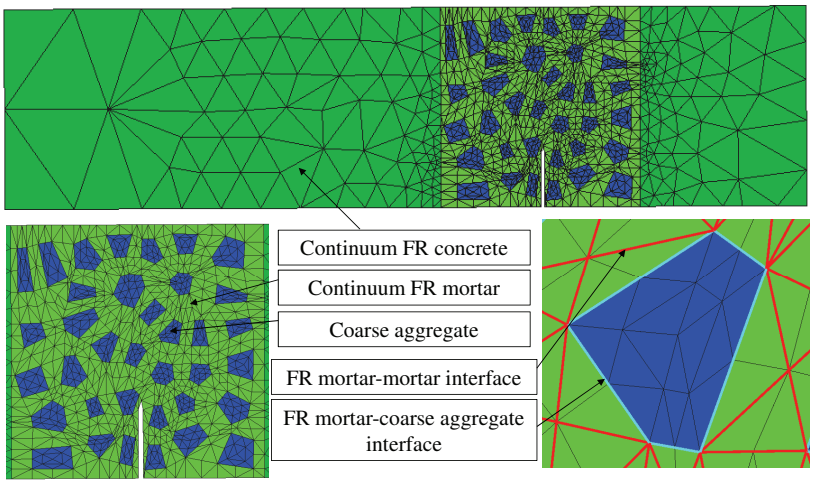

Figure 6.10: FE discretization including Fiber Reinforced concrete and mortar, coarse aggregates and interfaces.

Figure 6.10 shows the 2-D composite geometry and the structural FE discretization employed in the proposed analysis. A convex polygonal representation is adopted for representing the large aggregates. The polygonal geometry is numerically generated though standard Voronoi/Delaunay tessellation [Klein, 1989] from a regular array of points which is slightly perturbed as shown in Figure 6.11. Both the polygonal particles and the space between them (surrounding matrix) are meshed with finite elements for generating the modeling analysis. The continuum elements obtained by means of the above procedure are assumed to be linear elastics, whereas all non-linearities are concentrated within zero-thickness interface elements defined throughout the adjacent edges of the meshed elements. Non-linear fracture energy-based laws and fiber actions (in terms of both bridging and dowel effects) are introduced in those interface elements according to the formulation outlined in Chapter 3. In particular, aggregate-matrix interfaces do not take into account the fiber effects, while mortar-mortar joints consider the contribution of fibers in terms of bridging and dowel effects.

As can be seen in Figure 6.10, the mesoscopic discretization of the central notched portion of the beam takes into consideration three phases: (i) coarse aggregate, (ii) fiber reinforced mortar and (iii) interfaces. The zones with macroscopic discretizations of the beam include linear elastic elements representing the behavior of the fiber reinforced concrete located there. The elastic properties of all continuous finite elements are defined according to the “Mixture Theory” mentioned in Chapter 3. Thus, all the

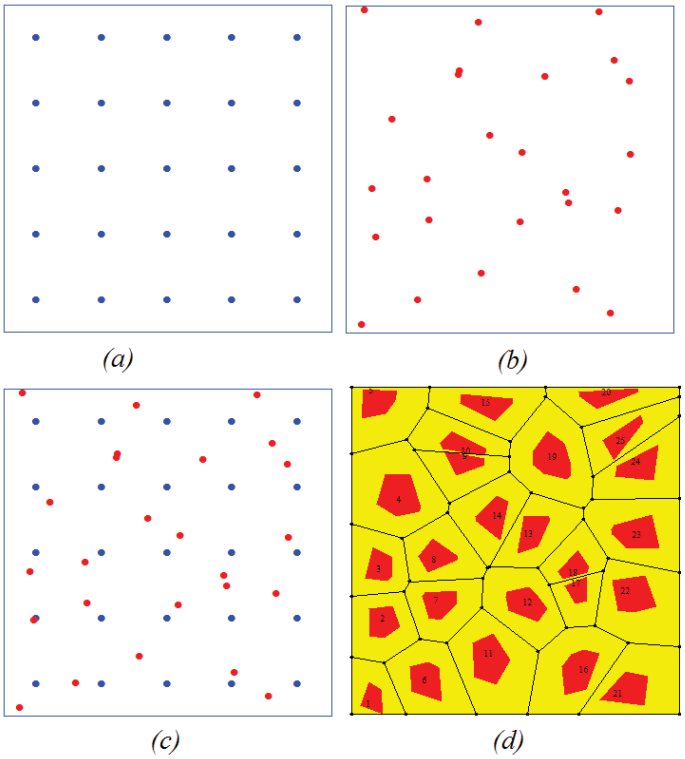

Figure 6.11: (a) Initial regular 2D distribution, (b) randomly perturbed positions, (c) superposition of the points and (d) Voronoi/Delaunay tessellation.

corresponding elastic parameters are defined as follows

$$p_c = \rho_A p_A + \rho_M p_M + \rho_F p_F \tag{6.1}$$

being p_c the parameter under consideration, ρ_A, ρ_M and ρ_F are the volume fractions of the coarse aggregates, matrix and fibers, respectively, while p_A, p_M and p_F are the elastic parameters of each composite component.

The simulation of $50 \times 100 \times 400\ mm^3$ pre-cracked concrete specimens tested under three-point bending by Carpinteri and Brighenti [2010] is reported in this section. Plane stress hypothesis and displacement-based control are assumed.

The specimens present a vertical notch ($2.0\,mm$ wide) at the bottom of the beam characterized by a depth of about $33\ mm$. The distance between the mid-length of the beam and the notch position varies from zero (pre-cracked beam with centrical notch as in Figure 6.12a) to $0.25l$ (pre-cracked beam with eccentrical notch as in Figure

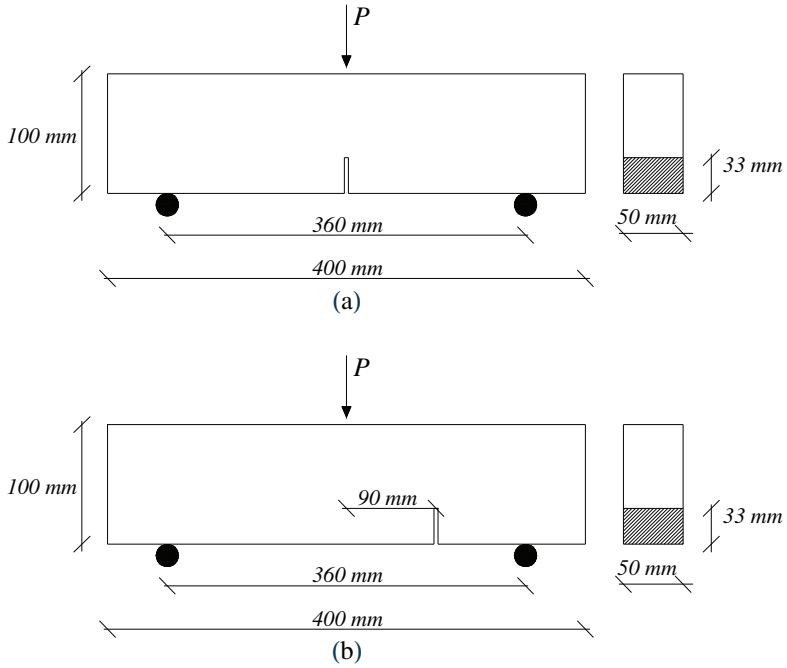

Figure 6.12: Geometry and boundary conditions of the three-point bending problem of fiber reinforced concrete beam according to Carpinteri and Brighenti [2010].

6.12b), being $l = 360\,mm$ the distance between the beam-end supports.

The mesoscopic discretization in the notched zone of the beam allows a better simulation of the crack evolution. This explicit mesoscopic mesh is achieved by means of the Voronoi/Delaunay theories [Lopez, 1999]. It includes 36 coarse aggregates embedded in a matrix representing both fiber reinforced mortar and small aggregates. As previously indicated, two families of interfaces are considered (see Figure 6.10):

- interfaces between coarse aggregate and fiber-reinforced concrete;
- interfaces in between fiber-reinforced cementitious mortar.

Three material types are considered:

- plain concrete,
- steel fiber reinforced concrete with fiber content $\rho_f = 0.25\%$ and
- the same as the previous SFRC but $\rho_f = 0.50\%$.

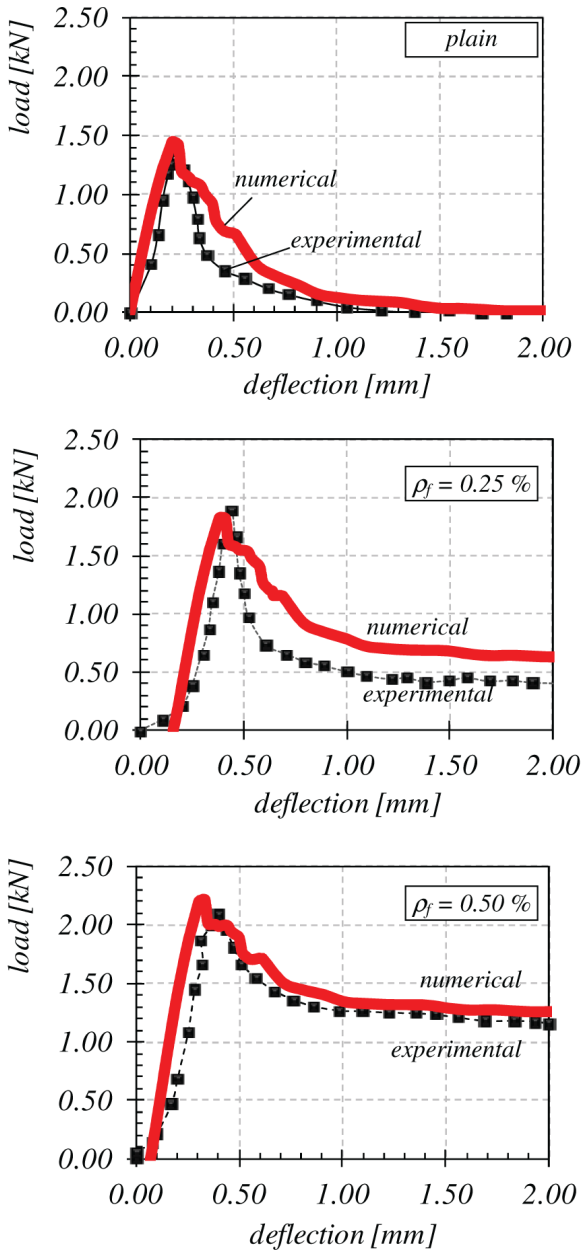

Figure 6.13: Load-deflection behavior of three-point beam with central notch: numerical simulation vs. experimental results by Carpinteri and Brighenti [2010].

The geometry and material properties are chosen according to the tests by Carpinteri and Brighenti [2010]. The mechanical parameters employed in the numerical evaluations are summarized in Table 6.2.

Figure 6.14: Crack paths of plain concrete and SFRC under three-point bending with centrical notch by Carpinteri and Brighenti [2010].

Table 6.2: Material parameters employed in the mesoscale analyses.

Continuum Aggregates	ρ_A	$E_A\,[GPa]$	ν_A	
	28%	60.00	0.20	
Continuum Mortars	ρ_M	$E_M\,[GPa]$	ν_M	
	72%	19.15	0.20	
Continuum Fibers	ρ_F		$E_F\,[MPa]$	ν_F
	$0-0.25\%-0.50\%$		200.00	0.30
Aggregate – Matrix Interface	$k_N\,[MPa/mm]$	$k_T\,[MPa/mm]$		$\chi_0\,[MPa]$
	$1.E+06$	$1.E+06$		2.4
	$c_0\,[MPa]$	$tg\phi_0 - tg\phi_r - tg\beta$		$G_f^I\,[N/mm]$
	4.8	$0.4-0.1-0.3$		0.120
	$G_f^{II}\,[N/mm]$	$\sigma_{dil}\,[MPa]$		α_χ
	1.200	10.0		-0.15
SFRC – SFRC Interface	$k_N\,[MPa/mm]$	$k_T\,[MPa/mm]$		$\chi_0\,[MPa]$
	$1.E+06$	$1.E+06$		3.2
	$c_0\,[MPa]$	$tg\phi_0 = tg\phi_r = tg\beta$		$G_f^I\,[N/mm]$
	5.6	$0.5-0.2-0.4$		0.200
	$G_f^{II}\,[N/mm]$	$\sigma_{dil}\,[MPa]$		α_χ
	2.000	10.0		-0.15
Fiber Bond – Slip	$\tau_{y,a}\,[MPa]$	$k_E\,[MPa/mm]$	$k_S\,[MPa/mm]$	$l_f\,[mm]$
	6.95	100.0	0.1	44.0
Fiber Dowel	k_{dow}	$d_f\,[mm]$	$f_c{}'\,[MPa]$	$\sigma_{y,s}\,[MPa]$
	2.8	0.98	40.0	800.0

Figures 6.14 and 6.16 illustrate the cracked configurations at ultimate stages as obtained in the experimental tests by Carpinteri and Brighenti [2010] and in the numerical simulations. In both cases, failure process leads to only one macro-crack, starting at

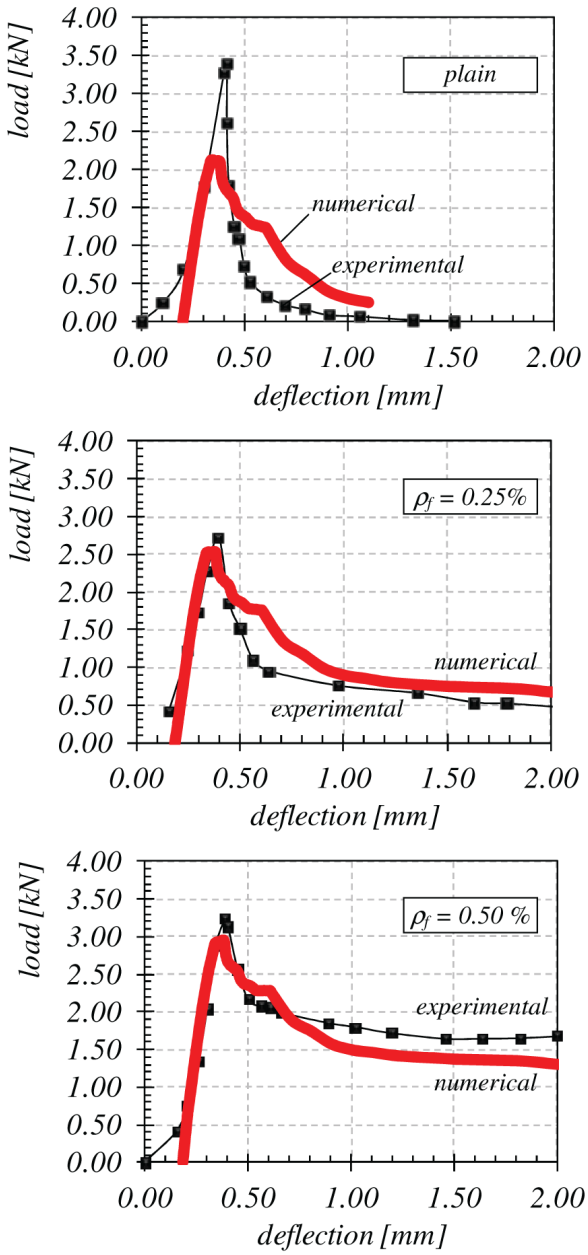

Figure 6.15: Load-deflection behavior of plain concrete and SFRC three point beams with eccentrical notch: comparison between numerical and experimental results [Carpinteri and Brighenti, 2010].

the top of the notch. Regarding the specimens with pre-fixed notch at mid-length of

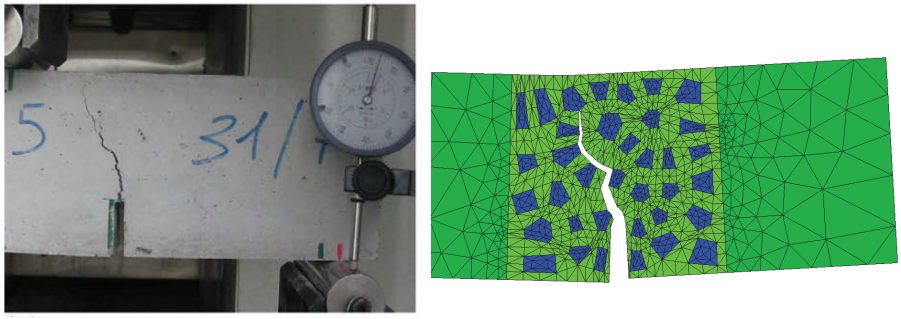

Figure 6.16: Crack paths of plain concrete and SFRC three-point beams with eccentrical notch at $0.25l$ (distance between the mid-length of the beam and the notch position) by Carpinteri and Brighenti [2010].

the beams, it can be observed that the crack evolves in an almost vertical direction (mode I type of fracture), while an inclined crack path (mixed mode of fracture) can be observed in case of eccentrical notch. Furthermore, Figures 6.14 and 6.16 outline that the crack evolves along aggregate-matrix interfaces, which represent in fact the weakest joints in concrete composites. The numerical results confirm the predictive capacity of the interface formulation for SFRC regarding both failure behavior and failure modes.

Figures 6.13 and 6.15 show the force-deflection curves against the corresponding experimental results. The load-displacement responses of plain concrete and SFRC beams emphasize the significant influence of the fiber reinforcement on the peak strength and the post-peak behavior. The fiber bridging effect on cracked concrete is well captured by the considered meso-mechanical approach with non-linear joint models in all mortar-mortar and mortar-aggregate interfaces. The post-peak response of fiber-reinforced concrete is much more ductile than that of plain concrete.

The comparative experimental and numerical results of the load-deflection behaviors of beams with central and eccentrical notch show an increment of the peak load in the last case. Actually, this fact mainly occurs because the weakened cross section (pre-notched zone) in case of the beam with eccentrical notch, does not coincide with the section with maximum bending moment. However, this effect is also due to the frictional behavior of the concrete material along the fracture that is realistically captured by the proposed model formulation.

6.3 Meso- and macroscopic FE Analysis with FRC Interfaces: Compressive Test

This section is intended to comparatively analyze the effect of different variables such as the adopted geometry and discretization of Boundary Value Problems related to SFRC test under compression. In the first case, cracking propagation is described at the meso-level through the proposed meso-mechanical approach already employed in the previous section using fracture energy-based zero-thickness interfaces. Then, in the second case, the SFRC specimens are discretized without its explicit mesoscopic structure in a macroscopic approach.

6.3.1 Compressive Test at mesoscopic level

The 2-D $10 \times 10\ cm^2$ concrete specimen with 6×6 arrangements of aggregates, proposed by Lopez [1999] (whose average size is of about $15\ mm$), is employed. The reference geometry and mesh for the SFRC sample is reported in Figure 6.17. Interface elements connecting matrix-aggregate and matrix-matrix continuum elements are highlighted by thicker lines in Figure 6.17c. Iso-parametric triangular continuum elements (Figure 6.17b) between interfaces are assumed with linear elastic behavior.

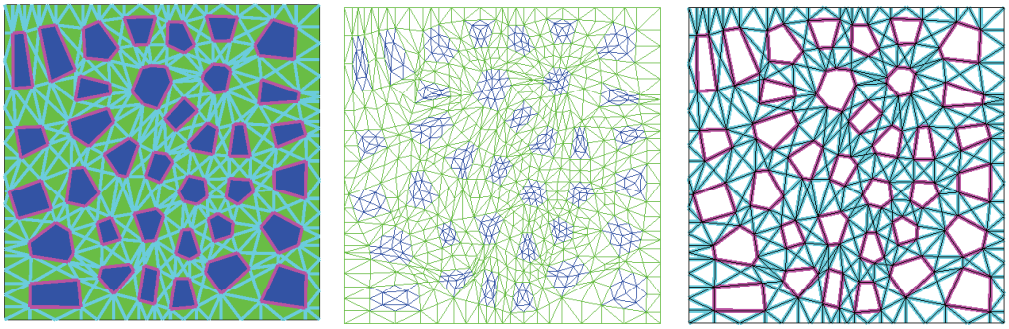

(a) (b) (c)

Figure 6.17: 2-D FE discretization for concrete specimens with 6×6 aggregates: (a) geometry, (b) continuum elements and (c) interfaces.

The numerical specimen proposed in Figure 6.17 is subjected to uniaxial compression along the $y-$ vertical axis. Displacement-based control is prescribed to all nodes of the upper and bottom faces of the specimen. In particular, fixed values equal to zero are imposed to the bottom nodes, while progressively increasing negative values for the upper ones. Horizontal displacements are not restrained, except for the node at the bottom left corner of the mesh, where such displacements are fully restrained. Nodes

at left and right sides are free of applied loads and displacements. Finally, plane stress conditions are considered in these analyses.

Three material types are considered:

- plain concrete,
- SFRC with fiber content $\rho_f = 1.0\%$ and
- SFRC having $\rho_f = 5.0\%$.

The material parameters used for the interface models are listed below:

- Matrix-to-coarse aggregate interfaces: $\chi_0 = 2.0\,MPa$, $c_0 = 4.0\,MPa$, $G_f^I = 0.06\,N/mm$ and $G_f^{IIa} = 0.6\,N/mm$.
- SFRC matrix-matrix interfaces: $\chi_0 = 2.5\,MPa$, $c_0 = 5.0\,MPa$, $G_f^I = 0.10\,N/mm$ and $G_f^{IIa} = 1.0\,N/mm$.

Then, the missing model parameters for the interfaces and continuous elements are the same to the ones employed in the mesoscale discretization interesting the notch region of Figure 6.10.

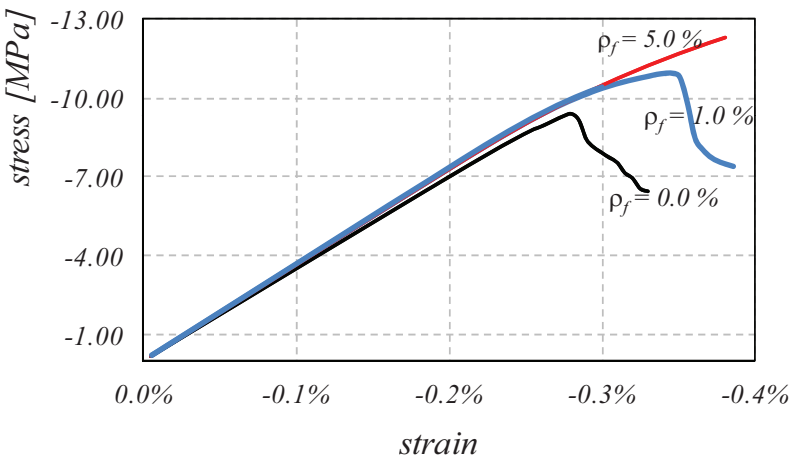

Figure 6.18: Results in uniaxial compression.

The obtained results are shown in Figure 6.18 where compressive stresses vs. vertical strains are depicted and compared. The average stress is measured by summing nodal

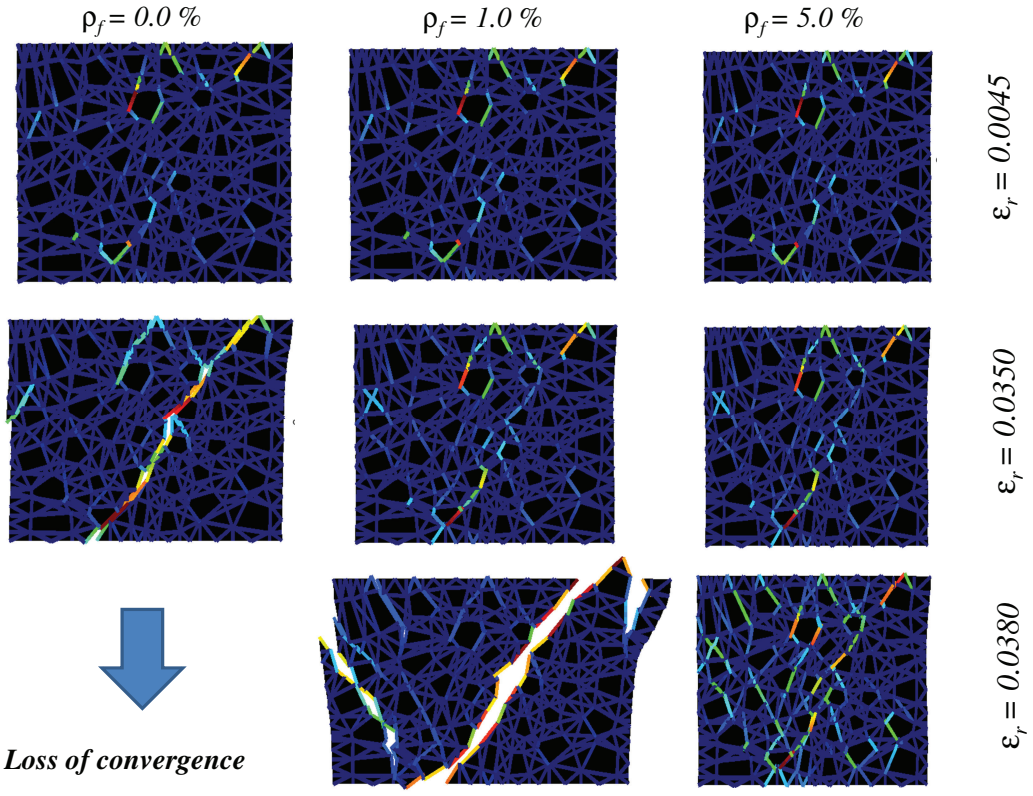

Figure 6.19: Sequence of micro- and macrocracks at various loading stages.

reactions and dividing it by the cross section of the specimen, while the mean strain is intended as the ratio between the vertical displacement and the specimen height.

Besides the quite low strength obtained for all mixes (possibly due to various factors, such as the assumption of plane stress conditions far away from the correct modeling of a cube under compression, the adoption of homogeneous compression, but also the fact that no particular calibration is performed for the assumed material parameters), the mentioned curves qualitatively predict behaviors quite similar to the experimental ones. As it can be observed the peak load is followed by a brittle post-peak response for the plain concrete specimen, while a clear enhanced post-cracking behavior in terms of peak strength and toughness is obtained for the SFRCs, specially for the mix with higher content of steel fibers.

The sequence of crack formed in the various loading stages is reported in Figure 6.19. The interface in red represents the joints in which a mayor plastic work is spent, while

the one in blue outlines the interface in elastic regime (either in loading or unloading stages). The cracked shape of the mesh at various strain stages is also represented: i.e., at $\epsilon = 0.0045$, $\epsilon = 0.0350$ and $\epsilon = 0.0380$.

It can be observed that for plain concrete at fully localized (and ultimate) state ($\epsilon = 0.0350$), one localized and inclined band develops: it divides the specimen into two blocks. The ultimate state for the SFRC with $\rho_f = 1.0\%$ (attained with the strain $\epsilon = 0.0350$) is characterized by two inclined macro-cracks, which split the tests in three parts. Then, when a very high fiber content is considered (SFRC with $\rho_f = 5.0\%$), a remarkable strain-hardening behavior is obtained and a deformed mesh with very diffuse micro-crackings can be clearly observed in the right side of Figure 6.19.

6.3.2 Compressive test at macroscopic scale

The concrete panel with the geometry of $9 \times 12\ cm^2$ (base and height, respectively) is considered in the analyses proposed in this section. The considered mesh for the analyzed SFRC specimen is detailed in Figure 6.20. Iso-parametric triangular continuum elements (Figure 6.20a) are assumed as linear elastics. Then, interface elements inserted between those continuum triangles are highlighted by thicker lines of Figure 6.20b.

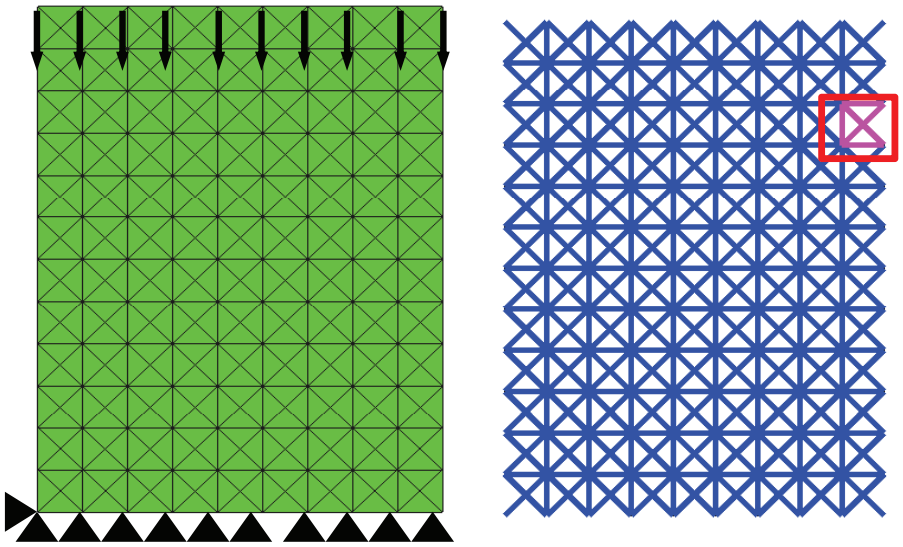

(a) (b)

Figure 6.20: 2-D FE discretization for concrete specimens at macro-level: (a) continuum elements and (b) interfaces.

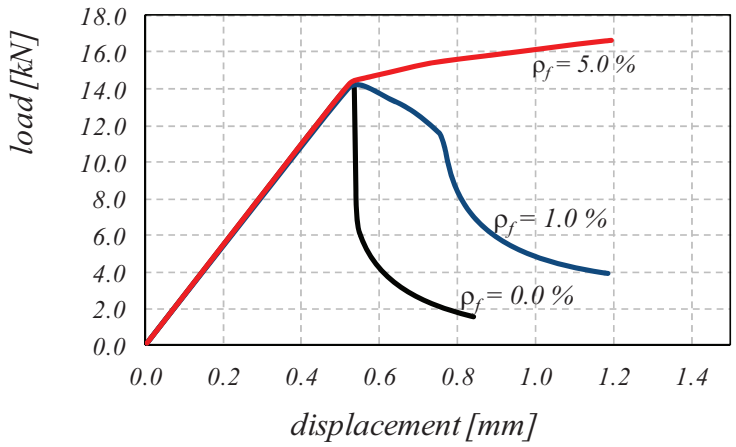

Figure 6.21: Results in uniaxial compression.

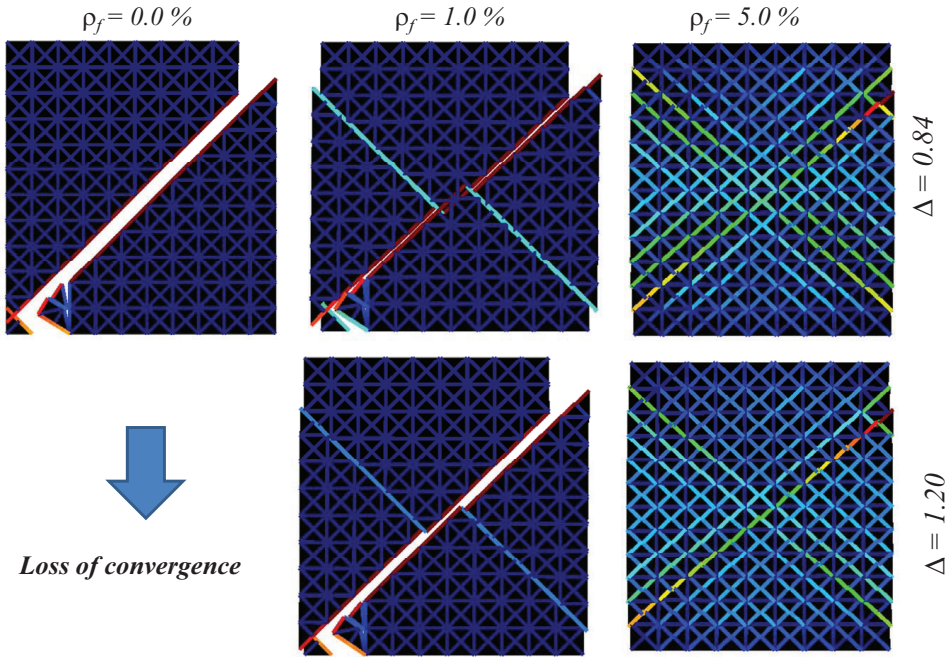

Figure 6.22: Sequence of micro- and macrocracks at various loading stages.

The numerical model depicted in Figure 6.20 is analyzed under a uniaxial compression along the $y-$ vertical axis. Particularly, displacements are imposed to all the nodes of the upper face, while the bottom nodes are restrained in the $y-$ direction. Moreover, the bottom left node is restrained against horizontal displacement. Nodes at left and right sides are free of any constraint. At last, 2-D plane stress conditions are considered

for these analyses.

Three material types are again considered similarly to the previous subsection: (i) plain concrete, (ii) SFRC with fiber content $\rho_f = 1.0\%$ and (iii) SFRC with $\rho_f = 5.0\%$. Moreover, the material parameters used for both continuum and interface materials and referred to the same employed in subsection 6.3.1 . Furthermore, the model parameters of seven interfaces, highlighted in the upper right corner of Figure 6.20b, are pre-degraded of 10% on they strengths (i.e., in terms of tensile and cohesive parameters of the plain interface model, as well as in terms of bond and dowel strengths).

The compressive force vs. vertical displacement are shown and compared for each kind of analyzed concrete in Figure 6.21. The curves proposed clearly remark the influence of the steel fibers on the global structural behavior of the numerical specimens. Particularly, a very brittle response in post-peak regime can be observed for the plain concrete. Whereas, the enhanced post-cracking behavior and toughness are recognized for the SFRCs with $\rho_f = 1.0\%$. Finally, a pronounced crack-hardening response interests the sample with high values of fiber percentage ($\rho_f = 5.0\%$).

As in subsection 6.3.1 the sequence of the crack pattern at various loading stages is reported in Figure 6.22. Particularly, the joint elements characterized by the red color represent the ones in which a mayor plastic work are dissipated, while the interfaces in blue are in the elastic range (either in loading or unloading). Figure 6.22 represents the cracked configuration of the mesh, at two displacement (Δ) stages: i.e., $\Delta = 0.84\,mm$ and $\Delta = 1.20\,mm$.

The following observations can be finally highlighted:

- plain concrete specimen is characterized, at ultimate state ($\Delta = 0.84\,mm$), by a strong localized and inclined band, which separates the specimen in two blocks;
- the ultimate state reported in Figure 6.22 for the SFRC with $\rho_f = 1.0\%$ at the displacement value $\Delta = 1.20\,mm$ defines a cracked pattern in which two inclined macro-cracks develop throughout the concrete sample;
- very high percentage of fibers leads to a more distributed crack pattern ($\rho_f = 5.0\%$).

The results are in full agreement with the fact that SFRC with an high fiber content reproduces a very high ductile response, with a remarkable strain-hardening behavior in terms of $F - \Delta$ curve. Figure 6.22 shows the very diffuse micro-cracks for the SFRC

with $\rho_f = 1.0\%$ (only microcraks appear into the specimen) confirming the soundness and capability of the proposed procedure.

6.4 Macroscopic FE analysis of shear test on SFRC

In this section the shear test on plain and steel reinforced mortar specimens is considered. The model considered with this aim is represented in Figure 6.23. The same material parameters assumed in subsection 6.2.2 are considered in the following.

The main purpose of these analyses is to evaluate the capability of the proposed interface element to predict the failure behavior of steel fiber reinforced mortar panels at the macroscopic level of observation when different fiber contents are considered. Non-linear interfaces are included along all contact lines between continuum finite elements in the macroscopic discretization of the mortar specimen. To assure appropriate transmission of the boundary conditions to the mortar specimen, the FE model includes not only the upper and lower shear frames but also a metallic shear box (Figure 6.23).

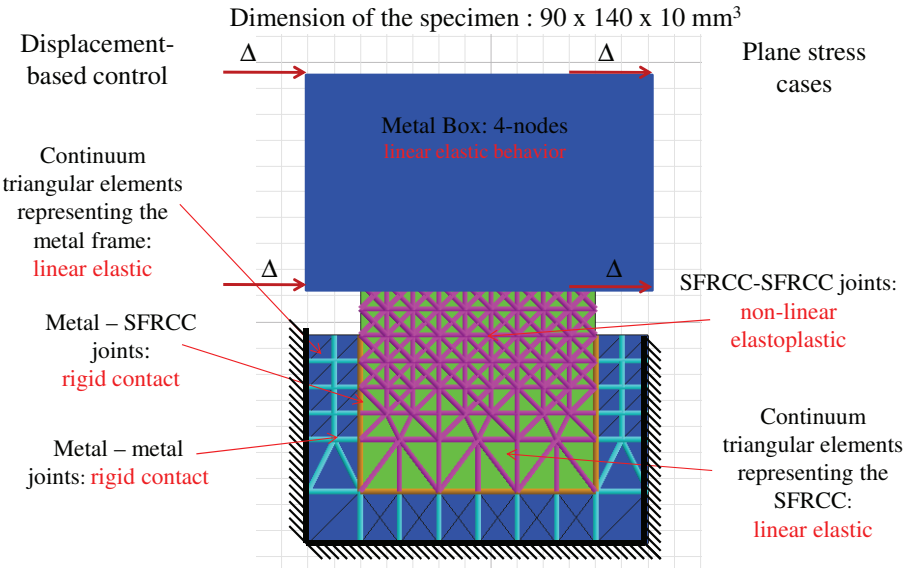

Figure 6.23: Geometry, boundary conditions and discretization of the shear tests on plain and steel reinforced mortar specimens.

Figure 6.24 shows the numerical predictions of the tangential load-displacement behavior corresponding to specimens with different fiber contents and including the plain concrete case as reference. The increase in strength, ductility and post-peak residual

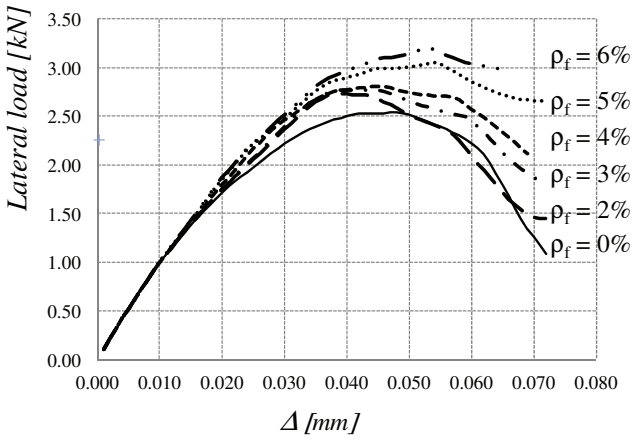

Figure 6.24: Numerical simulations dealing with the lateral load vs. lateral displacements of the shear tests.

strength with the fiber content is clear, while (as expected) the initial stiffness remains constant.

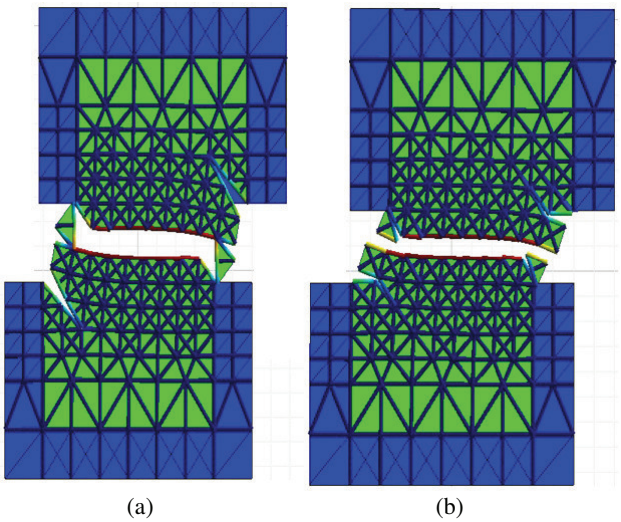

Figure 6.25: Final pattern of the (a) plain mortar and (b) steel fiber reinforced mortar (ρ_f = 6.0% fiber content) specimens after the numerical analyses with the shear box.

It is very interesting to compare the cracked configuration at final stage corresponding to the plain and ρ_f = 6.0% fiber content mortar specimens as shown in Figure 6.25. The plain mortar specimen shows a strong localization of failure in one inclined crack, normally oriented to the resulting tensile force, and followed by another, horizontal

crack in the middle of specimen. In the SFRC two inclined and less pronounced cracks can be recognized which are followed by the same horizontally oriented crack in the middle of the specimen.

These results demonstrate the phenomenological capabilities of the interface model to reproduce failure processes of SFRC, when it is applied in FE discretizations along all the element interfaces. Experimental studies are currently not available in literature to verify the numerical-to-experimental soundness of the proposed shear test simulation. However, the non-linear model is able to provide realistic results and to reproduce the influence of the fiber content on the overall composite mechanical response.

6.5 Closing remarks

In this chapter the predictive capabilities of a discontinuous approach for finite element failure analyses of steel fiber reinforced cementitious composite have been assessed at different levels of observation. The discrete crack formulation, whose constitutive formulation has been described in the previous chapters, has been employed to simulate the fracture behavior of SFRC at mesoscopic and macroscopic levels of analysis. The numerical results in this chapter demonstrate that the discontinuous approach based on non-linear interface formulation leads to realistic predictions of failure processes of SFRC under different load scenarios and considering a wide spectrum of stress states. The interfaces provide accurate results of failure behaviors when they have been considered both in mesoscopic and macroscopic FE discretizations of concrete and mortar components. The model is able to capture the significant influence of the steel fiber content on the structural peak strength and post-peak ductility in mode I and mixed-modes of failure.

7 Cracked hinge numerical model for fiber-reinforced concrete

Although the results reported in Chapter 6 clearly highlight the high predictive potential of such a meso-mechanical approach, it should be aware that it requires a significant computational effort. Therefore, a simpler and more practice-oriented model is presented in this chapter to take into account the fiber-matrix interactions, though within the framework of a "cracked-hinge" approach, which appears as a more feasible method to perform "structural scale" simulations fo FRCC members. The bridging effect of fibers in FRCC is introduced by means of the interface formulation proposed in Chapter 3, to obtain a meso-mechanical interpolation of the complex interactions actually developing between fibers and matrix.

Section 7.1 outlines the basic assumptions of the possible lumped-plasticity method, above mentioned, for simulating the observed post-cracking behavior of SFRC specimens presented in Chapter 2. In section 7.2 the bridging effects induced by fibers crossing the fracture surfaces in terms of bond-slip mechanisms is described. Then, section 7.3 reports the dowel action resulting in a shear transfer mechanism of steel fibers crossing cracks. Both models are briefly described while the complete description can be founded in Chapter 3 and 4. Comparisons between experimental data and numerical predictions are presented and discussed in section 7.4. Finally, some conclusions are highlighted in section 7.5.

7.1 Basic assumptions

The model formulation outlined in this section is based on an idea original proposed by Olesen [2001] where a nonlinear cracked hinge model has been developed with the aim to analysis the bending fracture behavior of fiber-reinforced concrete beams. Similar

proposals for simulating the fracture behavior of both plain and SFRC members have been proposed in literature a.o. by Zhang and Li [2004], Oh et al. [2007], Walter and Olesen [2008], Park et al. [2010], Buratti et al. [2011].

According to the fictitious crack method [Olesen, 2001], the following stress-strain and stress-crack opening relationships can be written in the notched section of Figure 7.1

$$\sigma_{SFRC} = E \cdot \varepsilon \tag{7.1}$$

$$\sigma_{SFRC} = \sigma\left[u_{cr}\right] + \sum_{f=0}^{n_f} \left[\sigma_f\left[u_{N,cr}\right] n_{N,f} + \tau_f\left[u_{T,cr}\right] n_{T,f}\right] \tag{7.2}$$

being σ_{SFRC} the stress of the considered cementitious composite, E the concrete elastic modulus, ε the elastic strain and $\sigma\left[u_{cr}\right]$ the stress-crack opening law of the plain concrete; σ_f and τ_f mean the bond-slip and dowel actions of the single considered reinforcement which are related to axial and tangential cracking displacements, $u_{N,cr}$ and $u_{T,cr}$ at fiber level, respectively (Figure 7.2). Moreover, $n_{N,f}$ and $n_{T,f}$ are the cosine directors of fiber for its normal and tangential direction, respectively. Finally, n_f represents the number of fibers crossing the analyzed strip in the crack section, considering, for simplicity, that each generic fiber crosses the fracture line at its mid-length, $l_{emb} = l_f/2$.

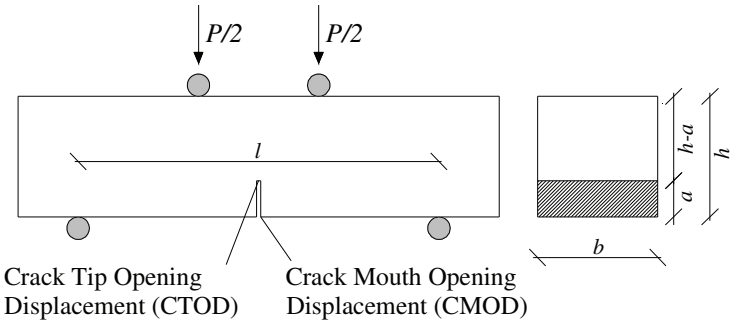

Figure 7.1: Geometrical description of the analyzed four-point bending scheme.

As a matter of principle, Eq. (7.2) is the same one proposed for the interface formulation in Chapter 3 (to see Eq. 3.2) that has also been employed in more general finite element models in Chapter 6.

The considered cosine directors for each fiber, given in Eq. (7.2), are finally based on

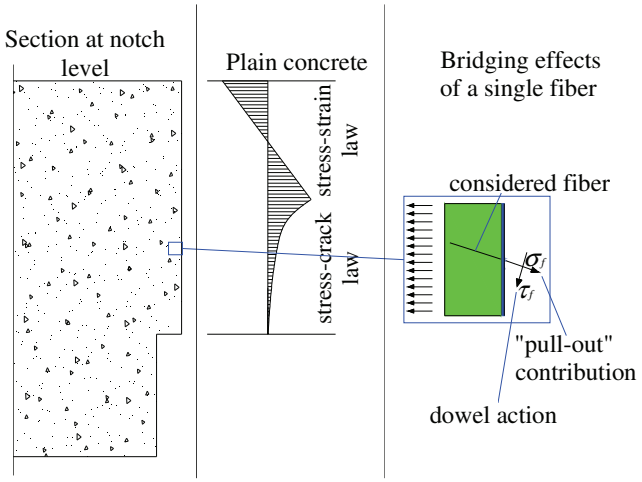

Figure 7.2: Stress distributions and fiber actions during the crack evolution.

the following relations

$$n_{N,f} = \cos\vartheta\cos\varpi;\ \ n_{T,f} = \sin\vartheta\cos\varpi. \tag{7.3}$$

being ϑ and ϖ the polar and the azimuthal angles of the single fiber crossing the crack surface.

The number of crossing fibers per strip, n_f, is evaluated through the proposal outlined by Dupont and Vandewalle [2005]

$$n_f = \alpha_{\vec{N}} \frac{\rho_f}{A_f} A_i \tag{7.4}$$

where ρ_f is the fiber content, A_f and A_i are the cross-sectional areas of a single fiber and the interface ($A_i = b \cdot h_s$, being b the base width and h_s the height of the analyzed strip), respectively.

The orientation factor can be estimated by means of the following relationship [Dupont and Vandewalle, 2005]

$$\alpha_{\vec{N}} = \frac{\alpha_{\vec{N},1} \cdot (b - l_f)(h - l_f) + \alpha_{\vec{N},2} \cdot \left[(b - l_f) l_f + (h - l_f) l_f\right] + \alpha_{\vec{N},3} \cdot {l_f}^2}{b \cdot h} \tag{7.5}$$

by geometrically averaging the orientation factors $\alpha_{\vec{N},1}$, $\alpha_{\vec{N},2}$ and $\alpha_{\vec{N},3}$, referred to the zone 1, 2 and 3 of the square cross section beam of Figure 7.3.

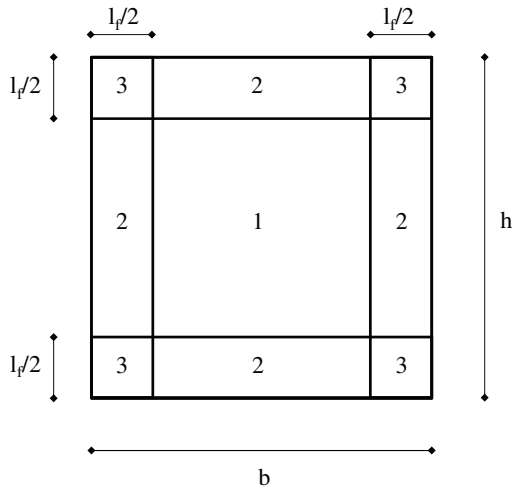

Figure 7.3: The three orientation zones for the square cross section beam: $b \times h \times l$ (base × height × length) having $l \geq b$ and $l \geq h$.

The stress-crack opening relationship, $\sigma\,[u_{cr}]$, of plain concrete matrix is based on the interface law proposed by Carol et al. [1997] and considering the case of tension only. Particularly, the interface loading criterion, the flow rule and the softening (evolution) law are defined as

$$\begin{aligned} f(\sigma,\kappa) = \sigma^2 - \sigma_y^2 \leq 0 \quad & \text{loading criterion} \\ \dot{u}_{cr} = \dot{\lambda}\frac{\partial f}{\partial \sigma} = 2\cdot\dot{\lambda}\cdot\sigma \quad & \text{plastic flow} \\ \sigma_y = f_t\left(1 - \frac{w_{cr}}{G_f^I}\right) \quad & \text{evolution law} \end{aligned} \tag{7.6}$$

where σ_y is the current tensile strength and κ the internal state variable. The incremental cracking opening, $\dot{u}_{cr}$, is defined by means of the classical flow rule, being $\dot{\lambda}$ the rate of the non-negative plastic multiplier. The variation of σ_y is assumed to be linear, from its maximum value f_t (tensile strength) to zero, based on the ratio between the work spent and the available fracture energy, $\frac{w_{cr}}{G_f^I}$. The rate of fracture work, $\dot{w}_{cr}$, is defined as follows

$$\dot{w}_{cr} = \sigma\cdot\dot{u}_{cr}. \tag{7.7}$$

Based on these hypothesis, the employed model exhibits the following closed-form solution under the well-known Kuhn-Tucker and consistency conditions [Carol et al.,

1997, Stankowski et al., 1993]

$$\sigma = f_t \exp\left(-\frac{u_{cr} f_t}{G_f^I}\right) \tag{7.8}$$

which relation deals with an exponential and negative type expression of the $\sigma - u_{cr}$ rule (Figure 7.4a).

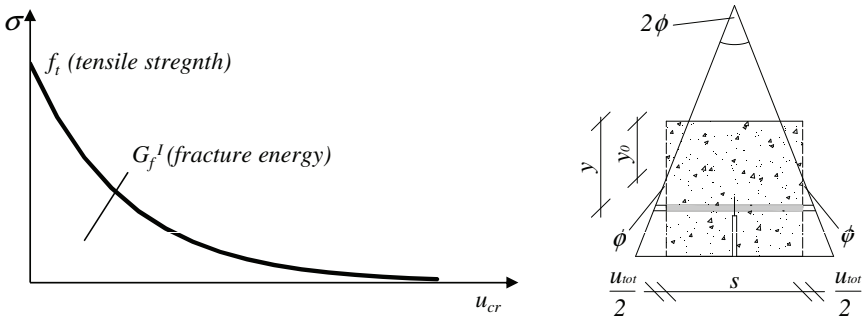

(a) (b)

Figure 7.4: Cracked hinge: (a) stress-crack opening displacement of plain concrete and (b) main geometrical assumption under deformation.

The total crack opening u_{cr}, at the considered strip, is obtained by subtracting the elastic part from the total displacement u_{tot},

$$u_{cr} = u_{tot} - s\frac{\sigma_{SFRC}[u_{cr}]}{E} \tag{7.9}$$

where

$$u_{tot} = 2 \cdot \phi \cdot (y - y_0) \tag{7.10}$$

being ϕ the angular deformation (relative angle of the two end sections of the crack hinge), while y and y_0 deal with the considered strip position and the depth of the neutral axis as depicted in Figure 7.4b. In Eq. (7.9), s represents the hinge length.

By solving Eq. (7.9) for σ_{SFRC} and substituting $u_{tot} = s \cdot \epsilon^*$, where ϵ^* is the mean longitudinal strain in the considered section

$$\varepsilon^* = \frac{2 \cdot \phi \cdot (y - y_0)}{s} \tag{7.11}$$

the following expression for σ_{SFRC} can be obtained

$$\sigma_{SFRC} = \frac{E \cdot 2 \cdot \phi \cdot (y - y_0) - u_{cr}[y]}{s} \tag{7.12}$$

Now, by substituting Eqs. (7.2) and (7.8) into Eq. (7.12) the expression of u_{cr}, at the y level of the considered strip, results

$$u_{cr}[y] = \frac{G_f^I \cdot W\left[-\frac{{f_t}^2 \cdot s \cdot \exp\left(-\frac{2 \cdot f_t \cdot \phi \cdot (y-y_0)}{G_f^I} + \frac{s \cdot (\sigma_f + \tau_f)}{E \cdot G_f^I}\right)}{E \cdot G_f^I}\right]}{f_t} + 2 \cdot \phi \cdot (y - y_0) + \frac{s \cdot (\sigma_f + \tau_f)}{E \cdot f_t} \tag{7.13}$$

where $W[...]$ represents the well-known Lambert W function (also known as product logarithm).

Finally, by adopting the above Eq. (7.13) into Eq. (7.8), the following composite stress σ_{SFRC} can be obtained

$$\sigma_{SFRC} = f_t \cdot \exp\left(\begin{array}{l} -\frac{2 \cdot f_t \cdot \phi \cdot (y-y_0)}{G_f^I} + \frac{s \cdot (\sigma_f + \tau_f)}{E \cdot G_f^I} - \\ W\left[-\frac{{f_t}^2 \cdot s \cdot \exp\left(-\frac{2 \cdot f_t \cdot \phi \cdot (y-y_0)}{G_f^I} + \frac{s \cdot (\sigma_f + \tau_f)}{E \cdot G_f^I}\right)}{E \cdot G_f^I}\right] \end{array}\right) + (\sigma_f + \tau_f). \tag{7.14}$$

Once the complete stress distribution is obtained in both elastic and post-cracking state, the external force P and/or the corresponding bending moment M can be easily obtained by equilibrium conditions between internal and external forces. Particularly, the axial equilibrium is commonly employed for obtaining the position of the neutral axis y_0. Once the latter is calculated, the resultant moment can be calculated by means of the bending equilibrium.

Then, both Crack-Tip and Mouth Opening Displacements ($CTOD$ and $CMOD$ as shown on Figure 7.1) can be easily calculated by evaluating u_{tot} of Eq. (7.10) for $y = h - a$ and $y = h$, respectively, as follows

$$\begin{aligned} CTOD &= u_{tot}[h - a] \\ CMOD &= u_{tot}[h]. \end{aligned} \tag{7.15}$$

7.2 Bond-slip bridging of fibers on concrete cracks

Fracture opening processes in concrete activate bridging effects induced by fibers. The axial (tensile) stresses in fibers are balanced by bond developing on their lateral surface embedded in concrete matrix. Thus, a simple equilibrium equation can be written

$$\frac{d\sigma_f[x]}{dx} = -\frac{4\tau_a[x]}{d_f} \tag{7.16}$$

where σ_f is the axial tensile stress developed in fibers and considered in Eq. (7.2), τ_a the local bond stress between fiber and matrix, and d_f the fiber diameter. This approach is strictly true in the case of considering synthetic fibers, while can be extended for steel ones when the length l_{emb} results in the condition that $|\sigma_{f,max}| \leq \sigma_{y,s}$, where $\sigma_{f,max}$ and $\sigma_{y,s}$ represent the maximum axial stress and the steel yielding, respectively.

A simplified bilinear bond-slip law is proposed to model the fiber-to-concrete debonding process as follows

$$\tau_a[x] = \begin{cases} -k_E s[x] & s[x] \leq s_e \\ -\tau_{y,a} + k_S (s[x] - s_e) & s_e < s[x] \leq s_u \\ 0 & s[x] > s_u \end{cases} \tag{7.17}$$

where $s[x]$ defines the debonded displacement between the fiber and concrete (at the point of the abscissa x). The positive constants k_E and k_S represent the elastic and softening slopes of such bond-slip relationships, respectively; $\tau_{y,a}$ is the shear bond strength, while s_e and s_u are the elastic and ultimate slips, respectively.

The complete derivation of this numerical model, and its validation against bond-slip experimental tests, has been proposed in a previous work published by the authors, see Caggiano et al. [2012c], Caggiano and Martinelli [2012] and completely reported in Chapter 4.

7.3 Dowel action of fibers crossing the concrete cracks

The dowel mechanism, resulting in a shear transfer action across cracks, represents an important component on the overall interaction between steel fibers and concrete matrix. A simple numerical sub-model for the dowel action is based on defining both stiffness and strength of the generic fiber embedded in the concrete matrix and subjected to a transverse force/displacement at the fracture level. On the one hand,

the well-known Winkler beam theory is used to describe the dowel force-displacement relationship, which is transformed in terms of dowel stress vs. relative displacements suitable for the cracked hinge model (namely $\tau_f\left[u_{T,cr}\right]$ of Eq. 7.2). On the other hand, the empirical model reported by Dulacska [1972] for RC-structures is taken as maximum dowel strength. The complete model for the dowel formulation has completely been reported in Chapter 3.

7.4 Numerical predictions

The composite model outlined in the previous sections is introduced in the cracked hinge zone with the aim to simulate the $150 \times 150 \times 600\ mm^3$ notched concrete specimens, tested under four-point bending presented in Chapter 2.

For the purpose of the numerical evaluations, three material types are considered:

- plain concrete,
- steel fiber-reinforced concrete having $\rho_f = 0.5\%$ and,
- steel fiber-reinforced concrete with $\rho_f = 1.0\%$.

The geometry and material properties are chosen according to the tests outlined in experimental campaign described in Chapter 2.

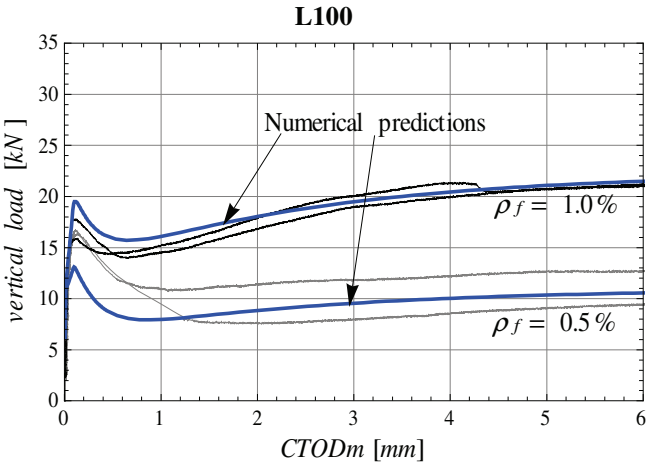

Figure 7.5: Load-$CTODm$ numerical predictions against the experimental data on SFRC L100-type by Caggiano et al. [2012a].

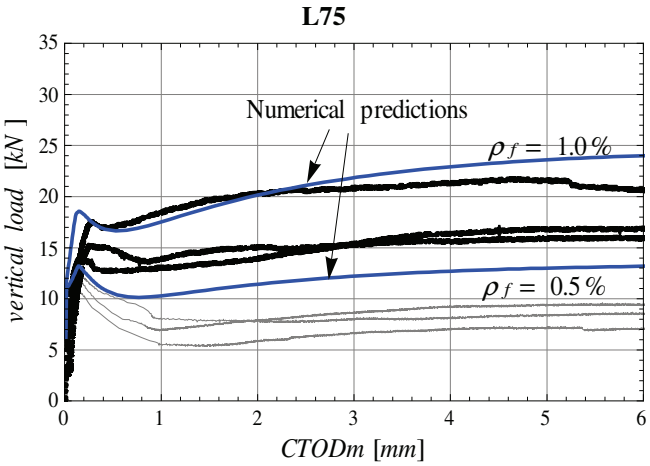

Figure 7.6: Load-$CTODm$ numerical predictions against the experimental data on SFRC L75-type by Caggiano et al. [2012a].

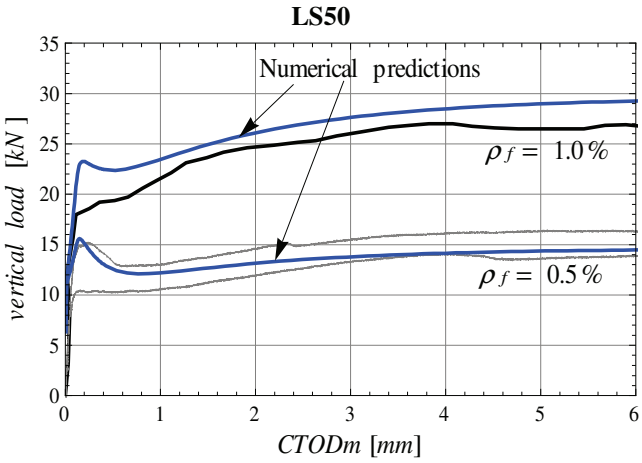

Figure 7.7: Load-$CTODm$ numerical predictions against the experimental data on SFRC LS50-type by Caggiano et al. [2012a].

The local bond-slip law is determined through an inverse identification on the test results obtained on specimens reinforced with only short fibers with $\rho_f = 1.0\%$. Then, such a calibrated parameters are used to simulate the behavior observed in all other tests. Particularly, the mechanical parameters employed in the numerical evaluations are: $f_t = 2.08$ MPa (tensile strength), $E = 31.5$ GPa (elastic modulus), $s = 75$ mm (hinge length), $G_f^I = 0.5$ N/mm (fracture energy), $\tau_{y,a} = 4.5$ MPa (shear bond strength), $k_E = 100.0\,N/mm^3$ (elastic stiffness), $k_S = 0.1\,N/mm^3$ (softening stiffness), $k_{dow} = 2.8$

(dowel parameter) and $c_1 = 0.15$ (coefficient of beam foundation). The assumed values for the orientation factors $\alpha_{\tilde{N}}$ are based on the theoretical proposal outlined by Dupont and Vandewalle [2005] and briefly reported in section 7.1. Particularly, the values 0.57 and 0.54 are determined for long and short fibers, respectively.

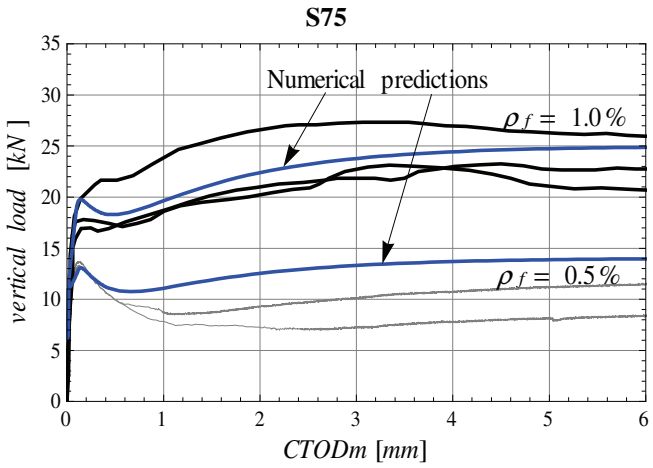

Figure 7.8: Load-$CTODm$ numerical predictions against the experimental data on SFRC S75-type by Caggiano et al. [2012a].

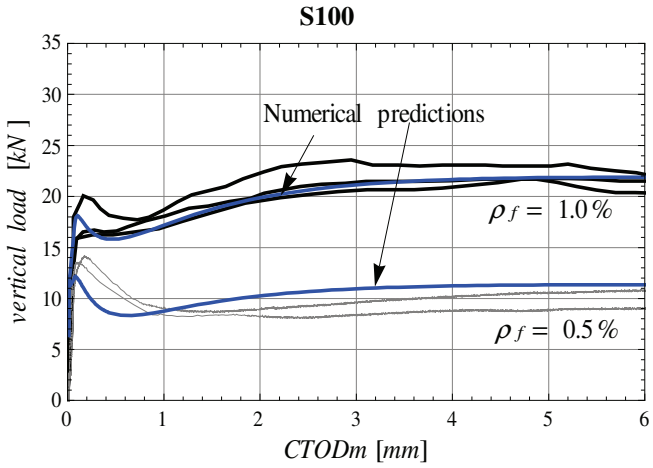

Figure 7.9: Load-$CTODm$ numerical predictions against the experimental data on SFRC S100-type by Caggiano et al. [2012a].

The numerical force-$CTODm$ curves, against the corresponding experimental results, are proposed from Figure 7.5 to 7.9. $CTODm$ represents the mean of the two opposite Crack Tip Opening Displacements ($CTODs$) registered by the transductor devices of

the experimental campaign (to see Chapter 2). The load-crack opening responses of SFRC beams emphasize the significant influence of the fiber reinforcement on the peak strength and the post-peak behavior. Fiber bridging effects on the pre-cracked concretes are well simulated by the considered numerical approach with the proposed non-linear separation law for SFRC.

The results of these numerical analyses demonstrate that the model leads to accurate simulations of the SFRC performance in terms of both peak strength and post-peak ductility of failure processes under mode I type of fracture, when different fiber types and contents are considered.

7.5 Closing remarks

The four-point bending behavior of notched SFRC beams has numerically been investigated and compared against experimental results on four-point bending tests. Two different amounts of steel fibers are considered and modeled at a numerical standpoint. A novel stress-crack opening model, based on a hinge-crack approach already available in the scientific literature, has been employed to reproduce and simulate the experimental results proposed in an other chapter of this thesis. As for the interface formulation, originally employed for meso-mechanical analyses as proposed in Chapter 6, the model has been based on the explicit modeling of the interaction between concrete and steel fibers. The numerical predictions, compared with the experimental measures, demonstrate the soundness and capability of the model to reproduce the mechanical response of SFRC components.

8 Elasto-plastic microplane formulation for FRCC

This chapter deals with an elasto-plastic microplane formulation aimed at simulating the failure behavior of Fiber Reinforced Cementitious Composites (FRCCs) within a continuum approach. This novel proposal, based on the microplane projections approach already available in scientific literature, assumes an hyperbolic maximum strength criterion in terms of normal and shear stresses, evaluated on generally orientated planes (microplanes). Moreover, an elliptical CAP model is proposed in terms of microplane stresses in the compression range. The well-known "Mixture Theory" is employed with the aim to characterize the fiber-to-concrete interactions. Such interactions are generally described by considering the two fundamental phenomena already referred as "bridging debonding effect" and "dowel action" (see Chapter 3). However, only the latter is deemed relevant for "high compression" stress states, namely around the CAP region. After describing the constitutive model, this chapter focuses on numerical analysis of FRCC failure behavior. Particularly, the soundness and capabilities of this approach are assessed and discussed against experimental data on FRCC samples.

After a short literature review discussed in section 8.1, the general basis of the microplane assumptions are outlined in section 8.2. The methodology to describe the composite material failure in FRCC members is then described in section 8.3. The well-know "Mixture Theory" by Trusdell and Toupin [1960] is taken into account therein to represent FRCC as a composite material made of plain concrete matrix and fibers. Then, sections 8.4 and 8.5 deal with the constitutive laws employed at the microplane level. Particularly, the fracture energy-based softening rules and the model description of the fiber-to-concrete interaction (i.e., crack-bridging and dowel effects) are therein discussed. Finally, section 8.6 reports some numerical applications of the proposed constitutive model. The proposed comparisons analyze significant information about

the influence of several parameters such as fiber types, strength criteria and the fracture energy.

8.1 Introduction

A large amount of theoretical works and numerical tools, based on elastic, plastic, damage, viscous or fracture principles, deal with the so-called Smeared Crack Approach (SCA). As largely outlined in the previous chapters, they are characterized by strong Finite Element (FE)-mesh size dependence of the localization band width (e.g., a finer discretization leads to a decreasing toughness of the analyzed numerical model) and loss of ellipticity of the constitutive differential equations [Willam et al., 1984, Oliver, 1989, Etse and Willam, 1994, Jirasek and Zimmermann, 2001, Rabczuk et al., 2005, Folino and Etse, 2012]. Nevertheless, the main advantages of employing smeared crack models are due to their lower computational cost and the easier to be implemented in classical commercial or open-source codes. On the contrary, models based on the Discrete Crack Approach (DCA) are more computationally expensive than SCA, and their main disadvantage resides on the low feasibility to be included in commercial FE codes. These facts represent the main motivations for formulating the new continuum-based approach presented in this chapter.

During the last decades, the well-known microplane theory has largely been used for predicting the mechanical behavior of quasi-brittle materials, such as concrete or rocks. The pioneer works have been proposed by Bazant and Gambarova [1984], Bazant and Oh [1985, 1992], Carol et al. [1992], Bazant et al. [1996b,a]. Further extensions including damage and plasticity concepts have been proposed by Carol and Bazant [1997], Kuhl et al. [2000], Kuhl and Ramm [2000], Leukart and Ramm [2003], Cervenka et al. [2005]. A well-established thermodynamically consistent approach has been described in the works by Carol et al. [2001] and Kuhl et al. [2001]. Other relevant microplane-based contributions can be found in several applications including concrete failure prediction under cyclic loads Ozbolt et al. [2001], for studying the mechanical response of polycrystalline shape memory alloys Brocca et al. [2002], micropolar continua formulation in the spirit of the “Cosserat media” Etse et al. [2003], Etse and Nieto [2004], strain-softening nonlocal models Bazant and Luzio [2004], Di Luzio [2007], large strains Carol et al. [2004], non-linear hardening-softening behavior of fiber reinforced concretes Beghini et al. [2007], quasi-brittle orthotropic composite laminates Cus, early age behavior of concrete structures Lee and Kim [2009] and dynamic impact loads Ozbolt and Sharma [2011].

8.2 Basic assumptions of the microplane-based material model

An elasto-plastic fracture energy-based microplane model is developed for simulating the FRCC macroscopic failure behavior in a smeared crack mode as shown in Figure 8.1. The following formulation is based on the approach proposed by Carol et al. [2001] and Kuhl et al. [2001].

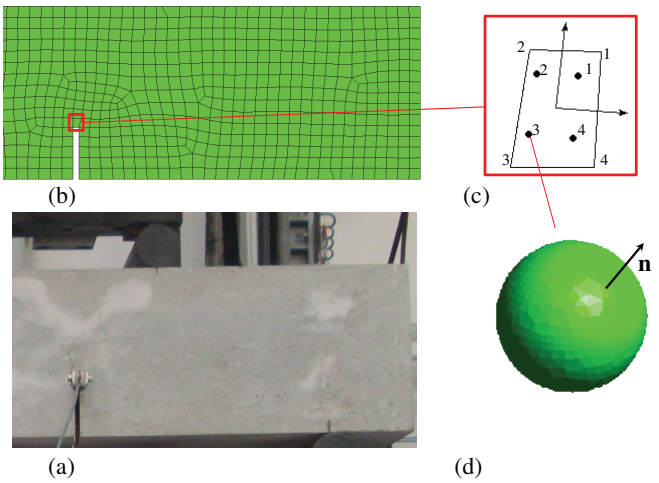

Figure 8.1: (a) Concrete specimen, (b) continuum discretization scale, (c) 4-node continuum FE and (d) spherical microplane region at gauss-point with a generalized normal direction.

8.2.1 Kinematic assumptions

The kinematic constraint assumes that the microplane normal and shear strains (ε_N and $\boldsymbol{\varepsilon}_T$, respectively) are calculated by means of the following relations

$$\begin{aligned} \varepsilon_N &= \boldsymbol{n} \cdot \boldsymbol{\varepsilon} \cdot \boldsymbol{n} \\ \boldsymbol{\varepsilon}_T &= \boldsymbol{\varepsilon} \cdot \boldsymbol{n} - \varepsilon_N \boldsymbol{n} \end{aligned} \tag{8.1}$$

or in index notation

$$\begin{aligned} \varepsilon_N &= \varepsilon_{ij} n_i n_j \\ \varepsilon_{T,k} &= \varepsilon_{kj} n_j - \varepsilon_N n_k \end{aligned} \tag{8.2}$$

being $\boldsymbol{\varepsilon}$ the macroscopic strain tensor (ε_{ij} in index notation) projected on the microplane direction $\boldsymbol{n}$ (with n_i in index notation).

8.2.2 Homogenization between macro- and microplane stress space

In Eqs. (8.3) and (8.4), σ_N and $\sigma_{T,k}$ are the microplane components of stress. The equilibrium between micro- and macroscopic stress tensor can be achieved by means of the application of the virtual work principle applied in the spherical microplane region

$$2\int_{\Omega}\left(\sigma_N\delta\varepsilon_N+\sigma_{T_r}\delta\varepsilon_{T_r}\right)\mathrm{d}\Omega=\frac{4\pi}{3}\sigma_{ij}\delta\varepsilon_{ij} \tag{8.3}$$

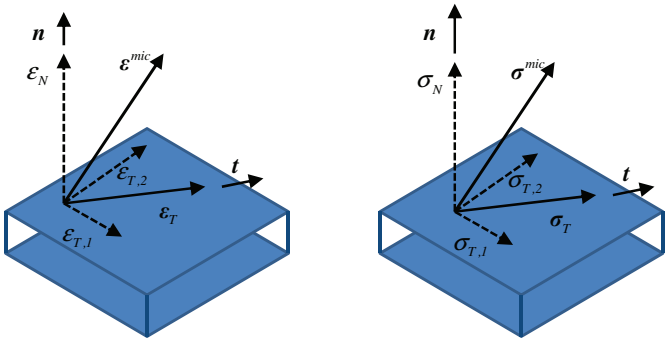

Figure 8.2: Strain and stress components at the microplane level.

where σ_{ij} denotes the components of the macroscopic stress tensor while Ω the boundary surface of one hemisphere. By combining Eqs. (8.2) and (8.3), the following relation for the macroscopic stress tensor can be derived

$$\sigma_{ij}=\frac{3}{2\pi}\int_{\Omega}\left(\sigma_N n_i n_j+\frac{\sigma_{T,k}}{2}\left[n_i\delta_{kj}+n_j\delta_{ki}\right]\right)\mathrm{d}\Omega. \tag{8.4}$$

Figure 8.2 shows the microplane strain $\boldsymbol{\varepsilon}^{mic}$ and stress vectors $\boldsymbol{\sigma}^{mic}$, with the corresponding projections on the microplane direction, $\boldsymbol{n}$, and its orthogonal.

8.3 Composite constitutive formulation for FRCC

A smeared crack microplane model for FRCC, based on the well-known "Mixture Theory" [Trusdell and Toupin, 1960], is formulated by means of the composite combination of three internal constitutive laws whose main features are detailed in sections 8.4 - 8.5 and briefly outlined below:

1. *Fracture energy-based plasticity formulation for plain mortar/concrete*, relating normal and tangential microplane stress components with the corresponding microstrains. Two failure criteria are considered. A maximum strength function is defined in terms of a three-parameter hyperbolic criterion by Carol et al. [1997], while only for high negative values of normal stress a novel elliptical CAP surface is proposed. Post-cracking behavior for controlling both yielding evolutions is controlled in terms of plastic work spent. A non-associated flow rule is considered to complete the material model for the hyperbolic part, while the fully-associated flow law is considered for the CAP formulation.

2. *Bridging effect of fibers loaded in tension* and involving the bond-slip interaction between fiber and matrix.

3. *Dowel action of fibers in concrete cracks*, based on elastic beam foundation concepts, to characterize the shear transfer mechanism of fibers crossing cracks. The dowel strength represents a relevant contribution in case of steel fibers and can be mainly neglected in case of plastic reinforcements.

Fiber reinforced concrete is modeled as a composite material made of a mortar matrix and randomly oriented fiber reinforcements. According to the basis of the "Mixture Theory", each infinitesimal volume of the continuum composite is made of the same amount and proportion of the various constituents. It follows that the corresponding composite stress field is given by the weighted sum (in terms of the volume fraction) of the constituent stresses

$$\boldsymbol{\sigma} = w[\rho_m]\boldsymbol{\sigma}^{mic} + \sum_{f=0}^{n_f} w[\rho_f]\left[\sigma_f(\varepsilon_N)\,\boldsymbol{n} + \tau_f(\boldsymbol{\varepsilon}_T)\,\boldsymbol{t}\right] \tag{8.5}$$

being $w[\rho_\#]$ the weighting functions proposed in Chapter 3 which depend on the volume fraction $\rho_\#$ of each constituent #; m and f deal with the mortar and fiber indices, respectively; σ_f and τ_f mean the bond-slip and dowel actions of the single considered fiber which are related to its axial and tangential strains, ε_N and $\boldsymbol{\varepsilon}_T$, respectively; n_f represents the number of fibers per microplane and finally, $\boldsymbol{n}$ and $\boldsymbol{t}$ are the fiber direction and its orthogonal, respectively. The evaluation of the total number of fibers crossing each microplane is calculated adopting the proposals given in Krenchel [1975] and Dupont and Vandewalle [2005]. Further details about these aspects can be found in Chapter 3.

8.4 Fracture energy-based cracking microplane model for plain concrete/mortar

The inelastic model for plain concrete failure behavior is outlined in this section. In particular, a detailed description of the microplane-based elasticity and post-peak formulation is given in the following subsections.

8.4.1 Microplane elasto-plasticity constitutive formulation

The microplane components of stress, σ_N and $\sigma_{T,k}$, are obtained from the microscopic free-energy potential, ψ_0^{mic},

$$\sigma_N = \frac{\partial\left[\rho_0 \psi_0^{mic}\right]}{\partial \varepsilon_N}, \qquad \sigma_{T,k} = \frac{\partial\left[\rho_0 \psi_0^{mic}\right]}{\partial \varepsilon_{T,k}} \tag{8.6}$$

being ρ_0 the material density.

The macroscopic free-energy potential per unit mass of material in isothermal conditions $\psi_0^{mac}(\boldsymbol{\varepsilon}, \boldsymbol{\kappa})$, with $\boldsymbol{\kappa}$ a set of thermodynamically consistent internal variables [Kuhl et al., 2001], resulted

$$\psi_0^{mac} = \frac{3}{2\pi} \int_{\Omega} \psi_0^{mic}\left(\boldsymbol{\varepsilon}^{mic}, \boldsymbol{\kappa}^{mic}\right) \mathrm{d}\Omega \tag{8.7}$$

being $\boldsymbol{\varepsilon}^{mic}$ the vector collecting the normal and shear strain components for the microplane and $\boldsymbol{\kappa}^{mic}$ the vector of the internal microplane variables for accounting the hardening/softening material behavior.

Fully uncoupled normal/tangential material laws are defined at the microplane level. The normal and the tangential stress components are given as the conjugate components to the corresponding microplane strains, i.e.

$$\sigma_N = \frac{\partial \psi_0^{mic}}{\partial \varepsilon_N^{el}}, \qquad \dot{\sigma}_N = E_N\left[\dot{\varepsilon}_N - \dot{\varepsilon}_N^p\right], \tag{8.8}$$

$$\sigma_{T,k} = \frac{\partial \psi_0^{mic}}{\partial \varepsilon_{T,k}^{el}}, \qquad \dot{\sigma}_{T,k} = E_T\left[\dot{\varepsilon}_{T,k} - \dot{\varepsilon}_{T,k}^p\right]. \tag{8.9}$$

where E_N and E_T are the microscopic elastic stiffnesses, while the superscripts "el" and "p" represent the elastic and plastic parts for the microstrains. In analogy to macroscopic plasticity-based models, the constitutive formulation of the microplane proposal is introduced in an incremental form. Actually, the additive decomposition into the elastic and plastic contributions takes place in both the normal (Eq. 8.8) and tangential strains (Eq. 8.9).

The incremental rate stress vector, $\dot{\boldsymbol{\sigma}}^{mic}$, and the rate of the microplane elastic strains, $\dot{\boldsymbol{\varepsilon}}^{el,mic}$, are connected by means of the following elastic stiffness operator

$$\boldsymbol{C}^{mic} = \begin{pmatrix} E_N & 0 & 0 \\ 0 & E_T & 0 \\ 0 & 0 & E_T \end{pmatrix}. \tag{8.10}$$

then

$$\dot{\boldsymbol{\sigma}}^{mic} = \boldsymbol{C}^{mic} \cdot \dot{\boldsymbol{\varepsilon}}^{el,mic}; \quad \dot{\boldsymbol{\sigma}}^{mic} = \boldsymbol{C}^{mic} \cdot \left(\dot{\boldsymbol{\varepsilon}}^{mic} - \dot{\boldsymbol{\varepsilon}}^{p,mic} \right), \tag{8.11}$$

As above mentioned, the model assumes a microplane strain decomposition into elastic and plastic components: i.e., $\dot{\boldsymbol{\varepsilon}}^{el,mic}$ and $\dot{\boldsymbol{\varepsilon}}^{p,mic}$, respectively.

The microscopic elastic moduli are related to the macroscopic ones as demonstrated in Bazant and Prat [1988a,b]

$$E_N = 3K + 2G \qquad E_T = 2G \tag{8.12}$$

being K and G the Bulk and shear macroscopic moduli, respectively.

8.4.2 Post-cracking behavior

The inelastic behavior is described at the microplane level in terms of normal/shear stress vs. strain relationship with the aim to characterize the non-linear fracture behavior of concrete.

The considered strength criteria $f\left(\dot{\boldsymbol{\sigma}}^{mic}\right)$ are given on the microplane stress-space as shown in Figure 8.3. Its expressions are represented by the three-parameter hyperbola by Carol et al. [1997] when $\sigma_N \geq \sigma_{N,CAP}$,

$$f\left(\dot{\boldsymbol{\sigma}}^{mic}\right) = \|\boldsymbol{\sigma}_T\|^2 - [c^{mic} - \sigma_N \tan(\phi^{mic})]^2 + [c^{mic} - \chi^{mic} \tan(\phi^{mic})]^2, \tag{8.13}$$

function of three material parameters: i.e., the tensile strength χ^{mic}, the cohesion c^{mic} and the internal friction angle ϕ^{mic}.

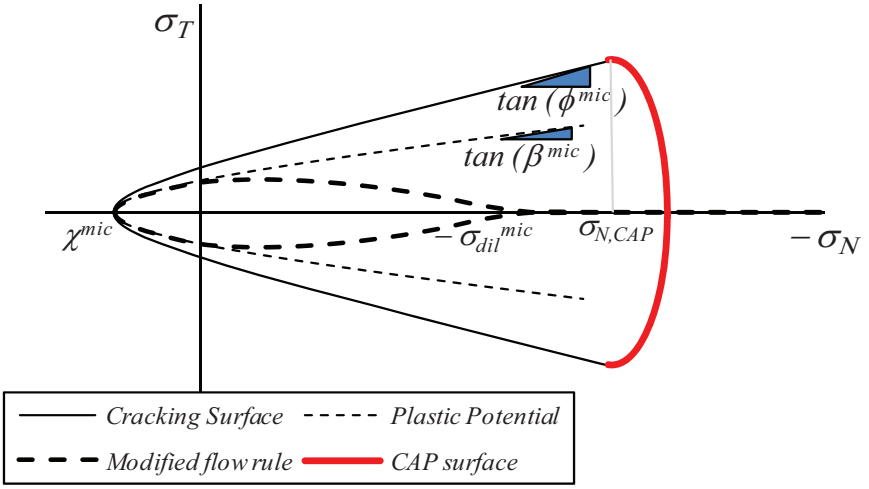

Figure 8.3: Maximum strength criteria and plastic flow rules.

On the contrary, if $\sigma_N < \sigma_{N,CAP}$ an elliptical function is taken into account as follows

$$f\left(\dot{\boldsymbol{\sigma}}^{mic}\right) = \|\sigma_T\|^2 - \frac{1}{R_{CAP}^2}\left[\left(\sigma_N - \sigma_{N,0}\right)^2 - \left(\sigma_{N,CAP} - \sigma_{N,0}\right)^2\right] \tag{8.14}$$

where R_{CAP}, $\sigma_{N,CAP}$ and $\sigma_{N,0}$ are model parameters. Particularly $\sigma_{N,CAP}$ represents that value of σ_N situated on the boundary between the hyperbola and the ellipse.

The plastic flow rule, defining the direction of inelastic strains, is represented by a general non-associated law for the formulation based on the hyperbolic model and an associated one for the elliptical CAP formulation.

Particularly, the rate of plastic strains can be generally written as

$$\dot{\boldsymbol{\varepsilon}}^{p,mic} = \dot{\lambda}\,\boldsymbol{m}^{mic} \tag{8.15}$$

where $\dot{\lambda}$ is the non-negative plastic multiplier derived by means of the classical Kuhn-Tucker and consistency conditions as follows

$$\dot{\lambda} \geq 0, \quad f\left(\dot{\boldsymbol{\sigma}}^{mic}\right) \leq 0, \quad \dot{\lambda}\, f\left(\boldsymbol{\sigma}^{mic}\right) = 0, \quad \dot{f}\left(\boldsymbol{\sigma}^{mic}\right) = 0, \tag{8.16}$$

while the vector $\boldsymbol{m}^{mic}$ can be reached by means of the transformation operator, $\boldsymbol{A}^{mic}$, applied to the normal flow direction, $\boldsymbol{n}^{mic} = \frac{\partial f}{\partial \boldsymbol{\sigma}^{mic}} = \left[\frac{\partial f}{\partial \sigma_N}, \frac{\partial f}{\partial \|\sigma_T\|}\right]^t$

$$\textit{Hyperbola}: \quad \boldsymbol{A} = \begin{cases} \begin{pmatrix} \frac{\tan(\beta^{mic})}{\tan(\phi^{mic})} & 0 \\ 0 & 1 \end{pmatrix} & \text{if} \quad \sigma_N \geq 0 \\ \begin{pmatrix} \left[1 - \frac{|\sigma_N|}{\sigma_{dil}^{mic}}\right] \frac{\tan(\beta^{mic})}{\tan(\phi^{mic})} & 0 \\ 0 & 1 \end{pmatrix} & \text{if} \quad -\sigma_{dil}^{mic} \leq \sigma_N < 0 \\ \begin{pmatrix} 0 & 0 \\ 0 & 1 \end{pmatrix} & \text{if} \quad \sigma_{N,CAP} \leq \sigma_N < -\sigma_{dil}^{mic} \end{cases} \tag{8.17}$$

$$\textit{Elliptical formulation}: \quad \boldsymbol{A} = \begin{pmatrix} 1 & 0 \\ 0 & 1 \end{pmatrix} \quad \text{if} \quad \sigma_N < \sigma_{N,CAP} \tag{8.18}$$

In Eq. (8.17), $\tan(\beta^{mic})$ represents the dilation angle of the plastic potential, as represented in Figure 8.3: $0 \leq \tan(\beta^{mic}) \leq \tan(\phi^{mic})$. Thereby, the parameter σ_{dil}^{mic} represents the normal stress at which the dilatancy vanishes (see in Carol et al. [1997] and Lorefice et al. [2008]). Moreover, Eq. (8.18) deals with the associated flow direction characterizing the CAP model.

Three main fracture mechanisms govern the post-cracking evolution:

- the mode I type of fracture reached along the horizontal axis of the failure criterion in the tensile region;
- the shear fracture modes with compression stress ranges;
- the pure compactation mode along the horizontal axis of the failure criterion in the CAP negative region.

The ratio between the work spent in fracture, w_{cr}, and the corresponding fracture energy parameters, G_f^I (defining the fracture energy released in pure mode I) and G_f^{IIa} (dealing with the fracture energy for the asymptotic mode II, similarly given in Chapter 3), defines a unified scaling parameter, $S\left[\xi_{p_i^{mic}}\right]$ introduced by Carol et al. [1997],

$$S[\xi_{p_i^{mic}}] = \frac{e^{-\alpha_{p_i}} \xi_{p_i^{mic}}}{1 + (e^{-\alpha_{p_i}} - 1)\xi_{p_i^{mic}}} \tag{8.19}$$

aimed at controlling the evolution of the model parameters by means of the following expression

$$p_i^{mic} = \left[1 - \left(1 - r_p^{mic}\right) S[\xi_{p_i^{mic}}]\right] p_{0i}^{mic} \tag{8.20}$$

where p_i^{mic} alternatively equals to χ^{mic}, c^{mic}, $tan(\phi^{mic})$ (hyperbolic function) and $\sigma_{N,CAP}$ (ellipse). These model parameters vary from their maximum values p_{0i}^{mic} to the corresponding residual ones $r_p^{mic} p_{0i}^{mic}$. The parameter α_{p_i} controls the decay form of the internal parameter as shown in Figure 8.4, while the non-dimensional variable $\xi_{\#} = \xi_{p_i^{mic}}\left[w_{cr}/G_f^{\#}\right]$ introduces the influence of the ratio between the current fracture work spent and the available fracture energy as follows

$$\xi_{\chi^{mic}} = \begin{cases} \frac{1}{2}\left[1 - cos\left(\frac{\pi w_{cr}}{G_f^I}\right)\right] & \text{if } w_{cr} \le G_f^I \\ 1 & \text{otherwise} \end{cases} \tag{8.21}$$

$$\xi_{c^{mic}} = \xi_{\tan(\phi^{mic})} = \xi_{\sigma_{N,CAP}} = \begin{cases} \frac{1}{2}\left[1 - cos\left(\frac{\pi w_{cr}}{G_f^{IIa}}\right)\right] & \text{if } w_{cr} \le G_f^{IIa} \\ 1 & \text{otherwise} \end{cases} \tag{8.22}$$

according to the function proposed in Caballero et al. [2008]. Figure 8.5 shows the typical curves obtained with Eqs. (8.21) or (8.22).

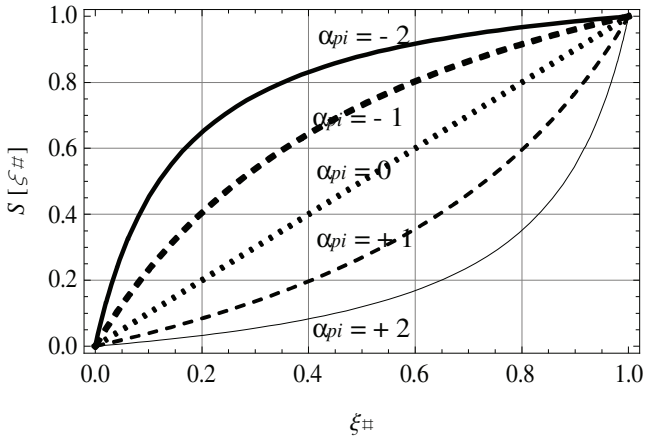

Figure 8.4: $S[\xi_{\#}]$ scaling function of the microplane model in terms of the $\xi_{\#}$ parameter, where the # symbol = χ^{mic}, c^{mic}, $\tan(\alpha^{mic})$ or $\sigma_{N,CAP}$.

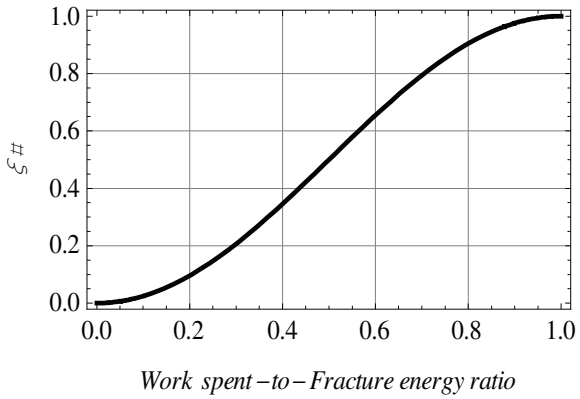

Figure 8.5: $\xi_\#$ functions, with $\# = \chi^{mic}, c^{mic}$, $\tan(\alpha^{mic})$ or $\sigma_{N,CAP}$, depending on the work spent-to-fracture energy ratio, w_{cr}/G_f^I or w_{cr}/G_f^{IIa}.

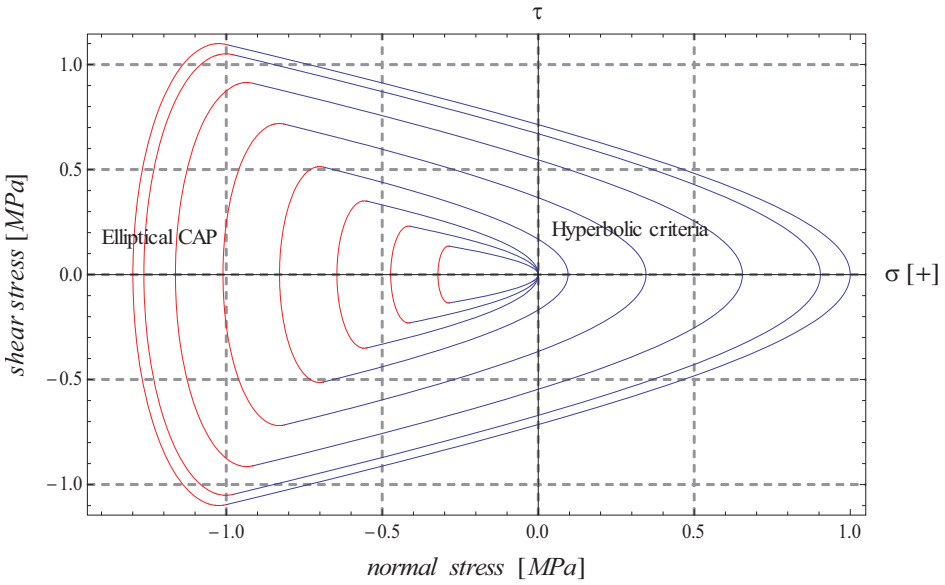

Figure 8.6: Yielding criteria at different ratios between work spent values and fracture energies: $\left(\frac{w_{cr}}{G_f^I}, \frac{w_{cr}}{G_f^{IIa}}\right) = (0.0, 0.0)$, $(0.2, 0.1)$, $(0.4, 0.2)$, $(0.6, 0.3)$, $(0.8, 0.4)$, $(1.0, 0.5)$, $(1.0, 0.6)$, $(1.0, 0.8)$ (from the biggest size up to smallest one).

In order to illustrate the main features of the proposed yielding surfaces and their evolutions based on the expressions (8.19-8.22), various plot examples are reported in Figure 8.6. The numerical values considered in these examples for the relevant mechanical parameters are: the initial strength values $\chi_0^{mic} = 1.0\,MPa$, $c_0^{mic} = 1.0\,MPa$, $\tan(\phi_0^{mic}) =$

0.3 and $\sigma_{N,CAP_0} = -1.0\,MPa$; the residual strengths $\chi_r^{mic} = 0.0\,MPa$, $c_r^{mic} = 0.0\,MPa$, $\tan(\phi_r^{mic}) = 0.1$ and $\sigma_{N,CAP_r} = -0.1\,MPa$; and all the shape coefficients $\alpha_{p_i} = 0.0$.

The expressions, defining the rate of plastic work $\dot{w}_{cr}$, are given by means of the following expressions

$$\begin{aligned} \dot{w}_{cr} &= \sigma_N \cdot \dot{\varepsilon}_N^p \cdot l_{cs}^I + \sigma_{T,k} \cdot \dot{\varepsilon}_{T,k}^p \cdot l_{cs}^{II} \qquad \text{if} \quad \sigma_N < \sigma_{N,CAP} \quad \text{or} \quad \sigma_N \geq 0 \\ \dot{w}_{cr} &= \sigma_{T,k} \cdot \dot{\varepsilon}_{T,k}^p \cdot l_{cs}^{II} \left(1 - \frac{|\sigma_N| tan(\phi^{mic})}{\|\boldsymbol{\sigma}_T\|}\right) \qquad \text{if} \quad \sigma_{N,CAP} \leq \sigma_N < 0 \end{aligned} \tag{8.23}$$

in which the strain components in each microplane, $\boldsymbol{\varepsilon}^{mic} = \left[\varepsilon_N, \varepsilon_{T_1}, \varepsilon_{T_2}\right]^t$, can be easily transformed in terms of crack-opening displacement through the following expressions

$$\varepsilon_N = \frac{u}{l_{cs}^I} \qquad \varepsilon_{T_1} = \frac{v_1}{l_{cs}^{IIa}} \qquad \varepsilon_{T_2} = \frac{v_2}{l_{cs}^{IIa}} \tag{8.24}$$

where u, v_1 and v_2 are the relative crack displacements, while l_{cs}^I and l_{cs}^{IIa} are homogenization characteristic lengths to be calibrated for the considered failure modes. They mainly represent the crack spacings in direct tension, under shear stress states with very high confinement, or the damaged zone under compressive compactions.

In principle, the adopted inelastic model, its evolution laws and the flow rule representations are similar to that proposed in the previous chapters for discrete crack analyses at material and mesoscale observation level.

8.5 Crack-bridging effect of fibers

Fiber actions deriving from fracture opening processes in concrete, and schematically proposed in Figure 8.7, take relevant bridging effects on the FRCC constitutive response.

On the one hand the bond mechanism between fibers and concrete matrix is taken into account as an axial (tensile) stress acting at the microplanes σ_f. It can be derived by equilibrium conditions of shear stresses reacting on the lateral contact surfaces of fibers embedded within the concrete matrix as outlined in Figure 8.7. On the other hand the dowel action, V_d of Figure 8.7 as result of the shear transfer mechanism, represents another important component on the overall bridging effect of steel fibers in fracture processes of FRCC. A simple analytical model for reproducing the dowel action of fibers crossing cracks is developed. It is based upon the definition of both stiffness and strength of a generic fiber embedded in the concrete matrix and subjected to a transverse force vs. displacement behavior.

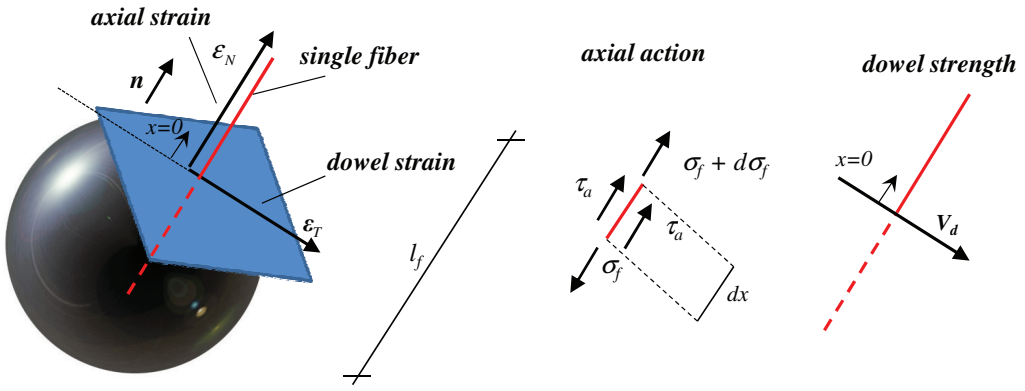

Figure 8.7: Microplane strain activating the fiber bridging effects.

For the sake of brevity, many details of the model derivations are not provided in this Chapter. The complete formulations for both the bond-slip and dowel action has completely been detailed in Chapters 3 and 4.

8.6 Numerical analyses about the material failure

This section presents the main features and capabilities of the proposed formulations comparing some numerical results against experimental data available in literature. In order to evaluate the numerical stability of the aforementioned formulation, the following simulation cases are analyzed in this section:

- uniaxial tension, and
- simple shear.

Particularly, the schematized test cases reported in Figure 8.8, considering a 1.0 cm-edge cubic sample under plane stress condition, are considered.

8.6.1 Tensile tests

Comparison with experimental data

Numerical predictions carried out in both plain and Steel Fiber Reinforced Concrete (SFRC), by adopting the proposed microplane formulation for analyzing tensile test cases, are presented in this section. The comparisons between model predictions

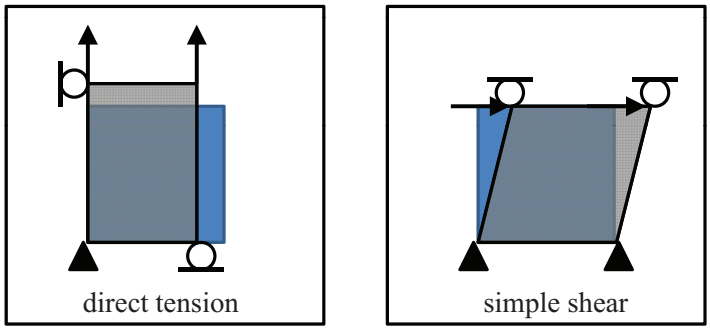

Figure 8.8: Load configurations and restraint conditions for uniaxial tension and simple shear.

and the experimental data by Li and Li [2001] are reported in Figure 8.9. The same set of experimental tests have been already analyzed in Chapter 5, where numerical simulations have been realized by using the interface model presented in Chapter 3.

Table 8.1: Fiber types employed in the experimental campaign by Li and Li [2001].

	Density $[g/cm^3]$	$d_f[mm]$	$l_f[mm]$	$\sigma_{y,s}[GPa]$	$E_s[GPa]$
Dramix type I	7.8	0.5	30	1.20	200
Dramix type II	7.8	0.5	50	1.20	200

The considered SFRC specimens contained two fiber types, namely “Dramix type I” and “type II” whose fundamental characteristics are given in Table 8.1. The model parameters of the proposed numerical analyses, adjusted according to the experimental data given in Li and Li [2001], result: $E_c = 39.5\,GPa$ and $\nu = 0.20$, $\tan\phi_0^{mic} = \tan\beta^{mic} = \tan\phi_r^{mic} = 0.6$, $\chi_0^{mic} = 4.0\,MPa$, $c_0^{mic} = 7.0\,MPa$, $G_f^I = 0.12\,N/mm$, $G_f^{IIa} = 1.2\,N/mm$, $\alpha_\chi^{mic} = -0.15\,N/mm$, $l_{cs}^I = 24\,mm$. While, the parameters of the fiber-to-concrete mechanisms are: $\tau_{y,a} = 2.35\,MPa$, $k_E = 52.5 MPa/mm$ and $k_S = 1.70 MPa/mm$ for the bond-slip strength; $\kappa_1 = 6.5$, $f_c = 10 \cdot \chi_0$ and $k_{dow} = 0.23$ for the dowel effect.

The stress-strain response for SFRCs with steel “Dramix type II”, characterized by fiber contents ranging between 3.0% to 4.0%, are given in the left side of Figure 8.9; while on the right of the same figure it is reported the numerical and experimental comparisons of SFRC tests characterized by considering the “Dramix type I”, whose fiber contents are 6.0%, 7.0% and 8.0%, respectively.

The numerical predictions compared with the corresponding experimental results demonstrate a very good agreement of the proposed formulation. The model predicts in a very realistic mode the mechanical response of the analyzed SFRC specimens.

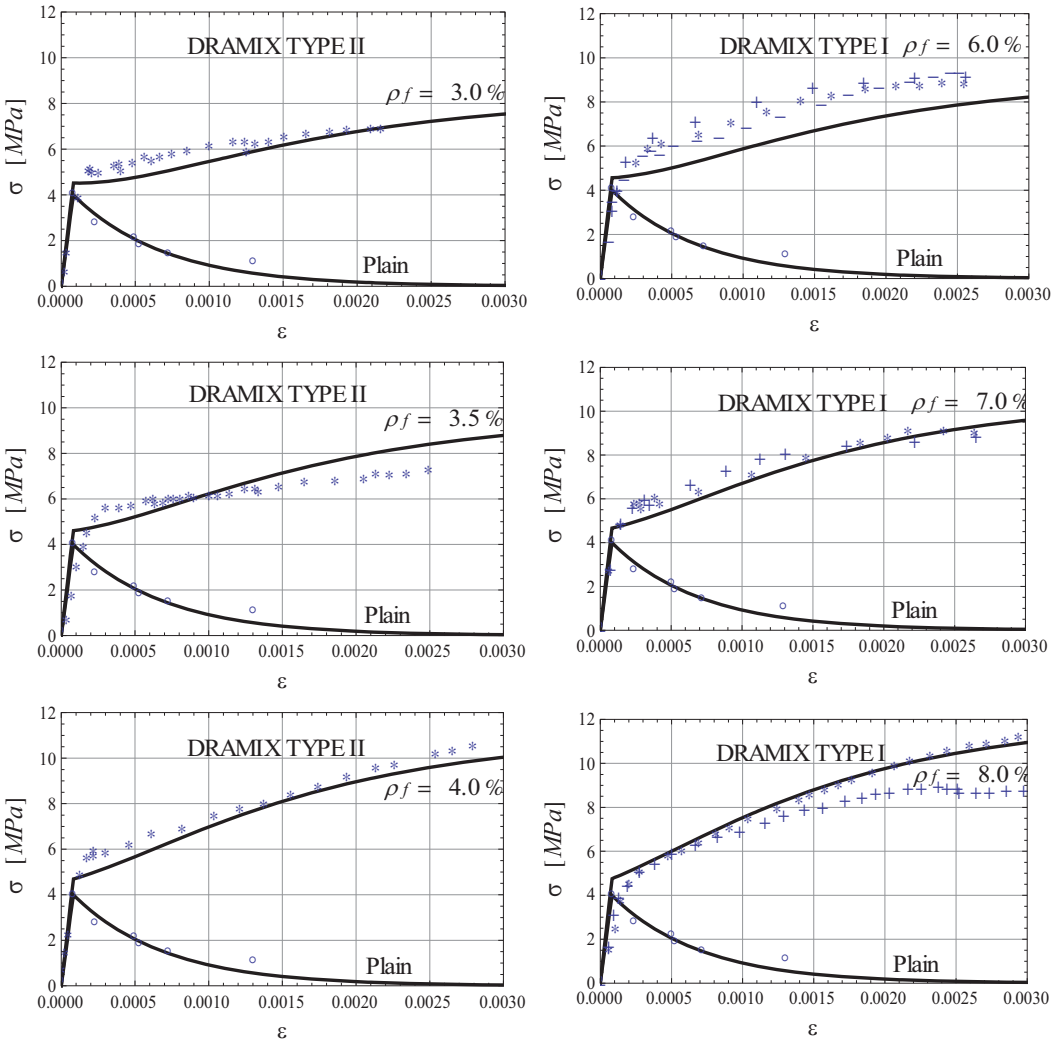

Figure 8.9: Comparison between the numerical predictions and the experimental results (dotted curves) by Li and Li [2001] of SFRCs with "Dramix type I" and "type II".

It is worth highlighting that all the other numerical curves have been obtained by just changing the fiber contents (ρ_f) and/or fiber types (e.g., l_f) according to the properties given by the experimental report [Li and Li, 2001]. This aspect is the key advantage of modeling the fiber effects in an explicit way: it gives the possibility of obtaining the overall macroscopic stress-strain response by just changing the fiber type and geometry.

Comparison with the interface model under uniaxial tension

This section addresses the effect of assuming a continuous based model like the one proposed in this chapter instead of the interface discontinuous formulation given in Chapters 3-6.

The simulations of 1.0 cm-edge cubic samples, as proposed in discontinuous schemes of Figures 6.1 and 6.2b reported in section 6.1, are reanalyzed according to a continuum approach in this section. Plane stress hypothesis and displacement-based control are assumed. Then, two material types are considered:

- plain concrete and
- steel fiber reinforced concrete with fiber percentage $\rho_f = 5.0\%$.

The same material parameters used in the tensile problems of the previous section 6.1 are adopted. To compare the response of the two mentioned approaches in terms of load-displacement laws (result of the structural response achieved by employing the discontinuous-based formulation of Figure 6.1), the load is now measured by multiplying the vertical stress by the cross section of the specimen (1×1 cm^2 in case of plane stress), while the vertical displacement is intended as the tensile strain which multiplies the specimen height (1 cm).

Three comparisons are reported:

- 1 horizontal interface vs. 1 microplane over the unit hemisphere,
- 2 horizontal interfaces vs. 2 microplanes over the unit hemisphere and
- 4 horizontal interfaces vs. 4 microplanes over the unit hemisphere,

as schematized in Figure 8.10.

The comparison in terms of tensile load-displacement law is shown in Figure 8.10. Based on such simulations, it can be observed that at least 2 microplanes over the unit hemisphere must be considered to achieve an acceptable accuracy of the numerical integration in case of pure tensile stress. The numerical responses of the tests involving 4 horizontal interfaces and 4 microplanes highlight that greater number of interfaces is responsable of a less ductile structural response in post-cracking regime.

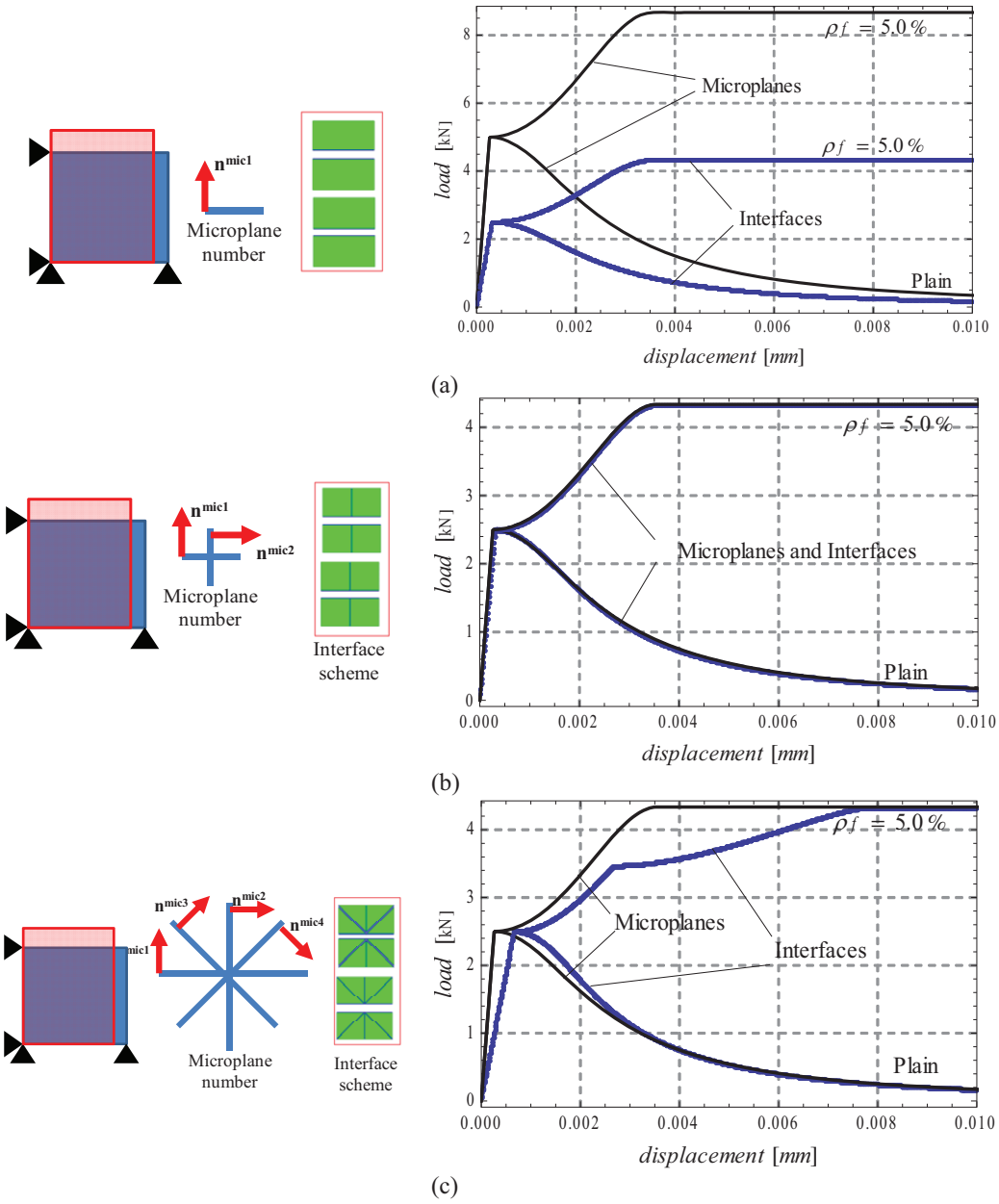

Figure 8.10: Interface-based simulations vs. microplane ones under tensile load cases.

8.6.2 Shear test results: influence of the integration approximation over the unit hemisphere

The macroscopic stress tensor (in components σ_{ij}) can be theoretically evaluated by imposing the equilibrium between micro- and macroscopic stress tensor through the

application of the virtual work principle over the unit hemisphere according to Eq. (8.3). However, the integration of Eq. (8.3) is transformed into a summation, which is characterized by a finite number of considered orientations (equal to the adopted discretizing microplanes).

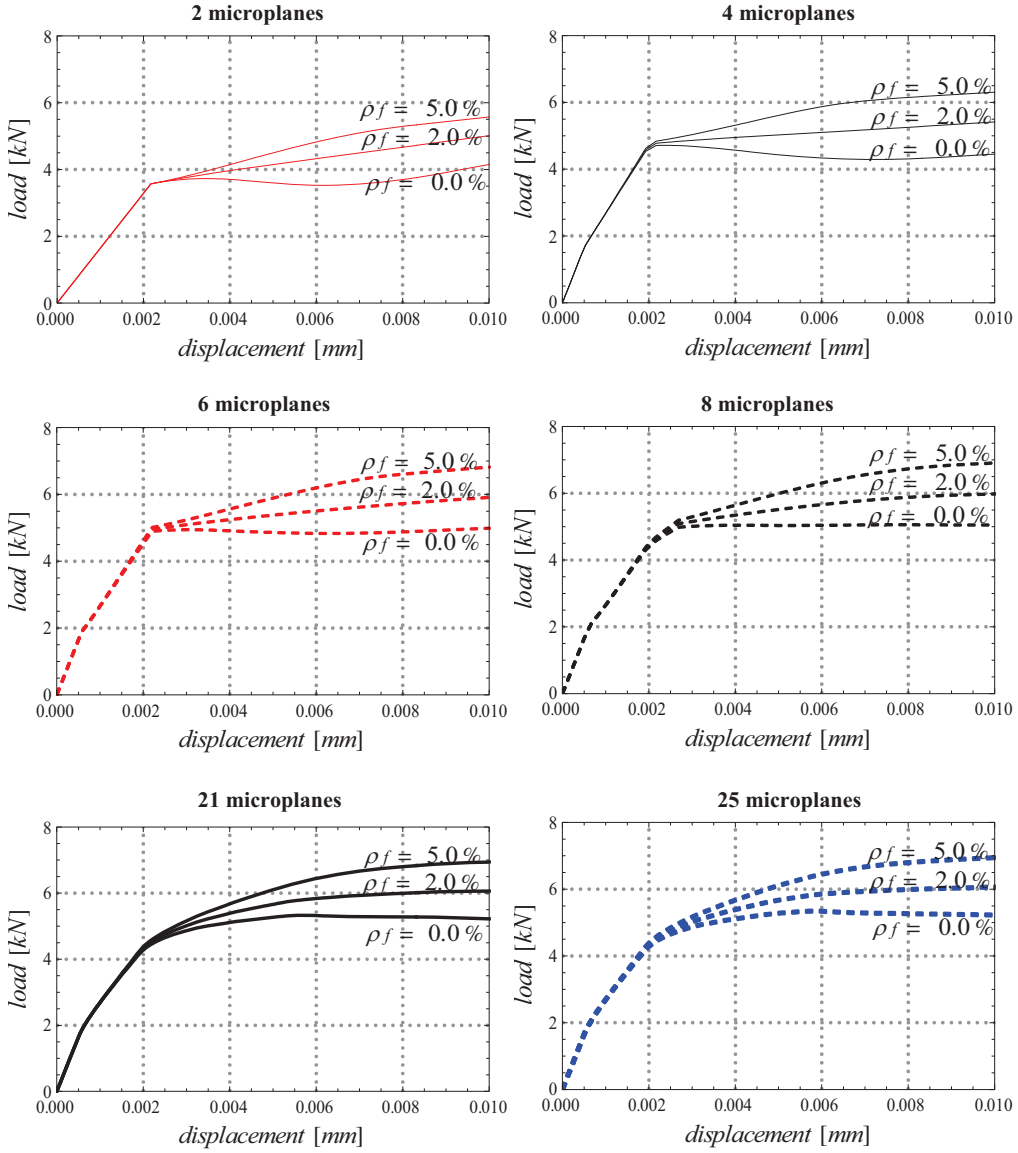

Figure 8.11: Lateral shear load - displacement by considering several integration points (varying from 2 to 25) and fiber percentages.

The accuracy of the numerical response, based on the number of the considered inte-

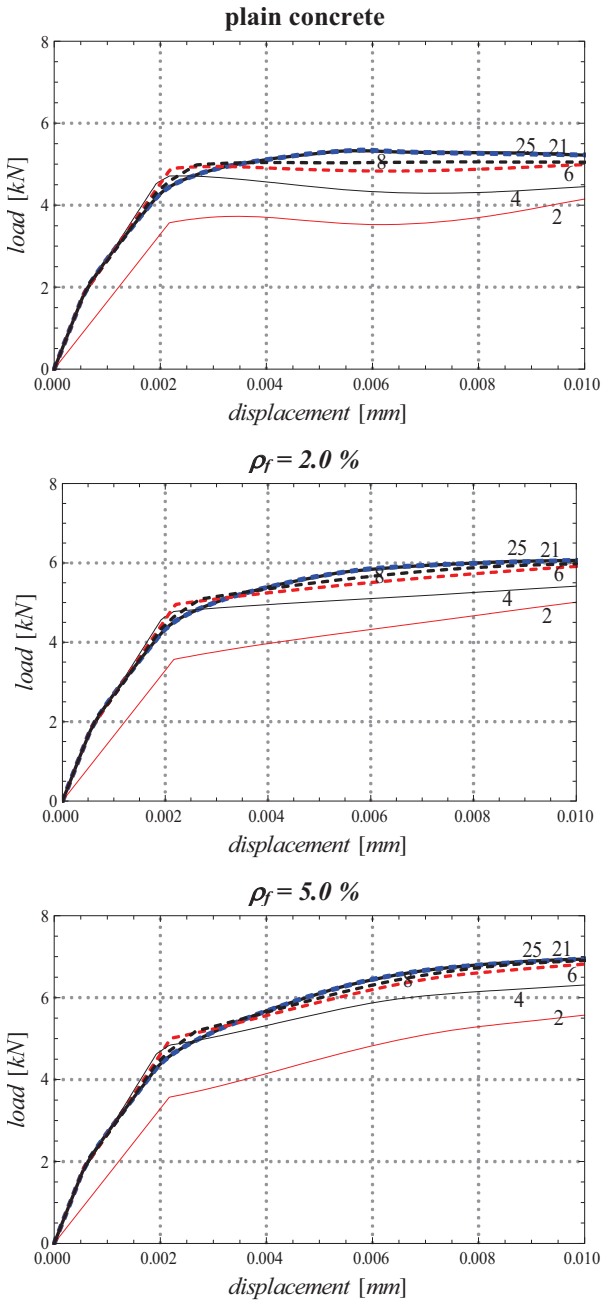

Figure 8.12: Lateral shear load - displacement comparisons when several microplane numbers and fiber contents are considered.

gration points at the unit hemisphere, is investigated in the case of simple shear. For this purpose, the same material parameters as in the tension problems of previous subsection are considered. Thus, 2, 4, 6, 8, 21 and 25 integration points (on the unit hemisphere) are considered for the numerical analyses. The result can be found in Figure 8.11 and 8.12, where the lateral load vs. displacement curves are plotted. Particularly, Figure 8.11 emphasizes the comparative response of three kinds of concrete:

- plain concrete,
- FRC with steel fibers characterized by fiber contents of 2.0% and
- FRC with 5.0% of steel fibers.

The figure clearly highlights the clear phenomenological effect of fibers when added on cementitious matrix. Fiber inclusions mainly enhance the mechanical property of SFRC in terms of both shear strength and ductility. Then, Figure 8.12 highlights the difference in responses when a different number of integration points are considered. It can be stated that an acceptable accuracy involves at least 21 points of integration, also demonstrated on the work by Bazant and Oh [1986]. A poor approximation, which takes place for integrations in which a number of considered points is lower than 21, can be observed around the peak strength and in the post-peak regime.

8.7 Closing remarks

A microplane-based plasticity approach, aimed at simulating the failure behavior of Fiber Reinforced Cementitious Composite (FRCC), has been presented in this chapter. It has been founded on the macroscopic smeared-crack approach considering the failure of FRCC in a continuum point of view. The constitutive model considers the well-known “Mixture Theory” to simulate the combined bridging interactions of fibers in concrete cracks. The interactions between steel fibers and concrete matrix, associated with bond-slip and dowel mechanisms respectively, have explicitly been accounted in the constitutive formulation. The numerical simulations demonstrate that the constitutive proposal mainly captured the fundamental behaviors of FRCC. Very good agreement between numerical results against experimental data, available in scientific literature, have been achieved in terms of peak-strength and post-cracking toughness.

9 Conclusions

This thesis addressed the mechanical behavior of Fiber Reinforced Cementitious Composite (FRCC). Particularly, it described the key results obtained in a wide experimental activity and formulated several theoretical models intended at analyzing FRCCs at different observation scales.

In the following sections a series of final comments and concluding remarks are reported and discussed.

9.1 Experimental activity

An extensive experimental campaign, performed at the Laboratory of Materials testing and Structures (LMS) of the University of Salerno, was performed for investigating the post-cracking behavior of FRCC. Four-point bending tests were performed of notched FRCC beams. Particularly, the possible influence of combining two different types of steel fibers on the resulting properties of FRCC was analyzed. Five combinations of long/short fibers were actually considered and the following observations emerged by analyzing the experimental results:

- The first-crack strength and the whole post-cracking behavior were mainly influenced by the amount of fibers.
- Softening response was observed for all specimens with a fiber content of ρ_f = 0.5%, whereas a rather plastic behavior characterized the post-cracking response of specimens with ρ_f = 1.0%.
- A slight influence of the long/short fiber combination was observed in terms

of first-crack strength: this parameter was almost irrelevant in the case of low amount of fibers ($\rho_f = 0.5\%$), while resulted in a more regular trend in the case of $\rho_f = 1.0\%$.

- The ductility indices, determined for all specimens, pointed out that no clear influence can be recognized to fiber combination in affecting the overall response of FRCC in the post-cracking regime.

As a matter of fact, the very low influence of fiber combination on the observed FRCC behavior was the key conclusion of the experimental activity. However, it is worth highlighting that this cannot be considered as a general conclusion, as in the case under consideration, the two "different" fibers were characterized by the same material, similar geometric details (i.e., hooked-ends) and rather close aspect ratios. Thus, the possible synergistic effect of combining different fibers should be investigated by considering two (or more) types of really "more different" fibers (i.e., in terms of materials, geometry and detailing). Therefore, further studies are needed for achieving a possible stable relationship between fiber type/amount/combination: such studies actually represent the possible future developments of this research.

9.2 Zero-thickness interface model formulation

Special focus of this thesis was reserved to the development of a novel constitutive formulation aimed at simulating the stress-crack opening displacement under arbitrary fracture modes: starting from simpler cases of pure mode I of cracking up to consider most complex fracture failure in mixed-modes.

An innovative approach for reproducing the fiber effects on the cracking phenomena of the concrete/mortar matrix was proposed. The well-known discrete crack approach based on zero-thickness interface elements was considered to model the interaction between fibers and mortar as well as its degradation during fracture processes under mode I, II and/or mixed ones. The matrix degradation was modeled by means of a fracture energy-based softening law formulated in the framework of the flow theory of plasticity. Then, two fundamental aspects of the fiber-mortar interaction were considered in the model, i.e. the bond behavior of fibers bridging the crack opening and the dowel effect derived by possible relative transverse displacements of the two faces of the crack. The inclusion of fibers and the above two effects were taken into account by means of the well-known Mixture Theory.

Such a constitutive proposal provides Readers with several key original contributions

listed below:

- A novel constitutive formulation to model the mechanical degradation and failure processes of FRCC under both mode I and/or mode II (mixed) types of fracture was introduced. As a matter of fact, the majority of existing constitutive models to simulate failure behavior of FRCC only take into account the fiber contribution to the traction-separation behavior under mode I tensile type of fracture, while fully neglect its contribution in mixed mode failure processes.

- A non-linear model for FRCC was implemented into interface elements (discrete or fix crack approach), instead of the classical smeared crack (continuous) approach. Classical models for concrete, based on the so-called smeared crack approach, suffer the strong FE-size dependence of the localization band width and loss of objectivity in softening ranges. Contrarily, in the Discrete Crack Approach (DCA), the discontinuity of the displacement field, due to cracking, is directly incorporated into the finite element formulation. One of the most effective procedures which adopts the DCA is the one based on Interface Elements (IE). The proposal discussed in this thesis actually belongs to this last group regarding crack propagation strategy within DCA.

- The discontinuous formulation took into account the fiber effect on concrete cracks due to both the bond-slip and dowel action. None of the existing proposals within the framework of DCA such as E-Fem, X-Fem, E-free Galerkin, etc., referred to composite materials with fibers, and to the explicit modeling of fiber effects in the post-cracking process. Actually, the proposed model formulation represents a novel contribution in this direction.

- Numerical applications at both the material and structural scale responses of FRCC members according to the “discontinuous approach” for the Finite Element Method demonstrated the soundness of the proposed model and its accuracy. The model simulated rather well several key features of FRCC tests under several stress cases. Particularly, the soundness and capabilities of this approach were assessed and discussed against experimental data available in scientific literature.

9.3 Fiber bond-slip characterization

Particular emphasis was dedicated to the description and modeling of the bond behavior of fibers embedded in cementitious matrices. The adhesive interaction between

fibers in concrete matrix is of key importance in controlling the post-cracking response of FRCC.

A unified formulation for simulating the overall bond behavior of fibers embedded in cementitious matrices was presented in this thesis. It was intended as a key element to be possibly employed in numerical models aimed at explicitly simulating the mechanical behavior of FRCC by taking into account the discrete nature of such materials and the contributions of the various constituents within the framework of the so-called discrete approaches. A series of final remarks can be drawn out on the bases of both the model formulation and the proposed applications:

- Two alternative constitutive models were proposed for obtaining the above mentioned formulation: i.e., the first one was founded on the fracture energy-based contact model, while, the second one was based on the simpler elasto-plastic behavior with isotropic linear softening.
- The limits derived by assuming a simplified bilinear shear-slip relationship for simulating the response of fibers under pull-out emerged in the final comparative analysis: although such a relationship allowed for a fully analytical solution of the problem under consideration, it lacked in simulating the highly non-linear response which developed in the post-peak stage.
- Thus, a more complex, but more accurate fracture energy-based softening model was also presented and the key aspects of the numerical procedure needed for handling such a relationship were outlined.
- The solutions obtained by considering both models were validated against experimental results obtained on pull-out tests of smooth and straight steel fibers, currently available in the scientific literature. Besides the weaknesses described for the above mentioned bilinear relationship, numerical simulations were generally in good agreement with the corresponding experimental data.
- Both models demonstrated the capability of the proposed unified formulation to capture the key aspects of complete pullout response of fibers taking into account the possible influence of relevant parameters, such as bond anchorage and fiber diameter.

As a final comment, it is worth highlighting that the proposed unified formulation (based on either of the bond models considered in this study) can be straightforwardly

employed in numerical models aimed at simulating the behavior of FRCC through discrete crack approaches, as such models (i.e., meso-mechanical ones) explicitly simulate the bond-slip response of fibers embedded in cementitious matrices. The adoption of the presented formulation within the framework of general meso-mechanical models of FRCC was, at the same time, the key motivation and the most relevant development of the proposed research.

9.4 Hinge-crack model

The results of the experimental campaign performed in this thesis were taken as a reference to validate a proposed stress-crack opening model based on a hinge-crack approach already available in the scientific literature. Therefore, a simpler and more practice-oriented model was proposed to take into account the fiber-matrix interactions, though within the framework of a "cracked-hinge" approach. This formulation appeared a more feasible method to perform "structural scale" simulations fo FRCC members. The model was intended as a reformulation of a fictitious crack model and based on fracture mechanics concepts where the stress-crack opening relationship was accounted in a similar way obtainable by considering the pure "mode I" case of the discontinuous proposal formulated in general sense for mixed-modes of fracture. The model predictions, compared with the corresponding experimental measures, demonstrated the soundness of the model to reproduce the mechanical response of FRCC members in terms of Force-Crack Tip Opening Displacement curves.

9.5 Microplane proposal

Finally, a microplane plasticity approach, aimed at simulating the failure behavior of Fiber Reinforced Cementitious Composite (FRCC), was also presented and discussed. It was based upon a continuum smeared-crack approach while its constitutive formulation considered the well-known "Mixture Theory" to taken into account the combined bridging interactions of fibers in concrete cracks. The model mainly employed the stress-crack opening law of the interface proposal, originally formulated in discontinuous manner and here straightforwardly extended in terms of a stress-strain relationship. Moreover, an elliptical CAP was proposed for the compressive microplane stress ranges. The numerical simulations demonstrated that the constitutive proposal mainly captured the fundamental behaviors of FRCC and very good agreement in terms of peak-strength and post-crack toughness was observed between numerical predictions and experimental results.

9.6 Future research lines

In the future, further researches should be performed to extend both the failure criterion and constitutive formulation proposed in this thesis with the aim to include other relevant issues such as time- and rate-dependent behaviors as well as temperature dependence in both early-age concretes or when FRCC structures were submitted to high temperatures.

Moreover, further developments should specifically be intended at bridging the divide existing between “Material Science” and “Structural Engineering” by possibly formulating a new class of numerical models featuring the most advanced accomplishments of the former field (i.e., coupled multi-physics models, multi-scale framework, homogenization techniques, etc.) and the most accurate methods for simulating the structural response and quantifying its safety levels (i.e., advanced constitutive formulations, finite element method in its more recent evolutions, etc.) to achieve a multidisciplinary breakthrough in structural safety.

The formulation of the aforementioned models and procedures, leading to a coordinated breakthrough of knowledge on concrete materials and structural engineering within clearly multiscale/multiphysics approaches, will be the direction of future research programme.

Bibliography

ACI-318-08/318R-08. *ACI Committee 318, Building code and commentary.* American Concrete Institute, ACI Farmington Hills, 2008.

ACI-544.1-96. *State-of-the-Art Report on Fiber Reinforced Concrete. Reported by ACI Committee 544, American Concrete Institute.* 1996.

ACI-544.2R-89. *Measurement of properties of fibre reinforced concrete. ACI Manual of Concrete Practice; Part 5: Masonry, Precast Concrete and Special Processes, American Concrete Institute.* 1996.

ACI-544.4R-88. *Design considerations for steel Fiber Reinforced Concrete.* American Concrete Institute, ACI Farmington Hills, 1996.

AFGC-SETRA. *Ultra High Performance Fibre-Reinforced Concretes, Interim recommendations.* AFGC Publication, France, 2002.

B. Akcay and M. Tasdemir. Mechanical behaviour and fibre dispersion of hybrid steel fibre reinforced self-compacting concrete. *Construction and Building Materials*, 28 (1):287 – 293, 2012.

F. Armero and C. Linder. Numerical simulation of dynamic fracture using finite elements with embedded discontinuities. *Int. J. of Fracture*, 160:119–141, 2009.

ASTM-C-1018. *Standard Test Method for Flexural Toughness and First-Crack Strength of Fiber-Reinforced Concrete (Using Beam With Third-Point Loading).* American Society for Testing and Materials, 1998.

B. Banholzer, W. Brameshuber, and W. Jung. Analytical evaluation of pull-out tests- The inverse problem. *Cement and Concrete Composites*, 28:564–571, 2006.

N. Banthia and N. Nandakumar. Crack growth resistance of hybrid fiber reinforced cement composites. *Cement and Concrete Composites*, 25(1):3 – 9, 2003.

N. Banthia and M. Sappakittipakorn. Toughness enhancement in steel fiber reinforced concrete through fiber hybridization. *Cement and Concrete Research*, 37(9):1366 – 1372, 2007.

N. Banthia and J. Trottier. Test methods for flexural toughness characterization of fiber reinforced concrete: Some concerns and a proposition. *ACI - Materials J.*, 92(1):48 – 57, 1995.

J. Barros and J. Figueiras. Flexural behavior of SFRC: Testing and Modeling. *ASCE - J. of Materials in Civil Engrg.*, 11(4):331–339, 1999.

J. Barros, V. Cunha, A. Ribeiro, and J. Antunes. Post-cracking behaviour of steel fibre reinforced concrete. *Material Structures*, 38(1):47 – 56, 2005.

Z. Bazant and P. Gambarova. Crack shear in concrete: crack band microplane model. *ASCE J. Struct. Eng.*, 110:2015–2035, 1984.

Z. Bazant and B. Oh. Crack band theory for fracture of concrete. *RILEM - Muterial Structures*, 93:155–177, 1983.

Z. Bazant and B. Oh. Efficient numerical integration on the surface of a sphere. *Zeitschrift fur angewandte Mathematik und Mechanik*, 66(1):37 – 49, 1986.

Z. Bazant and B. Oh. Compression failure of quasibrittle material: Nonlocal microplane model. *J. Eng. Mech. ASCE*, 118(3):540–557, 1992.

Z. Bazant and P. Prat. Microplane model for brittle plastic material: I. Theory. *J. of Engrg. Mechanics*, 114(10):1672–1689, 1988a.

Z. Bazant and P. Prat. Microplane model for brittle plastic material: II. Verification. *J. of Engrg. Mechanics*, 114(10):1689–1703, 1988b.

Z. Bazant, M. Tabbara, M. Kazemi, and G. Pijaudier-Cabot. Random particle model for fracture of aggregate or fiber composites. *J. of Engrg. Mech., ASCE*, 116:1686–1705, 1990.

Z. Bazant, Y. Xiang, M. Adley, P. Prat, and S. Akers. Microplane model for concrete: II: Data delocalization and verification. *J. Eng. Mech. ASCE*, 122(3):255–263, 1996a.

Z. Bazant, Y. Xiang, and P. Prat. Microplane model for concrete. I: Stress-strain boundaries and finite strain. *J. Eng. Mech. ASCE*, 122(3):245–255, 1996b.

Z. P. Bazant and G. D. Luzio. Nonlocal microplane model with strain-softening yield limits. *Int. J. of Solids and Structures*, 41(24–25):7209 – 7240, 2004.

Z. P. Bazant and B. H. Oh. Microplane model for progressive fracture of concrete and rock. *J. of Engrg. Mechanics*, 111(4):559 – 582, 1985.

A. Beghini, Z. Bazant, Y. Zhou, O. Gouirand, and F. Caner. Microplane model M5f for multiaxial behavior and fracture of fiber-reinforced concrete. *ASCE - J. of Materials in Civil Engrg.*, 133(1):66–75, 2007.

T. Belytschko, Y. Lu, and L. Gu. Crack propagation by element-free Galerkin methods. *Engrg. Fracture Mechanics*, 51(2):295 – 315, 1995.

T. Belytschko, D. Organ, and C. Gerlach. Element-free galerkin methods for dynamic fracture in concrete. *Computer Methods in Applied Mechanics and Engineering*, 187 (3-4):385 – 399, 2000.

S. Billington. Alterate approaches to simulating the performance of ductile fiber-reinforced cement-based materials in structural applications. In N. Bicanic, R. de Borst, H. Mang, and G. Meschke, editors, *Computational Modelling of Concrete Structures, Rohrmoos/Schladming, Austria*, pages 15–29, 2010.

S. Bishnoi and K. L. Scrivener. µic: A new platform for modelling the hydration of cements. *Cement and Concrete Research*, 39(4):266 – 274, 2009.

A. Blanco, P. Pujadas, A. de la Fuente, S. Cavalaro, and A. Aguado. Application of constitutive models in european codes to rc–frc. *Construction and Building Materials*, 40(0):246 – 259, 2013.

J. Bolander and S. Saito. Discrete modeling of short-fiber reinforcement in cementitious composites. *Advanced Cement Based Materials*, 6(3-4):76–86, 1997.

A. M. Brandt. Fibre reinforced cement-based (FRC) composites after over 40 years of development in building and civil engineering. *Composite Structures*, 86(1-3):3 – 9, 2008.

M. Brocca, L. Brinson, and Z. Bazant. Three-dimensional constitutive model for shape memory alloys based on microplane model. *J. of the Mechanics and Physics of Solids*, 50(5):1051 – 1077, 2002.

N. Buratti, C. Mazzotti, and M. Savoia. Post-cracking behaviour of steel and macro-synthetic fibre-reinforced concretes. *Construction and Building Materials*, 25(5): 2713 – 2722, 2011.

M. Butler, V. Mechtcherine, and S. Hempel. Experimental investigations on the durability of fibre-matrix interfaces in textile-reinforced concrete. *Cement and Concrete Composites*, 31:221–231, 2009.

A. Caballero, K. Willam, and I. Carol. Consistent tangent formulation for 3D interface modeling of cracking/fracture in quasi-brittle materials. *Computer Methods in Applied Mechanics and Engrg.*, 197:2804–2822, 2008.

A. Caggiano and E. Martinelli. A unified formulation for simulating the bond behaviour of fibres in cementitious materials. *Materials & Design*, 42(0):204 – 213, 2012.

A. Caggiano, M. Cremona, C. Faella, C. Lima, and E. Martinelli. Fracture behavior of concrete beams reinforced with mixed long/short steel fibers. *Construction and Building Materials*, 37(0):832 – 840, 2012a.

A. Caggiano, G. Etse, and E. Martinelli. Zero-thickness interface model formulation for failure behavior of fiber-reinforced cementitious composites. *Computers & Structures*, 98-99(0):23 – 32, 2012b.

A. Caggiano, E. Martinelli, and C. Faella. A fully-analytical approach for modelling the response of FRP plates bonded to a brittle substrate. *Int. J. of Solids and Structures*, 49(17):2291 – 2300, 2012c.

A. Caggiano, M. Pepe, E. Koenders, E. Martinelli, and G. Etse. *Numerical Modeling of Hydration Process and Temperatura Evolution in Early Age Concrete*. Mecánica Computacional, Volume XXXI. Number 12. Heat Transfer (A), 2012d.

I. Carol and Z. Bazant. Damage and plasticity in microplane theory. *Int. J. of Solids and Structures*, 34(29):3807 – 3835, 1997.

I. Carol, P. C. Prat, and Z. P. Bažant. New explicit microplane model for concrete: Theoretical aspects and numerical implementation. *Int. J. of Solids and Structures*, 29(9):1173 – 1191, 1992.

I. Carol, P. Prat, and C. Lopez. Normal/shear cracking model: Applications to discrete crack analysis. *J. of Engrg. Mechanics - ASCE*, 123:765–773, 1997.

I. Carol, M. Jirasek, and Z. Bazant. A thermodynamically consistent approach to microplane theory. Part I. Free energy and consistent microplane stresses. *Int. J. of Solids and Structures*, 38(17):2921 – 2931, 2001.

I. Carol, M. Jirasek, and Z. P. Bazant. A framework for microplane models at large strain, with application to hyperelasticity. *Int. J. of Solids and Structures*, 41(2):511 – 557, 2004.

A. Carosio, K. Willam, and G. Etse. On the consistency of viscoplastic formulations. *Int. J. of Solids and Structures*, 37(48-50):7349 – 7369, 2000.

A. Carpinteri and R. Brighenti. Fracture behaviour of plain and fiber-reinforced concrete with different water content under mixed mode loading. *Materials & Design*, 31(4): 2032 – 2042, 2010.

A. Carpinteri, B. Chiaia, and K. M. Nemati. Complex fracture energy dissipation in concrete under different loading conditions. *Mechanics of Materials*, 26(2):93 – 108, 1997.

CEB-FIP-90. *CEB, CEB-FIP Model Code 1990*. Bulletin d'information, Thomas Telford, London, pp. 203-205, 1993.

J. Cervenka, Z. Bazant, and M. Wierer. Equivalent localization element for crack band approach to mesh-sensitivity in microplane model. *Int. J. for Numerical Methods in Engrg.*, 62(5):700–726, 2005.

M. Cervera, M. Chiumenti, and R. Codina. Mixed stabilized finite element methods in nonlinear solid mechanics: Part ii: Strain localization. *Computer Methods in Applied Mechanics and Engineering*, 199(37-40):2571 – 2589, 2010.

B. Chen and J. Liu. Residual strength of hybrid-fiber-reinforced high-strength concrete after exposure to high temperatures. *Cement and Concrete Research*, 34(6):1065 – 1069, 2004.

CNR-DT-204. *Guidelines for design, construction and production control of fiber reinforced concrete structures*. National Research Council of Italy, 2006.

C. Comi and U. Perego. Fracture energy based bi-dissipative damage model for concrete. *Int. J. of Solids and Structures*, 38(36-37):6427 – 6454, 2001.

P. Cundall. *A computer model for simulating progressive large scale movements in blocky rock systems*. Proc. Int. Symp. Rock Fracture, ISRM, Nancy, France, 2-8, 1971.

V. Cunha, J. Barros, and J. Sena-Cruz. Pullout behavior of steel fibers in self-compacting concrete. *J. of Engrg. Mechanics - ASCE*, 22(1):1–9, 2010.

V. M. Cunha, J. A. Barros, and J. M. Sena-Cruz. A finite element model with discrete embedded elements for fibre reinforced composites. *Computers & Structures*, 94–95 (0):22 – 33, 2012.

CUR. *Bepaling van de Buigtrekterk de Buigtaaiheid en de Equivalente Buigtreksterkte van Staalvezelbeton.* Civieltechnisch Centrum Uitvoering Research en Regelgeving, The Netherlands, 12 pp., 1994.

DAfStB. *Richtlinie "Stahlfaserbeton" (Directive for SFRC).* Deutscher Ausschuss fur Stahlbeton, Germany - (In German), 2010.

E. Dawood and M. Ramli. Development of high strength flowable mortar with hybrid fiber. *Construction and Building Materials*, 24(6):1043 – 1050, 2010.

E. Dawood and M. Ramli. High strength characteristics of cement mortar reinforced with hybrid fibres. *Construction and Building Materials*, 25(5):2240 – 2247, 2011.

E. Dawood and M. Ramli. Mechanical properties of high strength flowing concrete with hybrid fibers. *Construction and Building Materials*, 28(1):193 – 200, 2012.

DBV. *Merkblatt "Stahlfaserbeton" (SFRC leaflet).* Deutscher Beton- und Bautechnik-Verein E.V., Germany - (In German), 2001.

R. De Borst and M. Gutierrez. A unified framework for concrete damage and fracture models including size effects. *Int. J. of Fracture*, 95:261–277, 1999.

R. de Borst, J. Pamin, R. Peerlings, and L. Sluys. On gradient-enhanced damage and plasticity models for failure in quasi-brittle and frictional materials. *Comp. Mech.*, 17:130–141, 1995.

G. De Schutter. Applicability of degree of hydration concept and maturity method for thermo-visco-elastic behaviour of early age concrete. *Cement and Concrete Composites*, 26(5):437 – 443, 2004.

S. Dei Poli, M. Di Prisco, and P. Gambarova. Shear response, deformations, and subgrade stiffness of a dowel bar embedded in concrete. *ACI Structural J.*, 89(6):665–675, 1992.

G. Di Luzio. A symmetric over-nonlocal microplane model M4 for fracture in concrete. *Int. J. of Solids and Structures*, 44(13):4418 – 4441, 2007.

M. di Prisco, G. Plizzari, and L. Vandewalle. Fibre reinforced concrete: new design perspectives. *Material Structures*, 42(9):1261 – 1281, 2009.

DIN-1048. *Prüfverfahren für Beton; Teil 1: Frischbeton.* Festbeton in Bauwerken und Bauteilen, 1991.

Y. Ding, Y. Zhang, and A. Thomas. The investigation on strength and flexural toughness of fibre cocktail reinforced self-compacting high performance concrete. *Construction and Building Materials*, 23(1):448 – 452, 2009.

Y. Ding, Z. You, and S. Jalali. Hybrid fiber influence on strength and toughness of RC beams. *Composite Structures*, 92(9):2083 – 2089, 2010.

Y. Ding, C. Azevedo, J. Aguiar, and S. Jalali. Study on residual behaviour and flexural toughness of fibre cocktail reinforced self compacting high performance concrete after exposure to high temperature. *Construction and Building Materials*, 26(1):21 – 31, 2012.

J. S. Dolado and K. van Breugel. Recent advances in modeling for cementitious materials. *Cement and Concrete Research*, 41(7):711 – 726, 2011.

K. Duan, X. Hu, and F. H. Wittmann. Size effect on specific fracture energy of concrete. *Engrg. Fracture Mechanics*, 74(1-2):87 – 96, 2007.

H. Dulacska. Dowel action of reinforcement crossing cracks in concrete. *ACI Structural J.*, 69(12):754–757, 1972.

D. Dupont and L. Vandewalle. Distribution of steel fibres in rectangular sections. *Cement and Concrete Composites*, 27(3):391 – 398, 2005.

E. Dvorkin, A. Cuitino, and G. Gioia. Finite elements with displacement embedded localization lines insensitive to mesh size and distortions. *Int. J. for Numerical Methods in Engrg.*, 30:541–564, 1990.

EHE08. *Comisión Permanente del Hormigón (Ministerio de Fomento), Instrucción del Hormigón Estructural*. Spanish Code - In Spanish, 2008.

R. Einsfeld, A. Elwi, T. Bittencourt, and L. Martha. Numerical simulation of fracturing in concrete structures using a combination of smeared and discrete approaches. *International Journal of Rock Mechanics and Mining Sciences*, 34(3-4):189.e1 – 189.e11, 1997.

B. El-Ariss. Behavior of beams with dowel action. *Engrg. Structures*, 29(6):899 – 903, 2007.

A. S. El-Dieb. Mechanical, durability and microstructural characteristics of ultra-high-strength self-compacting concrete incorporating steel fibers. *Materials & Design*, 30 (10):4286 – 4292, 2009.

EN-12390-3. *Testing of hardened concrete. Part 3: compressive strength of test specimens.* BSI, 2009.

EN-14651. *Test method for metallic fibrered concrete - Measuring the flexural tensile strength (limit of proportionality (LOP), residual).* NS-EN 14651:2005, 2005.

G. Etse. *Theoretische und numerische Untersuchung zum diffusen und lokalisierten Versagen in Beton.* PhD thesis, University of Karlsruhe, Karlsruhe, Germany, 1992.

G. Etse and M. Nieto. Cosserat continua-based micro plane modelling. Theory and numerical analysis. *Latin American applied research*, 34:229 – 240, 2004.

G. Etse and K. Willam. A fracture energy-based constitutive formulation for inelastic behavior of plain concrete. *ASCE-JEM*, 120:1983–2011, 1994.

G. Etse, M. Nieto, and P. Steinmann. A micropolar microplane theory. *Int. J. of Engrg. Science*, 41(13–14):1631 – 1648, 2003.

G. Etse, A. Caggiano, and S. Vrech. *Constitutive microplane and interface laws for multiscale analysis of steel fiber concrete.* ECCOMAS 2012 - European Congress on Computational Methods in Applied Sciences and Engineering, e-Book Full Papers, pp. 7459-7477, 2012.

Eurocode-2. *Design of concrete structures.* EN 1992-1-1, 2004.

A. Ezeldin and P. Balaguru. Normal- and high-strength fiber-reinforced concrete under compression. *ASCE - J. of Materials in Civil Engrg.*, 4(4):415–429, 1992.

A. Fantilli and P. Vallini. A cohesive interface model for the pollout of inclined steel fibers in cementitious matrixes. *J. of Advanced Concrete Technology*, 5(2):247–258, 2007.

A. P. Fantilli, P. Vallini, and B. Chiaia. Ductility of fiber-reinforced self-consolidating concrete under multi-axial compression. *Cement and Concrete Composites*, 33(4): 520 – 527, 2011.

Faserbeton-R. *Osterreichische Vereinigung fur Beton-und Bautechnik.* OBBV, Wien, 2002.

L. Ferrara and A. Meda. Relationships between fibre distribution, workability and the mechanical properties of SFRC applied to precast roof elements. *Materials and Structures*, 39:411–420, 2006.

G. Ferro, A. Carpinteri, and G. Ventura. Minimum reinforcement in concrete structures and material/structural instability. *Int. J. of Fracture*, 146:213–231, 2007.

fib Model-Code. *Model Code 2010 - First complete draft, Vol. 1*. Comité Euro-International du Beton-Federation International de la Precontrainte, Paris, 2010a.

fib Model-Code. *Model Code 2010 - First complete draft, Vol. 2*. Comité Euro-International du Beton-Federation International de la Precontrainte, Paris, 2010b.

P. Folino. *Computational Analysis of Failure Behavior of Arbitrary Strength Concretes*. PhD thesis, Universidad de Buenos Aires, LMNI-FI-UBA, 2012.

P. Folino and G. Etse. Performance dependent model for normal and high strength concretes. *Int. J. of Solids and Structures*, 49(5):701 – 719, 2012.

P. Folino, G. Etse, and A. Will. A performance dependent failure criterion for normal and high strength concretes. *ASCE J. of Engrg. Mechanics*, 135(12):1393 – 1409, 2009.

E. Gal and R. Kryvoruk. Meso-scale analysis of FRC using a two-step homogenization approach. *Computers & Structures*, 89(11-12):921 – 929, 2011.

A. Gens, I. Carol, and E. Alonso. An interface element formulation for the analysis of soil-reinforcement interaction. *Computers and Geotechnics*, 7(1-2):133–151, 1988.

R. Gettu. *Fibre Reinforced Concrete: design and applications*. BEFIB 2008, Bagneux, France, RILEM Publications S.A.R.L., PRO60, 2008.

R. Gettu, D. Gardner, H. Saldivar, and B. Barragan. Study of the distribution and orientation of fibers in SFRC specimens. *Materials and Structures*, 38:31–37, 2005.

A. Ghavami, A. Abedian, and M. Mondali. Finite difference solution of steady state creep deformations in a short fiber composite in presence of fiber/matrix debonding. *Materials & Design*, 31(5):2616 – 2624, 2010.

V. Gopalaratnam, S. Shah, G. Batson, M. Criswell, V. Ramakishnan, and M. Wecharatana. Fracture toughness of fiber reinforced concrete. *ACI - Materials J.*, 88(4):339 – 353, 1991.

V. S. Gopalaratnam and R. Gettu. On the characterization of flexural toughness in fiber reinforced concretes. *Cement and Concrete Composites*, 17(3):239 – 254, 1995.

P. Grassl and R. Rempling. A damage-plasticity interface approach to the meso-scale modelling of concrete subjected to cyclic compressive loading. *Engineering Fracture Mechanics*, 75(16):4804 – 4818, 2008.

T. Guttema. *Ein Beitrag zur realitatsnahen Modellierung und Analyse von stahlfaserverstarkten Stahlbeton- und Stahlbetonflachentragwerken.* PhD thesis, Universitat Kassel, 2003.

M. Hassanzadeh. Determination of fracture zone properties in mixed mode I and II. *Engrg. Fracture Mechanics*, 35(4-5):845–853, 1990.

T. Hettich, A. Hund, and E. Ramm. Modeling of failure in composites by X-FEM and level sets within a multiscale framework. *Computer Methods in Applied Mechanics and Engrg.*, 197(5):414–424, 2008.

A. Hillerborg, M. Modeer, and P. Petersson. Analysis of crack formation and crack growth in concrete by means of fracture mechanics and finite elements. *Cement and Concrete Composites*, 6(6):773–781, 1976.

M. Hsie, C. Tu, and P. Song. Mechanical properties of polypropylene hybrid fiber-reinforced concrete. *Materials Science and Engrg.: A*, 494(1–2):153 – 157, 2008.

X. Hu, R. Day, and P. Dux. Biaxial failure model for fiber reinforced concrete. *ASCE - J. of Materials in Civil Engrg.*, 15(6):609–615, 2003.

A. Hund and E. Ramm. Locality constraints within multiscale model for non-linear material behaviour. *Int. J. for Numerical Methods in Engrg.*, 70(13):1613–1632, 2006.

A. Idiart. *Coupled analysis of degradation processes in concrete specimens at the meso-level.* PhD thesis, Universitat Politecnica de Catalunya, ETSECCCP-UPC, 2009.

J. Jeong, P. Mounanga, H. Ramézani, and M. Bouasker. A new multi-scale modeling approach based on hygro-cosserat theory for self-induced stress in hydrating cementitious mortars. *Computational Materials Science*, 50(7):2063 – 2074, 2011.

M. Jirasek and Z. P. Bazant. Macroscopic fracture characteristics of random particle systems. *Int. J. of Fracture*, 69:201–228, 1994.

M. Jirasek and T. Zimmermann. Embedded crack model. Part II: combination with smeared cracks. *Int. J. for Numerical Methods in Engrg.*, 50(6):1291–1305, 2001.

JSCE-SF4. *Method of tests for flexural strength and flexural toughness of steel fibre reinforced concrete. Concrete Library of previous Japan Society of Civil Engineers (JSCE), Tokyo, 3, pp. 58-61.* 1984.

P. Kabele. Equivalent continuum model of multiple cracking. *Engineering Mechanics*, 9 (1-2):75–90, 2002.

L. Kaczmarczyk and C. J. Pearce. A corotational hybrid-trefftz stress formulation for modelling cohesive cracks. *Computer Methods in Applied Mechanics and Engrg.*, 198 (15-16):1298 – 1310, 2009.

A. Katz and V. Li. Inclination angle effect of carbon fibers in cementitious composites. *J. of Engrg. Mechanics - ASCE*, 121(12):1340–1348, 1995.

T. Kawai. Some considerations on the finite element method. *Int. J. Numer. Meth. Engrg.*, 16:81 – 120, 1980.

A. Khaloo and N. Kim. Influence of concrete and fiber characteristics on behavior of steel fiber reinforced concrete under direct shear. *ACI Materials J.*, 94(6):592–601, 1997.

D. Kim, A. Naaman, and S. El-Tawi. Comparative flexural behavior of four fiber reinforced cementitious composites. *Cement & Concrete Composites*, 30:917 – 928, 2008.

D. Kim, S. Park, G. Ryu, and K. Koh. Comparative flexural behavior of hybrid ultra high performance fiber reinforced concrete with different macro fibers. *Construction and Building Materials*, 25(11):4144 – 4155, 2011.

S.-M. Kim and R. K. A. Al-Rub. Meso-scale computational modeling of the plastic-damage response of cementitious composites. *Cement and Concrete Research*, 41(3): 339 – 358, 2011.

R. Klein. *Concrete and abstract Voronoi diagrams*. Lecture Notes in Computer Science, Springer-Verlag, Berlin, 1989.

E. Koenders. *Simulation of volume changes in hardening cement-based materials*. PhD thesis. Delft University of Technology, Delft, The Netherlands, 1997.

A. Kooiman. *Modelling steel fibre reinforced concrete for structural design*. Doctoral Thesis at the Technical University of Delft (The Netherlands), 2000.

H. Krenchel. *Fiber spacing and specific fiber surface*. In: Neville A, editor. Fibre reinforced cement and concrete. UK: The Construction Press; p. 69–79, 1975.

E. Kuhl and E. Ramm. Microplane modelling of cohesive frictional materials. *Europ. J. Mech./A: Solids*, 19:121–143, 2000.

E. Kuhl, E. Ramm, and K. Willam. Failure analysis of elasto-plastic material models on different levels of observation. *Int. J. of Solids and Structures*, 37(48–50):7259 – 7280, 2000.

E. Kuhl, P. Steinmann, and I. Carol. A thermodynamically consistent approach to microplane theory. Part II. Dissipation and inelastic constitutive modeling. *Int. J. of Solids and Structures*, 38(17):2933 – 2952, 2001.

F. Laranjeira, C. Molins, and A. Aguado. Predicting the pullout response of inclined hooked steel fibers. *Cement and Concrete Research*, 40(10):1471 – 1487, 2010.

F. Laranjeira, A. Aguado, C. Molins, S. Grunewald, J. Walraven, and S. Cavalaro. Framework to predict the orientation of fibers in FRC: A novel philosophy. *Cement and Concrete Research*, 42(6):752 – 768, 2012.

J. Lee and G. Fenves. Plastic-damage model for cyclic loading of concrete structures. *ASCE - JEM*, 124(8):892 – 901, 1998.

M. Lee and B. Barr. A four-exponential model to describe the behaviour of fibre reinforced concrete. *Materials and Structures*, 37(7):464–471, 2003.

Y. Lee and J. Kim. Numerical analysis of the early age behavior of concrete structures with a hydration based microplane model. *Computers & Structures*, 87(17–18):1085 – 1101, 2009.

J. Leite, V. Slowik, and H. Mihashi. Computer simulation of fracture processes of concrete using mesolevel models of lattice structures. *Cement and Concrete Research*, 34(6):1025 – 1033, 2004.

M. Leukart and E. Ramm. A comparison of damage models formulated on different material scales. *Computational Materials Science*, 28(3–4):749 – 762, 2003.

C. Leung and P. Geng. Micromechanical modeling of softening behavior in steel fiber reinforced cementitious composites. *Int. J. of Solids and Structures*, 35(31-32):4205–4222, 1998.

F. Li and Z. Li. Continuum damage mechanics based modeling of fiber reinforced concrete in tension. *Int. J. of Solids and Structures*, 38(5):777–793, 2001.

V. Li and Y. Chan. Determination of interfacial debond mode for fiber-reinforced cementitious composites. *J. of Engrg. Mechanics - ASCE*, 120(4):707–719, 1994.

V. Li, Y. Wang, and S. Backer. A micromechanical model of tension-softening and bridging toughening of short random fiber reinforced brittle matrix composites. *J Mech Phys Solids*, 39(5):607 – 625, 1991.

Z. Li, F. Li, T. Chang, and Y. Mai. Uniaxial tensile behavior of concrete reinforced with randomly distributed short fibers. *ACI Materials J.*, 95(5):564–574, 1998.

N. Libre, M. Shekarchi, M. Mahoutian, and P. Soroushian. Mechanical properties of hybrid fiber reinforced lightweight aggregate concrete made with natural pumice. *Construction and Building Materials*, 25(5):2458 – 2464, 2011.

G. Lilliu and J. van Mier. 3D lattice type fracture model for concrete. *Engrg. Fracture Mechanics*, 70:927–941, 2003.

T. Lim, P. Paramasivam, and S. Lee. An analytical model for tensile behaviour of steel fiber concrete. *ACI Materials J.*, 84(4):286–298, 1987.

C. Liu, M. Lovato, M. Stout, and Y. Huang. Measurement of the fracture toughness of a fiber-reinforced composite using the Brazilian disk geometry. *Int. J. of Fracture*, 87: 241–263, 1997.

Z. Liu, T. Menouillard, and T. Belytschko. An XFEM/Spectral element method for dynamic crack propagation. *Int. J. of Fracture*, 169:183–198, 2011.

C. Lopez. *Microstructural analysis of concrete fracture using interface elements. Application to various con-cretes (In Spanish)*. PhD thesis, Universitat Politecnica de Catalunya, ETSECCCP-UPC, 1999.

C. M. Lopez, I. Carol, and A. Aguado. Meso-structural study of concrete fracture using interface elements. I: numerical model and tensile behavior. *Materials and Structures*, 41(3):583–599, 2008a.

C. M. Lopez, I. Carol, and A. Aguado. Meso-structural study of concrete fracture using interface elements. II: compression, biaxial and brazilian test. *Materials and Structures*, 41(3):601–620, 2008b.

R. Lorefice, G. Etse, and I. Carol. Viscoplastic approach for rate-dependent failure analysis of concrete joints and interfaces. *Int. J. of Solids and Structures*, 45(9): 2686–2705, 2008.

H. Manzano, J. Dolado, and A. Ayuela. *Prediction of the mechanical properties of the major constituent phases of cementitious systems by atomistic simulations*. RILEM Proceedings PRO 58: 47–55, 2008.

H. Manzano, J. Dolado, and A. Ayuela. Elastic properties of the main species present in portland cement pastes. *Acta Materialia*, 57(5):1666 – 1674, 2009a.

H. Manzano, J. S. Dolado, and A. Ayuela. Structural, mechanical, and reactivity properties of tricalcium aluminate using first-principles calculations. *Journal of the American Ceramic Society*, 92(4):897 – 902, 2009b.

O. Manzoli, J. Oliver, G. Diaz, and A. Huespe. Three-dimensional analysis of reinforced concrete members via embedded discontinuity finite elements. *IBRACON*, 1(1): 58–83, 2008.

V. Mechtcherine. Towards a durability framework for structural elements and structures made of or strengthened with high-performance fibre-reinforced composites. *Construction and Building Materials*, 31(0):94 – 104, 2012.

G. Meschke and P. Dumstorff. Energy-based modeling of cohesive and cohesionless cracks via X-FEM. *Computer Methods in Applied Mechanics and Engrg.*, 196(21-24): 2338 – 2357, 2007.

F. Minelli and F. Vecchio. Compression field modeling of fiber-reinforced concrete members under shear loading. *ACI Structural J.*, 106(2):244–252, 2006.

D. J. Moes, N. and T. Belytschko. A finite element method for crack growth without remeshing. *Int. J. for Numerical Methods in Engrg.*, 46:131–150, 1999.

A. Naaman and H. Najm. Bond-slip mechanisms of steel fibers in concrete. *ACI Materials J.*, 88:135–145, 1991.

A. Naaman and H. Reinhardt. Proposed classification of HPFRC composites based on their tensile response. *Materials and Structures*, 39:547–555, 2006.

M. Nataraja, N. Dhang, and A. Gupta. Stress-strain curves for steel-fiber reinforced concrete under compression. *Cement and Concrete Composites*, 21(5-6):383 – 390, 1999.

NB. *Sprayed Concrete for Rock Support - Technical Specifications and Guidelines*. Norvegian Concrete Association, 7, 74 pp., 1993.

NBN-B-15-238. *Essai des betons renforces des fibres. Essai de Flexion sur eprouvettes prismatiques (Testing of fiber reinforced concrete. Bending test on prismatic specimens)*. Belgian Code - In French, 1992.

NFP-18409. *Beton avec fibres metalliques - Essai de flexion (Steel Fiber Concrete - Bending test)*. French Code - In French, 1993.

G. D. Nguyen. A thermodynamic approach to non-local damage modelling of concrete. *International Journal of Solids and Structures*, 45(7-8):1918 – 1934, 2008.

T.-H. Nguyen, A. Toumi, and A. Turatsinze. Mechanical properties of steel fibre reinforced and rubberised cement-based mortars. *Materials & Design*, 31(1):641 – 647, 2010.

B. Oh, J. Kim, and Y. Choi. Fracture behavior of concrete members reinforced with structural synthetic fibers. *J. of Engrg. Mechanics - ASCE*, 74:243–257, 2007.

J. Olesen. Fictitious crack propagation in fiber-reinforced concrete beams. *J. of Engrg. Mechanics - ASCE*, 127(3):272–280, 2001.

J. Oliver. Consistent characteristic length for smeared cracking models. *Int. J. for Numerical Methods in Engrg.*, 28:461–474, 1989.

J. Oliver. Modelling strong discontinuities in solid mechanics via strain softening constitutive equation. 1. fundamentals. *Int. J. for Numerical Methods in Engrg.*, 39: 3575–3600, 1996.

J. Oliver, A. Huespe, M. Pulido, and E. Chaves. From continuum mechanics to fracture mechanics: the strong discontinuity approach. *Engrg. Fracture Mechanics*, 69:113–136, 2002.

J. Oliver, A. Huespe, and P. Sanchez. A comparative study on finite elements for capturing strong discontinuities: E-FEM vs X-FEM. *Computer Methods in Applied Mechanics and Engrg.*, 195:4732–4752, 2006.

J. Oliver, D. Linero, A. Huespe, and O. Manzoli. Two-dimensional modeling of material failure in reinforced concrete by means of a continuum strong discontinuity approach. *Computer Methods in Applied Mechanics and Engrg.*, 197:332–348, 2008.

J. Oliver, D. Mora, A. Huespe, and R. Weyler. A micromorphic model for steel fiber reinforced concrete. *International Journal of Solids and Structures*, 49(21):2990 – 3007, 2012.

J. Ozbolt and A. Sharma. Numerical simulation of reinforced concrete beams with different shear reinforcements under dynamic impact loads. *Int. J. of Impact Engrg.*, 38(12):940 – 950, 2011.

J. Ozbolt, Y. Li, and I. Kozar. Microplane model for concrete with relaxed kinematic constraint. *Int. J. of Solids and Structures*, 38(16):2683 – 2711, 2001.

A. Pandolfi and M. Ortiz. An efficient adaptive procedure for three-dimensional fragmentation simulations. *Engineering with Computers*, 18:148–159, 2002.

A. Pandolfi, P. Guduru, M. Ortiz, and A. Rosakis. Three dimensional cohesive-element analysis and experiments of dynamic fracture in C300 steel. *Int. J. of Solids and Structures*, 37:3733–3760, 2000.

K. Park, G. Paulino, and J. Roesler. Cohesive fracture model for functionally graded fiber reinforced concrete. *Cement and Concrete Composites*, 40:956–965, 2010.

S. Park, D. Kim, G. Ryu, and K. Koh. Tensile behavior of ultra high performance hybrid fiber reinforced concrete. *Cement and Concrete Composites*, 34(2):172 – 184, 2012.

R. Peerlings, T. Massart, and M. Geers. A thermodynamically motivated implicit gradient damage framework and its application to brick masonry cracking. *Computer Methods in Applied Mechanics and Engrg.*, 193(30-32):3403 – 3417, 2004.

E. B. Pereira, G. Fischer, and J. A. Barros. Direct assessment of tensile stress-crack opening behavior of strain hardening cementitious composites (SHCC). *Cement and Concrete Research*, 42(6):834 – 846, 2012.

S. Pont and A. Ehrlacher. Numerical and experimental analysis of chemical dehydration, heat and mass transfers in a concrete hollow cylinder submitted to high temperatures. *International Journal of Heat and Mass Transfer*, 47(1):135 – 147, 2004.

F. Puertas, M. Palacios, H. Manzano, J. Dolado, A. Rico, and J. Rodríguez. A model for the c-a-s-h gel formed in alkali-activated slag cements. *Journal of the European Ceramic Society*, 31(12):2043 – 2056, 2011.

T. Rabczuk and T. Belytschko. Application of particle methods to static fracture of reinforced concrete structures. *Int. J. of Fracture*, 137(1-4):19–49, 2006.

T. Rabczuk, J. Akkermann, and J. Eibl. A numerical model for reinforced concrete structures. *Int. J. of Solids and Structures*, 42(5–6):1327 – 1354, 2005.

F. Radtke, A. Simone, and L. Sluys. A computational model for failure analysis of fibre reinforced concrete with discrete treatment of fibres. *Engrg. Fracture Mechanics*, 77 (4):597 – 620, 2010.

RILEM-TC162-TDF. *Test and design methods for steel fibre reinforced concrete: bending test.* 2002.

RILEM-TC162-TDF. Test and design methods for steel fibre reinforced concrete - σ - ϵ design method: final recommendation. *Mater Struct*, 36(262):560 – 567, 2003.

J. Rodriguez. *Study of behavior of granular heterogeneous media by means of analogical mathematical discontinuous models.* Thesis presented to the Universidad Politecnico de Madrid, at Madrid, Spain, in partial fulfillment of the requirements for the degree of Doctor of Philosophy (in Spanish), 1974.

J. Rots, P. Nauta, G. Kusters, and J. Blaauwendraad. Smeared crack approach and fracture localization in concrete. *Heron*, 30:1–49, 1985.

M. Sahmaran and I. Yaman. Hybrid fiber reinforced self-compacting concrete with a high-volume coarse fly ash. *Construction and Building Materials*, 21(1):150 – 156, 2007.

P. Sanchez, P. Blanco, A. Huespe, and R. Feijoo. Failure-oriented multi-scale variational formulation: Micro-structures with nucleation and evolution of softening bands. *Computer Methods in Applied Mechanics and Engineering*, 257(0):221 – 247, 2013.

E. Schauffert and G. Cusatis. Lattice discrete particle model for fiber reinforced concrete (LDPM-F): I. theory. *J of Eng Mech*, 138(7):826–833, 2012.

E. Schauffert, G. Cusatis, D. Pelessone, J. O'Daniel, and J. Baylot. Lattice discrete particle model for fiber reinforced concrete (LDPM-F): II: Tensile fracture and multiaxial loading behavior. *J of Eng Mech*, 138(7):834–841, 2012.

E. Schlangen, E. Koenders, and K. van Breugel. Influence of internal dilation on the fracture behaviour of multi-phase materials. *Engineering Fracture Mechanics*, 74 (1–2):18 – 33, 2007.

H. Schorn and U. Rode. *3-D modelling of process zone in concrete by numerical simulation*. In: Shah SP, Swartz SE, editors. Fracture of concrete and rock. New York: Springer Verlag; pp. 220-228, 1987.

P. E. C. Seow and S. Swaddiwudhipong. Failure surface for concrete under multiaxial load - a unified approach. *ASCE - J. of Materials in Civil Engrg.*, 17(2):219–228, 2005.

P. Shah and C. Ouyang. Mechanical behavior of fiber-reinforced cement-based composites. *J. of Engrg. Mechanics - ASCE*, 74(11):2727–2738, 1991.

S. Shah. Size-effect method for determining fracture energy and process zone size of concrete. *Materials and Structures*, 23:461–465, 1990.

J. Shannag, R. Brincker, and W. Hansen. Pullout behavior of steel fibers from cement-based composites. *Cement and Concrete Research*, 27:925–936, 1997.

SIA-162-6. *Stahlfaserbeton*. Schweizerischer Ingenieur und Architekten-Verein, Postfach, 8039 Zurich, 1999.

J. Simo and T. Hughes. *Computational Inelasticity*, volume 7. Interdisciplinary Applied Mathematics, Springer, New York, 1998.

I. Singh, B. Mishra, and M. Pant. An enrichment based new criterion for the simulation of multiple interacting cracks using element free Galerkin method. *Int. J. of Fracture*, 167:157–171, 2011.

S. Singh, A. Shukla, and R. Brown. Pullout behavior of polypropylene fibers from cementitious matrix. *Cement and Concrete Research*, 34(10):1919 – 1925, 2004.

L. Sorelli, A. Meda, and G. Plizzari. Bending and uni-axial tensile tests on concrete reinforced with hybrid steel fibers. *ASCE - J. of Materials in Civil Engrg.*, 17(5):519 – 527, 2005.

P. Soroushian and C. Lee. Distribution and orientation of fibers in steel fiber reinforced concrete. *ACI - Materials J*, 87(5):433–439, 1990.

P. Soroushian, K. Obaseki, and M. Rojas. Bearing strength and stiffness of concrete under reinforcing bars. *ACI Materials J.*, 84(3):179–184, 1987.

Stalfiberbetong. *Rekommendationer for konstruction, utforande och provning Betongrapport n.4.* Svenska Betongforeningen, Betongrapport, 1995.

H. Stang and J. Olesen. On the interpretation of bending tests on FRC materials. In N. Bicanic, R. de Borst, H. Mang, and G. Meschke, editors, *Third Int. Conference on Fracture Mechanics of Concrete and Concrete Structures (FRAMCOS-3), Gifu, Japan*, pages 511–520, 1998.

H. Stang, Z. Li, and S. Shah. Pullout problem: stress versus fracture mechanical approach. *J. of Engrg. Mechanics - ASCE*, 116(10):2136–2150, 1990.

T. Stankowski, K. Runesson, and S. Sture. Fracture and slip of interfaces in cementitious composites. I: Characteristics, II: Implementation. *ASCE - J. Engrg. Mech.*, 119(2): 292–327, 1993.

P. Stroeven. *Local strength reduction at boundaries due to nonuniformity of steel fibre distribution.* In: Proceedings of the international conference "Specialist Techniques and Materials for Concrete Construction", Dundee (UK), 8–10 September 1999, p. 377–87, 1999.

H. Tlemat, K. Pilakoutas, and K. Neocleous. Stress-strain characteristic of SFRC using recycled fibres. *Materials and Structures*, 39:365–377, 2006.

C. Trusdell and R. Toupin. *The classical field theories,*, volume III/I. Handbuch der Physik, Springer-Verlag, Berlin, 1960.

F. Ulm and O. Coussy. The chunnel fire i: Chemoplastic softening in rapidly heated concrete. *ASCE, Journal of Engineering Mechanics*, 125(3):272 – 282, 1999a.

F. Ulm and O. Coussy. The chunnel fire ii: Analysis of concrete damage. *ASCE, Journal of Engineering Mechanics*, 125(3):283 – 289, 1999b.

UNE-83510. *Hormigones con Fibras de Acero y/o Polipropileno. Determinacion del Indice de tenacidad de resistencia a primera fisura (Steel and/or polypropylene fiber concrete. Determination of the toughness index of the first crack strength)*. Spanish Code - In Spanish, 1989.

UNI-11039-1. *Steel fibre reinforced concrete - Definitions, classification and designation*. UNI Editions, Milan, Italy, 2003.

UNI-11039-2. *Steel fibre reinforced concrete - Test method to determine the first crack strength and ductility indexes*. UNI Editions, Milan, Italy, 2003.

UNI-EN-12620. *Aggregates for concrete*, volume Ref. No. EN 12620:2002 E. Europ. Committee for Standardization, Brussels, 2002.

M. Valle and O. Buyukozturk. Behavior of fiber-reinforced high-strength concrete under direct shear. *ACI Materials J.*, 90(2):122–133, 1993.

K. van Breugel. *Simulation of hydration and formation of structure in hardening cement-based materials*. PhD thesis. Delft University of Technology, Delft, The Netherlands, 1991.

J. van Mier, M. van Vliet, and T. Wang. Fracture mechanisms in particle composites: statistical aspects in lattice type analysis. *Mech. of Materials*, 34:705–724, 2002.

I. Vardoulakis and E. C. Aifantis. A gradient flow theory of plasticity for granular materials. *Acta Mechanica*, 87:197–217, 1991.

S. Vrech and G. Etse. Gradient and fracture energy-based plasticity theory for quasi-brittle materials like concrete. *Computer Methods in Applied Mechanics and Engrg.*, 199(1-4):136 – 147, 2009.

R. Walter and J. F. Olesen. Cohesive mixed mode fracture modelling and experiments. *Engrg. Fracture Mechanics*, 75(18):5163 – 5176, 2008.

X. Wang, S. Jacobsen, J. He, Z. Zhang, S. Lee, and H. Lein. Application of nano-indentation testing to study of the interfacial transition zone in steel fiber reinforced mortar. *Cement and Concrete Research*, 39:701–715, 2009.

G. Wells and L. Sluys. A new method for modelling cohesive cracks using finite elements. *Int. J. for Numerical Methods in Engrg.*, 50:2667–2682, 2001.

K. Willam, N. Bicanic, and S. Sture. *Constitutive and Computational Aspects of Strain-Softening and Localization in Solids*. ASME-WAM84, New Orleans, Symp. Vol. G00274 Constitutive Equations: Micro, Macro and Computational Aspects, 233-252, 1984.

Z. Xu, H. Hao, and H. Li. Experimental study of dynamic compressive properties of fibre reinforced concrete material with different fibres. *Materials & Design*, 33(0):42 – 55, 2012.

W. Yao, J. Li, and K. Wu. Mechanical properties of hybrid fiber-reinforced concrete at low fiber volume fraction. *Cement and Concrete Research*, 33(1):27 – 30, 2003.

M. Yip, Z. Li, B.-S. Liao, and J. Bolander. Irregular lattice models of fracture of multiphase particulate materials. *Int. J. of Fracture*, 140:113–124, 2006.

H. Yuan, J. Teng, R. Seracino, Z. Wu, and J. Yao. Full-range behavior of FRP-to-concrete bonded joints. *Engrg. Structures*, 26(5):553 – 565, 2004.

J. Zhang and V. C. Li. Simulation of crack propagation in fiber-reinforced concrete by fracture mechanics. *Cement and Concrete Research*, 34(2):333 – 339, 2004.

Z. Zhang, K. Liew, Y. Cheng, and Y. Lee. Analyzing 2D fracture problems with the improved element-free Galerkin method. *Engrg. Analysis with Boundary Elements*, 32:241–250, 2008.

A. Zubelewicz and Z. Bazant. Interface element modeling of fracture in aggregate composites. *J. of Engrg. Mechanics - ASCE*, 113:1619–1630, 1987.